# Large-eddy simulations of multi-phase plumes in crossflow and stratified flow

Elli Mitrou
School of Engineering
Cardiff University, Wales, UK

Supervised by:
Prof. Thorsten Stoesser
Dr. Bettina Bockelmann-Evans
Prof. Shunqi Pan
Dr. Zhihua Xie

This thesis is submitted in partial fulfilment of the
requirements for the degree of
*Doctor of Philosophy (Ph.D.)*
2020

## DECLARATION

This work has not been submitted in substance for any other degree or award at this or any other university or place of learning, nor is being submitted concurrently in candidature for any degree or other award.

Signed .................. (candidate) Date............

## STATEMENT 1

This thesis is being submitted in partial fulfilment of the requirements for the degree of PhD.

Signed .................. (candidate) Date............

## STATEMENT 2

This thesis is the result of my own independent work/ investigation, except where otherwise stated, and the thesis has not been edited by a third party beyond what is permitted by Cardiff Universitys Policy on the Use of Third Party Editors by Research Degree Students. Other sources are acknowledged by explicit references. The views expressed are my own.

Signed ................. (candidate) Date ..............

## STATEMENT 3

I hereby give consent for my thesis, if accepted, to be available online in the Universitys Open Access repository and for inter-library loan, and for the title and summary to be made available to outside organisations.

Signed ................. (candidate) Date ................

## STATEMENT 4: PREVIOUSLY APPROVED BAR ON ACCESS

I hereby give consent for my thesis, if accepted, to be available online in the University's Open Access repository and for inter-library loans after expiry of a bar on access previously approved by the Academic Standards & Quality Committee.

Signed ................. (candidate) Date ..................

## Acknowledgements

I would like to thank my supervisor, Professor Thorsten Stoesser, for giving me the opportunity to be part of the research group in Cardiff University, for his valuable comments and constructive discussions during my research. I would like to thank Dr. Bruno Fraga for his valuable inputs, guideness and constructive critisism and for sharing his knowledge on bubble plumes' dynamics with me, even though he wasn't one of my official supervisors. Without him, the completion of my PhD would not have been possible. I would like to thank the rest of the research group, Dr. Pablo Ouro and Dr. Ken Chua, for their advise.

My two-month visit in Texas A&M University in Texas, US, was a great experience and it's been a great honor collaborating with such brilliant minds as Professor Scott Socolofsky and Dr. Chris Lai, who helped me to move my research further.

Many thanks to EPSRC for the generous studentship in Water Informatics: Science and Engineering (WISE). Thanks to all the staff involved with WISE CDT from all four partner universities (Bristol University, Bath University, Cardiff University and University of Exeter) for their support during the four years of the programme. Special mention to WISE Cohort 1 PhD students that we started this journey together in 2014.

Last but not least, I thank my parents, Ioannis and Antonia, and my sister, Dem, for their love, unwavering support and understanding in my entire life. I wouldn't be where I stand today, without them by my side.

Cardiff, 2020. Elli Mitrou

# Abstract

The mixing and transport properties of bubble plumes make them an interesting and unique component of environmental and engineering applications, such as destratification and aeration of lakes or reservoirs, prediction of gas release from accidental well blow-outs or from natural vents, chemical and/or nuclear reactors. Understanding the hydrodynamics of the interaction between the gas and liquid phases is essential to predict more accurately their movement and therefore to achieve more efficient results in the aforementioned applications. The description of multi-phase flows has been a challenging task for both Computational Fluid Dynamics modellers and experimentalists, due to the different treatment of the carrier and dispersed phases.

Experimental studies have provided valuable information mainly about the bubbles' characteristics, whilst numerical methods arise as a tool to be used for more detailed study not only of the dispersed phase, but also for the surrounding continuous phase. In this thesis, a high-fidelity large-eddy simulation computational approach is adopted, including a Eulerian-Lagrangian method for the description of the dispersed phase. The combination of these numerical methods offers balance between computational resources and accuracy. The numerical approach is applied and validated with simulations of multi-phase plumes in crossflow and stratified ambient flow. A detailed investigation of the flow mechanisms and the interaction of liquid-gas phases are visualized through 2D and 3D streamlines, isosurfaces of and velocity contours. The numerical results have been thoroughly validated against experimental studies.

This study is among the first to attempt the case of bubble plume in crossflow numerically with a 3D code. And most likely the first one to employ an E-L arrangement, which is, given the limitations of interface tracking methods, among the most accurate applicable to this case. The results are reliable (given by the validation) and the insights provided (such as the Reynold stresses and the turbulent structures) cannot be predicted by other models.

# Contents

# List of Figures

# List of Tables

# Nomenclature

**Abbreviations**

| | |
|---|---|
| ADM | Approximate Deconvolution Models |
| BIT | Bubble-Induced Turbulence |
| CDS | Central Differencing Scheme |
| CFD | Computational Fluid Dynamics |
| CFL | Courant-Friedrichs-Levy |
| CV | Control Volume |
| DIF | Diffusion-number |
| DMM | Dynamic Mixed Model |
| DNS | Direct Numerical Simulations |
| DSM | Dynamic Smagorinsky model |
| EE | Eulerian-Eulerian approach |
| EL | Eulerian-Lagrangian approach |
| FDM | Finite Difference Method |
| FEM | Finite Element Method |
| FVM | Finite Volume Method |
| ICM | Interface-Capturing Methods |
| ILES | Implicit Large-Eddy Simulation |
| ITM | Interface-Tracking Methods |
| LES | Large-Eddy Simulations |
| LKM | Linear Kinematic Model |
| LMR | Local Mesh Refinement |

| | |
|---|---|
| LSM | Level-Set Method |
| PISO | Pressure-Implicit with Splitting of Operators |
| PLIC | Piecewise Linear Interface Calculation |
| QDNS | Quasi-Direct Numerical Solution |
| r.h.s | right hand side |
| RANS | Reynolds-Averaged Navier-Stokes |
| RK | Runge-Kutta |
| SFS | Sub-Filter Scale |
| SGS | Subgrid Scale |
| SIMPLE | Semi Implicit Method for Pressure Linked Equation |
| SIMPLEC | Semi-Implicit Method for Pressure Linked Equations-Consistent |
| SIMPLER | Semi Implicit Method for Pressure Linked Equation Revised |
| SLIC | Simple Line Interface Calculation |
| SM | Spectral Method |
| SSM | Scale-Similarity Model |
| URANS | Unsteady Reynolds-Averaged Navier-Stokes |
| VLES | Very-Large-Eddy Simulation |
| VOF | Volume of Fluid |
| WALE | Wall-Adapting Local Eddy-viscosity |

**Subscripts**

| | |
|---|---|
| $(\cdot)_t$ | turbulent value |
| $\infty$ | single particle system |
| f | fluid |
| g | gas phase |
| l | liquid phase |

**Greek Symbols**

| | |
|---|---|
| $\alpha$ | Fractional phase |
| $\alpha_g$ | Fractional gas phase |
| $\Gamma$ | kinematic diffusivity |
| $\nu$ | kinematic (molecular) viscosity |

| | |
|---|---|
| $\omega$ | magnitude of velocity gradient |
| $\partial$ | Indicates partial derivation operation |
| $\rho$ | fluid density |

**Superscripts**

| | |
|---|---|
| $(\cdot)'$ | fluctuation value |
| $\overline{(\cdot)}$ | time-averaged value |

**Roman Symbols**

| | |
|---|---|
| $C$ | species concentration |
| $C_S$ | Smagorinsky constant |
| $F_A$ | Added mass Force |
| $F_D$ | Drag Force |
| $F_G$ | Gravitational Force |
| $F_L$ | Lift force |
| $F_{TD}$ | Turbulent Dispersion Force |
| $F_{VM}$ | Virtual Mass Force |
| $g$ | gravitational acceleration |
| $l$ | characteristic length scale |
| $p$ | pressure |
| $Re$ | Reynolds number |
| $S_c$ | Schmidt number |
| $T$ | temperature |
| $t$ | time |
| $u$ | Eulerian velocity |
| $\mathrm{Pr}$ | Prandtl number |

# Chapter 1

# Introduction

## 1.1 Motivation

Multi-phase plumes are buoyancy driven flows where the buoyancy is provided by a continuous release of an immiscible dispersed phase, such as gas bubbles, liquid droplets or solid particles (Socolofsky and Adams, 2002). This study is mainly focused on gas bubble plumes, i.e. air bubble plumes. Gas bubble plumes are widely present in natural environments and engineering applications, such as aeration of reservoirs (Fig. 1.1(c) and Fig. 1.1(d)), nuclear reactors (Fig. 1.1(b)), gas leakage from natural vents or/and deep sea blowouts (Fig. 1.1(a)).

Destratification (mixing) or aeration of lakes and/or reservoirs can be achieved by addition of oxygen in order to maintain or improve the water quality for marine/freshwater life and aesthetic reasons (Imberger and Patterson (1989); McGinnis et al. (2004); Schladow (1992)). Thermal stratification during summer may result in lowered dissolved-oxygen levels below the thermocline of lakes and reservoirs. To avoid further deterioration of water quality, artificial destratification has been practiced (Beutel and Horne, 1999). Similarly, bubble plumes can be applied to prevent ice from river surface during winter (Ashton, 1982).

Under this scope, Cardiff Bay Barrage aeration system (Fig. 1.1(d)) has been an example of successful application of bubble plumes (*arup.com* 2018). Cardiff Bay Barrage was built due to the urban regeneration scheme of an area covering 11km$^2$ of South Cardiff and the former docklands. The barrage allows the formation of a freshwater lake, preventing the area from flooding, whilst investments were also attracted into the area. It was completed in April 2001, creating an impoundment of some 1.87km$^2$ and containing 16m$^3$ of water. The Cardiff Bay Barrage Act 1993 requires that the dissolved oxygen content throughout the bay is maintained at 5mg/l or greater. However, model studies and actual measurements showed that this body of water has a tendency to display low oxygen conditions towards its bed during the summer months (*xylemanaltics.co.uk* 2000). The installation of the aeration system was decided because it was the most affordable and most effective solution, as it increases dissolved oxygen by circulating the water within the impoundment for surface reaeration of the water body. Other benefits include destratification and the oxidation of benthic sediments. The work, conducted by Arup CO, included the supply and installation of 28.8km of reinforced self-sinking airlines at the bottom of the lake and in-flowing rivers.

Gas leakage, such as methane, from natural vents or accidental deep sea blowouts of gas and/or oil (Socolofsky et al. (2015); Yapa et al. (1999)) could be caused by deepwater oil and gas exploration, which results the release of multiphase plumes of oil and/or gas in the ocean. A recent example is the Deepwater Horizon oil spill in the gulf of Mexico in April 2010, which is considered to be the largest marine oil spill in the history of the petroleum industry. A key feature of the multiphase plumes in these examples is their ability to mix and transport with the surrounding water. Thus, the efficiency and performance of design would benefit from better understanding of bubble plume behavior depending on the ambient flow characteristics. For oil-well blowouts, mixing and transport determine the locations and toxicity of the impact; hence, mitigation and risk assessment benefit from better understanding of mixing processes in multiphase plumes.

Many processes in chemical, pharmaceutical and nuclear industry involve turbulent gas-liquid flows. The phenomena encountered in these processes are highly complex, such as those in bubble column reactors (Joshi, 2001). In a bubble column reactor, the flow patterns are generated not only by the interactions between the phases on a macroscopic scale, but also relate to small scale flows such as the wakes behind individual rising gas bubbles. The various scales interact and create complex, turbulent flow that is characterized by unsteady (time-dependent), three-dimensional wide range of time and length scales of turbulence, from small vortices shed by bubbles

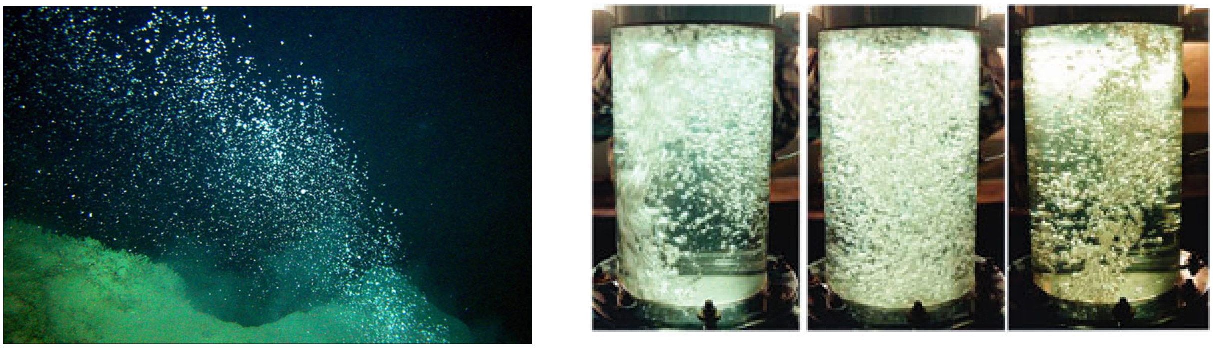

(a) Methane bubbles. Source: Watts, 2018

(b) Bubble swarms oscillating on sparger plate. Source: Rampure et al., 2009.

(c) Lake aeration

(d) Cardiff bay aeration. Source: *arup.com* 2018.

Figure 1.1: Bubble plumes applications

to macroscopic circulation patterns with the size of the reactor. These flow patterns relate to the operating and design variables. Therefore, a descriptive engineering model which provides thorough understanding of the hydrodynamics in gas–liquid bubbly flows is essential for analyzing, optimizing, designing and scaling-up of these processes.

Environmental conditions, such as ambient currents and stratification, are very influential in determining the behaviour of multiphase plumes in their applications. In the presence of ambient current, a multiphase plume will be deflected downstream. As the current becomes stronger, it starts to strip the entrained continuous phase fluid away from the dispersed bubbles, drops, or particles, reducing upward flux of entrained water. Eventually, when the crossflow becomes strong enough, the plume may reach an equilibrium condition where inflow through the plume leading edge is matched to outflow in the downstream wake. In this condition, the upward velocity of entrained fluid is minimized.

In spite of the important influence that crossflow and/or stratification can have on the behaviour of multiphase plumes, there are comparatively few numerical studies, using integral models, for multiphase plumes in the presence of currents (e.g. Dissanayake et al., 2018; Johansen, 2000; Yapa et al., 1999; Lima Neto et al., 2007), and a few quantitative data for velocity fields of multiphase plumes in crossflow (i.e. Zhang and Zhu, 2013; Davidson and Pun, 1999; Socolofsky et al., 2015). To optimize the application of multiphase plumes in environments where currents and/or stratification are present, it is important to improve the knowledge of the behaviour and performance of the multiphase plumes in the aforementioned ambients. For this purpose, this dissertation applies a Large-Eddy simulation method to study bubble plumes, a particular case of a multiphase plume, in crossflow and stratified ambient. This study particularly focuses on the understanding of physical mixing and transport processes in air bubble plumes and the influence of bubble plume on the surrounding environment.

## 1.2 Numerical methods of two-phase flows/ Current challenges

The understanding of the underlying physics of the interaction between the gas and liquid phases has been a challenging task for both Computational Fluid Dynamics modellers and experimentalists. Numerous numerical 2D and 3D simulations have been performed in order to describe and capture the structures of multi-phase plumes (and single-phase plumes) in stagnant ambient fluid.

Multi-phase flows problems require that the carrier and the dispersed phase are treated with different approaches. Three main approaches have been developed in order to simulate the continuous phase and they can be categorized from low to high computational cost into: 1) Reynolds-Averaged Navier Stokes simulations (RANS) with different closures, mostly k-$\varepsilon$ model, that models the entire turbulent spectrum through a turbulence model, solving for the time-averaged flow only; 2) Large-eddy simulation (LES) models that resolve the large-scale and most energetic turbulent motions directly and model only the unresolved subgrid-scale (SGS) effects; and 3) direct numerical simulation (DNS) models that directly resolve the entire turbulent spectra. Even though RANS methods were largerly used until the last decade due to their low computational cost, they rely on empirical closure models in order to simulate the turbulence in the flow. Multi-phase problems though are characterized by significant anisotropic turbulence triggered by the precence of the bubbles in the continuous flow, contrasting the main assumption of RANS models. DNS methods are considered currently as the most accurate approach for the description of turbulent flows, and hence multi-phase flows. However, the high computational requirements of DNS limits the application of the method to fundamental research on the liquid-particles interaction, preventing its employment for problems with large number (thousands or even millions) of particles. LES sits between RANS and DNS, and hence it is a compromise of accuracy and computational cost.

Regarding the dispersed phase simulation and the coupling with the continuous phase, three main approaches have been adopted: 1) Eulerian-Eulerian (EE) approach, i.e. both the carrier phase and the gas phase are computed in the same static Eulerian framework, 2) Eulerian-Lagrangian (EL), i.e. the carried liquid is calculated as in (1) and the gas phase is treated as Lagrangian markers, and (3) Interface Tracking (IT), i.e. the carried liquid is calculated as in (1) and some features of the interface between liquid and gas phases are resolved by the numerical method. Eulerian-Lagrangian based Large-Eddy Simulation (EL-LES) employs Lagrangian Particle Tracking (LPT) to simulate the dispersed phase. Each bubble is represented by a Lagrangian marker which describes a trajectory across the Eulerian mesh according to its own motion equations. EL gives detailed information about every bubble's position, force and velocity. It is more expensive than EE because each particle requires the calculation of a set of equations and a mapping procedure between the Lagrangian and Eulerian coordinates (Sokolichin et al., 1997).

Eulerian-Lagrangian based Large-Eddy Simulation (EL-LES) sits somewhere between EE-LES and IT-LES and it employs Lagrangian Particle Tracking (LPT) to simulate the dispersed phase (Dhotre et al., 2013). Each bubble is represented by a Lagrangian point which moves freely inside the Eulerian fluid mesh according to the Newton's second law of motion and interacts with the carrier fluid. Interface Tracking (IT) methods are the most accurate approach to a bubbly flow but also the most expensive, IT methods are extremely useful for the understanding of the underlying physical mechanisms of the fluid-bubble interactions but should be considered complementary to other, more practical approaches. Bubble-resolved simulations have the ability to predict the generation of bubble-wake-induced turbulence which usually adds to the carrier liquid turbulence and which is reflected in the energy spectrum. Different IT techniques have been developed such as Level Set, Volume of Fluid, Front Tracking or Constrained Interpolation Profile.

## 1.3 Objectives and accomplishments

The main aim of this thesis is the development, refinement and application of a computational methodology in order to simulate the hydrodynamics of gas bubble plumes in crossflow and vertically stratified ambients, with emphasis on the physics and the turbulent structures created by the interaction of bubble plumes with the ambient flow and vice versa. The former has been achieved with the validation of the proposed numerical approach with bubble plume experimental results in crossflow and stratified flows. The latter is accomplished with the study of the effect of ambient currents and stratification in the bubble plumes. The accomplishment of these objectives aim at a better understanding of the underlying physics of the bubble plumes, so that the performance of air bubble plumes will be improved and they can be used as an effective tool for numerous environmental applications.

This study has built on previous studies conducted in the Hydraulic Research Centre (HRC) of Cardiff University with the aid of the in-house-built 3D LES finite-difference Fortran code, named Hydro3D. An EL approach will be applied within a LES turbulence framework. The main challenge was the refinement of the ambient current and stratified ambient conditions in the Hydro3D code and the refinement of the Lagrangian tracker. The applied methodology is presented in Chapter 4. The validation and application are presented in Chapter 5 and 6.

The structure of the thesis is as follows:

- Chapter 2: Literature review of continuous (liquid) turbulent phase using LES. Details about numerical models to describe turbulence, discretization methods, boundary and initial conditions commonly used in LES problems are reviewed.

- Chapter 3: Literature review of dispersed (air) phase, with a review for the forces present between the dispersed and continuous phase and a review of previous dispersed bubbly flows in stagnant ambient.

- Chapter 4: The governing Navier-Stokes equations and the energy equation used in the in-house code Hydro3D are shown together with the description of the fractional-step method adopted. The Eulerian-Lagrangian Particle tracking algorithm for the description of the dispersed phase is presented. The Synthetic Eddy Method (SEM), which is used to generate the velocity inlet boundary for crossflow cases, and the Immersed boundary method, employed to represent the diffuser, are presented.

- Chapter 5: The computational approach is applied to the simulation of bubble plumes in crossflow. An initial validation is performed by analysing and comparing the numerical results with experiments conducted in Texas A&M University. Different crossflows have been applied to study the accuracy of the EL-LES method to represent moving bubbles in crossflow. The LES-computed velocities and Reynolds stresses are plotted against the experimental data. The hydrodynamics and wakes have been studied and visualised, too. The gas-liquid interaction is also highlighted for different gas flow rates.

- Chapter 6: The computational approach is applied for the simulation of bubble plumes in a stratified tank. An initial validation is performed with comparing the numerical results with experiments conducted by Socolofsky, 2001. The hydrodynamics in the tank are visualized by means of streamwise velocity contours, 2D and 3D streamlines and isosurfaces.
- Chapter 7: Conclusions of the thesis and outlook of this research are included in this chapter.

# Chapter 2

# Literature Review - Turbulent Continuous Phase

## 2.1 Role and Characteristics of Turbulence

Advanced numerical methods have been employed to study and solve complex and/or practical problems using numerical computational methods, taking advantage of increasing computational power. Almost all hydraulic flows (geophysical and/or man-made) are turbulent, with the exception of groundwater flows. Turbulence consists of unsteady and irregular eddies changing with time and this causes an additional difficulty in obtaining reliable predictions. Because of the important role of turbulence in hydraulic engineering problems, it is crucial that a realistic description of turbulence and its effects is introduced in computational problems.

Eddies associated with turbulence increase the momentum, heat and mass transfer and hence have significant influence on all aspects of the flow and associated phenomena such as temperature, concentration, distributions, sediment transport, etc. Therefore, a realistic simulation of the effect of turbulence is of major importance for an accurate prediction of the flow and associated phenomena.

The increase in momentum transfer caused by the fluctuating turbulent motion increases the friction on solid boundaries of the flow and as a consequence causes losses in flows through conduits and around structures. It thereby determines the flow rate and pressure drop in conduits and the water level in open channels, and it also determines the rate of energy dissipation. Turbulence has also a governing influence on the details of the flow development, such as the velocity distribution, the pressure distribution in the flow and along its boundaries and hence, the forces on structures, including unsteady forces. For example, turbulence causes the velocity distribution in pipe flow to be much more uniform than in laminar pipe flow (parabolic distribution) and it is turbulence that causes secondary motions in non-circular conduits and open channels.

The mixing due to the fluctuating turbulent motion is responsible for the spreading of jets and the entrainment of ambient fluid and also the dilatation of discharged pollutants; and this mixing is also responsible for the washing out of substances such as pollutants from semi-enclosed regions like bays, harbours and groyne fields, and the turbulence also governs the conditions in tanks and basins of all kinds, whether there is flow through or stirring.

Turbulence is responsible for the suspension of sediment particles, counteracting their settling by gravity, and it is also turbulence that erodes particles from a river bed. Hence, both bed-load and suspended-load sediment transport are governed by the turbulence motion.

Finally, turbulence also controls aeration by controlling the gas exchange and the free surface between water bodies and the atmosphere. It also has a great influence on the water quality by controlling flocculation and biological reactions within the water body.

Turbulent motions carry vorticity with rotation energy axes in all directions. Therefore, turbulent flows can be fairly irregular, unsteady and three dimensional, in contrast to laminar flows which are regular and can be steady as well as two-dimensional or one-dimensional. Turbulence consists of a spectrum of eddy sizes, interacting with each other. The eddy sizes may range from large eddies of the size of the flow domain, e.g. the pipe diameter or jet width, corresponding to low frequency fluctuations, to small eddies at which viscous forces act and dissipation takes place, corresponding to high frequency fluctuations. Flow quantities such as velocity, temperature or concentration undergo complex variations with space and time, manifested by turbulent fluctuations. These turbulent fluctuations cause strong momentum, heat and mass transfer and greatly increase the molecular transfer. The increased transfer and strong mixing are of the most characteristic features of turbulence. Therefore, simulating turbulence and its effects can be challenging for the modeller.

## 2.2 Numerical Approaches for Turbulent Flows

In this section, the three main approaches for simulating turbulent motions and their effects are briefly introduced. The complex details of turbulence are governed by the same basic equations as laminar flows, namely the unsteady 3-dimensional Navier-Stokes equations together with the continuity equation. In case of heat and/or mass transfer, the corresponding scalar transport equation has to be added.

Direct Numerical Simulation (DNS) is the method developed to solve these equations numerically, without introducing any model. In such an approach all scales must be resolved. Hence, the size of the numerical mesh must be smaller than the size of the small-scale motions where dissipation takes place. As the relation of the size of the smallest eddies to the size of the large-scale motion and hence the flow domain varies inversely with the Reynolds number (Reynolds, 1990) and the calculations always have to be 3D, the number of grid points and the computing cost required increase roughly with $Re^3$. As a consequence, for Reynolds numbers of practical relevance the number of grid points required becomes so large that the computational effort required usually exceeds the available computational capabilities. Even at medium Reynolds numbers and for simple flows, the computing effort is enormous. Hoyas and Jimenez (2006) developed a DNS model for plane channel flow at $Re$=87000 (based on channel height and bulk velocity) performed on 1.8x$10^{(10)}$ grid points using 2048 supercomputing processors in parallel for half year. Hence, at present DNS is not a method for practical calculations. However, it is a very useful tool for studying the details of turbulence at lower Reynolds numbers as the complete information on all details of the turbulent motion can be extracted from such simulations.

Computationally cheap numerical methods, without the direct solving of Navier-Stokes equations for turbulent flow, are the Reynolds-Averaged Navier-Stokes (RANS) methods. RANS methods are statistical methods in which the turbulent fluctuations are averaged out and only equations governing mean-flow quantities are solved.

Splitting up the instantaneous flow quantities into mean and fluctuating values and then averaging the non-linear original Navier-Stokes equation leads to the appearance of correlations between velocity fluctuations, which act like stresses on the mean flow and are called turbulent or Reynolds stresses. They represent transport of mean momentum by the turbulent fluctuations. Similarly, averaged scalar transport equations contain correlations representing the transport of heat or mass by the turbulent fluctuations. Hence, the correlations appearing in the averaged equations express the effect of turbulence on the mean quantities. These terms are unknown and must be described by a model before the mean-flow equations can be solved. The computing effort for solving the RANS equations yielding the mean quantities is much less than that required by DNS solving the fluctuating turbulent motion at all scales. Hence, RANS calculations can be performed for realistic problems, even for complex geometries and for larger flow regimes. A wide variety of RANS turbulence models has been proposed and developed and an extensive literature exists on the subject on such models (e.g. Rodi, 1993). Turbulence models of various complexity are in use ranging from the simple mixing-length model to Reynolds-stress models employing differential transport equations for the individual Reynolds stresses. Most models used in practice employ the eddy-viscosity/diffusivity concept and estimate the eddy viscosity by relating it to the mean-flow quantities via simple algebraic relations (mixing-length model) or model transport equations for the characteristic velocity and length or time scales of turbulence (e.g. k-$\epsilon$ model).

RANS methods are economical, but with limited generality and have difficulties in coping adequately with many of the complex flow phenomena often found in hydraulics and environmental flow problems, especially when large-scale structures play a dominant role for the transport of momentum, heat and mass or when details of the flow are important and need to be resolved, such as unsteady processes like vortex shedding or bimodal flow behaviour and unsteady forces on structures or bed elements. RANS methods can be used in unsteady calculations (URANS), but basically they can only cope with the unsteadiness of the mean flow, e.g. when the boundary conditions are time-dependent such as in tidal channel flow. They are suitable only when there is a clear scale separation, i.e. when the time-scale of the mean-flow unsteadiness is clearly larger than the time-scale of the turbulent fluctuations. The latter cannot be resolved in such calculations.

A method more suited and more powerful for solving problems involving the aforementioned complex phenomena is the Large-Eddy Simulation (LES) technique. This method is between DNS and RANS. Like DNS it also solves the 3D time-dependent flow equations, but only for the larger-scale motions in the spectrum that can be resolved on a given numerical grid. The motions with scales smaller than the grid size are filtered or locally averaged out and their effect must be accounted for by a Sub-Grid-Scale (SGS) model. In contrast to a RANS model, which must account for the effect of the entire spectrum of the turbulent motions, a SGS model must account only for the high wave-number part of the spectrum with small-scale motions. The effect of these is mainly dissipative and in some methods (implicit LES) is achieved alternatively by using a numerical scheme which introduces some numerical dissipation. As LES solves the 3D time-dependent Navier-Stokes and continuity equations, they are still computationally rather expensive, often because long running times are necessary to obtain reliable statistics. Away from walls, the larger turbulent eddies containing most of the energy and contributing most to the momentum, heat and mass transfer are virtually independent of Reynolds number, so that here LES does not have a Reynolds number problem as does DNS. However, near walls the length scale of turbulence decreases with increasing $Re$ so that the number of grid points required to resolve adequately the near-wall zone increases approximately with $Re^2$. So, again such wall-resolving LES require so much computing effort that their application is not possible at the high Reynolds numbers often occurring in practice.

## 2.3 Navier-Stokes Equations and Reynolds Averaging (RANS) Methodology

The Navier-Stokes equations, together with a corresponding equation for scalar quantities such as temperature or species concentration, are the fundamental equations of all simulation methods for fluid mechanics, and hence turbulent flows. For incompressible flows these equations expressing the conservation laws for mass, momentum, thermal energy/species concentration read in tensor notation:

- Mass conservation: continuity equation

$$\frac{\partial u_i}{\partial x_i} = 0 \tag{2.1}$$

- Momentum conservation: Navier-Stokes equations

$$\frac{\partial u_i}{\partial t} + \frac{\partial u_i u_j}{\partial x_j} = \frac{1}{\rho_r}\frac{\partial p}{\partial x_i} + \nu \frac{\partial^2 u_i}{\partial x_j \partial x_j} + g\frac{\rho - \rho_r}{\rho_r} \tag{2.2}$$

- Thermal energy / species concentration conservation:

$$\frac{\partial \phi}{\partial t} + \frac{\partial u_i \phi}{\partial x_i} = \Gamma \frac{\partial^2 \phi}{\partial x_i x_i} + S_\phi \tag{2.3}$$

where $u_i$ is the instantaneous velocity component in the direction $x_i$; $p$ is the instantaneous static pressure; and $\phi$ is a scalar quantity which may stand for either temperature $T$ or species concentration $C$. $S_\phi$ is a volumetric source/sink term expressing, for example, heat generation due to chemical or biological reactions or the settling of suspended sediment; $\nu$ is the kinematic (molecular) viscosity and $\Gamma$ is the diffusivity.

The Boussinesq approximation has been used in the above equations (2.1)-(2.3) so that the influence of variable density appears only in the buoyancy term, which is the last term of the right hand side (r.h.s) of Equation 2.2 involving the reference density $\rho_r$ and the gravitational acceleration $g_i$ in direction $x_i$. Together with an equation of state relating the local density $\rho$ to the local values of $T$ and $C$, Equations (2.1)-(2.3) form a closed set and are exact equations describing all details of the turbulent motion, including all fluctuations. The DNS method solves these equations with a suitable numerical technique, introducing no model.

In RANS method, the turbulent fluctuations are averaged out by a time filter applied to the fluctuating motion. In order to make clear the difference to the spatial filtering used in LES, the basics of Reynolds averaging are briefly introduced first, restricting the discussion to the velocity field. Time-averaged/filtered mean-flow quantities are introduced and defined as follows:

$$< u_i >= u_i^{RANS} = \frac{1}{T}\int_0^T u_i dt \quad , \quad < p >= p^{RANS} = \frac{1}{T}\int_0^T p dt \qquad (2.4)$$

The integration/averaging time $T$ should be much larger than the time scale of the turbulent fluctuations but smaller than the time scale of the mean motion if this is unsteady. The instantaneous quantities are split up into mean values and fluctuations around the mean, e.g. for $u_i$:

$$u_i(x_i,t) = u_i^{RANS}(x_i,t) + u^{'}_{iRANS}(x_i,t) \qquad (2.5)$$

Introducing 2.5 into the continuity and the Navier-Stokes Equations (2.1) and (2.2) and averaging according to the procedure in Equation (2.4) yields the Reynolds Averaged Navier-Stokes (RANS) equations governing the mean-flow quantities $u_i^{RANS}$ and $p^{RANS}$ calculated by the RANS method. These equations are formally identical to Equations (2.10)-(2.12) given later. When performed on the non-linear term $\partial u_i u_j / \partial x_j$ in the Navier-Stokes equations, the splitting and averaging procedure leads to the introduction of correlations between fluctuating velocities $< u^{'}_{iRANS} u^{'}_{jRANS} >$. These act like stresses and represent the Reynolds stresses $\tau_{ij}^{RANS} = - < u^{'}_{iRANS} u^{'}_{jRANS} >$ expressing the entire effect of turbulence on the mean motion and require modelling, i.e. a RANS model. Such a model accounts for all scales, including the effect of the large, energy containing ones that depend strongly on the boundary conditions and hence the flow situation considered. For this reason, it has been found impossible to develop a general model which can cope with all situations of practical interest.

## 2.4 The Idea of LES

Turbulence is a multi-scale phenomenon with a wide spectrum of scales of the fluid motion. Large and small scale motions have quite different features. The idea of LES is to calculate explicitly the motion of large scales (or eddies) by solving the governing 3D time-dependent equations and to model the motion of small scales. This avoids the problem of RANS method of having to model also the large-scale, energetic and boundary-condition dependent motion and at the same time the problem of DNS of having to resolve the small-scale dissipative motion. The latter, which represents only a small part of the spectrum, is more universal and hence easier to model than the large-scale motion, and it has been found that quite simple models are often sufficient. The fact that the small-scale motion does not have to be resolved removes the restriction of the method to low Reynolds number situation, which is inherent in DNS.

Figure (2.1a) illustrates the concept of LES in relation to energy flux and energy spectrum. The large scales extract energy from the mean flow (production zone) and transfer it to smaller scales in the energy cascade, and at the small eddies, which are modelled in an LES. The kinematic energy is withdrawn by the mechanism of dissipation (Rodi et al., 2013). An example of turbulent spectrum is given in Figure (2.1(b)), showing the distribution of the kinetic energy of the fluctuations with the wave number k of the turbulence which is proportional to the frequency but is the inverse of the eddy sizes. The $k_{cut-off}$ vertical dashed line (Fig. 2.1(b)) which defines the separation between large eddies and small scale turbulence is achieved via spatial filtering introduced by (Leonard, 1975). This filtering is based on the assumption that the small scales are isotropic and thus easier to model than the large scales which are more energetic and anisotropic. In a well-resolved LES, the cut-off separating the resolved and modelled length scales is usually found in the inertial subrange prior to the dissipation range, as depicted from Figure 2.1. Hence, the most important interaction to be accomplished by the SGS model is that between the large-scale energy-containing unresolved scales and the smallest resolved scales.

The large eddies are generally the most energetic ones and extract energy from the mean motion; they break up into smaller eddies and transfer their fluctuating energy to the smaller eddies with higher frequency fluctuations, a process called energy cascade. This breaking-up and transfer to smaller and smaller eddies continues until viscous forces become active and the fluctuations are damped. The small-scale turbulent motions, where viscous forces act, and also those in the inertial sub-range behave fairly randomly, so that the fluctuations can be described by a Gaussian probability density function. The larger eddies interact with the mean flow and de-

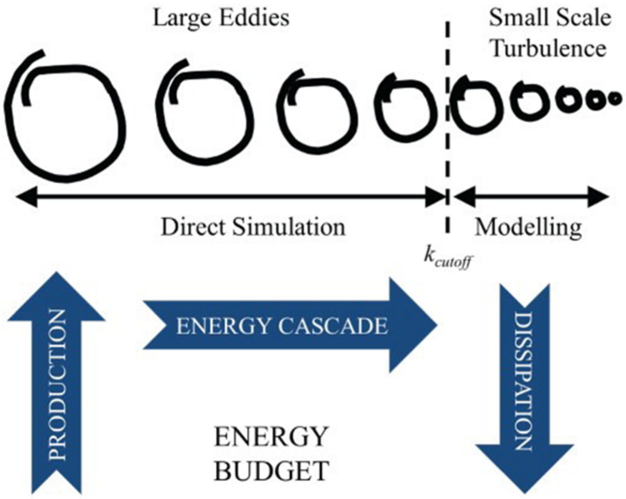

(a) Conceptual model of the LES model. Source: Stoesser et al., 2015

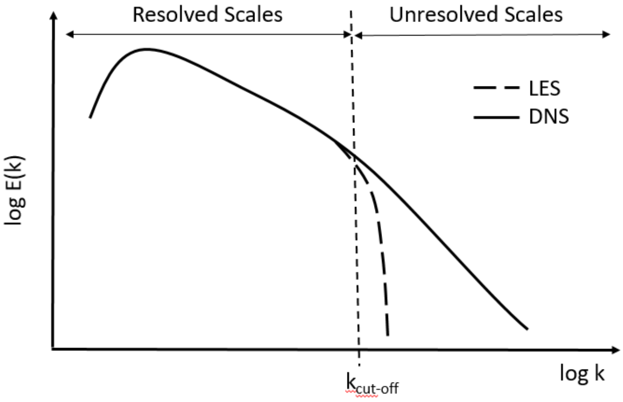

(b) Conceptual model of the LES model, adapted from Breuer, 2002

Figure 2.1: Concept of LES in relation to energy flux and energy spectrum

pend on the boundary conditions and are generally not entirely random, but often have some order and some correlated behaviour and are hence labelled as coherent. These coherent structures have a life-cycle, including birth, development and convection by the mean motion during which they retain their character, interaction between themselves and finally breakdown.

The first step in understanding the LES is to separate the turbulent motion into large scales or eddies to be resolved and small scales to be modelled. Several approaches for this separation will be introduced in the following. Ideally the separation should occur in a spectral region where only energy transfer takes place (i.e. no energy input from the mean motion, no dissipation), that is in the inertial subrange (see spectrum in Figure 2.1) so that clearly the energetic, boundary-condition dependent eddies are resolved and only the dissipative motion needs to be modelled. This is not always feasible, but at least the resolved eddies should contain most of the energy (i.e. $80\% - 90\%$). The scale separation is in practice often dictated by the grid fineness that can be afforded. Hence, LES can also be considered as a method that resolves as much of the motion as possible on a given /affordable grid.

### 2.4.1 Spatial Filtering / Averaging and Resulting Equations

As opposed to the RANS approach involving time averaging or filtering, in LES the small-scale motion is removed by spatial averaging or filtering. Local quantities $f$ are then split into resolved quantities $\overline{f}$ and deviations $f^{'}$.

$$f = \overline{f} + f^{'} \tag{2.6}$$

In practice, on a given grid, it is only the motions with scales larger than the mesh size that can be resolved, and hence the removal of the small-scale motion, and hence the averaging, is performed mostly by the numerical grid. Schumann (1975) introduced a method that resolves directly the discretized volume-balance equations related to the numerical solution. Motions with scales smaller than the mesh size fall through the mesh, and the quantity that is calculated is an average over the control volume formed by the grid.

A more general method independent of the numerical solution is filtering, first proposed by Leonard (1975). The resolved quantity $\overline{f}$ is in the filter method defined by:

$$\overline{f}(r,t) = \int_D G(r,r^{'},\Delta)f(r^{'},t)dV^{'} \tag{2.7}$$

Here $r$ is the location where $\overline{f}$ is to be determined and $r^{'}$ is the location where $f$ is considered in the spatial integration; the integration is performed over the entire flow domain $D$, and $G$ is a compactly supported (i.e. $\overline{f}$ assumes large values when $r^{'} \to r$ filter function with filter width $\Delta$, normalized so that

$$\int_D G(r,r^{'},\Delta)dV^{'} = 1 \tag{2.8}$$

For one spatial direction equation (2.7) reads:

$$\overline{f}(x_i,t) = \int_{D_i} G(x_i,x_i^{'},t)f(x_i^{'},t)dx_i^{'} \tag{2.9}$$

The most commonly used filter functions are the top-hat filter (Fig. 2.2(a)), the cut-off filter (Fig. 2.2(b)), and the gauss filter (Fig. 2.2(c)). For the top-hat filter $G = \frac{1}{\Delta}$ for $|x - x_i| \leq \Delta/2$ corresponding to averaging in this region, otherwise $G = 0$. The cut-off filter corresponds to cutting off all fluctuations beyond a certain wave number $k_{cut-off}$ in the spectrum while top-hat and Gaussian filters lead to a spectral distribution as shown in Figure 2.1(b) by the line designated LES. The larger the filter width $\Delta$, the larger is the part of the small-scale fluctuations filtered out and the smoother the variation of $\overline{f}$. It should be noted that, as opposed to Schumann's volume-balance approach, filtering leads to a continuous $\overline{f}$-function. Also, in general, applying the filter twice smooths further the f-distribution (i.e. $\overline{\overline{f}} \neq \overline{f}$ and also $\overline{f'} \neq 0$) (i.e. Pope, 2000; Sagaut, 2006; Lesieur et al., 2005).

Applying the filter operation to Equations (2.1)-(2.3) leads to the following filtered equations governing the resolved quantities in LES:

- Continuity equation:

$$\frac{\partial \overline{u_i}}{\partial x_i} = 0 \tag{2.10}$$

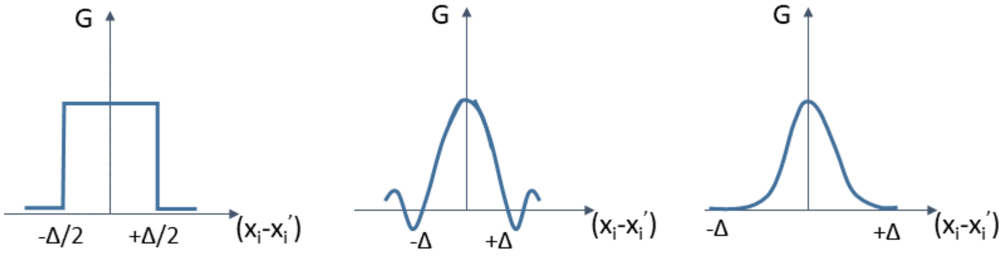

(a) Top-hat (b) Cut-off (c) Gauss

Figure 2.2: Filter functions G commonly used in LES

- Navier-Stokes equations:

$$\frac{\partial \overline{u_i}}{\partial t} + \frac{\partial \overline{u_i}\,\overline{u_j}}{\partial x_j} = \frac{1}{\rho_r}\frac{\partial \overline{p}}{\partial x_i} + \frac{\partial}{\partial x_j}\left(\nu \frac{\partial \overline{u_i}}{\partial x_j}\right) - \frac{\partial \tau_{ij}^{SGS}}{\partial x_j} + g_i \frac{\overline{\rho} - \rho_r}{\rho_r} \tag{2.11}$$

- Scalar transport equation:

$$\frac{\partial \overline{\phi}}{\partial t} + \frac{\partial \overline{u_i}\,\overline{\phi}}{\partial x_i} = \frac{\partial}{\partial x_i}\left(\Gamma \frac{\partial \overline{\phi}}{\partial x_i}\right) - \frac{\partial q_i^{SGS}}{\partial x_i} + \overline{S}_\phi \tag{2.12}$$

The non-linear term $u_i u_j$ in the Navier-Stokes equations (2.2) leads originally to the filter quantity $\overline{u_i u_j}$ in the convection term. When this is expressed as convection of the resolved quantities $\overline{u_i}\,\overline{u_j}$, the difference

$$\tau_{ij}^{SGS} = \overline{u_i u_j} - \overline{u_i}\,\overline{u_j} \tag{2.13}$$

represents the effect of the unresolved fluctuations on the resolved motion, acting like stresses which are therefore called subgrid-scale stresses. These stresses need to be modelled by a subgrid-scale model (see Section 2.5). They are analogous to the Reynolds stresses $\tau_{ij}^{RANS}$ in the RANS approach, but while the latter represent the effect of the entire turbulent fluctuations on the mean motion, $\tau_{ij}^{SGS}$ only accounts for the effect of the small-scale motion. Similarly, in the filtered scalar transport equation (2.12) a term

$$q_i^{SGS} = \overline{u_i \phi} - \overline{u_i}\,\overline{\phi} \tag{2.14}$$

appears which is the subgrid-scale turbulent flux and represents the effect of the unresolved small-scale motion on the resolved scalar field.

When writing according to Equation (2.6) the unfiltered velocities $u_i$ and $u_j$ appearing in the terms on the r.h.s of (2.13) as sum of the resolvable velocities ($\overline{u_i}$ and unresolved fluctuations ($u_i^{'}$), $\tau_{ij}^{SGS}$ can be split up to 3 terms, namely the Leonard stresses describing the interaction of fluctuations of the larger-scale resolvable field, cross terms standing for the interaction of resolvable and unresolvable fluctuations, and a fine-scale term representing the interaction of unresolvable fluctuations, $\overline{u_i^{'}u_j^{'}}$. In Section 2.5, models for the stress term $\tau_{ij}^{SGS}$ that appears in the filtered equation (2.11) are presented.

### 2.4.2 Relation of LES to DNS and RANS

When the filter width or grid size is small enough so that the fluctuations of all scales are resolved, the subgrid-stresses $\tau_{ij}^{SGS}$ go to zero and the original Navier-Stokes equations (2.1)-(2.2) are solved so that the simulation is a DNS. This occurs automatically because subgrid-scale models yield $\tau_{ij}^{SGS} \rightarrow 0$ when the filter width/grid size approaches zero. In the other extreme, i.e. the RANS method, all fluctuations are (time-)filtered/averaged out and only mean-flow quantities are solved for. When the mean flow is unsteady, the method is called URANS (Unsteady Reynolds-Averaged Navier-Stokes) and the time-filtering/averaging removes only the turbulent fluctuations, but not the lower-frequency unsteadiness of the mean flow. In any case, the effect of the entire turbulence, i.e. its fluctuations at all scales, is represented by the Reynolds stresses, $\tau_{ij}^{RANS}$, and needs to be accounted for by a model. In URANS, the equations for solving the mean-flow quantities are the same as the LES equations (2.10)-(2.12) for solving the resolved quantities, and both contain a turbulent stress term $\tau_{ij}$ that needs to be modelled. The difference lies in the model for this stress; while $\tau_{ij}^{SGS}$ requires only a model for the effect of the unresolved small-scale motion, $\tau_{ij}^{RANS}$ requires a model for the entire spectrum of the fluctuations. A RANS model involves velocity and length scales of the turbulence that are characteristic of the energetic, larger-scale motion contributing most to the Reynolds stresses, and the results of a RANS/URANS calculation should be independent of the numerical solution of the equations, including the spatial and temporal discretization. On the other hand, in LES the SGS model depends on the scale separation, i.e. the filter width and in practice generally the grid size, which determines the length scale of the small-scale motion to be modelled by the SGS model; and when the grid size determines the scale separation, the solution is grid dependent and as the discretization is refined approaches the DNS solution.

## 2.5 Subgrid-Scale (SGS) models

Spatial filtering/averaging introduces the Subgrid-Scale (SGS) stresses $\tau_{ij}^{SGS}$ and scalar fluxes $q_i^{SGS}$ for the resolved quantities in the equations used in LES, representing the effects of the unresolved, small-scale turbulence on the resolved/filtered motion. The most common method to account for this effect is through an explicit SGS model for $\tau_{ij}^{SGS}$. An other approach is to account for the SGS stresses through numerical dissipation introduced by the solution procedure (Implicit Large-Eddy Simulation (ILES) methods). However, in hydraulic flows, the most common method is still the use of an explicit SGS model, and in this section some of the most widely used SGS models are introduced.

The primary goal of an SGS-model is to dissipate the correct amount of energy from the directly calculated large-scale flow and to allow for a physically realistic exchange of energy between the resolved scales. A successful SGS model should then yield accurate statistics of the energy-containing scales of motion that are resolved by the simulation. The most important interactions to be modelled by the SGS model are those between the largest unresolved (subgrid) scales and the smallest resolved scales. In a well-resolved LES, the boundary between the resolved (larger) and unresolved (smaller) scales is situated within the inertial subrange (indicated by the thin dashed line in the spectrum in Figure 2.1). The effect of the SGS model on the spectral distribution of energy is visible in the vicinity of the cut-off wave number. Beyond this wave number, i.e. at smaller scales, the SGS model in a LES causes much faster energy dissipation than in the DNS. Figure 2.3 demonstrates the effect of the filter width and hence cut-off wave number on the resulting spectrum in a flow. In the left spectrum a fairly large filter width is used and hence a small cut-off wave number. Thus, the amount of unresolved scales is relatively large so that more SGS modelling effort is required, especially when the unresolved scales

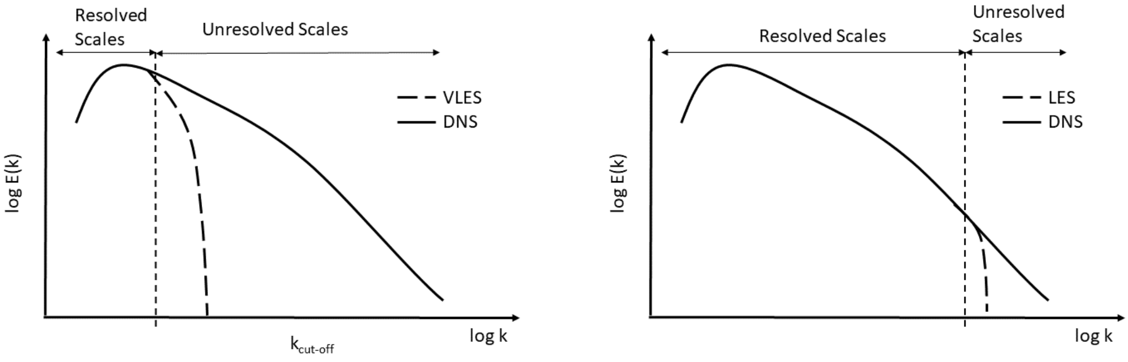

(a) LES spectrum with a large filter width (b) LES spectrum with a small filter width

Figure 2.3: Effect of filter width on the energy spectra of LES vs. DNS spectrum

represent energy-containing, anisotropic eddies. This approach is commonly referred to as Very-Large-Eddy Simulation (VLES). On the other hand, when a considerably smaller filter width is chosen so that the cut-off wave number is at the other end of the inertial subrange (Fig. 2.3(b)), more of the motion is resolved and less modelling effort is required so that quite simple SGS models can be employed.

A well-resolved Large-Eddy Simulation consists of energy conservation, hence one important requirement of a SGS-model is to provide physically correct dissipation, which is the only way the turbulent kinetic energy is removed from the resolved scales. A too large dissipation will artificially increase the diffusive fluxes leading to excessive damping of the resolved scales, decreasing the accuracy of the simulation. A too small SGS-model dissipation will result in a pile up of energy around the cut-off wave number. This results in inaccurate flow statistics or unstable numerical solution. Generally, the subgrid-scale stress tensor $\tau_{ij}^{SGS}$ is split into an isotropic and an anisotropic components as:

$$\tau_{ij}^{SGS} = \underbrace{\tau_{ij}}_{\text{anisotropic}} + \underbrace{\frac{1}{3}\tau_{kk}^{SGS}\delta_{ij}}_{\text{isotropic}} \tag{2.15}$$

The isotropic part of the SGS stress tensor contains the summation of the SGS normal stress $\tau_{kk}^{SGS}$ which is twice the kinetic energy $k^{SGS}$ of the SGS fluctuations and acts like a pressure. This component is therefore usually added to the filtered pressure term, which leads to a new pressure variable:

$$P = \overline{p} + \frac{1}{3}\tau_{kk}^{SGS} \tag{2.16}$$

This separation of the isotropic stress from the anisotropic part is convenient when employing SGS models relating $\tau_{ij}$ to the gradients of the resolved velocity via an eddy viscosity. This is in direct analogy to the use of such a relation in RANS models. The main modelling effort is then shifted to the determination of the eddy viscosity $\nu_t$.

In the following, the most commonly used eddy viscosity models are introduced in some detail, such as the purely algebraic Smagorinsky model and its dynamic variant, the WALE model, and a model employing a transport equation for the subgrid-scale fluctuating kinetic energy $k^{SGS}$. Only a brief overview is given of further models not based on the eddy-viscosity concept, as these are not so widely used.

### 2.5.1 Smagorinsky Model

The most popular eddy-viscosity SGS model is the Smagorinsky model (Smagorinsky, 1963). In analogy to the viscous stress in laminar flows, the anisotropic stress tensor $\tau_{ij}$ is approximated by relating it to the resolved rate of strain, $\overline{S_{ij}}$, which involves velocity gradients, via an artificial eddy (or turbulent) viscosity $\nu_t$ as:

$$\tau_{ij} = -2\nu_t\overline{S}_{ij} \quad \text{in which} \quad \overline{S}_{ij} = \frac{1}{2}\left(\frac{\partial \overline{u}_i}{\partial x_j} + \frac{\partial \overline{u}_j}{\partial x_i}\right) \tag{2.17}$$

It must be emphasized that the eddy viscosity is not a fluid property but characterizes the unresolved sub-grid-scale fluctuations and depends on the resolved velocity field, $\overline{u_i}$. Due to the decomposition of the SGS stress into an isotropic part and an anisotropic part in Equation (2.15), the latter can combined with the viscous stress term in Equation (2.11) and can be treated together in a numerical procedure.

From dimensional analysis follows that

$$\nu_t \propto lq \tag{2.18}$$

where $l$ and $q$ are respectively characteristic length and velocity scales of the subgrid-scale motion.

The selection of the characteristic length-scale $l$ in LES is much simpler and more straightforward than in RANS modelling. In LES, the largest scales of unresolved turbulence, which interact most actively with the resolved motion, are of the size of the filter width $\Delta$. Hence, the characteristic length-scale in the Smagorinsky model is chosen as:

$$l = C_s \Delta \tag{2.19}$$

in which $C_s$ is the Smagorinsky constant, an empirical parameter whose value can be obtained from theoretical considerations or a-priori and a-posteriori tests. The determination of the characteristic velocity scale can be done in analogy to Prandtl's mixing length theory, with the advantage that in LES the length scale is known already.

This leads to:

$$q = l \cdot \left|\overline{S}_{ij}\right| = C_s \Delta \cdot \left|\overline{S}_{ij}\right| \tag{2.20}$$

which yields the eddy viscosity as:

$$\nu_t = l \cdot q = l^2 \left|\overline{S}_{ij}\right| = (C_s \Delta)^2 \cdot \left|\overline{S}_{ij}\right| \tag{2.21}$$

The model has one adjustable parameter, the Smagorinsky constant $C_s$, which is assumed constant in the original formulation of the model. For isotropic turbulence, Lilly (1992) predicted $C_s = 0.165$ based on assuming local equilibrium in the inertial subrange. For shear flows (e.g. channel flows) optimum values were found to be $C_s = 0.065 - 0.1$ (Nezu and Nakagawa, 1993), which can yield a six times difference in the values of $\nu_t$ predicted by the Smagorinsky model. An important shortcoming of the Smagorinsky model is that $\nu_t$ as predicted by Equation (2.21) does not reduce to zero in the viscous sublayer, in which turbulent fluctuations should be damped as impermeable surfaces (i.e. walls) are approached. This is due to the fact that large velocity gradients prevail in the boundary layer and result in high values of the rate of strain $|\overline{S}|$. Hence, the turbulent eddy viscosity $\nu_t$ needs to be damped near impermeable surfaces by a damping function. The most popular of such $f(z^+)$ was proposed by Van Driest (1956) in the mixing length RANS model. It is used in the Smagorinsky model to reduce the length scale $l$:

$$l = C_s \Delta \cdot f\left(z^+\right) \quad \text{with} \quad f\left(z^+\right) = 1 - e^{-z^+/A^+} \tag{2.22}$$

where $z^+ = z u_* / \nu$ is the normal distance to the wall $z$ in wall units and $A^+$ is an empirical constant ($A^+ = 25$).

The Van Driest damping function is easy to implement but does not always produce accurate results. This is partly due to the fact that with the original van Driest damping (Eq. 2.22) all modelled SGS stresses scale linearly with the distance from the wall, i.e. $\tau_{ij} \propto (z^+)$, while the SGS components of the SGS stress tensor should scale with the cubed distance from the wall, (i.e. $\tau_{ij} \propto (z^+)^3$ according to Hinze, 1975). Hence, Piomelli et al. (1989) proposed a slightly modified version of the Van Driest (1956) damping function:

$$f\left(z^+\right) = \sqrt{\left(1 - e^{-z^+/A^+}\right)^3} \tag{2.23}$$

which provides the correct behavior for the most relevant components of the SGS stress tensor and is currently more in use than Equation (2.21).

A second shortcoming of the Smagorinsky model is that it cannot be used to calculate laminar-turbulent transition since the eddy viscosity is only zero if velocity gradients are absent, so that $\nu_t \geq 0$ while in laminar flow $\nu_t$ should be zero. The fact that in turbulent flows $\nu_t \geq 0$ implies that the kinetic energy is transferred only from large resolved scales to small scales, i.e. the Smagorinsky model is strictly dissipative and does not allow for a backscatter of energy from small unresolved scales to large scales.

Furthermore, in complex highly three-dimensional flows (e.g. flow around bluff bodies) the optimum value of $C_S$ varies locally within the flow domain and is basically impossible to determine a priori. The Smagorinsky constant needs to be further modified to account for rotation and stratification effects.

Despite the above mentioned shortcomings of the Smagorinsky model, it has been widely applied to many turbulent flow studies in hydraulic engineering. This is due to its simplicity in terms of calculating the SGS stresses via an algebraic relation and in terms of implementation into a code, for which the total viscosity term can be introduced as:

$$\nu_{total} = \nu + \nu_t \tag{2.24}$$

Furthermore, the Smagorinsky model has only one adjustable parameter, the effect of which on the statistics of the flow vanishes when decreasing the filter width.

Several modified eddy viscosity models were proposed to alleviate the deficiencies of the classical Smagorinsky model. They include the use of a modified velocity scale for the largest unresolved scales which also results in a model that does not need wall damping (WALE model), the use of a dynamic procedure to calculate the model coefficient (dynamic Smagorinsky model) and solving a transport equation for the SGS kinetic energy $k^{SGS}$ which provides the velocity scale of the largest unresolved scales (one equation SGS models). These three approaches will be discussed in the following subsections.

### 2.5.2 Dynamic Procedure

The main idea of the dynamic procedure is to calculate the model parameters of a base model (e.g. the constant $C_S$ when applied to the Smagorinsky model) by using the information available from the smallest resolved scales (Germano et al., 1991). To achieve this, Germano et al. (1991) suggested to introduce a second filter, i.e. a test filter, with width $\tilde{\Delta}$ larger than the original filter $\Delta$, and to employ the same model for calculating the sub-grid-scale stresses $\tau_{ij}$ and the stresses $T_{ij}$ resulting from the sub-test-filter motions. In analogy to Equation (2.13) defining $\tau_{ij}$, the stresses $T_{ij}$ read:

$$T_{ij} = \widetilde{\overline{u_i u_j}} - \overline{\tilde{u}_i \tilde{u}_j} \tag{2.25}$$

where the tilde represents the second (test) filter operation. When the correlation $\overline{u_iu_j}$ in Eq. (2.25) is decomposed into the contribution $\overline{u_iu_j}$ resolved on the grid $\Delta$ and the stresses $\tau_{ij}$ and the second filter is applied, there follows the relation known as Germano's identity:

$$T_{ij} = -L_{ij} + \tilde{\tau}_{ij} \tag{2.26}$$

where

$$L_{ij} = -\widetilde{\overline{u_i u_j}} + \tilde{\overline{u}}_i \tilde{\overline{u}}_j \tag{2.27}$$

representing the part of the sub-test-scale stresses that are resolved between $\tilde{\Delta}$ and $\Delta$, i.e. the smallest resolved scales. This term can be calculated explicitly from the resolved velocities.

For determining the value of the constant $C_S$ in the Smagorinsky model from the smallest resolved velocities, this model (Equations 2.17 and 2.21) is now applied to represent the anisotropic part of both $T_{ij}$ and $\tau_{ij}$ in Equation (2.26):

$$\tau_{ij} = -2\left(C_S \Delta\right)^2 \left|\overline{S}_{ij}\right| \overline{S}_{ij} \tag{2.28}$$

$$T_{ij} = -2\left(C_S \tilde{\Delta}\right)^2 \left|\tilde{\overline{S}}_{ij}\right| \tilde{\overline{S}}_{ij} \tag{2.29}$$

in which the double-filtered strain rate tensor is defined as:

$$\tilde{\overline{S}}_{ij} = \frac{1}{2}\left(\frac{\partial \tilde{\overline{u}}_j}{\partial x_j} + \frac{\partial \tilde{\overline{u}}_j}{\partial x_i}\right) \quad \text{and} \quad \left|\tilde{\overline{S}}_{ij}\right| = \sqrt{2\tilde{\overline{S}}_{ij}\tilde{\overline{S}}_{ij}} \tag{2.30}$$

Inserting $T_{ij}$ from Equation (2.29) and $\tau_{ij}$ from Equation (2.28) with second filter applied into Equation (2.26) yields:

$$L_{ij} = 2(C_S\Delta)^2 \left[\frac{\tilde{\Delta}^2}{\Delta^2}\left|\tilde{\overline{S}}_{ij}\right|\tilde{\overline{S}}_{ij} - \widetilde{\left|\overline{S}_{ij}\right|\overline{S}_{ij}}\right] = 2(C_S\Delta)^2 M_{ij} \tag{2.31}$$

in which

$$M_{ij} = \frac{\tilde{\Delta}^2}{\Delta^2}\left|\tilde{\overline{S}}_{ij}\right|\tilde{\overline{S}}_{ij} - \widetilde{\left|\overline{S}_{ij}\right|\overline{S}_{ij}} \tag{2.32}$$

From the filtered velocity field, i.e. $\overline{u_i}$, a test-filtered velocity field can be calculated explicitly by applying a filter procedure with a larger filter width. Filtered and test-filtered stress tensors, i.e. $\overline{S}_{ij}$ and $\tilde{\overline{S}}_{ij}$, as well as the test-filtered products of the stress tensors or velocities, i.e. $\widetilde{|\overline{S}_{ij}|\overline{S}_{ij}}$ and $\widetilde{\overline{u_i u_j}}$, can then also be calculated explicitly. Hence $L_{ij}$ (using Equation 2.25) and $M_{ij}$ (using Equation 2.32) can be computed to obtain the constant $C_S$. However, since Equation (2.31) is a tensor equation, it contains six independent equations to determine the parameter $C_S$ and can only be satisfied approximately or in some average sense. It should also be mentioned here that the ratio of the filter width $\tilde{\Delta}/\Delta$ appearing in Equation (2.32) is usually chosen as 2.

For closed-channel flow Germano et al. (1991) suggested to average over horizontal planes parallel to the upper and lower wall. Lilly (1992) improved the original averaging procedure by suggesting a least-square procedure to be applied to minimize the error $e_{ij} = L_{ij} - 2(C_S\Delta)^2 M_{ij}$ in Equation (2.30). This allows obtaining the value of $C_S$ that best satisfies the over-determined system of Equation (2.31). For this particular case, the norm of the error is:

$$E^2 = e_{ij}e_{ij} = L_{ij}^2 - 2\left(C_S\Delta\right)^2 L_{ij}M_{ij} + 4\left(C_S\Delta\right)^4 M_{ij}M_{ij} \tag{2.33}$$

The norm of the error is minimum when $dE^2/dC = 0$, in which $C = C_S^2$. This allows estimating $C$ from Eq. (2.34):

$$C\Delta^2 = \frac{1}{2}\frac{L_{ij}M_{ij}}{M_{ij}M_{ij}} \tag{2.34}$$

Calculating the parameter $C\Delta^2$ at each time step based on the resolved flow field is called the dynamic procedure. An advantage of the dynamic-procedure version of the Smagorinsky model (DSM) is that it predicts the behavior of $\nu_t$ near solid surfaces correctly without the need of empirical damping functions. Furthermore, the DSM predicts zero values of $\nu_t$ in laminar flow, and does not require special corrections to account for rotational and stratification effects.

As Equation (2.34) predicts $C\Delta^2$ rather than $C$, the DSM is independent of the definition of the turbulence length scale (e.g. $\Delta = (\Delta_1\Delta_2\Delta_3)^{(1/3)}$ or $\Delta = (\Delta_1^2 + \Delta_2^2 + \Delta_3^2)$, where $\Delta_i$ are the mesh sizes in the individual coordinate directions $x_i$). This is advantageous if mesh cells are strongly anisotropic.

Local and instantaneous negative values for $C$ (or $C\Delta^2$) and hence eddy viscosities are possible, which, in theory, corresponds to the backscatter effect, i.e. an energy transfer from small unresolved scales to large scales. However, negative eddy viscosities tend to destabilize the numerical procedure and should be avoided.

Furthermore, strong variations of $C$ in space and time can also lead to numerical instabilities. One partial remedy is a procedure called clipping, which limits the computed eddy viscosity to values greater than zero i.e. $\nu_t > 0$, or the total viscosity to be greater than zero, i.e. $\nu + \nu_t > 0$. Far more common than the clipping procedure is the application of some sort of averaging procedure, either in space or in time, depending on the flow problem. One possibility is to average the numerator and denominator in Equation (2.34) over one or more homogeneous directions in the flow (if any exist). By applying the spatial averaging operator $\{\}$, Equation (2.34) can be rewritten as:

$$C\Delta^2 = \frac{1}{2}\frac{\{L_{ij}M_{ij}\}}{\{M_{ij}Mij\}} \tag{2.35}$$

In complex three-dimensional flow, i.e. flows in which there is no homogeneous direction, the spatial distribution of $C$ as predicted by the dynamic procedure can be vastly heterogeneous across small regions. This high spatial variability can also generate numerical instabilities, so that instead of averaging over homogeneous flow directions, a local averaging and/or filtering of the predicted field of $C$ is applied. As a (negative) consequence, the result depends on the volume chosen for averaging or on the stencil of the filtering operator. Alternatively, Akselvoll and Moin (1993) applied an averaging procedure in time for fully inhomogeneous flows. They have chosen a special form of time averaging which acts like a low pass filter:

$$C^{n+1}_{filtered} = \left(1 - f_i\right) C^n + f_i C^{n+1} \tag{2.36}$$

here $C^n$ is the value of $C$ from the previous time step. Breuer and Rodi (1994) applied this methodology to the channel flow in a bend. They chose values of $f_i$ of the order $10^{-3}$ so that all high frequency oscillations could be damped out and only the low frequency variations remained.

An alternative averaging approach for applying the dynamic procedure in flows with complex configurations was proposed by Meneveau et al. (1996). These authors suggested using Lagrangian averaging, i.e. the averages in Equation (2.34) are taken over a fluid particle path line (backwards in time).

By using Langrangian averaging in the estimation of the model coefficient, the number of points at which a model predicts negative values and the spatial variability in the values of the dynamic coefficient is reduced. As a result, the robustness of the numerical simulation is improved. The Lagrangian Dynamic Model can also be combined with other models such as the scaled dependent dynamic model (Porte-Agel et al., 2000) and dynamic mixed models (Zang et al., 1993). Sarghini et al. (1999) provide a detailed comparison of the performance of the dynamic mixed model with and without Lagrangian averaging with the dynamic Smagorinsky model and with the constant coefficient Smagorinsky model for 2D channel flows and 3D boundary layers. The use of Lagrangian averaging was found to improve the accuracy of the results compared to implementations in which local or plane averaging was used to estimate the nominator and denominators in the expressions of the model coefficients.

Further methods exist for improving robustness of the dynamic procedure for the Smagorinsky model, especially for inhomogeneous flows. One such approach is the dynamic localization model of Ghosal et al. (1995) in which the integral equation is solved to determine the model coefficient. Several simpler alternatives of the dynamic localization model exist that reduce the computational overhead related to solving exactly the integral equation (e.g. Piomelli and Liu, 1995).

### 2.5.3 WALE model

The Wall-Adapting Local Eddy-viscosity (WALE) model (Nicoud and Ducros, 1999) had found increasing interest recently as it is a relatively simple eddy-viscosity model that can account for wall effects without employing wall-damping functions. Nicoud and Ducros (1999) proposed to use information from the resolved velocity-gradient tensor $g_{ij} = \partial \overline{u}_i / \partial x_j$ to calculate the eddy viscosity. The WALE model uses the traceless symmetric part of the square of $g_{ij}$ to calculate the eddy viscosity as:

$$\nu_t = (C_w \Delta)^2 \frac{\left|G^a_{ij}\right|^{6/2}}{\left(\overline{S}_{ij}\overline{S}_{ij}\right)^{5/2} + \left|\left(G^a_{ij}\right)\right|^{5/2}} \tag{2.37}$$

where $G^a_{ij}$ is the traceless part of $G_{ij} = 1/2(g_{ik}g_{kj} + g_{jk}g_{ki})$. $C_w$ is a model constant for which values in the range of 0.45-0.5 were recommended based on information extracted from simulations of isotropic homogeneous turbulence (Nicoud and Ducros, 1999).

One of the advantages of the model is that it predicts correctly the behaviour of the eddy viscosity near solid surfaces i.e. $\nu_t = O(z^3)$. Another advantage is that the WALE model can be applied to complex geometries with either structured or unstructured grids because no explicit filtering associated with the introduction of a test filter as in the dynamic procedure is needed. Moreover, despite using a constant coefficient, the model predicts a zero value of $\nu_t$ in laminar shear flow (eg., in particular in the case of wall bounded laminar flow) and can be used to correctly simulate flows with regions in which relaminarization or transition to turbulence occur.

### 2.5.4 Transport-equation SGS models

The above introduced SGS models relate the SGS stress tensor locally to the resolved velocity field, ignoring thereby non-local and history effects on the SGS stresses. The simplest way to account for such effects is to use instead of the SGS velocity scale according to Equation (2.20) the turbulent kinetic energy $k = \frac{1}{2}\tau_{kk}$ of the SGS motions as the (square of the) SGS velocity scale and to solve a transport equation for $k$. Hence

$$q = k^{1/2} \tag{2.38}$$

and there follows from Equation (2.18) for the eddy viscosity (Schumann, 1975):

$$\nu_t = C_\nu \Delta k^{1/2} \tag{2.39}$$

and hence for the SGS stresses

$$\tau_{ij} = -2C_\nu \Delta k^{1/2} \overline{S}_{ij} \tag{2.40}$$

here $C_\nu$ is a model constant. In the original model of Yoshizawa (1982), the SGS kinetic energy $k$ is determined from the following model transport equation

$$\frac{\partial k}{\partial t} + \frac{\partial}{\partial x_j}\left(\overline{u}_j k\right) = \frac{\partial}{\partial x_j}\left[\left(\nu + C_k \Delta k^{1/2}\right)\frac{\partial k}{\partial x_j}\right] + 2C_\nu \Delta k^{1/2}\overline{S}_{ij}\overline{S}_{ij} - C_\epsilon \frac{k^{3/2}}{\Delta} \tag{2.41}$$

where $C_\epsilon$ and $C_k$ are additional constants. In Yoshizawa and Horiuti (1985), the model constants were estimated as $C_\nu = 0.05, C_k = 0.1$ and $C_\epsilon = 1.0$.

The above transport-equation SGS model is analogous to eddy-viscosity based transport-equation RANS models. However, in the latter the turbulent length scale appearing in the eddy-viscosity relation and in the dissipation term of the $k$-equation has to be estimated empirically or determined from an additional equation ($\epsilon$-equation or $\omega$-equation in $k - \epsilon$ or $k - \omega$ models, respectively), while in the SGS model the relevant length scale is the specified filter width $\Delta$.

As was mentioned already, neglecting the history and transport terms (terms on the left hand side and 1st term on the right hand side) and equilibrating the remaining production and dissipation terms yields directly the Smagorinsky model according to Equation (2.21). This is again in analogy to RANS models where the assumption of local equilibrium between production of turbulent kinetic energy leads to the zero-equation mixing-length model.

In order to allow a variation and adjustment of the model coefficient, the dynamic procedure can be employed to estimate $C_\nu$ (Menon et al., 1996; Davidson, 1998) as:

$$C_\nu = \frac{1}{2} \frac{L_{ij} M'_{ij}}{M'_{ij} M'_{ij}} \tag{2.42}$$

with $L_{ij}$ being the Leonard stress (Eq. 2.25) and $M'_{ij}$ defined as:

$$M'_{ij} = -\tilde{\Delta} K^{1/2} \tilde{\overline{S}}_{ij} + \widetilde{\Delta k^{1/2} \overline{S}_{ij}} \tag{2.43}$$

where $K$ is the kinetic energy calculated using the test filtered velocities.

In most one-equation SGS models the eddy viscosity in the momentum equations and in the k-equation are identical so that $C_\nu = C_k$. In analogy to the dynamic Smagorinsky model, the constant $C_\nu$ can attain negative values. While negative values of $C_\nu$ are not critical in the $k$-equation, the value of $C_\nu$ in the momentum equations needs extra treatment to ensure numerical stability. Krajnovic and Davidson (2002) suggest a regularization procedure, similar to the procedure used for the dynamic Smagorinsky model.

In principal, one-equation SGS models have several advantages over the standard

Smagorinsky model or the dynamic Smagorinsky model, respectively. An important advantage is the fact that the one-equation model allows for backscatter without destabilization of the numerical solution procedure, because the $k$-equation requires an SGS energy balance. Ghosal et al. (1995) show that this approach is stable and provides always positive values for the SGS energy. One-equation models furthermore provide the correct asymptotic behaviour near solid walls and allow for simulation of transitional flows (Ghosal et al., 1995). Another advantage is that, in theory, no averaging procedure is required when employing a dynamic procedure to determine $C_\nu$ and $C_\epsilon$. On the other hand, in one-equation models it is necessary to solve one extra transport equation, which makes the model computationally more expensive than the dynamic Smagorinsky SGS model. Thus far, one-equation models have been employed primarily in the meteorological community, e.g. Moeng (1984), and to predict flows with combustion (Kim and Menon, 1995), which is because other effects (e.g. buoyancy, large-scale SGS roughness, chemical reactions) play a role for which solving a transport equation offer advantages.

### 2.5.5 SGS Models not Based on the eddy viscosity concept

**Scale-Similarity Model**

The Scale-Similarity Model (SSM) of Bardina et al. (1980) does not use the eddy-viscosity concept. Rather, the idea is to assume that the smallest resolved scales are similar to the largest unresolved scales and to use that information to obtain an expression for the SGS stresses $\tau_{ij}$. This is justified as the most important interactions are those between the largest unresolved (subgrid) scales and the smallest resolved scales. To obtain an expression for $\tau_{ij}$ one has first to define these scales. By definition, the unresolved velocity $u_i^{'}$ (at length scale smaller than $\Delta$) can be written as $u_i^{'} = u_i - \overline{u}_i$, where $u_i$ is the (unfiltered) velocity component and $\overline{u}_i$ is the filtered velocity. The velocity of the largest unresolved scales is defined as $\overline{u_i^{'}}$, yielding with the above decomposition $\overline{u_i^{'}} = \overline{u_i} - \overline{\overline{u_i}}$. Bardina et al. (1980) suggested to also filter the resolved field $\overline{u}_i$ yielding $\overline{\overline{u_i}}$ in order to obtain the smallest resolved scales $\hat{u}_i$ by subtracting $\overline{\overline{u_i}}$ from the resolved velocity, i.e. $\hat{u}_i = \overline{u_i} - \overline{\overline{u_i}}$. This shows that $\overline{u_i^{'}} = \hat{u}_i$ which is justified by assuming that the corresponding scales have similar structures near the cutoff wavenumber. The SGS stresses can now be assumed to be the same as the ones due to the resolved field $\overline{u}_i$, i.e.

$$\tau_{ij} = \overline{u_i u_j} - \overline{u}_i \overline{u}_j \approx C_B \left( \overline{\overline{u}_i \overline{u}_j} - \overline{\overline{u}}_i \overline{\overline{u}}_j \right) \tag{2.44}$$

where $C_B$ is the Bardina constant, for which usually a value of $C_B = 1.0$ is assumed. Compared to predictions obtained with the Smagorinsky eddy-viscosity model, the SSM model showed an improvement in predicting SGS stresses as it can account for backscatter in a physical way. However, the SSM model does not dissipate enough energy from the large scales and is, in most applications, combined with a dissipative model such as the Smagorinsky model, yielding a mixed model.

### Dynamic Mixed Model

Two versions of the Dynamic Mixed Model (DMM) are mentioning in the following. In both models, the SSM model is combined with the Smagorinsky model. The DMM as proposed by Zang et al. (1993), assumes the Bardina constant to be unity and combines the SSM model with the original Smagorinsky model in the following way:

$$\tau_{ij} = \overline{\overline{u}_i \overline{u}_j} - \overline{\overline{u}}_i \overline{\overline{u}}_j - 2 C_S^2 \Delta^2 \left| \overline{S}_{ij} \right| \overline{S}_{ij} \tag{2.45}$$

In the DDM proposed by Salvetti and Banerjee (1995), both coefficients i.e. the Bardina coefficient $C_B$ and the Smagorinsky constant $C_S$ are determined dynamically. In complex turbulent flows, the use of this variant of the DDM has shown that the spatial and temporal variations of $C_S$ are reduced substantially compared to those predicted by the dynamic Smagorinsky model. Even without averaging, the numerical model is much more stable. However, numerical instabilities can still develop if at some locations the backscatter is large and occurs over large periods of time.

### Approximate Deconvolution Models (ADM) and Sub-Filter Scale Models (SFS)

The idea of Approximate Deconvolution Models (ADM) or Sub-Filter Scale (SFS) models, respectively, is to use the information from the filtered (resolved) velocity field to reconstruct, the subgrid (unresolved) and unfiltered quantities. This can, in theory, be done by an inverse filtering, also called deconvolution. However, inverse filtering requires information from the unresolved scales so that the reconstruction can only be approximated. In the Approximate Deconvolution Model (ADM), Stolz and Adams (1999) use a truncated series expansion of the inverse filter to approximate the unfiltered velocity field. This approximation of the unfiltered variables is then used to compute the nonlinear terms in the filtered Navier-Stokes equations, which avoids the need to compute additional subgrid scale terms. Chow et al. (2005) argue that for accurate simulation of high Reynolds number boundary layer flows the resolvable Subfilter-Scale (SFS) stresses should not be neglected. They proposed to use explicit filtering and reconstruction of the velocity field using Taylor series expansion to calculate the resolvable SFS-stresses. For the SGS stresses a dynamic eddy-viscosity model is employed. By combining reconstruction and eddy-viscosity models (eg. the Smagorinsky model) higher order versions of Bardina's mixed model are obtained.

The advantage of the ADM or SFS models is that they contain no parameters and can account for backscatter in a physical way. In a-priori and a-posteriori tests, e.g. turbulent channel flow (Stolz et al., 2001; Gullbrand and Chow, 2003) comparisons between filtered DNS stresses and the ADM or SFS model showed that the stresses predicted by the two models gave improved agreement with DNS over a standard Smagorinsky SGS-model predictions. Another interesting approach is the one of Stolz et al. (2005) who proposed a high-pass filtered eddy-viscosity (Smagorinsky) model in which the variable model coefficients are determined by high-pass filtering of the resolved variables. The model does not need wall-damping functions to correctly predict the viscous sublayer of wall bounded turbulent flows nor a dynamic estimation of the model coefficient. Its performance is similar to that of the dynamic Smagorinsky model (Stolz et al., 2007).

### 2.5.6 SGS Models for the Scalar Transport Equation

In calculations with scalar transport using the LES method, a model for the subgrid scalar fluxes is needed for the solution of the filtered scalar equation. The sub-grid-scale scalar fluxes $q_i^{SGS}$ appearing in the filtered transport equations (2.12) for a conserved or non-conserved scalar $\overline{\phi}$ (e.g. contaminant, concentration of suspended sediment, temperature) can be modelled in direct analogy to eddy-viscosity models through a gradient-diffusion SGS model:

$$q_i^{SGS} = \overline{u_i\phi} - \overline{u}_i\overline{\phi} = \Gamma_t \frac{\partial \overline{\phi}}{\partial x_i} \tag{2.46}$$

where $\Gamma$ is the SGS eddy difusivity. The simplest approach for calculating $\Gamma_t$ is to assume proportionality between eddy diffusivity and eddy viscosity through the turbulent Schmidt number, $Sc_t$ (or in case of temperature the turbulent Prandtl number, $Pr_t$ so that:

$$\Gamma_t = \frac{\nu_t}{Sc_t} \; or \; \Gamma_t = \frac{\nu_t}{Pr_t} \tag{2.47}$$

Typical values for $Pr_t$, or $Sc_t$ are in the range $0.3 - 0.7$ (Deardorff, 1974; Moeng, 1984; Andren et al., 1994).

The use of constant and prescribed turbulent Schmidt or Prandtl numbers can be avoided by employing a dynamic procedure for calculating the SGS turbulent scalar fluxes in analogy to the one for calculating the SGS-eddy viscosity (Moin et al., 1991). The eddy diffusivity $\Gamma_t$ can be calculated with the same algebraic formulation as the one used for the eddy viscosity (Equation 2.21) as:

$$\Gamma_t = C_\Gamma \Delta^2 \cdot \left|\overline{S}_{ij}\right| \tag{2.48}$$

The coefficient $C_\Gamma$, the analogue of the dynamic Smagorinsky constant in the dynamic procedure, is calculated using the resolved velocity and scalar fields:

$$C_\Gamma \Delta^2 = \frac{1}{2} \frac{L_i^{"} M_i^{"}}{M_i^{"} M_i^{"}} \tag{2.49}$$

in which

$$L_i^{"} = \widetilde{\overline{u_i}\overline{\phi}} - \tilde{\overline{u}}_i \tilde{\overline{\phi}} \tag{2.50}$$

is the analogue to the Leonard stress (Eq. 2.27) and

$$M_i^{"} = \frac{\tilde{\Delta}^2}{\Delta^2} \left|\tilde{\overline{S}}_{ij}\right| \frac{\partial \tilde{\overline{\phi}}}{\partial x_i} - \widetilde{\left|\overline{S}_{ij}\right| \frac{\partial \overline{\phi}}{\partial x_i}} \tag{2.51}$$

is the scalar analogue to $M_{ij}$ (given by Equation 2.32). As in the dynamic Smagorinsky model, the test-filtered scalar field can be computed from the resolved (filtered) scalar field. Again an averaging procedure is required to calculate the coefficient $C_\Gamma$. Recent simulations of flow and mass transfer processes over cavities in which both eddy viscosity and eddy diffusivity were computed using the dynamic procedure provided accurate predictions (Chang et al., 2006; Constantinescu et al., 2009).

## 2.6 Numerical Methods

The governing partial differential equations for LES that were introduced in the previous section need to be solved with an adequate numerical method, which is comprised of various components. These components are (a) approximation of the derivatives through algebraic operators, (b) discretization of the physical domain with a computational grid that consists of a finite number of cells, points or elements at which the continuous functions of the variables are represented and (c) solution of the resulting system of algebraic equations for discrete instants in time. In this section, some fundamentals of numerical methods are introduced and only the aspects of special relevance to LES are discussed in more detail. In-depth treatment of the diverse discretization schemes, grid generation techniques and solution procedures of the algebraic equations can be found in standard Computational Fluid Dynamics (CFD) textbooks (e.g. Ferziger and Peric, 2002; Versteeg and Malalasekera, 2007; Hirsch, 2007).

The goal of LES is to simulate three-dimensional, unsteady, turbulent flues and hence methods that were developed for laminar flows or that have been successful in the context of RANS may not be adequate for LES. Moreover, in LES the unsteadiness of the flow that is comprised of eddies of different size, frequency, energy content and longevity, respectively needs to be reproduced correctly. This puts a high demand on the numerical method, which needs to meet certain requirements in terms of its accuracy however, as will be discussed below, a high order of the method alone does not guarantee a correct reproduction of the flow physics.

In general, the accuracy of a large-eddy simulation depends on:

i. the selected discretization scheme to approximate the derivatives in space and time and to some extent its formal order of accuracy;

ii. grid spacing and time step; that is how closely the discrete system approximates the continuum;

iii. the capabilities of the subgrid-scale model used;

iv. the adequacy of the boundary conditions

v. the solution method for solving the incompressible flow equations.

The order of accuracy of the discretization scheme in space and time (i) and the grid spacing and time step (ii) are closely related because the truncation error of the numerical approximation of the derivatives (see section 2.6.1) is generally smaller the finer the grid and the smaller the time step. It should be pointed out already here and will be shown later in the chapter that high-order numerical schemes, in spite of their high formal accuracy, may not be suitable in LES because they may not provide an accurate description of the large-scale eddies and their transport and decay into smaller ones. Furthermore, in most LES the filter width and hence the size of the smallest resolved eddies is specified by the mesh size, and it is therefore the motion of these eddies that is most negatively affected by the truncation error of the numerical scheme. On the other hand, exactly these scales provide information that is used in the subgrid-scale model. Hence, in LES there is a strong interaction between the subgrid-scale model employed and the numerical scheme as well as the grid resolution. This is particularly evident in the method of Implicit Large Eddy Simulation (ILES). The basis of ILES is that, for instance, upwind (biased) schemes produce a certain amount of numerical dissipation, which results in removal of energy mainly from the smaller resolved scales, thereby substituting and avoiding the use of an explicit subgrid-scale model.

In general, the finer the grid, the smaller is the portion of the spectrum that requires modelling and hence the impact of both the subgrid-scale model and the numerical scheme on the solution process. Therefore, the capabilities of the subgrid-scale model (iii) become particularly important when the LES is carried out on coarser grids. This is of relevance in LES of hydraulic interest as in practice the number of grid points and hence the grid spacing that can be achieved is often determined by the available computer hardware.

An important aspect of numerical methods for LES is stability because in LES the computed variable distributions are non-smooth and progressively more heterogeneous as the Reynolds number increases. Hence, certain stability conditions need to be obeyed, which generally results in an upper limit of the time step. Due to the strong interconnection between temporal and spatial scales in LES, the time step should, however, not only be set to achieve numerical stability but should also be compatible to the grid spacing from a physical point of view, as will be explained below in Section 2.6.1

In most LES, and in particular those of practical hydraulic interest, the flow is physically bounded (e.g. free surface, rough walls, inflow boundary), for which adequate boundary conditions are needed (iv). These are often referred to as supergrid models, as they introduce approximations, and inadequate or unphysical boundary conditions can introduce errors to the solution that can easily exceed the errors due to truncation or due to subgrid-scale modelling by several orders of magnitude.

The incompressibility of the working fluid implies that the flow must be divergence free at every instant in time. As a consequence, momentum and continuity equations need to be coupled, resulting in a solution method of the system of governing equations that is prone to inaccuracies (v). In LES, the solution method chosen requires careful consideration with respect to maintaining the conservation properties. In most LES, the above mentioned coupling is achieved through a Poisson-type equation for the pressure, which is solved implicitly using a suitable matrix solution procedure.

In Section 2.6.1, the most often used methods in LES for discretizing the governing equations in space and time are introduced. Section 2.6.2 points out sources of errors in numerical methods and how they influence the numerical solution. Section 2.6.3 introduces basic concepts of the solution of the governing equations for incompressible flows and how LES is affected. Finally, in Section 2.6.4 a number of possibilities on how to discetize complex LES domains are presented. Obviously, this chapter does not (and is not meant to) cover all details of numerical methods in CFD, but is rather tailored to LES in order to safeguard high quality simulations.

### 2.6.1 Discretization Methods

The main numerical methods used in LES are the following:

i. Finite Difference Method (FDM)
ii. Finite Volume Method (FVM)
iii. Finite Element Method (FEM)
iv. Spectral Method (SM)

By far the most two common methods used in LES are finite-difference and finite-volume methods. A few LES have been carried out with the finite element method (e.g. LES of flow around tube bundles by Rollet-Miet et al., 1999), but finite-difference and finite-volume methods are computationally more efficient so that the FEM has not found much attention for LES. Spectral methods are the most accurate ones and offer the fastest solvers, however their numerical properties require the solution of the Navier-Stokes equations in a domain with at least one homogeneous direction, cyclic boundary conditions in this direction and equidistant grids. Spectral methods are very popular for DNS and LES of decaying isotropic turbulence (e.g. Menon et al., 1996) in which the SM is used in all three spatial directions, and for channel flow (e.g. Moser et al., 1999) in which the SM is used in two directions (streamwise, spanwise) and another method, e.g. FD, in the wall-normal direction. The spectral method is very attractive for fundamental studies of turbulent flows but is not very common in the context of LES in hydraulics due to its limitation to very simple geometries. In the following, FDM and FVM are introduced and discussed in more detail.

#### Finite Difference Method (FDM)

The basic idea behind the FDM is to replace the partial derivatives of first and second order that appear in the governing equations of LES with algebraic difference quotients using values at a finite number of discrete points in the flow domain. This

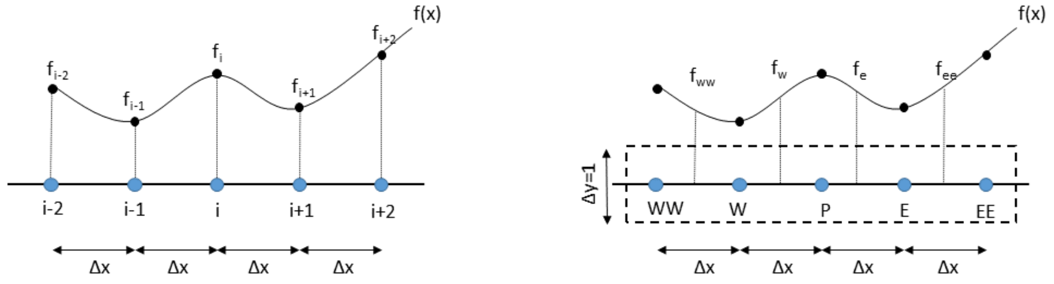

(a) Finite difference

(b) Finite volume

Figure 2.4: Finite difference (a) and Finite volume (b) computational stencils for 1D problems

then leads to a system of algebraic equations for each of the flow variables, which can be solved numerically. The finite-difference method uses Taylor series expansions or polynomial fitting to derive difference quotient expressions for the derivatives at discrete grid points, expressing them through variable values at neighbouring grid points. This is explained here by reference to a one-dimensional variable distribution as shown in Figure 2.4(a).

This figure provides an example of a continuous function $f(x)$, being represented as a series of discrete values $f_i$ at discrete points $(i)$. The value $f_{i+1}$ at point $(i+1)$ can be expressed in terms of a Taylor series expanded about point $(i)$ as:

$$f_{i+1} = f_i + \left.\frac{\partial f}{\partial x}\right|_i (\Delta x)^1 + \left.\frac{\partial^2 f}{\partial x^2}\right|_i \frac{(\Delta x)^2}{2} + \left.\frac{\partial^3 f}{\partial x^3}\right|_i \frac{(\Delta x)^3}{6} + ... \tag{2.52}$$

Similar expansions can be made for other points $(i+2, i-1, i-2, etc)$. Expression (2.52) is exact if an infinite number of terms on the right hand side is retained and/ or if $\Delta x \rightarrow 0$. In a numerical method, Equation (2.51) is truncated and the accuracy of the solution depends on which terms are neglected. The more terms are neglected, the lower is generally the accuracy of the solution. This can be demonstrated by investigating the Finite Difference (FD) approximation of the first derivative of a function $f(x)$, $\partial f/\partial x$. With (2.52) and similar Taylor series expansions for other neighbouring points, the following approximations can be derived:

$$\text{1st Order} \quad \left.\frac{\partial f}{\partial x}\right|_i = \frac{f_{i+1} - f_i}{\Delta x} + \tau_1 \tag{2.53a}$$

$$\text{2nd Order} \quad \left.\frac{\partial f}{\partial x}\right|_i = \frac{f_{i+1} - f_{i-1}}{2\Delta x} + \tau_2 \tag{2.53b}$$

$$\text{3rd Order} \quad \left.\frac{\partial f}{\partial x}\right|_i = \frac{-f_{i+2} + 6f_{i+1} - 3f_i + 2f_{i-1}}{6\Delta x} + \tau_3 \tag{2.53c}$$

$$\text{4th Order} \quad \left.\frac{\partial f}{\partial x}\right|_i = \frac{-f_{i+2} + 8f_{i+1} - 8f_{i-1} + f_{i-2}}{12\Delta x} + \tau_4 \tag{2.53d}$$

The above represent the first order forward (or upwind) difference (2.53a), the third order forward-biased difference (2.53c), and the second (2.53b) and fourth (2.53d) order central-difference approximations. The truncation term, $\tau_m$, represents the higher order terms not accounted for the difference approximations and us the difference between the exact (Taylor) solution of the derivative and its discrete approximation. For instance, the truncation terms of the 1st order forward difference and the 2nd order central difference are:

$$\tau_1 = -\frac{(\Delta x)^1}{2} \left.\frac{\partial^2 f}{\partial x^2}\right|_i - \frac{(\Delta x)^2}{6} \left.\frac{\partial^3 f}{\partial x^3}\right|_i - ... = O\left(\Delta x^1\right) \tag{2.54a}$$

$$\tau_2 = -\frac{(\Delta x)^2}{6} \left.\frac{\partial^3 f}{\partial x^3}\right|_i - \frac{(\Delta x)^4}{120} \left.\frac{\partial^5 f}{\partial x^5}\right|_i - ... = O\left(\Delta x^2\right) \tag{2.54b}$$

The neglect of the truncation terms introduces an error into the finite-difference approximation, and the rate at which this decreases as $\Delta x$ decreases determines the accuracy of the approximation, respectively the order of the scheme ($m$). Comparing the dominant term in (2.54a) with the one in (2.54b) it is seen that, as $\Delta x$ goes to zero, the second order truncation error, $\tau_2$, approaches zero much faster than $\tau_1$. Hence, using the same grid, the 2nd order finite-difference approximations of the first derivative are more accurate than 1st order finite-difference approximations.

The 2nd order finite-difference approximation of the second derivative, $\partial^2 f/\partial x^2$, is obtained by substituting Equation (2.53b) for the first derivative in Equation (2.52), neglecting terms with third and higher derivatives, and solve for the second derivative:

$$\text{2nd Order} \quad \left.\frac{\partial^2 f}{\partial x^2}\right|_i = \frac{f_{i-1} - 2f_i + f_{i+1}}{\Delta x^2} + \tau_2 \tag{2.55}$$

This most commonly used central-difference approximation for the second derivative is second-order accurate, because, on a uniform grid, the leading term in the truncation error involved $(\Delta x)^2$. This approximation is second-order accurate also on non-uniform grids (Ferziger and Peric, 2002). Higher-order approximations (e.g. 4th order) for the second derivative can be obtained by including more neighbouring points however, a fourth order scheme for the second derivatives is only reasonable when convective terms are discretized using fourth order or higher approximations. Furthermore, in convection-dominated flows (as in hydraulic engineering) the gain in accuracy when using higher order approximations for the diffusion terms is minimal and does not warrant the extra computational effort.

In finite-difference schemes (as well as in any other numerical scheme) the accuracy of a simulation depends on both the grid spacing and the chosen difference quotient approximations of the first and second derivative. An important property of finite-difference approximations is that, as the grid spacing approaches zero, all terms in the truncation error approach zero as well. Finite-difference approximations that exhibit such asymptotic behaviour are called consistent, which is an important asset of any numerical solution. However, the choice of consistent and accurate approximations of the spatial derivatives is only one aspect to consider when performing LES.

In general, finite-difference methods are easy to implement into a Navier-Stokes solver, but the finite-difference methods necessitates the computational grid to be structured, which is quite a restrictive requirement when dealing with complex, three-dimensional geometries as are common in hydraulics. The restriction can be relieved by multi-block grids, by using the FDM or curvilinear coordinates, by making use of immersed-boundary method, or by a combination of the three techniques.

### Finite Volume Method (FVM)

In the FV method the governing differential equations are integrated over a finite number of Control Volumes (CVs) that comprise the flow domain (an example of a 2D finite-volume discretization is given in Figure 4.5). This results in a balance equation for each CV that expresses the rate of change of a quantity in the CV as the sum of its flux through the CV faces, and in the case of momentum also of pressure forces acting on the CV faces and of volume forces (such as gravity). Here, the balance equation is, for the sake of simplicity, derived for the general 1D unsteady convection-diffusion equation (without source terms), which reads:

$$\frac{\partial f}{\partial t} + u\frac{\partial f}{\partial x} = \Gamma\frac{\partial^2 f}{\partial x^2} \tag{2.56}$$

in which $u$ is the convective velocity and $\Gamma$ is the diffusion coefficient and, again for the sake of simplicity, $u$ and $\Gamma$ are assumed constant. The most common finite-volume approach is to represent the computational domain by a suitable numerical grid and then locate the computational node at the centroid of the CV (Ferziger and Peric, 2002). This is sketched in Figure 2.4(b) for a Cartesian 1-D finite-volume domain with the CV around node $P$, for which integration of (2.56) between $w(est)$ and $e(ast)$ yields:

$$\int_w^e \frac{\partial f}{\partial t} + \int_w^e u\frac{\partial f}{\partial x}dx = \int_w^e \Gamma\frac{\partial^2 f}{\partial x^2}dx \tag{2.57}$$

resulting in

$$\underbrace{\frac{\partial}{\partial t}\left(\frac{1}{\Delta x}\int_w^e f dx\right)}_{\text{f}}\Delta x + \underbrace{uf_e - uf_w}_{\text{C=net convective flux}} = \underbrace{\Gamma\left[\left.\frac{df}{dx}\right|_e - \left.\frac{df}{dx}\right|_w\right]}_{\text{D=net diffusive flux}} \tag{2.58}$$

In Equation (2.58) the transient term represents the rate of change of the average quantity $\overline{f}$ in the CV, the treatment of which will be discussed below. Convection and diffusion are expressed as surface fluxes (C and D) through the two CV faces devoted $e$ (for east) and $w$ (for west). This flux-balance equation leads to automatic conservation of the quantity considered, one of the advantages of the finite-volume method. As can be seen from equation (2.58), in the FVM the variable values and their gradients at the cell faces appear and have to be obtained by interpolation. The simplest interpolation is a linear one using nodal values of neighboring CVs (W and E in Fig. 2.4b). For a uniform grid, the net convective flux then yields:

$$C = u\left[f_e - f_w\right] = u\left[\left(\frac{f_E + f_P}{2}\right) - \left(\frac{f_P + f_W}{2}\right)\right] = u\Delta x\left(\frac{f_E - f_W}{2\Delta x}\right) \tag{2.59}$$

The term in parenthesis on the r.h.s of Equation 2.59 is exactly the same as derived by the FDM (i.e Equation 2.53b), which is why the linear interpolation between nodes to approximate values at the cell faces in a finite-volume method is referred to as Central Differencing Scheme (CDS). For the net diffusive flux there follows for uniform grid spacing:

$$D = \Gamma\left[\left.\frac{df}{dx}\right|_e - \left.\frac{df}{dx}\right|_w\right] = \Gamma\left[\left(\frac{f_E - f_P}{\Delta x}\right) - \left(\frac{f_P - f_W}{\Delta x}\right)\right] = \Gamma\Delta x\left[\left(\frac{f_W - 2f_P + f_E}{\Delta x^2}\right)\right] \tag{2.60}$$

in which the gradients at the cell faces are estimated using the nodal values on either side of the face. Hence this is referred to as CDS scheme for the diffusive fluxes and corresponds to the FD analogue given in Equation (2.55).

Another popular interpolation assumes that the flow is convection-dominated so that, in the case of u being negative, $f_w = f_P$ and $f_e = f_E$. The resulting upwind-differencing scheme reads:

$$C = u\left[f_e - f_w\right] = u\left[f_E - f_P\right] = u\Delta x\left(\frac{f_E - f_P}{\Delta x}\right) \tag{2.61}$$

The term in parenthesis on the r.h.s of Equation (2.61) is equivalent to the first-order differencing expression derived in the context of the FDM (i.e Equation 2.53a).

The challenge in FV methods is the interpolation from nodal values to CV surface values for which many different schemes of varying order are available. A number of FVM-interpolation schemes have been derived from the finite-difference analogues and can be found in standard CFD text books (e.g. Versteeg and Malalasekera, 2007; Hirsch, 2007). In general, the advantage of the finite-volume method over other methods is that conservation is enforced formally in each CV volume and hence for the entire solution domain. The FV method can be used for complex geometries as it can be implemented for all types of grids. The main disadvantage, e.g. when compared to the FD method, is that FV schemes of accuracy higher than two are more difficult to develop in two or three dimensions.

### Time Discretization

The discretization of the time derivative in the filtered Navier-Stokes equations using finite differences is very similar to the discretization in space, and an approximation analogous to the first-order expression (2.52a) can, for instance, be derived from a Taylor series as:

$$\frac{\partial f}{\partial t} = \frac{f^{n+1} - f^{n}}{\Delta t} + \tau_1 \tag{2.62}$$

in which $f^n$ is the value of $f$ at time $t_n$, $f^{n+1}$ is the yet unknown value of $f$ at time $t_{n+1}$ and $\tau_1$ is the truncation error. For the sake of deriving the fundamental principles of time discretization, the convection-diffusion equation (2.56) is considered and is written as:

$$\frac{\partial f}{\partial t} = -u\frac{\partial f}{\partial x} + \Gamma\frac{\partial^2 f}{\partial x^2} = F \tag{2.63}$$

where $F$ is the sum of the spatial derivative terms for convection and diffusion. Neglecting the truncation term $\tau_1$ and combining Equations (2.62) and (2.63) yields:

$$\frac{f^{n+1} - f^{n}}{\Delta t} = F \tag{2.64}$$

in which the spatial derivatives in $F$ are to be replaced by discrete approximations. Time-discretization schemes in which $F$ is calculated using values at $t_n$ are called explicit, because $F$ can be calculated explicitly using known values only. If $F$ is estimated using values at $t_{n+1}$, an implicit time-discretization scheme results because the right hand side of Equations 2.63 and 2.64 involve yet unknown values of $f$. In general, explicit time-discretization schemes are easier to program and are computationally more efficient than implicit schemes because the latter lead to algebraic difference equations involving several unknowns and require matrix solver. On the other hand, explicit schemes face more restrictions on the time step for numerical stability. However, in LES the stability-restricted time step is also demanded by the physics of the flow, and hence many LES codes employ explicit time discretization schemes.

The simplest time-discretization schemes are explicit and implicit Euler methods, in which the variable $f^{n+1}$ is calculated from:

$$\frac{f^{n+1}-f^{n}}{\Delta t}=F^{n} \tag{2.65a}$$

$$\frac{f^{n+1}-f^{n}}{\Delta t}=F^{n+1} \tag{2.65b}$$

where superscripts $n$ and $n+1$ refer to the instant in time at which the spatial derivatives of the term $F$ are calculated. Euler methods can be considered as the analogues of forward and backward differencing in space and are first-order accurate in time. Euler methods are called two-point methods, because values of $f$ at two instances in time are involved. A second-order accurate two-point method can be constructed by applying the trapezoidal rule to approximate $F$, which yields the (semi)-implicit Crank-Nicholson method:

$$\frac{f^{n+1}-f^{n}}{\Delta t}=\frac{1}{2}\left[F^{n}+F^{n+1}\right] \tag{2.66}$$

It is relatively easy to construct methods of higher order by considering additional values of $f$ in time, known as multi-point methods, or by using values between $t_n$ and $t_{n+1}$, known as predictor-corrector methods. A second order explicit three-point method that is popular in LES (e.g. Thomas and Williams, 1995) is the second order Adams-Bashforth scheme, which reads:

$$\frac{f^{n+1}-f^{n}}{\Delta t}=\frac{1}{2}\left[3F^{n}-F^{n-1}\right] \tag{2.67}$$

Generally, multi-point methods may produce non-physical solutions or tend to be unstable if the time step is large, even when chosen within a given stability limit (Ferziger and Peric, 2002). One way of overcoming numerical instabilities is to use a safety factor on the chosen time step (see discussion of Equation 2.71) or by computing intermediate solutions of $f$ between $t^n$ and $t^{n+1}$, which is known as predictor-corrector or multi-stage method. Runge-Kutta (RK) methods are of this type; for instance, a second order RK method consists of the following two steps:

$$\frac{f^{*,n+1/2} - f^n}{\Delta t} = \frac{1}{2} F^n \tag{2.68a}$$

$$\frac{f^{n+1} - f^n}{\Delta t} = F^{*,n+1/2} \tag{2.68b}$$

where $f^{*,n+1/2}$ is a predicted value at $t_{n+1/2}$ that is being corrected in the second step to provide $f^{n+1}$ using the predicted value $f^{*,n+1/2}$. The method is explicit and does only require values of previous time steps or the initial condition at the first time step, respectively. Since RK methods compute intermediate values between $t^n$ and $t^{n+1}$, they are more stable than multi-point methods such as the Adams Bashforth method and hence are quite popular for LES. Higher-order Runge-Kutta methods are easy to develop however, the higher the order the more intermediate data need to be stored. Hence in LES either the basic second order RK method or "low storage variants" are common (Breuer, 1998; Hinterberger et al., 2008).

The representation of the time derivative in the FVM according to Equation (2.58) is straightforward. For the 1D case described by Figure (2.4b) it is determined as:

$$\int_w^e \frac{\partial f}{\partial t} dx = \frac{\partial \overline{f}}{\partial t} \Delta x \approx \frac{\partial f}{\partial t} \Delta x \qquad \text{with} \quad \overline{f} = \frac{1}{\Delta x} \int_w^e f dx \tag{2.69}$$

in which the volume integral is approximated as the product of the mean integrand and the volume. In the FV method it is assumed that the value at the node is an accurate estimate of the volume-averaged value $\overline{f}$. The time derivative in Equation (2.69) is then treated in exactly the same way as in finite-difference methods and any explicit or implicit method can be employed.

In contrast to RANS, in LES the unsteadiness of the motion is of great importance and hence higher-order time-discretization schemes and small timesteps $\Delta t$ are desirable. In theory, all time discretization methods produce stable solutions if $\Delta t$ is sufficiently small. However, explicit time-discretization methods are subject to rigorous stability conditions, which are generally known as the CFL-condition (Courant-Friedrichs-Levy condition, Courant et al., 1928), and the Diffusion-number

(DIF) condition:

$$CFL = \frac{|u|\Delta t}{\Delta x} < 1 \tag{2.70a}$$

$$DIF = \frac{\Gamma \Delta t}{\Delta x^2} < 0.5 \tag{2.70b}$$

While Equation (2.70a) is important when diffusion is small, Equation (2.70b) is important for diffusion-dominated flows. In LES (and DNS) Equation (2.70a) includes also an important physical constraint on the simulation, i.e. that on a given mesh the time variation (turbulent fluctuations) of the flow corresponding to the variation in space is resolved properly. What follows is that in LES also implicit time-discretization methods should obey the CFL condition and hence most LES use explicit time-discretization schemes, because there is then no need to solve large matrix systems through a matrix solver, which is time consuming. While the CFL condition applies in most regions of flow, the DIF condition becomes important near solid boundaries, which is where viscous forces dominate. This leads to a combined stability criterion commonly used in LES (Miller, 1971):

$$\Delta t < \frac{fac}{\frac{|u_i|}{\Delta x_i} + \frac{2(\nu+\nu_t)}{\Delta x_i^2}} \tag{2.71}$$

where the sum of the molecular and SGS-viscosity $(\nu+\nu_t)$, replaces the diffusion coefficient $\Gamma$ in Equation (2.70b), and $fac$ is an additional safety factor (in LES usually $0.2 < fac < 0.8$) accounting for the non-linearity of the governing equations. Breuer (2002) suggests $fac = 0.2$ for Adams-Bashforth schemes and $fac = 0.6$ for Runge-Kutta based time-discretization schemes, which confirms the above mentioned stability issue of Adams-Bashforth schemes when applied to solving the Navier-Stokes equations. Condition (2.71) can be quite restricitve in wall-resolving LES, where the grid spacing near the wall (especially in the direction normal to the wall) is very small. As a result, the DIF-required time steps (i.e. due to the second part of the denominator in Equation (2.71) where $\nu$ remains finite) can be much smaller than what is needed in terms of reproducing an accurate time dependence of the fluctuations. To avoid the time step to be dominated by the diffusion-number condition, sometimes LES is carried out using an implicit time-advancement such as the Crank-Nicholson scheme (e.g. Krajnovic and Davidson, 2002). An alternative to using an implicit scheme is to do time splitting, that is using an explicit scheme for convective terms and an implicit scheme for diffusive terms. This removes the necessity for very small time steps near the walls and hence makes it a very popular method in LES (e.g. Zang et al., 1993; Salvetti et al., 1997; Armenio et al., 1999; Omidyeganeh and Piomelli, 2011). For instance, for the LES of channel flow over ripples, Zedler (2001) employs the second-order explicit Adams-Bashforth method for the convective terms and the implicit Crank-Nicholson method for the diffusive terms.

Finally, it should be mentioned that in LES the selection of both the time-discretization scheme and the time step should match the selected discretization schemes in space. If as a minimum a second order scheme is used to discretize the derivatives in space, due to the strong interconnection of temporal and spatial scales, a minimum second order time discretization is obligatory. This is particularly relevant in (almost all) LES approaches in which the grid spacing is equal (or proportional) to the filter width and hence the spatial discretization determines the frequency up to which the turbulent fluctuations are resolved and vice versa.

### 2.6.2 Numerical Errors

As discussed above, the numerical scheme can have great influence on the accuracy and quality of LES of turbulent flows and discretization errors influence negatively the simulation results. This aspect will be discussed further by considering the 1D pure advection equation with a constant convective velocity $u > 0$:

$$\frac{\partial f}{\partial t} + u\frac{\partial f}{\partial x} = 0 \tag{2.72}$$

If the convection term is discretized using the first-order backward scheme (which is the backward analogue of Equation 2.53a) and the time derivative is discretized using the explicit Euler scheme (Equation 2.65a), the following discrete equation is obtained:

$$\frac{f_i^{n+1} - f_i^n}{\Delta t} + u\frac{f_i^n - f_{i-1}^n}{\Delta x} = 0 \tag{2.73}$$

The truncation error is $O(\Delta t, \Delta x)$ and the scheme is stable for $CFL = u\Delta t/\Delta x < 1$. Hirt (1968) proposed to replace $f_i^{n+1}$ and $f_{i-1}^n$ in Equation (2.73) by their Taylor series expansions around $f_i^n$ in time and space to obtain the following so-called modified equation (also given in Hirsch, 2007):

$$\frac{\partial f}{\partial t} + u\frac{\partial f}{\partial x} = \frac{u\Delta x^1}{2}(1 - CFL)\frac{\partial^2 f}{\partial x^2} - \frac{u\Delta x^2}{6}\left(2CFL^2 - 3CFL + 1\right)\frac{\partial^3 f}{\partial x^3} + H \quad (2.74)$$

where $H$ represents higher order terms. The r.h.s of the modified equation expresses the difference of the exact solution of Equation (2.72) to the solution obtained from the discrete equation (i.e. Equation 2.73) and hence represents the numerical (truncation) error when using this approximation. The individual terms of the r.h.s of Equation (2.74) can be analysed in terms of their physical meaning. For stability purposes CFL<1, hence the first term on the r.h.s of Equation (2.74) is a positive, diffusion-like term that is proportional to the grid spacing $\Delta x^1$, and hence the term $\frac{u\Delta x^1}{2}(1 - CFL)$ is the numerical (or artificial) viscosity. The effect of this term on the numerical solution is that wave amplitudes are reduced, or in other words, large gradients in the solution are smoothed. The subsequent error is referred to as numerical diffusion. In the context of LES, the artificial diffusion leads to an increase in dissipation of kinetic energy, amplifying the subgrid scale model. If the convective term of Equation (2.72) is discretized using a second-order central-differencing scheme, the term involving the second derivative on the r.h.s of Equation (2.74) disappears and the leading error term involves the third derivative. This impacts the numerical solution by a phase shift of the propagating waves but without altering the amplitude. This term introduces a dispersion error, which does not extract energy from the flow, but it produces numerical wiggles, which can lead to a destabilization of the entire numerical scheme.

The effect of the dissipation and dispersion errors on the numerical solution can be studied by looking at the propagation of a wave of a given amplitude (e.g., assume unit amplitude) and fixed wavenumber $k$. The exact solution of Equation (2.72) governing the transport of a solitary wave is given as:

$$f(x,t) = e^{ik(x-ut)} \quad (2.75)$$

which describes the propagation of a wave of an arbitrary wavenumber with no damping or amplification of its amplitude in time. Ideally, the numerical discretization scheme should preserve the shape of the wave in the discrete solution, i.e. it should not artificially damp the amplitude of the wave or alter its propagation speed. However, due to the fact that the numerical solution is only an approximation this is not the case, and as discussed in the context of Equation (2.74), first-order approximations of derivatives add a diffusion-like term of the form $\alpha \cdot \partial^2 f/\partial x^2$ with $\alpha > 0$ to the pure advection equation, which then takes the form of an advection-diffusion equation:

$$\frac{\partial f}{\partial t} + u\frac{\partial f}{\partial x} = \alpha\frac{\partial^2 f}{\partial x^2} \tag{2.76}$$

for which the exact solution reads:

$$f(x,t) = e^{-\alpha k^2 t} e^{ik(x-ut)} \tag{2.77}$$

The result is that the amplitude of the wave will decay with time but the speed of the wave, $u$, remains the same. The expression of the amplification factor in Equation (2.77) shows that the decay is faster for large wavenumbers, $k$, which corresponds to small wavelengths. Hence, the presence of diffusive terms in the modified equation/ truncation error damps the wave amplitude especially at high wavenumbers.

If the spatial derivative of Equation (2.72) is approximated with a second-order central-differencing scheme, a dispersion-like term of the form $\beta \cdot \partial^3 f/\partial x^3$ with $\beta > 0$, is added so that it becomes:

$$\frac{\partial f}{\partial t} + u\frac{\partial f}{\partial x} = -\beta\frac{\partial^3 f}{\partial x^3} \tag{2.78}$$

for which the exact solution is:

$$u(x,t) = e^{\iota k(x-ut)} e^{-\iota k^3 \beta t} \tag{2.79}$$

The second term on the r.h.s of Equation (2.79) is a complex number with modulus of one. This means that the amplitude of the wave remains equal to one (no dissipation), but the speed of the wave changes from $u$ to $u - \beta k^2$. The wave celerity is now a function of the wavenumber and the error in the wave speed is larger for large $k$

(small wavelengths). Hence, the presence of odd-derivative terms in the truncation error makes the waves propagate at different speeds in the numerical solution, which results in numerical wiggles in the solution especially in regions where the gradients are high.

### 2.6.3 Solution Methods for Incompressible Flow Equations

The solution of the governing LES equations for incompressible flows is complicated by the fact that the pressure does not have its own governing equation. The continuity equation is rather a constraint enforcing a divergence-free velocity field and is mainly used to derive a Poisson equation for determining the pressure. In most numerical methods used in LES, velocity and pressure are solved for sequentially, i.e. the momentum equations are solved first for the three (projected) velocities, and the pressure is solved subsequently from the Poisson equation; its gradients are then used to enforce a divergence-free flow field, i.e. correcting the velocities to satisfy the continuity equation. The procedure is known as the projection method and different prominent variants exist. An alternative is the method of artificial compressibility, but this is hardly used for LES. In the following the two main variants of the projection method are presented and discussed. The first variant is the fractional-step method (Chorin, 1968) which follows the above described three-step procedure, i.e (step 1) solve momentum equations to obtain a projected (not necessarily divergence-free) flow field, (step 2) solve the Poisson equation for the pressure (gradients) using a matrix solver and (step 3) use the obtained pressure gradients to correct the velocity field from step 1. The solution of the momentum equations can be either with an explicit or implicit time-discretization method, but since the Poisson equation is of elliptic nature its solution requires a matrix solver. The second variant of the projection method is the SIMPLE (Semi Implicit Method for Pressure Linked Equation) method. Its main difference to the fractional-step method is that the projected velocity obtained in step 1 is corrected in a multi-step or iterative procedure, which is why it is called semi-implicit. Basically, the SIMPLE procedure is as follows: (step 1) advance the velocity field in time with a guessed pressure field to obtain a projected velocity field, (step 2) solve the Poisson equation for a pressure correction variable, (step 3) correct the pressure using the pressure correc-

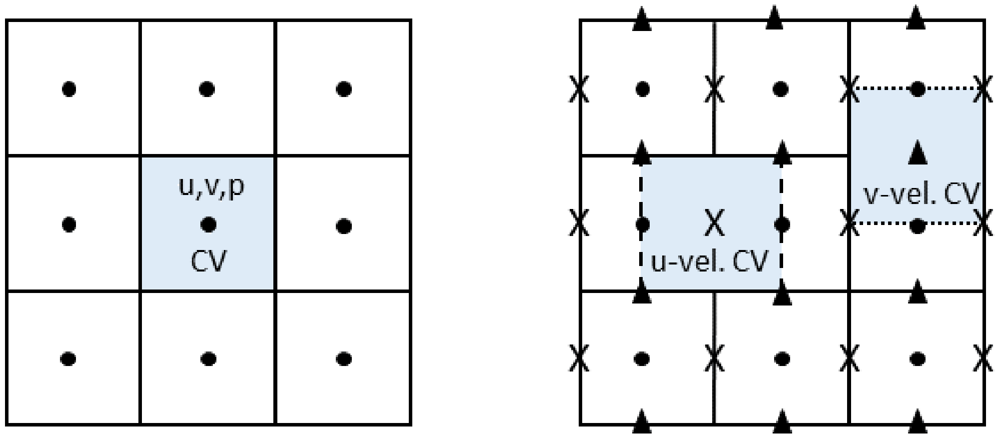

(a) Collated grid (b) Staggered grid

Figure 2.5: Collated (a) and Staggered (b) variable arrangements in Cartesian grid.

tion variable and the velocities using the gradient of the corrected pressure, (step 4) check the updated velocity for continuity and if not fulfilled return to step 2. The SIMPLE method was originally developed for steady flows and its relatively poor convergence rates (mainly due the slow convergence of the Poisson equation) led to several, but only slightly improved schemes, e.g. SIMPLEC, SIMPLER or PISO (Ferziger and Peric, 2002) for such flows. In LES, SIMPLE-type methods have been quite successful as the turbulent flow develops over an initial phase in which the Poisson equation does have to be solved to machine accuracy but only to a certain degree. Once the flow is fully developed, the small timesteps of LES imply that the velocity and the pressure fields do not change much from one instant in time to the next. Hence the projected velocity field is already a very good estimate of the divergence-free velocity field.

The selection of the variant of the projection method depends on the chosen grid. As will be discussed below, grids with a staggered variable arrangement (called simply staggered grids) are advantageous. A staggered finite-volume grid, in which each variable is stored at a different location and has its own Control Volume (CV) is sketched in Figure (2.5b) In this 2D situation, the pressure is stored in the cell center and the velocities are stored at the faces of the pressure cell. This arrangement is more complicated than the collocated grid in which all variables are stored at one location (Fig. 2.5a). However, solving the momentum and Poisson equations on staggered grids removed the necessity of one additional interpolation of the pressure to determine the gradients required in the momentum equations. Hence, this "strong coupling", which also ensures the conservation of kinetic energy allows the use of fractional-step method in contrast to the iterative procedure of the SIMPLE-type methods. However, a staggered arrangement is more difficult to implement, especially for complex geometries using body-fitted curvilinear grids (Fig. 2.6). Grid generation and coding the Navier-Stokes equations for a grid with collocated variable arrangement is much easier. However, solving the momentum equations on a collocated arrangement requires pressure values at the CV faces, which are (linearly) interpolated from the nodal values. This additional interpolation leads to a "decoupling" of velocities and pressure and requires extra treatment, e.g. momentum interpolation (e.g. Rhie and Chow, 1983; Miller and Schmidt, 1988) to avoid unphysical oscillations in the numerical solution. The momentum interpolation adds an additional term to the Poisson equation, which destroys the energy conservation property of the solution process and requires an iterative procedure within the time step to make the flow field divergence free. The order of the space-discretization scheme is not influenced negatively by using a momentum interpolation (e.g. Melaaen, 1992) because the additional momentum interpolation term involves $\Delta x^2$, and hence a 4th order truncation error (Fröhlich, 2006). Direct comparisons of methods using staggered and collocated grids were, however, mainly carried out for steady RANS calculations and not for high-resolution unsteady LES.

Finally, matrix solvers are needed in LES of incompressible flows, either for the velocity variables when an implicit time-discretization scheme is used, but in any case for the solution of the Poisson equation for the pressure. The most efficient matrix solvers are of iterative nature and the set of algebraic equations is solved only to a certain convergence criterion. This criterion is set by the user, but mass and momentum balances need to be fulfilled to a certain degree of accuracy. What follows is that inaccuracies due to non-convergent matrix solutions can become larger than for instance due to the discretization error. However, in general the speed of the solver is more critical than its accuracy and different approaches and acceleration techniques exist (Hirsch, 2007; Ferziger and Peric, 2002; Versteeg and Malalasekera, 2007)

### 2.6.4 LES Grids

The grid provides the discrete representation of the physical domain in which the governing equations are solved. The variables are generally defined at the grid nodes in FDM, or, in case of a collocated grid, in the center of the control volumes in FVM. In the following, the four main types of grids sketched in Figures (2.6)-(2.9) for the flow around a circular cylinder are discussed, as well as their suitability for use in LES.

#### Structured grids

Figure (2.6) depicts a structured, curvilinear 2D grid for the flow around a circular cylinder which consists of grid lines in 2 different directions. The grid nodes are identified using indices for each direction (e.g. $i$ for the x-direction, $j$ for the y-direction for the 2D grid in Figure 2.6). Grid lines in one direction cross only once any grid line in the other direction so that each grid node is uniquely defined as $(i, j)$ in a 2D grid and $(i, j, k)$ in a 3D grid. In the FVM, the finite volume is described by the gridlines connecting the grid vertices (e.g. shaded area Figure 2.5) and has its node in the center of the CV. This results in a simple connectivity matrix and allows the utilization of efficient techniques (sparse matrix solvers) for solving the discretized governing equations. This feature is particularly important in LES and DNS because the solution of the Poisson equation is generally the most time-consuming part of the solution procedure (can take up to 80% of the total CPU time), especially for grids with a large number of points in the three directions. Depending on the shapes of the grid lines, structured grids are classified as H, O or C type (Thompson et al., 1985). The discretization of the governing equations is simpler on Cartesian grids, but for complex geometries curvilinear, boundary-fitted grids are often used in flows of hydraulic interest. The main disadvantage of structured grids is the difficulty to control the distribution of the grid points in domains of complex geometry. Highly skewed and/or high-aspect-ratio grid cells are known to reduce the accuracy of the numerical solution and create convergence problems. The use of structured grids in complex domains often results in clustering of grid points in regions where this is not really needed, hereby increasing unnecessarily the CPU

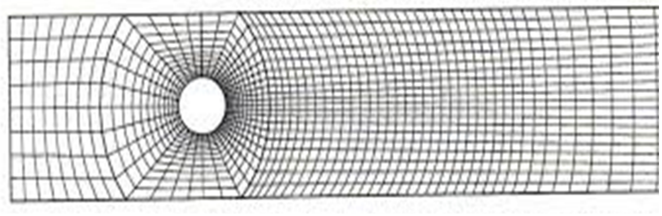

Figure 2.6: A structured, body-fitted, curvilinear grid for channel flow around a circular cylinder.

time. In some cases (e.g. domains with multiple bodies) it is topologically impossible to generate a structured mesh for the whole domain. Some of the problems/ concerns are illustrated in Figure (2.6) for the case of circular cylinder. The grid is refined near the cylinder to account for the large gradients there, but unfavorable grid aspect ratios and grid skewness present in the stagnation regions may lead to inaccuracies and problems with the convergence. The grid is stretched away from the cylinder, and hence a greater discretization error is expected for the wake region. However, if only the near field around the cylinder is of interest, this is accepted deliberately in order to save computating time. Altogether the use of a structured grid is not ideal for this geometry. Alternatives are block-structured grids, or Cartesian grids with Immersed Boundary Method- both are introduced below, On the other hand, structured grids have been applied successfully in many LES of open channel flow in which the channel width and depth does not vary strongly.

### Block-structured grids with matching or non-matching interfaces

For computational domains of complex shape or for domains in which the generation of a single structured grid for the whole domain results in highly skewed grid cells, block-structured grids are the best alternative to structured grids. Figure (2.7) depicts a block-structured grid for the channel flow around a circular cylinder. The original physical domain is divided into two sub-domains, for which in each a structured grid is generated. Here, an O-grid wraps around the cylinder allowing small, orthogonal cells in the vicinity of the cylinder and coarser, slightly skewed cells away from it. In the example depicted here, the O-grid is connected to a stretched H-grid at the downstream side of the cylinder, using the same number of grid points at the

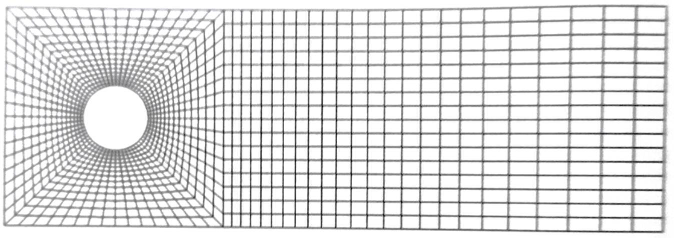

Figure 2.7: A block-structured grid for channel flow around a circular cylinder with an O-grid around the cylinder and an H-grid for the downstream part of the flow.

interface between two neighboring blocks. This is referred to as matching interface. Block-structured grids in LES require an overlap region, and the higher the order of the scheme the larger should be this region. If the number of cells of the grid on either side of the interface is different, the block-structured grid has a non-matching interface and variables have to be interpolated at the boundaries between the blocks. The use of block-structured grid with non-matching interfaces can greatly simplify the grid generation process for complex domains, allowing much more flexibility compared to the case of matching interfaces. This is of interest in LES, because it allows using local refinement strategies with very fine meshes in regions with very high velocity gradients. For the situation depicted in Figure (2.7), a very fine mesh can be used around the cylinder, resolving the boundary layer there, thus allowing for accurate predictions of drag and lift forces. A coarser grid can be then be used in the downstream section of the flow, in which eddies are convected in the direction of one set of grid lines away from the region of interest. The major drawback of non-matching interfaces of block-structured grids is the need to interpolate the variables between blocks, which violates the conservation properties. They are of particular importance in LES, as their violation tends to introduce errors of dissipative nature, and hence the quality of LES diminishes. Finally, block-structured grids with completely overlapping blocks should be mentioned, which are known as Chimera grids. To date, such grids are used mainly in RANS simulations of flows with moving bodies.

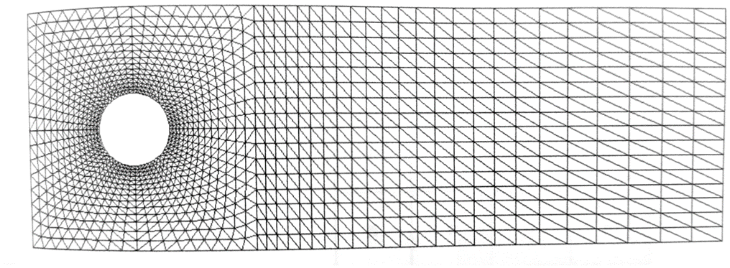

Figure 2.8: An unstructured grid for channel flow around a circular cylinder allowing for clustering a large number of elements near the cylinder.

### Unstructured grids

An alternative to block-structured grids are unstructured grids in which the CVs can have a variable number of neighbors (Fig. 2.8). Unstructured grids have the highest degree of flexibility in terms of the capability to generate grids for very complex domains, thereby clustering the grid nodes in regions where this is required as well as relatively rapid, but gradual, transition in cell size when moving away from the region of interest. Unstructured grids have become very popular in commercial CFD solvers due to their ability to represent any geometry. Subsequently, a number of commercial grid-generation software packages became available, with which grids can be generated rapidly and automatically, even under a certain number of constraints (e.g. minimum/maximum volume of the CV, total number of CVs in the sub-domain, maximum skewness allowed for the CVs, etc). The irregularity in the data structure is the main reason why the solvers used to invert the system of discretized equations are much slower than those for structured grids. Of particular importance for LES is the use of Finite Volume (FV) method with unstructured grids. Even for very complex domains, the discrete conservation of mass and momentum can be exactly satisfied. The use of unstructured grids with hexahedral elements is recommended for LES, especially in regions with large velocity gradients. Based on experience with LES on unstructured grids, tetrahedral or mixed tetrahedral and hexahedral elements can introduce unphysical oscillations in the solution.

### Structured Grids Together with the Immersed Boundary Method (IBM)

The IBM method (eg. see Mittal and Jaccarino, 2005; Iaccarino and Verzicco, 2003; Fadlun et al., 2000) is another alternative of increasing popularity that allows simulations in very complex domains. Though originally proposed as a method to be used in conjunction with Cartesian or cylindrical grids, it can, in theory, also be used in any grid environment. In the IBM, the grid does not need to conform to the shape of the physical domain boundaries, and modifications are needed in the solution of the Navier-Stokes equations to properly account for physical boundaries not represented explicitly by the grid. Figure (2.9) depicts the simplest and most efficient grid, i.e. a structured Cartesian grid, to be employed together with the IBM for the simulation of channel flow around a circular cylinder. The physical domain boundaries of the cylinder are immersed or embedded within the grid and the no-slip boundary condition of the cylinder requires extra treatment. The general idea is to account for the presence of the boundaries of an object in a flow domain by adding forcing terms in the governing flow equations in the vicinity of the immersed boundary.

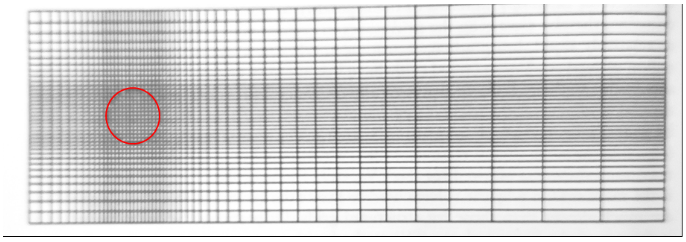

Figure 2.9: A structured, Cartesian grid for channel flow around a circular cylinder using the immersed boundary method.

An example of a typical immersed boundary treatment is illustrated in Figure (2.10). The body is immersed in the Cartesian grid and the velocity of the fluid in the boundary is known, i.e. through the no-slip condition. The no-slip condition is imposed on the surrounding fluid by adding a force term to the momentum equations, in Figure (2.10) at the first grid node inside the immersed boundary. The magnitude of the force is such that enforces a pre-determined target velocity for that node, and the target velocity is determined through a reconstructed velocity field using the values

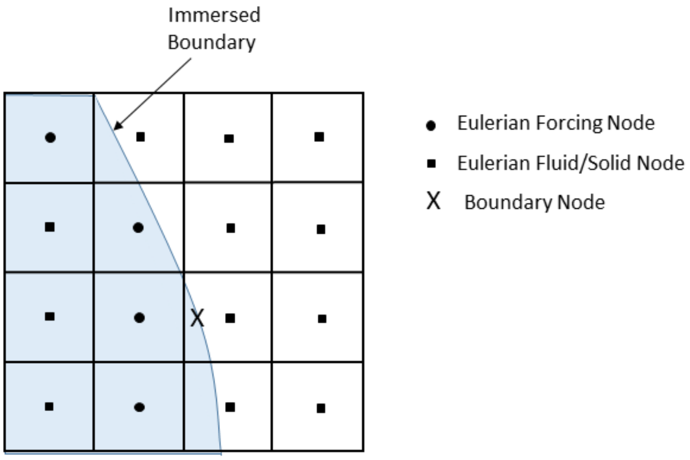

Figure 2.10: Illustration of the immersed boundary method.

from the neighboring (fluid) grid nodes and the no-slip velocity on the immersed boundary. Several interpolation schemes are available and detailed reviews of the different approaches are provided by Iaccarino and Verzicco (2003) and Mittal and Jaccarino (2005).

The IBM method is particularly powerful for simulations with moving boundaries due to its simplicity and accuracy, which makes it very attractive for LES of such flows. In such simulations, the underlying (Cartesian/cylindrical) grid is stationary, which ensures the observation of conservation principles, and at the same time allows the use of fast and efficient sparse matrix solvers. The IBM has been successfully used in a number of simulations of hydraulic interest, for instance for the flow around artificial submerged vegetation (Stoesser et al., 2009), the flow of meandering channel with large bedforms (Kang et al., 2011) or the flow through a porous bed.

## 2.7 Boundary and Initial Conditions

Large Eddy Simulations are carried out in finite-size computational domains chosen by the user. Boundary conditions must be specified at all boundaries of this domain, as well as initial conditions for the dependent variables within the entire domain at the start of the simulation in order to solve the governing differential equations. The computational domain depends strongly on the geometry and flow conditions of the problem considered. The boundaries of the computational domain can be of various types, for example the physical boundaries (the bed consisting of a solid or permeable wall and the free surface). The wall boundary at the bed may be horizontal or inclined. Vertical man-made walls or/and idealized vegetation elements may also be present as physical boundaries. In addition, artificial boundaries are usually introduced in order to limit the size of the calculation domain. An inflow and an outflow boundary needs to be chosen by the user limiting the domain in the streamwise direction. However, the domain can be limited in other directions when the flow is considered statistically homogeneous by introducing artificial periodic boundaries. Often the conditions at the boundaries cannot be formulated to represent exactly the real physical conditions prevailing at the boundaries, e.g. when details of a rough wall are unknown or velocity fluctuations at the inflow or at a free surface need to be approximated. Hence models are necessary for these approximations and these are named super-grid models. The uncertainties and possible errors introduced due to such super-grid modelling can be orders of magnitude larger than those due to subgrid-scale modelling and hence the quality of a LES is generally greatly affected by the treatment of each boundary in the numerical simulation.

The specification of boundary conditions depends on the numerical procedure employed. In finite-volume methods, conditions must be provided that allow the evaluation of the convective and diffusive fluxes at the faces of the numerical control volumes coinciding with boundaries in the discretized filtered Navier-Stokes equations. This requires the specification of either the fluxes or the values of the dependent variables at the boundaries, or a means to express these as a function of interior data. This amounts to either specifying values at the boundaries, e.g. all three velocity components at the inflow plane, called Dirichlet condition, or the specification of fluxes generally involving gradients, such as at the outflow or at walls, in a Neumann condition. A third possibility is to apply periodic conditions when periodicity of the statistical quantities in certain directions can be assumed. This approach is popular and often employed as a physically more realistic alternative to inlet/outlet conditions, especially when details of the flow at the inlet/outlet are needed to ensure accuracy of the calculations in a domain but are not known, and in cases with homogeneity of the flow in certain directions to keep the size of the computation domain in these directions relatively small.

### 2.7.1 Periodic Boundary Conditions

Periodic conditions can be used at artificial boundaries when the flow is statistically homogeneous in a certain direction or the geometry is periodic in one or two directions. Examples where periodic boundary conditions in natural flows can be applied are given in the following.

A developed open channel flow where periodicity in the streamwise direction prevails as the distribution of statistical quantities over the cross section is the same at each cross section. In wide open channels, i.e. without the influence of side walls and in the absence of secondary motions, the flow is homogeneous in the spanwise direction and hence periodicity can be assumed also in this direction. Further, for instance in cases with dense emergent vegetation, bottom friction is negligible and the numerical simulation resolving the flow around the individual vegetation elements is to good approximation homogeneous in the vertical direction. Hence not the entire depth needs to be covered in the calculation but only a slice assuming vertical periodicity which allows to reduce considerably the number if grid points required.

The flow over a cube matrix exhibits geometric periodicity in stream- and spanwise direction. When the vertical planes bounding the computational domain are chosen such that they lie in the middle between consecutive cubes in either direction, then the statistical quantities are the same on opposite planes and hence periodic conditions can be applied. The flow between the planes is in this case of course not homogeneous and the instantaneous flow is not periodic; it is characterizes by turbulent structures, the largest of which carry the biggest amount of kinetic energy and hence these large structures are the greatest contributors to the flow statistics. This implies that the extent of the computational domain at whose boundaries periodicity is enforced has to be selected with great care. If the distance between streamwise periodic boundaries is considerably smaller than the size of the largest turbulence structures occurring in the flow, such structures will be artificially confined within the domain, which leads to a non-physical flow behaviour and hence to erroneous statistics. Therefore the proper choice of distance between periodic boundaries is essential in a LES that uses periodic boundary conditions. For an open-channel flow over a smooth bed the minimum distance between streamwise periodic boundaries, $l_x$, can be estimated to be six times the water depth, $h$, assuming that the longitudinal extent of the largest turbulence structures is typically less than three times the water depth. The spanwise distance between periodic boundaries in the cross-streamwise direction is not as critical as that in the streamwise direction; however structure lock-in in the spanwise direction should be avoided by proper choice of the spanwise distance, $l_y$, which can be estimated to be at least twice the water depth. Using periodicity in the vertical direction in emergent vegetation flow, the vertical extent of the domain should be of the order of the distance between vegetation elements in order to resolve all relevant turbulent structures.

The numerical treatment of periodic boundaries is such that on both ends of the simulation domain so-called ghost cells are added to the domain and the variables at one side of the domain are copied after every computed time step into the ghost cells of the other side and vice versa. In spanwise and vertical directions, all variables i.e. the three velocity components and the pressure are exchanged, which requires no further treatment. In the streamwise direction a pressure gradient is required between upstream and downstream end that balances the shear stresses acting on the walls. Usually, pressure values are also exchanged and an external force that drives the flow is added to the filtered momentum equations as a source term. The magnitude of the force is chosen to ensure a constant mass flux.

### 2.7.2 Outflow Boundary Conditions

The outflow boundary in a LES is artificial boundary and has to be placed as far downstream of the region of interest as possible. However, the distance between the region of interest and the outflow boundary is constrained by the relatively high resolution requirements of LES so that the most important condition to be satisfied is that the region of interest is not affected by the artificial conditions imposed at this boundary. Due to the elliptic nature of Navier-Stokes equations, the outlet boundary conditions affect the flow in the upstream direction, but as most flows in hydraulic engineering are convection dominated, in effect the values at the boundary have only minor influence on the solution inside the domain. For such flows, the easiest way to approximate the values at the outlet boundary is to assume zero gradients along streamwise gridlines, which is an extrapolation of 0th order. For the convective terms this treatment yields:

$$\frac{\partial u_i}{\partial x_i} = 0 \tag{2.80}$$

Diffusive fluxes are approximated with one-sided differences. In situations where obstructions cause larger and persistent eddies, the outflow boundary cannot be placed sufficiently far downstream and hence the condition (2.80) is not applicable. In this case eddies are convected to the outlet and may result in negative velocities there, so that instantaneously fluid enters the domain. This scenario would lead to a negative pressure gradient near the outlet and hence to numerical oscillations which can travel upstream and destabilize the flow in the interior of the domain. Damping of such pressure oscillations can be achieved by grid stretching or by artificially increasing the viscosity in the vicinity of the outlet. With that, eddies are artificially stretched and/or weakened and possible pressure oscillations are decreased.

A more physically reasonable and now mostly used alternative to damping the turbulence near the outlet is to employ a convective boundary condition. This condition requires solving an unsteady 1D convection equation along streamwise gridlines, i.e.

$$\frac{\partial u_i}{\partial t} + U_{conv}\frac{\partial u_i}{\partial x} = 0 \tag{2.81}$$

This equation is solved for the velocity components on the boundary using a first order backward difference scheme to compute the spatial derivative and an explicit discretization scheme for the time derivative. The convective velocity $U_{conv}$ can be set in such a way that global mass conservation is achieved. The convective boundary condition is today the standard and preferred outlet condition for LES and has been found to work well in many applications including flow around a circular cylinder (Breuer, 1998), flow over a backward facing step (Le et al., 1997), or the flow over a hill (Garcia-Villalba et al., 2009).

### 2.7.3 Inflow Boundary Conditions

In LES the inflow boundary is usually an artificial boundary at which values of the quantities to be computed, i.e. $u_i$ and $p$, have to be specified. As mentioned above, flows in hydraulics are convection dominated, hence the values specified at the inflow boundary influence greatly the values inside the calculation domain. As a consequence, in open-channel flow simulations physically realistic velocity and pressure values are needed at the upstream end of the domain. The easiest and by far the most common treatment of the inlet boundary is to prescribe the velocity contribution over the inlet as a Dirichlet boundary condition and to extrapolate the pressure from the inside to the inlet plane. However, in contrast to RANS calculations not only the time-averaged velocity distribution is required but also the specification of physically realistic velocity fluctuations is needed. This poses a significant challenge in LES, since high resolution (spatially and temporally) velocity data at the inlet plane of the flow domain, for instance from experiments, is rarely available.

In some situations, where the approach flow is uniform and virtually free of turbulence, or when the turbulence and large-scale flow structures are a result of flow separation inside the calculation domain, prescription of a time-averaged velocity profile at the inflow boundary may be sufficient. Examples for this are the flow over a backward facing step (Fureby, 1999; Le et al., 1997) or the flow around long square and circular cylinders (Rodi et al., 1997; Breuer, 2000). In the first two cases the location of flow separation is predefined through the geometry (sharp corners) and hence does not depend on the upstream flow conditions. However, in cases in which the approach flow carries turbulence and its conditions influence the downstream flow, neglecting the turbulence at the inflow could lead to significant errors or to extremely long and hence resources-consuming development lengths. For instance, the location of flow separation on curved surfaces is known to be influenced by the upstream turbulence, Garcia-Villalba et al. (2009) calculated the flow over a three-dimensional mildly sloped hill and stressed the importance of matching the turbulent inflow conditions to the experimental ones in order to accurately predict the location of flow separation on the hill.

Recently, considerable research has been dedicated to generating adequate inflow boundary conditions for LES. This issues is also important in Hybrid LES/RANS methods at the transition from RANS to LES zones/regions.

The most common and practical methods for generating inflow conditions for LES will be discussed in the following.

### Precursor simulations

For channel-type flows, realistic inlet conditions can be obtained from pre-cursor simulations of an upstream placed sub-channel, the geometry and wall boundary conditions of which match those at the inlet of the actual calculation domain. The sub-channel flow is assumed to be developed so that the boundary conditions are chosen to be periodic in the streamwise direction. Once the flow field has developed into a fully turbulent and statistically steady state, the time-varying velocity data at one cross-section are copied to the inlet plane of the main simulation. Ideally, not only the geometry, but also the grid and temporal resolution match exactly the conditions at the inlet plane. If not, interpolation of velocity data in space and/or in time is required, which, especially if performed in time, could lead to unphysical turbulence spectra. One possibility is to perform the pre-cursor simulations before the actual simulation and write the results for one plane into a file from which the main simulation then reads the data as inlet boundary condition, This can be a challenge in terms of storage due to the high resolution requirements in space and time of the pre-cursor simulation which should cover the same physical time as the actual simulation. If less physical time is stored, the precursor results need to be fed-in repeatedly. A further possibility is to run the pre-cursor simulation calculations parallel to the main simulation and to feed-in the results of the periodic sub-domain directly as inlet boundary condition of the main simulation. This treatment inevitably leads to an increase in the required computational resources of the entire simulation. In cases in which the straight-channel pre-cursor simulation does not match the desired or (statistically) known inlet conditions of the main simulation, the use of forcing terms and rescaling of turbulent fluctuations are adequate measures to better approximate the inlet conditions. Forcing and rescaling has been done successfully by Garcia-Villalba et al. (2009) who rescaled velocities and turbulent fluctuations of a closed smooth channel to match closely the profiles of mean velocity and turbulent kinetic energy of thick boundary layer that was artificially created at the upstream end of a wind tunnel experiment.

### Time-averaged Velocity Profile Superimposed with Synthetic Turbulence

The easiest but least successful method of generating a turbulent inlet velocity field is superimposing synthetic turbulence on the mean velocity field. Though the random numbers can be scaled to match experimental *rms* values, the resulting velocity signal is not physically realistic as the spectrum of the prescribed fluctuations does not exhibit a decay towards higher frequencies as is the case in real turbulence. More importantly, almost immediately downstream of such an artificially created velocity signal, the high frequency fluctuations are damped quickly by the numerical method demanding a divergence free flow field. This influences negatively the low frequency more energetic fluctuations. As a result, the flow requires a certain approach flow length over which the velocity signals adjust themselves towards physically realistic turbulence. This length is hard to estimate a-priori and depends on the geometry and Reynolds number. In LES, every grid point that can be saved by avoiding a long "adjustment length" is important so that in simulations in which the proper upstream conditions are important, alternative, more advanced methods should be favoured.

Several studies have addressed the poor performance of the use of random noise superimposed on a velocity profile by generating more realistic turbulence for the inlet plane. The idea of generating synthetic turbulent fluctuations to be superimposed onto a time-averaged velocity profile makes use of Taylor's frozen turbulence hypothesis, in order to relate spatial and temporal turbulence. By using an approximate convective velocity it can be assumed that turbulence statistics such as turbulence intensities and Reynolds stresses from spatial simulations are similar to those from temporal simulations.

**Method of Lee et al.** Based on this assumption, Lee et al. (1992) suggested generating stochastic turbulent fluctuations with a prescribed energy spectrum from inverse Fourier transformations. This can be accomplished by providing two transversal wave numbers, the frequency of the spectrum and random phase angles in the streamwise direction. The use of Lee et al. (1992) procedure ensures that the resulting signals do not contain excessive small-scale motions which would have resulted if simply random numbers were used to generate the velocity fluctuations. For the flow over a backward facing step, Le et al. (1997) superimpose a mean velocity profile with fluctuations with a prescribed energy spectrum following the method suggested by Lee et al. (1992). Because of the inhomogeneity in the wall-normal direction, calculated fluctuations are rescaled to conform to the three normal Reynolds stress components and the wall-normal shear stress associated with a turbulent boundary layer profile. As mentioned above, the incompressibility condition must also be considered, which implies that the generated inflow fluctuations must be zero when summed over the inflow plane. Though fairly realistic velocity signals were achieved, a certain approach length is still required for the flow to develop into physically correct turbulence; this approach length however is considerably shorter than the one needed if white noise was superimposed at the inlet.

In an effort to improve the velocity signals at the inlet plane the fluctuations at each point can be manipulated, for instance through the phase angle to compute the Fourier coefficient, to attain specific spatial correlations expressing the coherence of a turbulent flow (Kondo et al., 2002).

**Digital Filter Method** Klein et al. (2003) proposed a general and efficient method for generating artificial turbulent inflow conditions for spatially inhomogeneous flows based on a digital filtering approach. The digital filtering approach does not assume flow similarity or equilibrium.

In the first step of this approach, a provisional velocity field $u_m$ is generated for each velocity component from a random data series $r_m (m = 1...k)$, which possesses prescribed two-point statistic and zero mean ($\overline{u_m} = 0$), using a digital filter defined by:

$$u_m = \sum_{n=-N}^{N} b_n r_{m+n} \tag{2.82}$$

where $b_n$'s are the filter coefficients that have to be determined and $N$ is the extent of the filter support (filter size). The random data series $r_m$ has to satisfy zero-mean ($\overline{r_m} = 0$) and unit variance ($\overline{r_m r_m}$) $= 1$. With this, one can show that the following relation holds between the two-point correlation function of $u_m$ and the filter coefficients $b_j$ (in 1D for x-direction):

$$R_{uu}\left(k\Delta x\right) = \frac{\overline{u_m u_{m+k}}}{\overline{u_m u_m}} = \frac{\sum\limits_{j=-N+k}^{N} b_j b_{j-k}}{\sum\limits_{j=-N}^{N} b_j^2} \tag{2.83}$$

where $k\Delta x$ is the distance from the reference point considered and $\Delta x$ is the grid spacing in $x$. For a given two-point correlation $R_{uu}$ the filter coefficients $b_j$ can be determined by inverting relation (2.83). Klein et al. (2003) prescribe the two-point correlation by assuming a Gaussian shape and by specifying the integral length scale $L_x$. This is consistent with homogeneous turbulence, but other correlation shapes can be used. The filter size $N$ is chosen to be twice the ratio of length scale to grid spacing ($N = 2L_x/\Delta x$).

In the second step, the time series from the first step having zero mean, unity variance and zero cross-correlations are modified using a linear transformation (Lund et al., 1998), such that one obtains new velocity time series with desired first (mean values) and second order point statistics (correlations between the different velocity components). The single point statistics are generally obtainable from experiment or from RANS in a hybrid method.

The aforementioned procedure allows obtaining instantaneous velocity data in the inflow plane with appropriate spatial correlations from an initial set of 3D random data. The method was validated by Klein et al. (2003) for two cases (DNS of plane turbulent jet, 2D DNS of primary break up of liquid jet) in which the turbulence scales were spatially uniform over the entire inlet plane.

Veloudis et al. (2007) proposed a new version of the digital filtering approach developed by Klein et al. (2003) that allows for spatial variation of the input turbulence length scales, instead of assuming a single prescribed spectrum at all inflow points, at a reasonable computational cost. The increased accuracy of the modified method using spatially varying turbulence length scales was demonstrated for the case of channel flow with a periodically repeating constriction. In particular, the prediction of the turbulence profiles was found to be more accurate compared to the case when a constant turbulence length scale was assumed. The use of Fast Fourier Transform for the 3D filtering process resulted in significantly higher computational speed.

A computationally very efficient digital-filter-based approach for generation of turbulent inflow conditions for spatially developing flows was proposed by Xie and Castro (2008). The method allows prescribing the integral length scales and the Reynolds stress tensor. It also allows for the use of spatially varying turbulence scales. The increase in efficiency with respect to the method of Klein et al. (2003) is mainly due to the fact that only one set of 2D random data, rather than a set of 3D data, is filtered to generate a set of 2D data with the prescribed spatial correlations at each time step. An exponential function with two weight factors is used to correlate the data at the current time step with the one at the previous time step. The other methods use a full 3D digital filter, which is computationally much more expensive. The main validation test cases were channel flow and flow over an array of staggered cubes.

A useful description of the digital filter method can also be found in the Appendix A of Touber and Sandham (2009).

**2D Vortex Method** The random 2D vortex method of Mathey et al. (2006) deserves attention too because of its simplicity and success in some recent hybrid RANS-LES simulations and because it is already implemented in some commercial CFD codes. This method is mainly suited for generating inflow turbulence at the transition face from RANS to LES zones in hybrid calculations. With this method, velocity fluctuations are generated from a fluctuating two-dimensional vorticity field in the inflow plane perpendicular to the streamwise direction with unit vector $\overrightarrow{e_x}$ in this direction. For this, N individual vortices are placed randomly over the inflow plane (with positions $\overrightarrow{x_i} = (x, y_i, z_i)$) and the vorticity of those is determined by their circulation $\Gamma_i$ and a spatial decay function $\eta(\overrightarrow{x})$ involving the size of the vortices $\sigma$. By superposition of the N individual vortices the fluctuation velocity $\overrightarrow{u'}$ at a point $\overrightarrow{x}$ in the inflow plane is then calculated from the vorticity distribution of the vortices via the Bio-Savart law as:

$$\overrightarrow{u}\left(\overrightarrow{x}\right) = \frac{1}{2\pi}\sum_{i=1}^{N}\Gamma_i \frac{(\overrightarrow{x_i} - \overrightarrow{x}) \times \overrightarrow{e_x}}{|\overrightarrow{x} - \overrightarrow{x_i}|^2}\left(1 - e^{\frac{|\overrightarrow{x}-\overrightarrow{x_i}|^2}{2\sigma^2}}\right) e^{\frac{|\overrightarrow{x}-\overrightarrow{x_i}|^2}{2\sigma^2}} \qquad (2.84)$$

The fluctuating velocity components $v^{'}$ and $w^{'}$ can be obtained as components of the fluctuating velocity vector $\overrightarrow{u^{'}}$. The circulation $\Gamma_i$ and the vortex size $\sigma$ appearing in (2.84) are determined from the mean turbulent kinetic energy $k$ and dissipation rate $\epsilon$ via:

$$\Gamma_i \propto \sqrt{k}\,(\overrightarrow{x_i}) \tag{2.85}$$

with the distribution of $k$ and $\varepsilon$ over the inflow plane known from the upstream RANS calculation (or by estimation). To ensure that the vortices always belong to resolved scales, the minimum value of $\sigma$ is bounded by the local grid size so that $\sigma \geq \Delta$. The individual vortices are moved randomly to another position at each time step. Further, after a characteristic time scale $\tau$, which is the time the vortices would take to be convected a certain distance in the streamwise direction, the sign of the circulation $\Gamma_i$ of each vortex is changed randomly.

This vortex method described so far generates only velocity fluctuations $v^{'}$ and $w^{'}$ in the inflow plane normal to the streamwise direction. For generating the streamwise fluctuations $u^{'}$ Mathey et al. (2006) suggest a Linear Kinematic Model (LKM) which mimics the effect of the 2D vortices on the streamwise velocity field.

The 2D vortex method was validated successfully for channel and pipe flow and separated flow over periodic hills (Mathey et al., 2006) and the flow over the Ahmed car body (Mathey and Cokljat, 2005).

### 2.7.4 Free Surface Boundary Conditions

The water surface in hydraulic engineering flows represent the boundary between water and the air above it. The water surface can distort into various shapes and will adjust itself according to the flow, turbulence and bathymetric or geometric conditions in a channel. Generally the distortion by turbulence is fairly small and in most cases much smaller than mean surface variations in non-uniform channels, flood waves, tidal channel, ocean waves of flows over hydraulic structures. Mathematically, at a free surface a kinematic as well as a dynamic boundary condition applies. The kinematic boundary condition states that there is no convective mass transfer through the free surface; hence the fluid velocity component normal to the free surface is equal to the free surface velocity (Fig. 2.11). The kinematic condition in

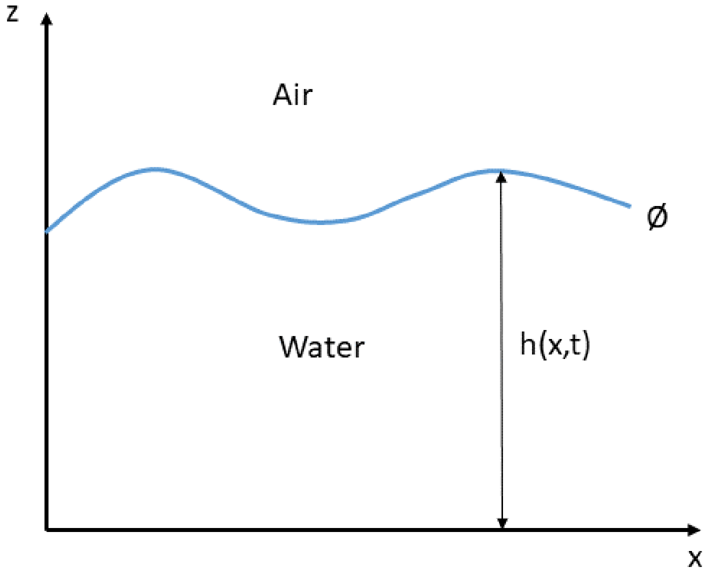

Figure 2.11: Illustration of the free surface as an interface between air and water.

Eulerian form reads:

$$\frac{\partial \overline{h}}{\partial t} - \overline{u}_3 = -\overline{u}_1 \frac{\partial \overline{h}}{\partial x} - \overline{u}_2 \frac{\partial \overline{h}}{\partial y} \tag{2.86}$$

in which $\overline{h}$ is the filtered water depth, and $\overline{u_i}$ represents the filtered velocity components at the surface. The presence of non-linear terms in the unfiltered kinematic boundary condition leads to subgrid scale terms after filtering, which are additional unknown quantities that would need to be modelled but are usually neglected (e.g. Hodges and Street, 1999). The dynamic boundary condition requires that all forces acting at a sharp interface are in equilibrium. In other words, the forces exerted by water on air are equal and opposite to the forces exerted by air on water. Force intensities per unit area that are found at the free surface of an open channel are pressure, acting normal to the surface, viscous stresses, acting both normal and tangential to the surface, and surface-tension, acting both normal and tangential to the free surface.

The implementation of kinematic boundary condition into the solution algorithm of the filtered Navier-Stokes equations is not straightforward because neither shape nor position of the free surface are known. There are two principal numerical methods for calculating the location of the free surface (Ferziger and Peric, 2002), i.e. Interface-

Tracking Methods (ITM) and Interface-Capturing Methods (ICM), also known as moving-mesh and fixed-mesh methods. In an interface-tracking, or moving-mesh method for open channel flow, the governing equations are only solved for the water phase and the computational mesh is moved after every time step so that the boundary of the computational domain coincides with the free surface geometry. An ITM requires a boundary-fitted, moving grid together with an appropriate algorithm that readjusts the grid in the entire domain each time the surface has moved. So far, ITMs have been used mainly in the context of RANS modelling, following different strategies to compute the free-surface elevation. An ITM in the context of LES has been presented by Hodges and Street (1999) who simulated the interaction of waves with a turbulent channel flow. These authors used an explicit time-discretization scheme to advance the free surface by solving the kinematic boundary condition and solved a Poison-type equation after every time step to compute a new boundary-orthogonal grid. The Reynolds number in this case is rather low ($Re_\tau$=171) so that the turbulent eddies and the surface deformations caused by them have rather large length and time scales. At Reynolds numbers of practical interest with much smaller turbulent length and time scales the recalculation of a new mesh would be extremely expensive. In fact, Hodges and Street state that in such cases of small surface deformations their method is not suitable. To avoid the creation of a new mesh after every time step Fulgosi et al. (2003) used a mapping scheme that transfers the curvilinear physical space into an orthogonal coordinate system. Fulgosi et al. (2003) employed this technique for a DNS of wind-sheared free-surface deformations.

In interface capturing methods the boundary between the two phases is not defined sharply through the numerical mesh, hence the mesh includes both phases. Probably the earliest ICM was proposed by Harlow and Welch (1965). Their Marker-and-Cell (MAC) method introduces meshless particles into the water near the free surface, which are moved according to the velocity components in their vicinity. Though the MAC scheme can handle complex interfaces such as breaking waves, a large number of particles are needed, which makes the method computationally expensive. Alternatively the free surface position can be determined by the contour of a scalar function which does not need to coincide with grid lines. The Volume of Fluid method (VOF) is such an approach, where the fraction of the liquid phase is determined by the solution of a transport equation for the void fraction $F$ (Hirt and

Nichols, 1981). Per definition $F$ is unity in any cell/point that is occupied by water and zero otherwise. One important procedure in VOF method is that the surface has to be reconstructed in terms of the volume fraction for which different techniques exist (e.g. SLIC, Simple Line Interface Calculation method by Noh and Woodward (1976) or PLIC, Piecewise Linear Interface Calculation by Youngs, 1982). Thomas et al. (1995) combined the kinematic boundary condition based on the water depth $h$ (Eq. 2.84) with the VOF method, which is applied to a LES of straight open channel flow by Shi et al. (2000). Recently, the Level-Set Method (LSM), which originated in computer graphics has become a popular interface-capturing method for multiphase flows. The LSM was originally proposed by Osher and Sethian (1988) and was developed for computing and analyzing the motion of an interface between two phases in two or three dimensions. In the LSM the conservation equations are solved for both liquid and gas phase and the interface moves at the local velocity which can be expressed in a Lagrangian way. The LSM has been recently employed in an LES of the flow over fixed dunes by Yue et al. (2005a). Not only were Yue et al. (2005b) able to accurately and realistically calculate the unsteady free surface motion but they also provided evidence of boils, upwelling and downdraft.

By far the most large-eddy simulations in hydraulics were performed with the so-called rigid-lid approximation as boundary condition for the free surface. In this, instead of the actual free surface as adjusting boundary in an interface-tracking method, a fixed boundary, generally a flat surface, is used which is treated as a frictionless wall. Hence, the calculations are in fact carried out for a closed conduit with an artificially introduced fixed upper boundary where the shear stress is zero (in the absence of wind shear) and the velocity normal to the boundary is also zero, but where the pressure can vary as it does along a wall. In fact, the boundary conditions for the pressure and the normal velocity are as described earlier for a wall, while the shear stress at the boundary is simply set to zero which altogether amounts to using symmetry conditions at the boundary. The problem of having to determine the surface elevation while knowing the pressure at the surface has been shifted to knowing the location of the boundary but having to determine the variation of the pressure there. The surface-elevation-gradient terms $g\partial h/\partial x$ and $g\partial h/\partial y$ in the momentum equations for free surface flows are thereby replaced by the pressure gradients $\partial p/\partial x$ and $\partial p/\partial y$ so that the dynamic effects of surface-elevation variations are properly accounted for by the rigid lid approximation method. In fact, the surface elevation that would evolve can be retrieved from the pressure variations through the following relation:

$$\Delta h_k = z_k - z_{ref} = \frac{p_k - p_{ref}}{\rho g} \tag{2.87}$$

where $p_k$ and $z_k$ are local pressure value and surface elevation and $p_{ref}$ and $z_{ref}$ are the corresponding quantities at the reference location. However, by suppressing the actual surface deformation a certain error is introduced in the continuity equation, but this is small when the surface deviation is small compared with the local water depth, say below 10% of the depth. This is virtually always the case for surface disturbances due to turbulence and hence the rigid-lid approximation is the preferred free-surface boundary condition in DNS and LES calculations. For example, Lam and Banerjee (1992) and Pan and Banerjee (1995) studied the turbulent structures in DNS of open channel flow using the rigid-lid approximation. Komori et al. (1993) included the surface variations in their computation by solving Equation 2.86 for the water depth and compared the results with the ones from Lam and Banerjee (1992). They found that the free-surface deformations there did not differ from the simulations using a flat rigid lid. The rigid-lid approximation was also used in many RANS calculations and in LES for situations with relatively small mean surface variations, However, large errors must be expected for the mean variations when these are not small compared to the local water depth as can be the case in coastal and ocean engineering problems where the variation of the mean free surface is usually much more pronounced.

### 2.7.5 Smooth-Wall Boundary Conditions

The no-slip condition at walls is also valid for turbulent flow and its fluctuating velocities, and hence the natural boundary condition there is for impermeable walls to set all components of the resolved velocity to zero. Because of steep gradients and strongly reduced size of the dominant eddies very near walls, high numerical resolution is necessary, which means that several grid points must be placed within the viscous sublayer. When a finite-volume method is used, it is not the velocity at the wall that must be specified but the momentum flux at the lower boundary of the wall-adjacent cell, which is the wall shear stress (Fig. 2.12). The wall shear stress is equal to the molecular viscosity times the velocity gradient at the wall, i.e.

$$\tau_w = \mu \left( \frac{\partial \overline{u}_t}{\partial z} \right)_w \tag{2.88}$$

in which $\overline{u}_t$ is the resolved velocity parallel to the wall. In the viscous sublayer the velocity increases linearly with distance from the wall, and since this sublayer has to be resolved properly in this approach, the gradient in Equation 2.88 can be replaced by $\overline{u_{t1}}/z_1$ where $z_1$ is the distance of the first grid point from the wall which is located in the middle of the wall-adjacent cell (Fig. 2.12). This allows calculating the instantaneous wall shear stress from the resolved tangential velocity at the first grid point. Concerning the boundary condition for the pressure, there are several possibilities which depend on the flow problem considered and also on the numerical procedure used. In fully-developed straight channel flow without obstacles, the exact pressure condition is a zero wall-normal gradient von Newmann condition, i.e. $\frac{\partial p}{\partial z}\big|_w = 0$. In the more general case with curved walls, e.g. the flow around an obstacle or in the a bend, this condition does not hold because wall-normal pressure gradients occur. In this case the pressure at the boundary is approximated through a linear extrapolation from the known values inside the flow domain.

In the region very close to the wall (viscous sublayer, buffer region) the major part of the turbulence production occurs and small-scale structures such as high- and low- speed streaks must be resolved. An approach achieving this is called a wall-resolving LES. For this, a good resolution is necessary not only normal to the wall but also in the wall-parallel directions, and in fact the resolution must be similar to that in a DNS. Hence this approach is called a Quasi-Direct Numerical Solution (QDNS, Spalart et al., 1997). Chapman (1979) was the first to analyze the resolution requirements of flow over a flat plate and found that $z_1^+ \approx 1$, $\Delta x^+ \approx 100$, $\Delta y^+ \approx 20$ is necessary as minimum resolution. This was later confirmed by other authors, e.g. Piomelli, 2008. Chapman (1979) also estimated that the number of grid points required for such an LES is proportional to $Re_L^{1.8}$. For channel flow Baggett et al. (1997) estimate the required grid points to be proportional to $Re_\tau^2$, where $Re_\tau$ is the

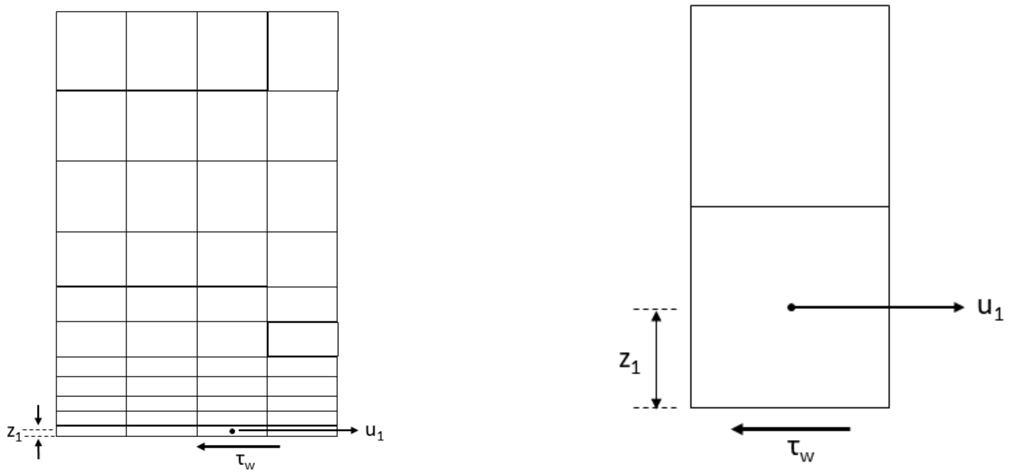

(a) (b)

Figure 2.12: Near-wall numerical mesh cells for finite-volume LES (a) for wall resolving LES and (b) for LES with wall function.

friction Reynolds number.

It is clear that at high Reynolds numbers of practical interest, calculations with such fine resolution are not feasible. Such LES are cheaper than a complete DNS but are still too expensive. A way out is to avoid resolving the details of the structures in the near-wall region by LES through the use of special near-wall models. One approach is to place the first grid point outside the region where resolution is particularly expensive, generally in the log-law region (Fig. 2.12b), and to bridge the near-wall region by wall functions. Another approach is to calculate the near-wall region by a RANS model, which also requires quite fine resolution in the wall-normal direction but not in the wall-parallel directions so that considerable saving is achieved. In both cases, the near-wall models must provide the wall shear stress but also proper information on the fluctuations for the resolved region further away from the wall. Hence such models can be considered as a kind of special subgrid-scale model.

In the following, the most commonly used wall functions are introduced; these basically relate the instantaneous wall shear stress to the resolved velocity at the grid point placed in the middle of the wall-adjacent cell in a finite-volume procedure (Fig. 2.12).

**Schumann's model** The most popular wall-function model is due to Schumann (1975) who proposed the following relation

$$\overline{\tau}_w = \frac{<\overline{\tau}_w>}{<\overline{\tau}_1>}\overline{u}_1 \tag{2.89}$$

between the instantaneous wall shear stress $\overline{\tau}_w$ and the instantaneous velocity $\overline{u}_1$ at the first grid point, assuming that these are in phase and that the proportionality factor is the ratio of the time-averaged shear stress and velocity at the first grid point, $<\overline{\tau}_w> / <\overline{\tau}_1>$. Schumann (1975) further assumed that this ratio is determined by the following logarithmic law of the wall

$$<\overline{u}^+>=\frac{<\overline{u}>}{u_*} = \frac{1}{\kappa}\ln z^+ + B \tag{2.90}$$

i.e. that the first grid point lies in a region where this law prevails. In Equation (2.90) $z^+ = zu_*/\nu$ is the normal distance from the wall in wall units, $u_*$ is the friction velocity $u_* = \sqrt{<\overline{\tau}_w/>\rho}$, $\kappa$ is the von Karman constant (=0.4) and B another constant depending on the roughness of the wall ($\approx 5.0$ for smooth walls). The log law (Eq. 2.90) is valid in the $z^+$-range $30 \leq z^+ \leq 500$.

The time-averaged values $<\overline{u}_1>$ and $<\overline{\tau}_w>$ have to be determined by time-averaging during the time-marching solution; for flows with homogeneous directions this can be supported by averaging in these directions. Further, an iterative solution of Equation (2.90) is necessary to determine the friction velocity $u_*$ and hence the wall shear stress $<\overline{\tau}_w>$ from the velocity $<\overline{u}_1>$. In the special case of developed channel flow, the time-averaged wall-shear $<\overline{\tau}_w>$ is known from the imposed pressure gradient.

For practical applications it is important that the wall-function relation (2.89) can be applied also when the first grid point comes to lie in the viscous or buffer layer. This can be achieved by replacing Equation (2.90) with the following three-layer formulation for the velocity distribution (layer I: viscous sublayer, layer II: buffer layer, layer III: logarithmic layer):

$$<u^+>=z^+ \quad \text{, I: for} \quad 0 \leq z^+ < 5 \tag{2.91a}$$

$$< u^+ >= \alpha_1 \ln\left(z^+\right) + b_1 \quad \text{, II: for} \quad 5 \leq z^+ < 30 \tag{2.91b}$$

$$< u^+ >= \alpha_2 \ln\left(z^+\right) + b_2 \quad \text{, III: for} \quad 30 \leq z^+ < 300 \tag{2.91c}$$

with constants $\alpha_1 = 5.0$, $\alpha_2 = 2.0$ or $1/\kappa$, $\beta_1 = -3.05$, $\beta_2 = 5.2$

In complex flows, the direction of the wall shear stress is not known a priori and the two components $\overline{\tau}_{w,x}$ and $\overline{\tau}_{w,y}$ have to be determined from the two wall-parallel components of the velocity at the first grid point, $\overline{u}_1$ and $\overline{v}_1$. This is achieved with the following relations:

$$\overline{\tau}_{w,x} = \frac{< \overline{\tau}_w >}{\sqrt{< \overline{u}_1 >^2 + < \overline{v}_1 >^2}} \overline{u}_1, \overline{\tau}_{w,y} = \frac{< \overline{\tau}_w >}{\sqrt{< \overline{u}_1 >^2 + < \overline{v}_1 >^2}} \overline{v}_1 \tag{2.92}$$

**Werner-Wengle model** The Schumann model is based on relations derived from flat-wall situations and requires the determination of mean values and an iterative procedure for obtaining the mean wall shear stress from the logarithmic velocity law. In order to avoid the latter possibly elaborate procedures and aiming at an application to more complex situations, Werner and Wengle (1993) proposed a wall-function model that does not involve a law for the time-averaged values but directly a distribution from the instantaneous velocity, assuming again that the instantaneous wall shear stress is in phase with this. A two-layer distribution is assumed, with a linear profile for the inner, mainly viscous layer and a power law for the outer turbulent layer:

$$< u^+ >= z^+ \quad \text{I: for} \quad 0 \leq z^+ < 11.82 \tag{2.93a}$$

$$\overline{u}^+ = \alpha_2 \left(z^+\right)^m \quad \text{II: for} \quad 11.82 \leq z^+ < 1000 \tag{2.93b}$$

with parameters $\alpha_2 = 8.3$ and $m = 1/7$. The change-over from the inner to the outer layer is at $z_m^+ = 11.8$. Integration of these velocity distributions over the wall-adjacent cell in a finite-volume procedure then yields directly the wall shear stress:

$$\overline{\tau}_w = \rho \frac{2\nu}{\Delta z_1} \overline{u}_1, \overline{u}_1 = \frac{\nu}{2\Delta z_1} \left(z_m^+\right)^2 \tag{2.94a}$$

$$\overline{\tau}_w = \rho \left[ \frac{1-m}{2} C_m^{\frac{1+m}{1-m}} \left(\frac{\nu}{\Delta z_1}\right)^{1+m} + \frac{1+m}{C_m} \left(\frac{\nu}{\Delta z_1}\right)^m \overline{u}_1 \right]^{\frac{2}{1+m}} \overline{u}_1 > \frac{\nu}{2\Delta z_1} \left(z_m^+\right)^2 \tag{2.94b}$$

where $\Delta z_1 = 2z_1$ is the height of the wall-adjacent cell (Fig. 2.12) and $C_m = 8.3$. In complex flows, the wall-shear stress components can then be determined from

$$\overline{\tau}_{w,x} = \frac{\overline{\tau}_w}{\sqrt{\overline{u}_1^2 + \overline{v}_1^2}} \overline{u}_1, \overline{\tau}_{w,y} = \frac{\overline{\tau}_w}{\sqrt{\overline{u}_1^2 + \overline{v}_1^2}} \overline{v}_1 \tag{2.95}$$

The Werner-Wengle model is applicable to situations with flow separation and has been used with some success for such flows, even though the assumed velocity distributions are questionable in these regions.

**Piomelli et al's model** Piomelli et al. (1989) extended Schumann's model based on the experimental observation that the correlation between wall shear stress and velocity at a near wall point increases when there is a time delay between velocity and shear stress. This is due to the also experimentally observed fact that the near-wall structures mainly responsible for the velocity and shear-stress fluctuations are inclined. Piomelli et al. (1989) accounted for this in their model by relating the wall shear stress in point A to the velocity at a point B along an inclined near-wall structure. Hence they proposed to replace (2.89) by the "shifted boundary condition":

$$\overline{\tau}_w = \frac{< \overline{\tau}_w >}{< \overline{\tau}_1 >} \overline{u}_1 \left( x + \Delta s \right) \tag{2.96}$$

in which $\Delta s$ is the streamwise displacement of point B with respect to point A and is defined via the angle of inclination of the structures, $\Theta$, and the wall distance of point B, $y_1$. From experiments and DNS the optimal inclination angle was determined to lie in the range $\Theta = 8^o - 13^o$. For $30 < y_1^+ < 50$ the smaller value applies so that $\Delta s = z_1 \cot 8^0$ while for larger wall distances $\Delta s = z_1 \cot 13^0$ yields better results. For plane channel flow, the inclusion of the displacement $\Delta s$ improved the results over Schumann's formulation, and for this flow Balaras et al. (1995) obtained excellent agreement with experimental and DNS data for a range of Reynolds numbers. For more complex flows, where the mean-flow direction is not known a priori, the direction of the displacement must also be determined, which complicates the application of the model.

### 2.7.6 Rough-Wall Boundary Conditions

The above wall boundary conditions/models are applicable to geometrically simple flows over smooth walls for which the near-wall flow can be resolved or approximated with some model. However, in flows of hydraulic-engineering interest walls, e.g. the bed of a river, are often rough so that one of the challenges of LES of such flows is the accurate inclusion of wall roughness. Similar to flow over smooth walls, specification of the wall shear stress or some a-priori knowledge of the velocity profile over the rough wall is needed. This by itself is not an easy task as the law of the wall for rough boundaries is still subject of ongoing research and several different formulations exist. In his overview, Patel, 1998 therefore calls the implementation of rough wall boundary conditions the "Achilles Heel of CFD", even though Patel's article aimed at the RANS modelling community. There are several different concepts of dealing with rough walls in LES. The most common ones are introduced in the following.

**Explicit resolution of roughness elements** One basic possibility to account for wall roughness is to resolve the flow around the individual roughness elements, specifying as boundary condition the no-slip condition (zero velocity) at the walls of these elements.

The success of Direct Numerical Simulations (DNS) and Large-eddy Simulations (LES) in revealing details of the turbulent channel flow over smooth walls has initiated DNS and LES studies of flow over walls with roughness elements. Such fundamental studies resolved the individual elements through the numerical grid, the numerical effort thereby being extremely high. Successful LES of that kind are reported for flows over relatively simple and exactly defined roughness elements like square bars (Leonardi et al., 2003; Ikeda and Durbin, 2007; Stoesser and Nikora, 2008), wavy walls (Calhoun and Street, 2001; Calhoun et al., 2001), spheres (Singh et al., 2007) or typical open-channel bedforms such as sand dunes or ripples (Yue et al., 2005a; Yue et al., 2005b, Yue et al., 2006; Stoesser et al., 2008; Zedler, 2001. An alternative to using body-fitted grids to explicitly resolve individual roughness elements is the Immersed Boundary Method (IBM) as employed for instance by Cui et al., 2003; and Bhaganagar et al., 2004. In high-*Re* flows of hydraulic interest, e.g. open-channel flow over rough beds, explicit resolution of the flow around roughness elements has had limited success mainly for two reasons: (1) the detailed topology of the rough surface is unknown and (2) the requirements in terms of grid resolutions to represent individual roughness elements (using ten or more points per roughness element) are exceeding current computing resources. For instance, a LES (employing the IBM) of the flow over a rough surface that is composed of small sandgrains (e.g. $H/k = 30$) in a $6H$x$3H$x$H$ domain requires approximately 0.2x$10^9$ gridpoints, with each sandgrain being resolved by only $10^3$ points. Moreover, in open-channel flow over an alluvial bed the rough surface comprises sediments of widely different size which can range from micro-meters to decimeters with relative submergences ranging from one to several hundred, making the specification of accurate boundary conditions an almost insurmountable challenge. Hence, for calculating flows of practical interest, alternative methods must be used in which the individual roughness elements are not resolved.

**Rough-wall law based boundary conditions** To date most numerical simulations of flow over rough walls have been based on the Reynolds-Averaged Navier Stokes (RANS) equations, where the effect of roughness has been accounted for by wall functions involving roughness functions determined empirically from experiments. This RANS-type treatment is quite common in LES of atmospheric-boundary layer flow. The first grid point is placed outside the roughness layer (Fig. 2.13), which is the (rough) equivalent of the buffer layer in smooth walls, and an instantaneous shear stress is imposed at the boundary, in effect at the lower boundary of the first grid cell. Following the approach of Schumann (1975) discussed above, this stress can be determined for Equation 2.88, with the ratio of time-averaged shear stress and velocity at the first grid point, $< \overline{\tau_w} > / < u_1 >$ now obtained from a logarithmic law of the wall for rough walls:

$$\frac{< u >}{u_*} = \frac{1}{k} \ln \left( z^+ \right) + 5.5 - \Delta B \tag{2.97}$$

The last term on the r.h.s of Equation (2.97), $\Delta B$, expresses the downshift of the velocity profile (from the one over a smooth wall) when plotted on a semi-logarithmic Clause plot. The magnitude of the downshift $\Delta B$ depends on the equivalent grain roughness, $k_s$, which is a common length scale used to quantify the roughness. The roughness Reynolds number, $k_s^+ = u_* k_s/\nu$ is used to distinguish between the three roughness regimes, hydraulically smooth, transitional roughness, and fully rough for which $\Delta B$ is calculated as (Cebeci and Bradshaw, 1977):

$$\Delta B = \begin{cases} 0, & \text{for } k_s^+ < 2.5 \\ \left[5.5 - 8.5 + \frac{1}{k}\ln\left(k_s^+\right)\right] \sin\left[0.426\left(\ln k_s^+ - 0.81\right)\right], & \text{for } 2.5 \le k_s^+ < 90 \\ 5.5 - 8.5 + \frac{1}{k}\ln\left(k_s^+\right), & \text{for } k_s^+ \ge 90 \end{cases} \tag{2.98}$$

In hydraulics there are different types of bed roughness (Rijn, 2007), the two most relevant are grain roughness and bed-form roughness. For smooth beds $k_s \approx 0$, and the smooth bed log law applies. For laboratory channels in which a smooth bed is technically roughened with individual sand grains the equivalent grain roughness is approximately the main grain diameter, i.e. $k_s \approx d_{50}$. In natural beds, or in laboratory channels with a gravelly or sandy bed, higher sandgrain roughness values are recommended because larger grains will dominate the surface as a result of bed armoring or washing out of finer grains. Therefore, van Rijn (1984) recommended $k_s = 3d_{90}$, however other approximations are available depending on the bed material, e.g. Einstein (1942) recommended $k_s = d_{65}$ for sand; Hey (1978) suggested $k_s = 3.5d_{84}$ for coarse gravel.

For bed forms such as ripples or dunes, both grain roughness and form roughness have to be accounted for. A common approximation is given by van Rijn (1984) as $k_s = 3d_{90} + 1.1\Delta(1 - e^{-25\Delta/\lambda})$, in which $\Delta$ is the bed-form height and $\lambda$ is the bed form length.

Once the equivalent grain roughness has been determined, the shear stress at the lower boundary of the first grid cell above the virtual origin (i.e. $z = 0$), $\overline{\tau_w}$, can be calculated as a function of the filtered horizontal velocity ($\overline{u}_i$) at the first grid point, which is located some vertical distance, $z^{'}$, above the rough boundary (Fig. 2.13). The components of this shear stress can be expressed through the following

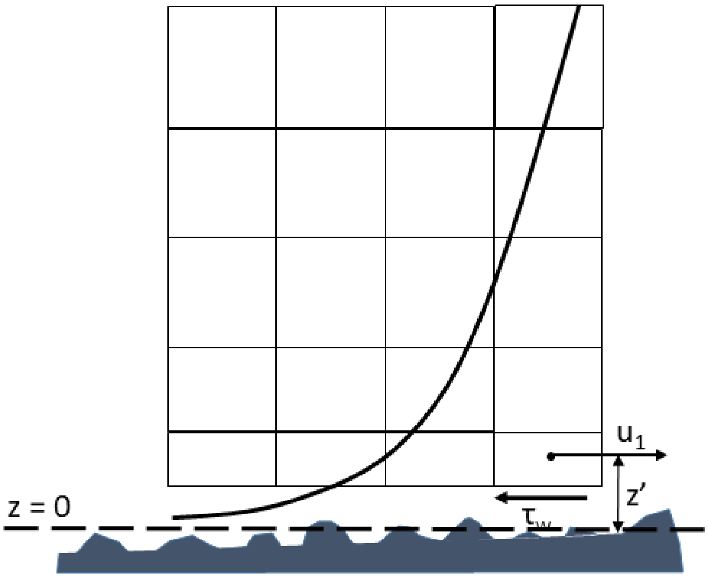

Figure 2.13: Near-wall numerical mesh cells for finite-volume LES over a rough boundary.

quadratic relation as:

$$\tau_{w1} = - < \overline{\tau_w} > \frac{\overline{u}_i}{< u\left(z'\right) >} = c_D[< u\left(z^{'}\right) >]^2 \frac{\overline{u}_i}{< u\left(z'\right) >} \tag{2.99}$$

where $\overline{u}_i$ are the filtered, tangential velocity components at the first grid point off the virtual rough wall and $< u(z^{'}) >$ is the time-averaged streamwise velocity at this location. $c_D$ is a drag coefficient, which, in case of a fully rough boundary (i.e. for $k_s^+ \geq 90$ in Eq. 2.98), is determined by:

$$c_D = \kappa^2 \left[\ln\left(30z/k_s\right)\right]^{-2} \tag{2.100}$$

Equation 2.100 can be considered the hydraulic-engineering analogue to what has been used widely in the atmospheric boundary layer community. There, the formulation of the drag coefficient is as follows (Moeng, 1984; Porte-Agel et al., 2000, Chow et al., 2005):

$$c_D = \kappa^2 \left[\ln\left(z/z_0\right)\right]^{-2} \tag{2.101}$$

where $z_0$ is a roughness length that has to be determined from experiments. When comparing Eq. 2.101 with Eq. 2.100 it is obvious that $k_s = 30z_0$.

Instead of obtaining the instantaneous wall stress through the time-averaged velocity, Saito et al. (2012) derived a dynamic ordinary differential equation, which allows calculating the instantaneous friction velocity, $u_*$, at the virtual origin. Once $u_*$ is obtained, an instantaneous version of equation 2.97 can be solved explicitly for an instantaneous local slip velocity at the virtual origin.

The validity and accuracy of a log-law based boundary condition in LES of channel flow over rough beds is currently a topic of ongoing research. There are several uncertainties and assumptions involve in this treatment. For instance, a relatively coarse grid near the roughness may lead to inaccuracies of the velocity gradient or for flows with low water-depth-to-roughness-height the grid is too coarse over the entire water depth to resolve the dominating turbulent structures. Another uncertainty includes the virtual origin of the rough bed, which can result in inaccuracies regarding the shear stress or for large roughness in a continuity defect. However, one of the greatest uncertainties of using wall functions is the fact that due to the absence of local variations in bathymetry, the effects of local pressure gradients and streamline curvature on the flow are neglected. In particular, if the bed is comprised of exposed roughness elements, local flow separation and recirculation can be substantial contributors to turbulence production and are likely to affect the flow over a substantial portion of the water depth. However, for flows at high relative submergence the log-law based semi-slip condition can provide reasonable results if (1) the effect of the roughness on the velocity profile can be estimated a-priori (e.g. by knowledge of the equivalent sand-grain roughness and zero-plane displacement) (2) the interaction of the flow in the roughness layer with the outer layer is very weak or absent, which is true if the roughness height is small. For this to hold Jimenez (2004) proposes water-depth-to-roughness-height $\gg 40$.

**Momentum forcing** A more natural way to account for the turbulence producing roughness but also avoiding the expensive explicit resolution of roughness is to consider the rough bed in a spatially averaged sense. In the momentum forcing approach the effect of the roughness on the flow and turbulence above the rough bed over a predefined volume is simulated. Such an approach was presented by

Nakayama and Sakio (2002) who suggested adding extra dispersive stress terms to the momentum equations and using a slip boundary condition at a suitably chosen boundary to mimic the roughness. The dispersive stresses are a result of spatially averaging the Navier-Stokes equations over a control volume in which the velocity profiles are heterogeneous in space due to the rough bed (Nikora et al., 2007). The method of Nakayama and Sakio (2002) reproduces the flow statistics fairly well but requires a priori knowledge of the magnitude of the dispersive stresses, which they obtained from a DNS simulation. With increasing computational power, advanced numerical methods have been employed to study and solve complex and/or practical problems using numerical computational methods. In hydraulics, almost all flows (geophysical and/or man-made) are turbulent, with the exception of groundwater flows. Turbulence adds additional difficulty in obtaining reliable predictions and this is due to its unsteady and irregular motion of eddies. Eddies associated with turbulence increase the momentum, heat and mass transfer and hence have significant influence on all aspects of the flow and associated phenomena such as temperature, concentration, distributions, sediment transport. Therefore, a realistic simulation of the effect of turbulence is of major importance for an accurate prediction of the flow and associated phenomena.

Also for vegetation roughness; to avoid the computationally very expensive resolution of vegetation elements, less costly approaches were developed in the meteorological community using a vegetative momentum force The idea is to compute a drag force and add it to the right hand side of the momentum equations such as the following time-dependent drag force for vegetation (Shaw and Schumann, 1992; Kanda and Hino, 1994):

$$F = C_D \alpha V^2 \frac{\overline{u_i}}{|V|} \tag{2.102}$$

in which $C_D$ is a drag coefficient, $\alpha$ is the leaf density in [m$^2$/m$^3$], and $|V|$ is the magnitude of the velocity vector ($\sqrt{\overline{u_i}\overline{u_i}}$). The drag force acts as a momentum sink and causes energy losses by stem and leaf drag, However, this treatment alone does not produce realistically the turbulence resulting from the flow around the plants and the wake flow downstream of the plants. Hence, a modification of the SGS stresses is also needed.

### 2.7.7 Initial Conditions

The specification of initial conditions for large-eddy simulations requires values for each variable (velocity, pressure, scalar) in the entire computational domain. The correctness of these initial values is only important if the calculated results are needed from the start of the simulation. In large-eddy simulations of hydraulic problems this is hardly the case; rather flow and turbulence of a fully developed state are of interest. In analogy to laboratory experiments in hydraulics, LES requires a certain approach length (in the laboratory it is the channel entrance section while in most LES it is the initial simulation period) for the flow to develop and to reach a state that is independent of the previously specified initial conditions. In order to estimate the length of the initial simulation period the flow-through time unit $T_{ft}$ defined as

$$T_{ft} = u(bulk)/(\text{length of domain}) \tag{2.103}$$

or the eddy turn-over time unit $T_{to}$ defined as:

$$T_{tot} = u_{*}/(\text{water depth}) \tag{2.104}$$

where $u_{*}$ is the friction velocity, can be employed. The period in terms of these two time units however depends on the flow situation and the Reynolds number, but as a rough guideline, at least six time units of either one are needed for the flow to be considered fully developed. It is recommended to monitor the velocity or pressure signal at various points in the flow to check the validity of the estimates made and make modifications to the initially chosen development period if necessary.

# Chapter 3

# Literature Review - Dispersed Phase

## 3.1 Introduction

Multi-phase flows are often encountered in engineering applications and industries, such as chemical process industry; petroleum; pharmaceutical; agricultural; biochemical; electronic; and power-generation industries. The modelling of gas-liquid flows and their dynamics has become increasingly important in these areas, in order to predict flow behaviour with greater accuracy and reliability. There are two main flow regimes in gas-liquid flows: separated (e.g. annular flow in vertical pipes, stratified flow in horizontal pipes) and dispersed flow (e.g. droplets or bubbles in liquid). In this section, the numerical methods and techniques commonly used to describe dispersed bubbly flows will be reviewed.

The description of bubbly flows involves modelling of a deformable (gas-liquid) interface separating the phases; discontinuities of properties across the phase interface; the exchange between the phase; and turbulence modelling. Most of the dispersed flow models are based on the concept of a domain in the static (Eulerian) reference frame for description of the continuous phase, with addition of a reference frame for the description of the dispersed phase. The dispersed phase may be described in the same static reference frame as the continuous, leading to the Eulerian-Eulerian (EE) approach or in a dynamic (Lagrangian) reference frame, leading to the Eulerian-Lagrangian (EL) approach.

In the EL approach, the continuous liquid phase is modelled using an Eulerian approach and the dispersed gas phase is treated in a Lagrangian way; that is, the individual bubbles in the system are tracked by solving Newton's second law, while accounting for the forces acting on the bubbles. An advantage of the EL approach is the possibility to model each individual bubble and also incorporating bubble coalescence and breakup directly. Since each bubble path can be calculated accurately within the control volume, no numerical diffusion is introduced into the dispersed phase computation. However, a disadvantage is that the larger the system gets the more equations need to be solved, i.e. one for every bubble.

The EE approach describes both phases as two continuous fluids, each occupying the entire domain, and inter-penetrating each other. The conservation equations are solved for each phase together with interphase exchange terms. The EE approach can suffer from numerical diffusion. However, with the aid of higher order discretization schemes, the numerical diffusion can be reduced sufficiently and can offer the same order of accuracy as with EL approach (Sokolichin et al., 1997). The advantage here is that the computational demands are far lower compared to the EL approach, particularly for systems with higher dispersed void fractions.

The major difficulty in modelling multiphase turbulence is the wide range of length and time scales on which turbulent mixing occurs. The largest eddies are typically comparable in size to the characteristic length of the mean flow. The smallest scales are responsible for the dissipation of turbulence kinetic energy. The Direct Numerical Simulation (DNS) approach, with no modelling, resolves all the scales present in turbulence. However, it is not feasible for practical engineering problems involving high Reynolds number flows. The Reynolds-Averaged Navier–Stokes (RANS) approach is more feasible; it models the time-averaged velocity field either by using turbulent viscosity or by modelling the Reynolds stresses directly.

The large eddy simulation (LES) falls between DNS and RANS in terms of the fraction of the resolved scales. In LES, large eddies are resolved directly on a numerical grid, while small, unresolved eddies are modelled. The principle behind LES is justified by the fact that the larger eddies, because of their size and strength, carry most of the flow energy (typically 90%) while being responsible for most of the transport, and therefore they should be simulated precisely (resolved). On the other hand, the small eddies have relatively little influence on the mean flow and thus can be approximated (modelled). This approach to turbulence modelling also allows a significant decrease in the computational cost over direct simulation and captures more dynamics than a simple RANS model.

In RANS models the assumption of isotropic turbulence is often made for the core of the flow, which is not valid in dispersed bubbly flows. In dispersed bubbly flows the velocity fluctuations in the gravity direction are typically twice those in the other directions. This assumption is not made in LES for large structures of the flow, giving LES an advantage over RANS for the core regions of the flow. However, the situation is different close to the walls, where LES assumption of isotropic turbulence is heavily violated, due to the absence of large eddies close to the walls.

## 3.2 LES for Dispersed Bubbly Flows

In dispersed bubbly flows, the large-scale turbulent structures interact with bubbles and are responsible for the macroscopic bubble motion, whereas small-scale turbulent structures only affect small-scale bubble oscillations. Since large scales (carrying most of the energy) are explicitly captured in LES and the less energetic small scales are modelled using a subgrid-scale (SGS) model, LES can reasonably reproduce the statistics of the bubble-induced velocity fluctuations in the liquid. There are three important considerations for modelling of dispersed bubbly flows:

(1) Filtering operation. Depending on the magnitude of the turbulence and the size of the bubbles, a separation of length scales of the interface should be applied. The separation of these scales forms the basis for "filtering" the Navier–Stokes equations and applying proper model equations for multi-phase flows. For the dispersed flow, it is important to identify the scales at which the governing equations are to be applied; microscales, i.e. scales which are small enough to describe individual bubble shapes; mesoscales, i.e. scales which are comparable to bubble sizes; and macroscales, i.e. scales which entail enough bubbles for statistical representation.

(2) The grid-scale equations. Depending on the ratio of the length scales introduced

above, with an affordable grid resolution, a proper form of the governing equations must be chosen. For instance, if the mesh size is in the microscale order, single-fluid interface tracking techniques are more appropriate to solve the problem. If, on the other hand, the grid size is large enough for statistical description of bubbles, the EE approach can be used. Should the grid size be comparable to the meso-scales, we are in a limiting area for both approaches, and special care must be taken in order to solve equations which describe the underlying physics consistently.

(3) The physical models. Depending on the selected gridscale equations, physical models of various complexities should be employed. The options here are numerous, whether they concern turbulence modelling or interphase modelling, but these models are generally simpler in case more of the microscales are resolved.

In the following sections, we describe each of these three elements to model turbulent dispersed bubbly flow.

### 3.2.1 Filtering Operation

The aim of filtering the Navier-Stokes equations is to separate the resolved scales from the SGS (non-resolved).The interface between the phases, and the level of detail required in its resolution/modelling, defines the filter in a multiphase flow.

When LES is applied at a micro-scale, filtering of turbulent fluctuations needs to be combined with interface tracking methods. These methods have been developed and used in both dispersed flow and free surface flow (Toutant et al., 2009a; Toutant et al., 2009b; Bois et al., 2010; Magdeleine et al., 2010; Lakehal et al., 2008). Interface tracking methods require that all phenomena having an influence on space and time position of the interface are also simulated. For the amount of details required and the large size of practical problems of interest, these types of models should merely be seen as a support for the modelling and validation of more macroscopic approaches and cannot address a real industrial-scale problem (Bestion, 2012).

When LES is applied at a macro-scale, the interface resolution is not considered. However, in practical simulations, these would require too coarse grids, leading to poor resolution of turbulence quantities. Much more often we are in the meso-scale region, in which the mesh size is comparable to bubble sizes. This pushes the main

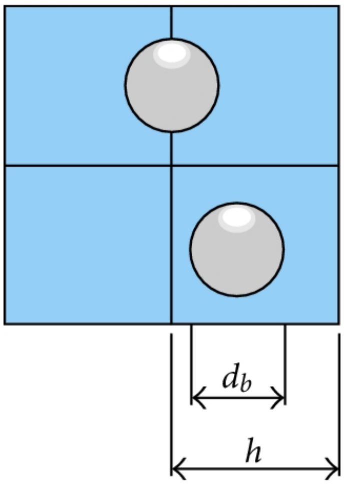

Figure 3.1: Illustration of Milelli condition

assumptions of the EE approach to its limit of validity, and the grid is not fine enough for full interface tracking. In other words, the mesh requirement for EE multiphase modelling conflicts with the requirements of LES approaches (Niceno et al., 2008).

The issue of the requirement of the mesh size was first addressed by Milelli et al. (2001) who carried out a systematic analysis and performed a parametric study with different mesh sizes and bubble diameters. He showed that for case of a shear layer laden with bubbles it was possible to provide an optimum filter width $1.2 < \Delta/d_b < 1.5$, where $\Delta$ is the filter width and $d_b$ is the bubble diameter (shown in Figure 3.1). This means that the grid space should be at least 50% larger than the bubble diameter.The constraint imposed on the ratio $\Delta/d_b$ implies that the interaction of bubbles with the smallest resolved scales is captured without additional approximation.

### 3.2.2 Grid-Scale Equations

The principle of the LES formulation is to decompose the instantaneous flow field into large-scale and small-scale components via a filtering operation. If $\overline{\phi}_f$ denotes the filtered or grid-scale component of the variable $\phi_f$ that represents the large-scale motion then:

$$\phi_f = \overline{\phi}_f + \phi_f^{'} \tag{3.1}$$

where $\phi$ is the variable of interest, subscript $f$ refers either to the liquid or the gas phase. In the remainder of this chapter, the bars of all resolved variables will be omitted for the sake of simplicity. The following filtered equations are obtained:

$$\partial/\partial t\left(\alpha_f \rho_f u_f\right) + \Delta \cdot \left(\alpha_f \rho_f u_f\right) = 0 \tag{3.2}$$

$$\partial/\partial t\left(\alpha_f \rho_f u_f\right) + \Delta \cdot \left(\alpha_f \rho_f u_f u_f\right) = -\bigtriangledown \cdot \left(\alpha_f \tau_f\right) - \alpha_f \bigtriangledown p + \alpha_f \rho_f g + M_f \tag{3.3}$$

where the r.h.s of Equation (3.3) is, respectively, the stress, the pressure gradient, the gravity, and the momentum exchange between the phases due to interface forces. The SGS stress tensor which reflects the effect of the unresolved scales on the resolved scales is modelled as:

$$\tau_f = -\mu_{eff,f}\left(\bigtriangledown u_f + \left(\bigtriangledown u_f\right)^T - \frac{2}{3} I \left(\bigtriangledown \cdot u_f\right)\right) \tag{3.4}$$

where $\mu_{eff,f}$ is the effective viscosity.

In the EE approach, separate equations are required for each phase (e.g. in Eq. (3.3), $f = l, g$, together with the interphase exchange terms (Drew, 1971). In most studies, turbulence is taken into consideration for the continuous phase by SGS models. The dispersed gas phase is modelled as laminar, but influence of the turbulence in the continuous phase is considered by a Bubble-Induced Turbulence (BIT) model.

In the EL approach, there are two coupled parts: a part dealing with the liquid phase motion and a part describing the bubbles motion. The dynamics of the liquid are described in a similar way as in the EE approach, whereas the bubble motion is modelled through the Newton's second law.

Since the governing equations for the liquid and gas phase are expressed in the Eulerian and Lagrangian reference frames, respectively; a mapping technique is used to exchange interphase coupling quantities. Depending upon the volume fraction of the dispersed phase, one-way (e.g. $\alpha_g < 10^{-6}$) or two-way coupling between gas phase to liquid phase ($10^{-6} < \alpha_g < 10^{-3}$) prevails. In both cases, bubble-bubble interactions (i.e., collisions) can be neglected, but the effect of the bubbles on the turbulence structure in the continuous phase has to be considered for higher volume fraction and does not play any role in lower volume fraction of gas phase (Elgobashi, 1991).

#### Two-way Coupling

Two way coupling consists of Forward Coupling (Liquid to Bubble) and Backward or Reversed Coupling (Bubble to Liquid).

In the forward coupling, calculated liquid velocities, velocity gradients, and pressure gradients on an Eulerian grid are interpolated to discrete bubble locations for solving the Lagrangian bubble equation motion.

The forces available at each bubble's centroid need to be mapped back to the Eulerian grid nodes in order to evaluate the reaction force $F$. The two-way interaction (forward and backward) is accomplished with a mapping method, for example, PSI-cell method (Crowe et al., 1977), modified PSI-wall-method (Hu, 2005), or mapping functions discussed by Deen et al. (2004).

### 3.2.3 Interfacial Forces

The motion of a single bubble with constant mass can be written according to Newton's second law:

$$m_b \frac{dv}{dt} = \sum F \tag{3.5}$$

The bubble dynamics are described by incorporating the most significant forces acting on a bubble rising in a liquid. It is assumed that the total force, $\sum F$, is composed of separate and uncoupled contributions originating from lift, drag, added mass, gravity, virtual mass force and turbulent dispersion force:

$$\sum F = F_L + F_D + F_G + F_A + F_{VM} + F_{TD} \tag{3.6}$$

For each force the analytical expression or a semi-empirical model is used, based on bubble behaviour observed in experiment or in DNS. The influence/contribution of these forces are as follows.

**Lift Force**

The lift force is still poorly understood, and thus experimental and numerical efforts have been conducted for its determination. The value of the lift coefficient may differ in bibliography, and this is due to different handling of factors responsible for bubble dispersion, for example the interaction between the bubbles and the influence of turbulent eddies in the liquid phase. Modeling of the lift force for capturing an accurate bubble plume dispersion is important. However, there is an uncertainty regarding the appropriate value and correlation representing lift coefficient. There is also recommendation that bubble size-dependent lift coefficient should be chosen (Tabib et al., 2008).

The major parameters affecting the lift force acting on a spherical particle in a simple unbounded shear flow are (i) relative velocity between a particle and an ambient fluid, (ii) shear rate of an ambient fluid, (iii) particle rotational speed, and (iv) surface boundary condition (non-slip or slip at particle surface). The deformation of a particle causes the associated wake modification and the modified interaction with surrounding flow structures resulting in lift force modification.

In RANS approach, a constant value of the lift coefficient ($C_L = 0.5$) is commonly used, while the value of the turbulent dispersion coefficient is varied (0.1 to 1.0) to get good agreement with the experimental data. However, in LES, bubble dispersion caused by liquid phase turbulent eddies is implicitly calculated, and a more realistic contribution of the lift force can be used.

The lift force model and lift coefficient ($C_L$) correlations have been described by a number of researchers using three approaches, namely (1) analytical approach; (2) numerical approach; and (3) experimental approach.

In the analytical approach, some assumptions are made to derive the analytical form of the lift force. Saffman (1965) described the lift force acting on a sphere moving through a very viscous liquid with velocity $u_{r\infty}$ relative to a uniform simple shear:

$$F_{L\infty} = 6.46\rho_f \nu_f^{1/2} u_{r\infty} r_p^2 \omega^{1/2} \tag{3.7}$$

where $\rho_f$ is the fluid density, $\nu_f$ is the fluid kinematic viscosity, $r_p$ is the particle radius, $u_{r\infty}$ is the relative velocity of particle and fluid measured on the streamline through the center and $\omega$ is the magnitude of velocity gradient.

Auton (1987) defined the lift force on a spherical body in a rotational flow of an inviscid fluid as:

$$F_{L\infty} = C_{L\infty} \frac{4}{3} \pi \rho_f r_p^3 u_{r\infty} x \left(\nabla x u_f\right) \tag{3.8}$$

where $C_{L\infty} = 0.5$ (constant value).

Magnaudet et al. (2003) derived an analytical expression for the lift force acting on deformable bubble of arbitrary viscosity moving in a viscous fluid in a linear shear flow near a wall:

$$F_{L\infty}^d \approx \left( \frac{4}{5} \pi \omega v_{r\infty} \left( 1 + \frac{3}{8} \tilde{l} + \frac{9}{64} \tilde{l} \right) + \frac{169}{70} \omega^2 \tilde{l}^2 \right) e_x \tag{3.9}$$

where $e_x$ is the unit vector perpendicular to the wall and directed away from it.

In the numerical approach, numerical solutions obtained under some assumptions are utilized to obtain an empirical correlation. A numerical simulation of single bubbles in a Poiseuille flow (Tomiyama et al., 1993; Tomiyama et al., 1995) suggested that the bubble migration towards the pipe center was related closely to a slanted wake behind a deformed bubble. Thus, it has been indicated that the bubble size and complex interaction between a bubble wake and a shear field around the bubble play an important role in the lateral bubble migration (Serizawa and Kataoka, 1994).

McLaughlin (1991) described the force on a small rigid sphere in a linear shear flow as following:

$$F_{L\infty} = 6.46\rho_f \nu_f^{1/2} u_{r\infty} r_p^2 \left( \frac{J}{2.255} \right) \omega^{1/2} \tag{3.10}$$

Legendre and Magnaudet (1998) studied numerically the three-dimensional flow around a spherical bubble moving steadily in a viscous linear shear flow by solving the full Navier–Stokes equations. They assumed that the bubble surface was clean so that the outer flow obeyed a zero-shear–stress condition and did not induce any rotation of the bubble. They developed an empirical correlation for the lift force on a spherical bubble in a viscous linear shear flow at finite Reynolds number by means of a numerical simulation

$$F_{L\infty}e_y = \rho_f \frac{4}{3}\pi r_b^3 C_{L\infty}\nu_{r\infty}x\omega_V \quad \text{for} \quad 0.1 \leq N_{Re\infty} \leq 500 \quad , \quad 0.01 \leq G_{S\infty} \leq 0.25 \tag{3.11}$$

where $F_{L\infty}$ is the lift force perpendicular to the flow direction, $r_b$ is the sphere radius, $\rho_f$ is the density of the fluid phase and $\omega_V$ the relative velocity with respect to the fluid velocity and vorticity, which must be evaluated at the centre of the bubble.

Single bubble Reynolds number and dimensionless velocity gradient are, respectively, defined as:

$$N_{Re\infty} \equiv \frac{|u_{r\infty}|\, d_b}{v_f} \quad \text{and} \quad G_{s\infty} \equiv \frac{r_p\omega}{u_{r\infty}} \tag{3.12}$$

where $d_b$ is the sphere diameter, $v_f$ is the kinematic viscosity of the fluid phase and $\omega$ the magnitude of the velocity gradient. The lift coefficient $C_{L\infty}$ of a spherical bubble is given by:

$$C_{L\infty} = \sqrt{C_{L\infty}^{lowN_{Re\infty}}\left(N_{Re\infty}, G_{S\infty}\right)^2 C_{L\infty}^{highN_{Re\infty}}\left(N_{Re\infty}\right)^2} \tag{3.13}$$

where

$$\begin{cases} C_{L\infty}^{lowN_{Re\infty}}\left(N_{Re\infty}, G_{S\infty}\right) = \dfrac{6}{\pi 2\left(2N_{Re\infty}G_{S\infty}\right)^{1/2}} \dfrac{2.255}{\left(1+0.1N_{Re\infty}/G_{S\infty}\right)^{3/2}} \\ C_{L\infty}^{highN_{Re\infty}}\left(N_{Re\infty}\right) = \dfrac{1}{2}\left(\dfrac{1+16N_{Re\infty}^{-1}}{1+29N_{Re\infty}^{-1}}\right) \end{cases} \tag{3.14}$$

Legendre et al. (2003) investigated hydrodynamic interactions between two spherical clean bubbles rising side by side in a viscous liquid by solving the Navier-Stokes equations in the range of $0.02 \leq N_{Re\infty} \leq 500$ and $2.25 \leq L_S^* \leq 20$

$$\begin{gathered} C_L^{'} \equiv F_L/\left(\pi r_b^2 \rho_f v_{r\infty}^2/2\right) \approx \\ -6L_S^{*-4} \times \left[\left\{1 - \frac{40}{N_{Re\infty}} + O\left(N_{Re\infty}^{-3/2}\right)\right\} + L_S^{*-3} + O\left(N_{Re\infty}^{-1}L_S^{*-2}, L_S^{*-5}\right)\right] \end{gathered} \tag{3.15}$$

where $L_S^*$ is the distance between bubble centers normalised by bubble radius.

In experimental approaches, experimental data are utilized to obtain an empirical correlation. In the 1980s and 1990s, extensive experiments were performed to identify important parameters to determine the lateral bubble migration characteristics. The experiments showed that relatively small and large bubbles tend to migrate toward a channel wall and center (for example Liu, 1993; Hibiki and Ishii, 1999; Hibiki et al., 2001; Hibiki et al., 2003). Kariyasaki (1987) studied the lift force acting on air bubble in a uniform shear flow and defined lift force as follows:

$$F_{L\infty} = 1.26\pi\rho_f \left|v_{r\infty}\right|^2 d_p^2 \left(\frac{\rho_f v_f^2}{d_p \sigma}\right)^{1.2} \frac{N_{Re\omega\infty}}{N'_{Re\infty}} \quad , \quad N'_{Re\infty} = \frac{\left|v_{r\infty}\right| d_p}{\nu_f} \tag{3.16}$$

Sridhar and Katz (1995) defined lift force for microscopic bubbles entrained by a vortex:

$$F_{L\infty} = 0.295\pi\rho_f r_p^2 u_{r\infty}^2 G_{S\infty}^{1/4} \quad , \quad \text{for} \quad 20 < N_{Re\infty} < 80 \quad \text{and} \quad 250\mu m < r_p < 400\mu m \tag{3.17}$$

Tomiyama et al. (2002) measured bubble trajectories of single air bubbles in simple shear flows of glycerol–water solutions to evaluate transverse lift force acting on single bubbles. Based on the experimental result, they assumed the lift force caused by the slanted wake had the same functional form as that of the shear-induced lift force, and proposed an empirical correlation of the lift coefficient:

$$\begin{aligned} F_{L\infty} = F_{SL\infty} + F_{WL\infty} = \\ -\left(C_{SL\infty} + C_{WL\infty}\right)\rho_f \frac{\pi d_p^3}{6}\left(v_{g\infty} - v_f\right) \times v_f = \\ -C_{L\infty}\rho_f \frac{\pi d_p^3}{6}\left(v_{g\infty} - v_f\right) \times v_f \end{aligned} \tag{3.18}$$

where $F_{SL\infty}$ is the shear-induced lift force and $F_{WL\infty}$ is the lift force due to a slanted wake.

Experiments by Tomiyama (2004) imply that a slight bubble deformation might change the direction of the lift force acting on a bubble and this results agree with the numerical simulation results by Takagi and Matsumoto (1995).

Takemura and Magnaudet (2003) studied experimentally the wall-induced migration of bubbles rising near a vertical wall in a quiescent liquid in the range of $a \leq N_{Re\infty} \leq 100$. Fully contaminated bubbles were repelled by the wall due to the interaction of the wall with the far-field of the particle wake. The repulsive force decreased with increasing $N_{Re\infty}$ and the distance between the bubble center and the wall. For contaminated bubble:

$$C^{'}_{L\infty} \equiv F_{L\infty} / \left(\pi r_b^2 \rho_f v_{r\infty}^2 / 2\right) = C^{'}_{L\infty 0} \alpha^2 \left(\frac{l_{SW}}{b r_p}\right)^c \tag{3.19}$$

$$\alpha = 1 + 0.6 N_{Re\infty}^{0.5} - 0.55 N_{Re\infty}^{0.08} \quad , \quad b = 3.0 \tag{3.20}$$

$$c = -2.0 \tanh\left(0.01 N_{Re\infty}\right) \tag{3.21}$$

$$C^{'}_{L\infty 0} = \begin{cases} \left(9/8 + 5.78 \times 10^{-6} \tilde{l}^{4.58}\right) \beta^2 e^{-0.292\tilde{l}} & \text{for} \quad 0 < \tilde{l} < 10 \\ 8.49 \beta^2 \tilde{l}^{-2.09} \quad \text{for} \quad 10 \leq \tilde{l} < 300 \end{cases} \tag{3.22}$$

For $N_{Re\infty} < 35$ clean bubbles were repelled by the wall due to the interaction of the wall with the far-field of the particle wake, whereas for $35 \leq N_{Re\infty} \leq 100$ the attractive force to the wall acted on clean bubbles due to the lateral pressure gradient predicted by irrotational flow theory. For clean bubble:

$$C^{'}_{L\infty} = C^{'}_{L\infty 0} \alpha'^2 \left(\frac{l_{SW}}{b r_p}\right)^c + \alpha" C^{'}_{L\infty\infty}$$

$$\alpha' \approx 1 + 2.0 \tanh\left(0.17 N_{Re\infty}^{0.4} - 0.12 N_{Re\infty}^{0.05}\right)$$

$$\alpha" = 1 - \exp\left(-0.22 N_{Re\infty}^{0.45}\right) C^{'}_{L\infty\infty} = -\frac{3}{8}\tilde{l}^4 \left(1 + \frac{1}{8}\tilde{l}^3 + \frac{1}{6}\tilde{l}^5\right) + O\left(\tilde{l}^{10}\right)$$

### Drag Force

In a single particle system, transitions between bubble shape regimes occur when drag law governing fluid-particle system changes. Since the drag and lift force are the components of pressure and viscous stress to the directions parallel and perpendicular to the flow direction, these forces are closely related. The drag force is defined as:

$$F_D = \frac{1}{2} C_{D\infty} \rho_f u_{r\infty} \left|u_{r\infty}\right| \pi r_b^2 \tag{3.23}$$

The drag laws developed by Ishii and Chawla (1979) are as follows:

For viscous regime, the drag coefficient is given by an empirical correlation as:

$$C_{D\infty} \equiv -\frac{16}{NRe\infty}\left(1 + 0.1N_{Re\infty}^{0.75}\right) \tag{3.24}$$

For distorted-particle regime:

$$C_{D\infty} = \frac{4}{3}r_d\sqrt{\frac{g\Delta\rho}{\sigma}} = \frac{\sqrt{2}}{3}N_\mu N_{Re\infty} \tag{3.25}$$

For spherical-cap bubble regime, the drag coefficient reaches a constant value of:

$$C_{D\infty} = \frac{8}{3} \tag{3.26}$$

The transition criterion between viscous and distorted-particle regimes is determined by Equations (3.24) and (3.25) as:

$$N_\mu = \frac{24\sqrt{2}\left(1 + 0.1N_{Re\infty}^{0.75}\right)}{N_{Re\infty}^2} \tag{3.27}$$

### Added Mass Force

The concept of added mass, one of the classic achievements of theoretical fluid dynamics, contrasts the acceleration, caused by a given force $F$, of a particle of mass $m_p$ in a fluid. In a vacuum Newton's law states that $m_p\alpha_0 = F$, while in a fluid it holds that $m_p\alpha_1 < F$ where $\alpha_1 < \alpha_0$. The part of the force corresponding to $(\alpha_0 - \alpha_1)$ is spent on the acceleration of the surrounding fluid, which in effect, is equivalent to increasing particle mass by the specific amount $m_\alpha$ of fluid mass being accelerated together with the particle, $(m_p + m_\alpha)\alpha_1 = F$. The problem is in the determination of $m_\alpha$.

The product $(m_\alpha\alpha_1)$ is an unsteady inertial force that opposes the motion of a particle whenever its velocity changes. When a particle moves in a stagnant fluid, this force is usually written as:

$$F_\alpha = -m_\alpha(dv/dt) \tag{3.28}$$

If the fluid itself has a non-zero velocity $u$, the force is expressed as:

$$F_\alpha = m_\alpha(du/dt - dv/dt) \tag{3.29}$$

The added mass $m_\alpha$ is the part $C$ of the fluid mass displaced by the particle of volume $V$,

$$m_\alpha = C\rho V \tag{3.30}$$

where $C$ is the added mass coefficient. The problem here is to determine $C$.

Thus far the simplest case has been considered, in which the particle is of a simple shape (sphere) and moves without rotation in an unbounded inviscid fluid. In this case, the quantity $C$ is a scalar and takes the value of 0.5. When the particle has a lower degree of symmetry and is allowed to rotate, we have a second-order tensor C with 6 components (6x6 matrix). Matrix C acts on the vector $\alpha$ of (linear and angular) acceleration to produce vector F of (force + torque), $F_\alpha = -(\rho V)Ca$. Consequently, $\alpha$ and $F$ are generally misaligned. The components $C_{ij}$ termed inertia coefficients (analogous to the concept of inertia tensor used in rigid body motion) correspond to the inertia effects acting in different direction of particle forces and rotation (torques). They are determined by the geometry of the problem: particle shape, particle configuration and presence of boundaries. Since they are not dependent on the physical nature of the particles, these coefficients apply, without discrimination, to bubbles, drops and solids. Tensor C may be simplified by the presence of symmetry and by the choice of a suitable coordinate system.

The theoretical approach to added mass has been described in a number of advanced texts on fluid mechanics (e.g. Batchelor, 1967; Birkhoff, 1960; Lamb, 1932; Milne-Thomson, 1968; Robertson and Sibulkin, 1965; Yih, 1988), as well as in those focusing on fluid inertia forces (Newman, 1977). In addition, analytical and experimental results for the added mass coefficients of various bodies (e.g. rectangular shapes, rotating ellipsoids etc) can be found in Brennen (1982).

Much has also been written about the practical applications of added mass. As added mass is an important issue when particles move in fluids with unsteady motion, one are of naval research focuses on the strong forces of inertia experienced by floating and underwater objects.

Multiphase fluid dynamics is another area of research in which dispersed particles are also exposed to these forces (Clift, 1978; Michaelides, 2006; Wallis, 1990). Here, the simplest case is a single dispersed particle translating in an unbounded domain. Two factors complicate the situation; the presence of domain boundaries and the presence of other particles. We need added mass coefficient $C$ for the following typical situations: particles approaching a wall, two or more particles in certain configurations (doublets, triplets, arrays etc), expanding/collapsing particles, oscillating particles, rotating particles, etc. Some of these simpler situations have already been solved, most of them having been approached analytically from the perspective of potential flow theory. In addition, experiments have been performed on the forces acting on oscillating bodies, where the period depends on added mass coefficient $C$.

Added mass force may be relevant in cases where the density of the dispersed (particulate) phase $\rho_p$ is comparable to, or even lower than, that of the continuous (carrying) phase $\rho$. This applies to liquid-liquid (drops in liquids) and solid-liquid (solids in liquids) systems and, in particular, to gas-liquid systems (bubbles in liquids) where, because the interphase density ratio $\rho/\rho_p$ is $\sim 10^3$, almost all the inertia is concentrated in the carrying liquid phase.

Added mass force also plays an important role in the hydrodynamics of bubble columns. Few experimental and analytical studies have been conducted, and most of the data in this area have been obtained using multiphase CFD simulations (Jakobsen, 2005; Joshi, 2001; Ranade, 2002; Prosperetti and Tryggvason, 2007). Delnoij et al. (1997) carried out an EL simulation of a partially aerated bubble column and concluded that added mass plays an important role in the vicinity of the gas distributor. While performing linear stability analysis of a 1D EE model of a bubble column, Leon-Becerril and Line (2001) found that added mass has a significant effect on homogeneous-heterogeneous flow regime transition. Subsequently, Leon-Becerril et al. (2002), carrying out 3D EE simulations of a partially aerated rectangular bubble column, found it necessary to include added mass in the model in order to reproduce bubble plume oscillations (Becker et al., 1994). Leon-Becerril et al. (2002) simulated mixing in a fully aerated rectangular column, again reporting the importance of added mass force. Monahan et al. (2005) observed that added mass force is important in stabilizing homogeneous regimes, and cannot be neglected in large columns. In the model for homogeneous-heterogeneous regime transition in bubble columns developed by Bhole and Joshi (2005) the added mass coefficient was a relevant control parameter. Added mass force can also affect the values of the terms describing the production of turbulent kinetic energy due to the presence of gas-liquid interfaces (e.g. Mudde and Simonin, 1999; Joshi, 2001). Chahed et al. (2003) introduced turbulence correlations related to added mass into their expression for interphase force, and found them to be of great importance in the computation of the void fraction in non-homogeneous bubbly flows. Various experimental studies have also been conducted (e.g. Cai and Wallis, 1993; Kendoush et al., 2007; Odar and Hamilton, 1964; Takahashi et al., 1992).

Other results have also shown the ambiguity of the problem of added mass force. Mudde and Simonin (1999) concluded that it is necessary to use added mass force in EE simulations of bubble plume. However, different codes showed less need for added mass (Oey et al., 2003) oscillatory plume being reproducible without factoring in added mass force. Deen et al. (2001) and Zhang et al. (2006) reported that added mass forces had negligible effect on their EE simulation results for a centrally aerated rectangular bubble column (except at the very top and bottom of the column). Likewise, Tabib et al. (2008) reported that added mass had no significant influence on the results they obtained using a 3D transient simulation of a cylindrical bubble column.

It is clear that added mass force is an important parameter in the description of multiphase systems, and can even play the dominant role in certain specific flow situations. Added mass force particularly applies in those situations where the density ratio $\rho/\rho_p$ is large, the motion unsteady, the particle shape and configuration liable to change and the presence of boundaries influential (Simcik et al., 2008).

### Virtual Mass Force

The virtual mass force is proportional to the relative acceleration between the phases and is negligible once a pseudosteady state is reached. It has little influence on the simulation results for bubble plumes (e.g. Deen et al., 2001; Dhotre et al., 2008). It is mainly because of the acceleration and deceleration effects are restricted to small end regions of the column. A constant coefficient is used in almost all investigations.

**Turbulent Dispersion Force**

In the RANS approach, the drag and lift forces depend on the actual relative velocity between the phases, but the ensemble equations of motion for the liquid only provide information regarding the mean flow field. The random influence of the turbulent eddies is considered by modelling a turbulent dispersion force. By analogy with molecular movement, the force is set proportional to the local bubble concentration gradient (or void fraction), with a diffusion coefficient derived from the turbulent kinetic energy. The value of the turbulent dispersion coefficient is chosen to get an agreement with the measurement data and is not known a priori.

In LES, the resolved part of the turbulent dispersion is implicitly computed, and hence the information from LES can be used for calculating the magnitude of the force. The methodology depends on scales at which LES is to be applied. For instance, at the mesoscale, in the EL approach, bubbles dispersed by drag and lift through turbulent eddies can be computed. At micro-scale LES, bubble coalescence and breakup phenomena should be considered along with a reasonable number of bubbles.

### 3.2.4 Effect of Bubble-Induced Turbulence (BIT)

In the EE approach, the turbulent stress in the liquid phase is considered to have two contributions, one due to the inherent, that is, shear-induced turbulence that is assumed to be independent of the relative motion of bubbles and liquid and the other due to the additional bubble-induced turbulence (Sato and Sekoguchi, 1975). There are two modelling approaches to account for the effect of BIT. The first approach is proposed by Sato and Sekoguchi (1975) and Sato et al. (1981):

$$\mu_{BI,l} = \rho_f C_{\mu,BI} \alpha_g d_b \left| u_g - u_l \right| \tag{3.31}$$

with $C_{\mu,BI}$ as a model constant which is equal to 0.6 and $d_b$ as the bubble diameter.

Milelli et al. (2001) found that the modelling of the bubble-induced turbulence did not improve the results. They tried two different formulations: the Tran model and the Sato model and found that they have negligible effect. This was attributed to the fact that the bubble-induced viscosity (and turbulence) is not crucial, the turbulence being mainly driven by the liquid shear, and a low void fraction ($\approx 2\%$ leading to $\mu_{BI,l} \approx 10^{-2}$kg/(ms)) did not significantly modify the situation. It was thought that in a case in which the bubbles actually drive the turbulence (via buoyancy and/or added mass forces), the situation would be different. However, in subsequent studies, similar observations were made in bubble plumes (Deen et al., 2001; Dhotre et al., 2008; Niceno et al., 2008).

The second approach for the modelling of BIT allows for the advective and diffusive transport of turbulent kinetic energy. This model incorporates the influence of the gas bubbles in the turbulence by means of additional source terms in the $k_{SGS}$ equation and is taken to be proportional to the product of the drag force and the slip velocity between the two phases. This approach was used in the study of Niceno et al. (2009) through the use of a one-equation model. They found significant influence of the additional source terms as used by Pfleger et al. (1999).

## 3.3 LES Prediction of the Flow Pattern for Dispersed Bubbly Flows

This section is a review of different LES studies that were performed using the EE and EL approaches for simulating flow patterns in gas-liquid bubbly flows.

### 3.3.1 Eulerian-Eulerian (EE) Studies

Milelli et al. (2001) reported for the first time a two-phase LES study with EE approach. A statistical investigation of a 2D flow configuration was conducted. One of the main findings of the studies is the definition of the optimum ratio of the cut-off filter width (i.e. grid) to the bubble diameter ($d_b/\Delta$) at 1.5. This means that the mesh size should be at least 50% larger than the bubble diameter so that (a) bubble size determines the largest scale modelled and (b) its interaction with the smallest calculated scale above the cut-off is captured. Milelli's finding is also supported by the scale-similarity principle of Bardina et al. (1980).

Milelli (2002) investigated a free bubble plume using a LES-EE approach and compared their predictions with the experiment of Anagbo and Brimacombe (1990). Different SGS models were tested and it was found that the mean quantities of the flow were not strongly affected by the different SGS models. Moreover, it was found that the dispersed phase had little impact on the turbulence of the continuous phase. The turbulent energy spectrum taken in the bubbly flow region revealed a power-law distribution oscillating between $-5/3$ and $-8/3$ in the inertial subrange. Hence, there was no influence of modifying the SGS model to account for bubble-induced dissipation. Further, it was observed that the lift coefficient value plays a major role in capturing the plume spreading and that the lift coefficient may differ for an LES compared to the one in a RANS approach. This was due to different handling of interaction between the bubbles and influence of turbulent eddies in the liquid phase, which are two factors responsible for the bubble dispersion.

Deen et al. (2001) reported LES for gas-liquid flow in a square cross-sectional bubble column for the first time. They investigated the performance of RANS and LES approaches, the influence of the inter-phase forces, and the bubble-induced turbulence. It was found that the RANS approach ($k-\epsilon$ model) overestimated the turbulent viscosity and could only predict low frequency unsteady flow. On other hand, LES reproduced high frequency experimental data and predicted a strong transient bubble plume movement in accordance the experimental results. Furthermore, the lift force was identified as being the force responsible for the transient spreading of the bubble plume and in absence of it, i.e. only with drag force, the bubble plume showed no transverse spreading. Deen et al. (2001) identified three contributors to the effective viscosity of the continuous phase: i.e. the molecular, the shear-induced turbulent (modelled using Smagorinsky model), and the bubble-induced turbulent viscosities (Sato and Sekoguchi, 1975). The effects of the virtual mass force and the BIT on the simulated results were found to be negligible, confirming Milelli's findings.

Bove et al. (2004) reported LES with EE approach for the same square cross-sectional bubble column as used by Deen et al. (2001). The influence of numerical modelling of the advection terms and the inlet conditions on LES performance was studied. The upwind first-order and higher-order Flux Corrected Transport (FCT) schemes for both the phase fraction equations and the momentum equations were employed.

The simulations using a second-order FCT scheme showed relatively good agreement with the measurement data of Deen et al. (2001). It was also showed that the proper discretization of the momentum and volume fraction equations is essential for correct prediction of the flow field. Further, the LES results were found to be very sensitive to the inlet boundary conditions. Three different inlet configurations showed that the inlet modelling influences the predicted fluid flow velocity and the turbulent viscosity. In this work, the sparger (a perforated plate) was not modelled due to the difficulty in adapting the mesh grid to the geometry. It was also suggested that near wall region description in the SGS models is important, and the lack of the near wall modelling can lead to erroneous prediction of frictional stresses at the wall. A drag model for the contaminated water was used, which gave a better prediction of the slip velocity. However, the velocity profile was underestimated for both the gas and liquid phase. The reason for the under-prediction was not clear; whether it was due to the drag force model or the value of the lift coefficient or the near wall modelling. Need for further work in this direction was suggested.

Zhang et al. (2006) reported LES in a square cross-sectional bubble column using an EE approach. The work of Deen et al. (2001) was extended with the addition of BIT in the $k - \epsilon$ turbulence model for the prediction of the dynamic behaviour of the square bubble column. A sensitivity analysis on the Smagorinsky constant was carried out. It was found that higher $C_S$ values led to higher effective viscosity which dampens the bubble plume dynamics. A good agreement with the measurements was obtained with $C_S$ in the range of 0.08–0.10. In Zhang et al. (2006) study was also confirmed that the lift force plays a critical role for capturing the dynamic behaviour of the bubble plume.

Zhang et al. (2009) followed a procedure similar to that used by Darmana et al. (2005), with an EE approach to simulate flow, mass transfer, and chemical reactions in square cross-sectional bubble column (Deen et al., 2001). Zhang et al. (2009) studied physical and chemical absorption of $CO_2$ bubbles in water and in an aqueous sodium hydroxide (NaOH) solution. They used a bubble number density equation for coupling of flow, mass transfer, and chemical reaction. The authors demonstrated the influence of the mass transfer and chemical reaction on the hydrodynamics, bubble size distribution, and gas holdup.

Dhotre et al. (2008) reported LES with an EE approach for a gas-liquid flow in a square cross-sectional bubble column. The influence of two SGS models was studied, namely Smagorinky and Dynamic model of Germano et al. (1991). It was found that both the Smagorinsky model ($C_S = 0.12$) and the Germano model predictions were in agreement with the measurements. An investigation of the $C_S$ value obtained from the Germano model was conducted and it was found that the reason of the similar performance of the two SGS models was the probability density function of $C_S$ (from Germano model) over the entire column. The value of $C_S$ has the highest probability in the range of 0.12–0.13. Like Zhang et al. (2006), the authors confirmed that with a proper BIT model, RANS also performed well for mean quantities of flow variables. It was further concluded that the Germano model can give correct $C_S$ estimations for the configuration under consideration and, in general, can be used for other systems where $C_S$ is not known as "a priori" from previous analysis.

Dhotre et al. (2009) extended the work of Dhotre et al. (2008) and reported LES with EE approach for a gas-liquid flow in a large-scale bubble plume. The numerical results were compared with the experimental data from Simiano (2005) and a RANS model at three different elevations of the bubble plume. The LES-EE approach captured well the transient behaviour of the plume and predicted the second-order statistics of the liquid phase accurately. In the RANS approach the turbulent dispersion force was required to reproduce the bubble dispersion; however, in LES, bubble dispersion is implicitly calculated by resolving the large-scale turbulent motion responsible for bubble dispersion. Dhotre et al. (2009) found good agreement with the experimental data at higher elevations, while discrepancies were observed at lower elevation, near the injector. The reason for the discrepancies was attributed to the absence of modelling bubble coalescence and breakup. This was also found in the work of Hengel et al. (2005), where it was shown that most of the coalescence occurs in the lower part of the column and recommended to consider bubble size distribution and coalescence and breakup models for reproducing the bubble behaviour near the sparger.

Niceno et al. (2008) investigated LES with EE approach for a gas-liquid flow in a square cross-sectional bubble column. The applicability of a one-equation model for the SGS kinetic energy ($k_{SGS}$) was investigated. The influence of two approaches for bubble-induced turbulence was studied: (1) an algebraic model (Sato and Sekoguchi, 1975) and (2) extra source terms (as used in Pfleger et al., 1999) in the transport equation for SGS kinetic energy approach. It was found that the latter approach improved the quantitative prediction of the turbulent kinetic energy. The modelled SGS kinetic energy for the Pfleger model found to be much higher than for the Sato model, indicating the Pfleger model needs a more appropriate constant for LES. It was also suggested that the modelled SGS information can be used to access the SGS inter-facial forces, in particular the turbulent dispersion force. In their work, the effect of SGS turbulent dispersion force could not be determined as the bubble size was almost equivalent to the mesh size.

Extending the work of Niceno et al. (2008), Niceno et al. (2009) compared two different codes (Neptune and CFX-4) and two subgrid-scale models for the simulation of gas-liquid flow in a square cross-sectional bubble column using LES-EE. The prediction from the Neptune CFD code (applying the Smagorinsky model) and from the CFX-4 CFD code (one-equation model) was compared with the measurement data of Deen et al. (2001). Agreement between the predictions from the two SGS models was found to be good, and it was concluded that the influence of the SGS model was small. This is in contradiction with earlier work of Hengel et al. (2005), where they showed significant contribution of the SGS model. It remains to be seen if this was due to the fine mesh used by the authors ($\Delta/d_b = 1.2$). Niceno et al. (2009) argued that with the known flow pattern in a bubble column, that is, a dominant bubble plume meandering between the confining walls, the biggest eddy having most energy is of the size of the domain cross section. Thus, the grid used in their work was a compromise between sufficiently fine to capture the most energetic eddies, and sufficiently coarse to stay close to the Milelli criterion (Milelli et al., 2001). Furthermore, the limitations of LES with EL or EE approach without resolving interface were pointed out; the most influential inter-facial forces (drag and lift) are modelled for the large-scale field and their effect from the small scale remains a question.

Tabib et al. (2008) reported LES using EE approach in a cylindrical column for a wide range of gas velocity. In their study it was confirmed the importance of a suitable lift coefficient and drag force model, in accordance with previous studies.

The influence of different spargers (perforated plate, sintered plate, and single hole) and turbulence models ($k-\epsilon$, RSM, and LES) was studied, comparing the numerical results with experimental data from Bhole et al. (2006). The main findings from the study were that the RSM performs better than the $k-\epsilon$ model; the LES was successful in predicting the averaged flow behaviour and was able to simulate the instantaneous vortical-spiral flow regime in the case of a sieve plate column, as well as the bubble plume dynamics in case of single-hole sparger.

Tabib and Schwarz (2011) extended the work of Niceno et al. (2008) and attempted to quantify the effect of SGS turbulent dispersion force for different particle systems, where the particle sizes would be smaller than the filter size. The formulation of de Bertodano (1992) was applied to approximate the turbulent diffusion of the bubbles by the SGS liquid eddies for a gas-liquid bubble column system (Tabib et al., 2008). The bubble size was in range of 3–5 mm. The mesh used in simulations was coarser than the bubble diameter. They found a high contribution from the SGS turbulent dispersion force, when compared with the magnitude of the other interfacial forces (like drag force, lift force, resolved turbulent dispersion force, and force due to momentum advection and pressure). Tabib and Schwarz (2011) concluded that for LES with EE approach, when the mesh size is bigger than bubble size, the SGS turbulent dispersion force should be used, and that a one-equation SGS-TKE model overcomes a conceptual drawback of EE LES model.

### 3.3.2 Eulerian-Lagrangian (EL) Studies

Hengel et al. (2005) reported LES with EL approach for a gas-liquid flow in a square cross-sectional bubble column. The liquid phase was computed using LES, and a Lagrangian approach was used for the dispersed phase. A discrete bubble model (DBM) originally developed by Delnoij et al. (1997) and Delnoij et al. (1999) was used and extended to incorporate models describing bubble breakup and coalescence. The mean and fluctuating velocities predicted in the simulations showed a good agreement with the experimental data of Deen et al. (2001). The influence of the SGS model on the predictions was studied. It was found that without SGS model, the average liquid velocity and liquid velocity fluctuations are much lower compared to the case with a SGS model. This was due to the lower effective viscosity, which led to less dampening of the bubble plume dynamics. In this work also, the authors confirmed the important role of the lift coefficient in capturing the plume dynamics. They considered two lift coefficients ($C_L = 0.5$ and 0.3) and found that a smaller value of the lift coefficient led to higher average velocity and velocity fluctuations and less spreading of the plume, which resulted in overprediction of the average velocity in the centre of the column.

Hu and Celik (2008) reported LES with an EL approach for the gas-liquid flow in a flat bubble column. The mapping technique called particle-source-in-ball (PSI-ball) for coupling the Eulerian and Lagrangian reference frames were developed in this study, which is a generalization of the conventional particle-source-in-cell (PSI-cell) method. Second-order statistics of the pseudoturbulent fluctuations were presented. The predicted mean quantities (such as mean liquid velocity) were in good agreement with the experimental data of Sokolichin and Eigenberger (1999). An accurate prediction of the instantaneous flow features was given, including liquid velocity fluctuations and unsteady bubble dispersion pattern. The influence of the Smagorinsky constant was also studied and found that the constant for multiphase systems falls in a relatively smaller range than for single-phase flows. Higher values of the $C_S$ showed an excessive damping effect to the liquid field, which led to a steady-state solution. This observation is in accordance with studies from Zhang et al. (2006) and Hengel et al. (2005). Furthermore, authors proposed to use $C_S$ as a modeling parameter rather than a physical constant, as the interphase coupling terms used as well as the high frequency turbulent fluctuations contribute to the turbulent kinetic energy dissipation.

Lain (2009) reported an LES with EL approach for a gas-liquid flow in a cylindrical bubble column. The interaction terms between liquid and gas phases was calculated using the particle-source-incell (PSI-cell) approximation of Crowe et al. (1977). The bubbles were considered as a local source of momentum, and a source term was added. A simple model for the subgrid liquid fluctuating velocity to account for the BIT considered in this work was found to have no influence on the predictions. As in previous works, it was confirmed a strong dependency of the bubble dispersion in the column on the value of transverse lift force coefficient used. The lift coefficient depends on the bubble-liquid relative velocity and was the main mechanism responsible for the spreading of bubbles across the column crosssection. The numerical results were compared with particle image velocimetry (PIV) measurements (Bröder and Sommerfeld, 2002) and $k-\epsilon$ calculations.

Darmana et al. (2009) used the LES with EL approach for simulating the gas-liquid flow in a bubble column and validated the model with experimental data of Harteveld et al., 2004. Seven sparger designs and their influence on the flow structure were investigated. It was found that the model captures the influence of different gas sparging very well. However, in all cases simulated, a systematic overprediction of dispersed phase distribution (25%) was found, which was attributed to an inaccuracy of the drag force and the turbulence model at high gas void fractions.

Darmana et al. (2005) used LES with EL approach to simulate flow, mass transfer, and chemical reaction in a bubble column. They considered mass transfer, rate in liquid-phase momentum equation and reaction interfacial forces in the bubble motion equation. Also, the presence of various chemical species was accounted through a transport equation for each species. Darmana et al. (2005) estimated the mass transfer rate from the information of the individual bubbles directly. They used the model to simulate the reversible two-step reactions found in the chemisorption process of $CO_2$ in an aqueous NaOH solution in a lab-scale pseudo-2D bubble column reactor. They found good agreement between simulation and measurement for the case without mass transfer. In absence of an accurate mass transfer closure, the authors found that the overall mass transfer rate was lower compared to the measurement. However, the influence of the mass transfer on the flow agreed well with experimental data.

Sunkorn et al. (2011) reported LES with the EL approach for a gas-liquid flow in a square cross-sectional bubble column. They modelled the continuous liquid phase using a Lattice-Boltzmann (LB) scheme, and a Lagrangian approach was used for the dispersed phase. For the bubble phase, the Langevin equation model (Sommerfeld et al., 1993) was used for estimating the effect of turbulence. The bubble collisions were described by a stochastic interparticle collision model based on the kinetic theory developed by Sommerfeld (2001). The predictions showed a very good agreement with the experimental data for the mean and fluctuating velocity components. It was also found that their collision model leads to two benefits: the computing time is dramatically reduced compared to the direct collision method and secondly it also provides an excellent computational efficiency on parallel platforms. Sunkorn et al. (2011) claim that the methodology can be applied to a wide range of problems.The investigations are valid for lower global void fraction, and further work is required to consider it for higher void fraction systems.

Bai et al. (2012) used LES with EL approach to investigate the effect of the gas sparger and gas phase mixing in a square cross-sectional bubble column. The liquid phase was computed using LES, and a Lagrangian approach was used for the dispersed phase. They used the DBM and investigated the effect of two SGS models: Smagorinsky (1963) and Vreman (2004). They compared the vertical liquid velocity and turbulent kinetic energy of the liquid phase at three different heights with PIV data and found that the model proposed by Vreman performed better than Smagorinsky model.

They further investigated the effect of the gas sparger properties (sparged area and its location) on the hydrodynamics in a bubble column and characterized the macromixing of the gas phase in the column in terms of an axial dispersion coefficient. They compared the predicted liquid phase dispersion coefficient with the literature correlations. The range of superficial gas velocity investigated in work is low compared to what is common in industrial application. For large-scale reactors at high superficial velocities, Bai et al. (2012) recommended to extend the discrete bubble modelling with bubble coalescence and breakup.

## 3.4 Brief Overview of Other Numerical Approaches

Esmaeeli and Tryggvason (1996) and Esmaeeli and Tryggvason (1998) used direct numerical simulations to examine the motion of up to 324 freely evolving two-dimensional and up to 49 three-dimensional bubbles respectively, at low yet finite Reynolds numbers (around 1-2, depending on volume fraction and dimensionality). Tryggvason et al. (2001) used Direct Numerical Simulations on multiphase flows, using a front-tracking method. The method is based on writing one set of governing equations for the whole computational domain and treating the different phases as one fluid with variable material properties. Bunner and Tryggvason (2002) conducted direct numerical simulations of the motion of up to three-dimensional buoyant bubbles in periodic domains. The full Navier-Stokes equations are resolved by a parallelized finite-difference/front-tracking method that allows a deformable interface between the bubbles and the suspending fluid and the inclusion of surface tension. Lu et al. (2005) and Roghair et al. (2011) used a front-tracking/finite-volume method to fully resolve all flow scales including 16 bubbles and the flow around them. Yujie et al. (2012) used the volume of fluid (VOF) method to directly simulate approximately 50 bubbles. Badreddine et al. (2015) has proposed a new methodology, which is called Finite Size Lagrangian particle tracking (FSL) for the modeling of a single air bubble rising in stagnant water, and in linear shear flow. The new methodology inherits features of Lagrangian Particle Tracking (LPT) and Interface Tracking (IT) methods and it is proposed to simulate finite size bubbles whose diameter is larger than the grid cell but not well resolved for accurate IT methods. Immersed Boundary Method (IBM) techniques have been also developed for viscous flow around solid particles: The IB method was extended to Stokes flow around suspended particles (Fogelson and Peskin, 1988) and Navier-Stokes flow around fixed cylinders (Lai and Peskin, 2000). Hofler and Schwartzer, 2000 used similar ideas to compute many-particle systems, albeit at relatively low Reynold numbers. (Uhlmann, 2005) developed a computationally efficient IBM for particle-laden flows that is embedded in a finite-volume/ pressure-correction method using two different grid: a fixed, uniform and continuous Cartesian grid for the fluid phase and a uniform grid attached to and moving with the surface of the particles. A variety of two-dimensional and three-dimensional simulations are presented, ranging from the flow around a single cylinder to the sedimentation of 1000 spherical particles. Improvements of the original method proposed by Uhlmann, 2005 was reported by Breugem, 2012. Kempe and Frolich, 2012 presented a model for particle-particle and particle-wall collisions during interface-resolving numerical simulations of particle-laden flows. Schwartz et al., 2015 developed a time scheme for an IB method which enables the efficient, phase-resolving simulation of very light particles in viscous flow.

# Chapter 4

# Numerical Framework of Hydro3D Model

## 4.1 Governing equations

The in-house finite-difference-based Large-Eddy Simulation code Hydro3D is the numerical model employed in this study. Hydro3D solves the filtered Navier-Stokes equations on staggered grid for the continuous (liquid) phase and has been validated thoroughly for turbulent flows (e.g. Bomminayuni and Stoesser, 2011; Stoesser et al., 2015; Cevheri et al., 2016; Liu et al., 2016; Ouro et al., 2017; McSherry et al., 2018). The dispersed (bubbles) phase is predicted by a Lagrangian Particle Tracking algorithm and has been previously validated for the case of raising bubbles in a stagnant tank (Fraga et al., 2016; Fraga and Stoesser, 2016).

### 4.1.1 Continuous phase

The Navier-Stokes equations are used to resolve three-dimensional, unsteady, turbulent, incompressible fluids in a Cartesian rectangular grid.

In the Large-Eddy Simulation (LES) framework, the continuity and momentum equations are spatially filtered and normalised with the Reynolds number *Re*, and are presented in Eq. 4.1 and 4.2 respectively. The governing equations are solved in the whole fluid domain.

$$\frac{\partial u_i}{\partial x_i} = 0 \tag{4.1}$$

$$\frac{\partial u_i}{\partial t} + \frac{\partial (u_i u_j)}{\partial x_j} = -\frac{\partial p}{\partial x_j} + 2\nu \frac{\partial (S_{ij})}{\partial x_j} - \frac{\partial \tau_{ij}}{\partial x_j} + \xi_i \tag{4.2}$$

where $x_j$ denote the spatial location vectors (i.e. $x_j = x, y, z$ for $j = 1, 2, 3$), $u_i$ and $u_j$ ($i, j$= $1, 2, 3$) denote the filtered resolved velocity components in $x-$, $y-$ and $z-$directions, normalised on the reference velocity $U$, $p$ is the resolved pressure divided by density,$S_{ij}$ is the strain rate tensor and $\tau_{ij}$ is the unresolved turbulence. $Re = UL/\nu$ is Reynolds number, where $\nu$ is the kinematic viscosity and $L$ is the reference length scale.

The term $\xi_i$ is a source term that accounts for the contribution of the dispersed phase to the flow:

$$\xi_i = -\frac{1}{V_p} \sum_{p=1}^{M} F^*_{p,i} \Delta V \tag{4.3}$$

where $V_p$ is the volume of the particle, and $F^*_{p,i}$ is the summation of the forces acting to the particles and will be be explained further in Section (4.4).

Turbulent flows are characterized by a wide spectrum of turbulence scales in the fluid motion. The idea of LES is to calculate explicitly the motion of larger and more energetic eddies by solving the governing 3D Navier-Stokes equations, while modeling via spatial filtering the motions of the isotropic smaller eddies (Leonard, 1975). In LES, the general rule of spatial filtering is that the filter width is equal to the grid size, and those turbulent scales smaller than the grid size are modelled, using a subgrid-scale (SGS) model and this is what the term $\tau_{ij}$ represents in Eq. 4.2. The assumption of filtering process is reasonable as the small scales are isotropic and thus easier to model than the large scales which are more energetic and anisotropic (Stoesser, 2014).Further reduction of the LES requirements can be achieved using, for instance, a Local Mesh Refinement (LMR) method which allows to use fine grid resolutions in the areas of interest while coarser ones in which such a resolution is not needed, (Cevheri et al., 2016).

In this thesis, the Smagorinsky (Smagorinsky, 1963) and Wall-Adapting Local Eddy viscosity (WALE) (Nicoud and Ducros, 1999) SGS models are adopted. The unresolved velocity fluctuations are accounted using a subgrid stress tensor, $\tau_{ij}$, included in the momentum equation (Eq. 4.2), and reads:

$$\tau_{ij} = \tau_{ij}^{\alpha} + \frac{1}{3}\tau_{kk}\delta_{ij} \tag{4.4}$$

Here, the former term corresponds to the anisotropic component and the latter to the isotropic components, where $\delta_{ij}$ is the Kronecker delta. In the standard Smagorinsky SGS model, the eddy or turbulent viscosity, $\nu_t$, is approximated as,

$$\nu_t = (C_s\Delta)^2 \left|S_{ij}\right| \quad \text{, where} \quad \left|S_{ij}\right| = \sqrt{2S_{ij}S_{ij}} \tag{4.5}$$

$$S_{ij} = \frac{1}{2}\left(\frac{\partial u_i}{\partial x_j} + \frac{\partial u_j}{\partial x_i}\right) \tag{4.6}$$

where $C_s$ is the Smagorinsky constant set to 0.1 (Rodi et al., 2013), $\Delta = (\Delta x \Delta y \Delta z)^{1/3}$ is the filter size equal to the mesh cell size, and $S_{ij}$ is the resolved rate of strain from the filtered resolved velocities. This artificial viscosity is then used to calculate the anisotropic subgrid stress tensor, as

$$\tau_{ij}^{\alpha} = -2\nu_t\overline{S}_{ij} \tag{4.7}$$

The WALE model, introduced by Nicoud and Ducros, 1999, has gained popularity as is can account for wall effects without employing wall-damping functions which makes it a suitable to the simulation of immersed bodies in which the fluid mesh is not conformed to their geometry (Cevheri et al., 2016). One of the main advantages of the model is that it predicts correctly the behaviour of the eddy viscosity near solid surfaces. The turbulent viscosity $\nu_t$ is calculated as follows:

$$\nu_t = (C_w\Delta)^2 \frac{\left(s_{ij}^d s_{ij}^d\right)^{3/2}}{\left(\overline{S_{ij}S_{ij}}\right)^{5/2} + \left(s_{ij}^d s_{ij}^d\right)^{5/4}} \tag{4.8}$$

where $s_{ij}^d$ is the traceless symmetric part of the square of the velocity gradient tensor ($g_{ij}$) presented in Equation (4.9), $S_{ij}$ is the resolved rate of strain from Equation (4.6) calculated from the filtered resolved fluid velocities, and $C_w$ is the constant of the WALE model assumed to be 0.46 as considered in Cevheri et al., 2016.

$$s_{ij}^{d} = \frac{1}{2}\left(\overline{g_{ik}g_{kj}} + \overline{g_{jk}g_{ki}}\right) - \frac{1}{3}\delta_{ij}\overline{g_{kk}}^{2} \quad \text{with} \quad g_{ij} = \frac{\partial \overline{u}_i}{\partial x_{ij}} \tag{4.9}$$

## 4.2 Fractional-step method

The spatially filtered Navier-Stokes equations in the LES framework presented in Equations (4.1) and (4.2) are advanced in time using the so-called fractional-step method based on the projection method developed by Chorin, 1968. The main advantage of this method is that the velocity and pressure computations are decoupled. In the present framework, the fluid is solved in a Cartesian rectangular grid with staggered storage of the velocities using central fourth-order finite-differences approximations. In a staggered grid, velocity vectors are stored at the middle of the cell faces while the pressure is stored in the cell centre. Hence, four different grids are used to compute $u$, $v$, $w$ and $p$.

The fractional-step method uses two steps for implicit coupling of pressure and velocity terms (Kim and Moin, 1985). In the first step, the intermediate velocities, $u_i^*$, are initially predicted without enforcing the incompressibility constraint using a two-stage explicit Runge-Kutta method as follows:

$$u_i^{*,n+\frac{1}{2}} = u_i^n + \frac{\Delta t}{2}\left[R^n - \frac{\partial}{\partial x_i}p^{n-\frac{1}{2}}\right] \tag{4.10}$$

$$u_i^{*,n+1} = u_i^n + \Delta t\left[R^{*,n+\frac{1}{2}} - \frac{\partial}{\partial x_i}p^{n-\frac{1}{2}}\right] \tag{4.11}$$

where

$$R = \left[-\frac{\partial(u_i u_j)}{\partial x_j} + \left(\frac{1}{Re} + \nu_t\right)\frac{\partial^2 u_i}{\partial x_i \partial x_j}\right] \tag{4.12}$$

In the second step, the intermediate velocities are projected onto the divergence-free vector fields through a Poisson equation, which calculates an increment to the pressure field, $\delta p$:

$$\nabla^2(\delta p) = \frac{1}{\Delta t}\frac{\partial}{\partial x_i}u_i^{*,n+1} \tag{4.13}$$

where $\nabla^2$ is the Laplacian operator.

Equation (4.13) is solved iteratively using the multigrid method (Ferziger and Peric, 2002), and the velocity field is updated as follows:

$$u_i^{n+1} = u_i^{*,n+1} - \Delta t \frac{\partial(\delta p)}{\partial x_i} \tag{4.14}$$

$$p^{n+\frac{1}{2}} = p^{n-\frac{1}{2}} + \delta p \tag{4.15}$$

The Poisson equation is then solved with the new pressure, and an iterative process is established.The iteration continues until the divergence-free condition of the computed velocity field within some tolerance is satisfied. It is observed that the overall algorithm is second-order accurate and stable on either uniform or locally defined grids when the ghost cell pressures at coarse-fine grid interfaces are treated with a specific interpolation algorithm, which is described in Section (4.3).

Hydro3D employs a Cartesian grid with a staggered arrangement of pressure and velocity variables, which has the advantage of avoiding the odd-even coupling between the pressure and velocity without requiring special interpolation algorithms. On a staggered grid, scalar quantities such as pressure and divergence are stored at the cell centres, and vector quantities such as velocity and pressure gradient are stored at the middle of the cell faces. Figure (4.1(a)) presents a schema showing the storage of pressures and velocities on a 2D staggered grid, either side of an LMR interface: the indices $(I, J)$ and $(i, j)$ correspond to coarse and fine grid points, respectively. The indices of $u$ velocity on the east face and $v$ velocity on the north face of the shaded-fine cell are $(i, j)$, and $u$ velocity on the west face and v velocity on the south face of the same cell are $(i-1, j)$ and $(i, j-1)$, respectively. The indexing of coarse cells is handled analogously. One or more layers of ghost cells, denoted in Figure (4.1(b)) by dashed lines, are appended around each side of the physical domain in order to provide numerical boundaries and to facilitate spatial approximations of cells at the fine-coarse interfaces without requiring complicated discretisation stencils of non-uniform grids.

Equation (4.12) contains partial derivatives in space of first and second order, and in LES, the accurate approximation of these is key to the success of the simulation

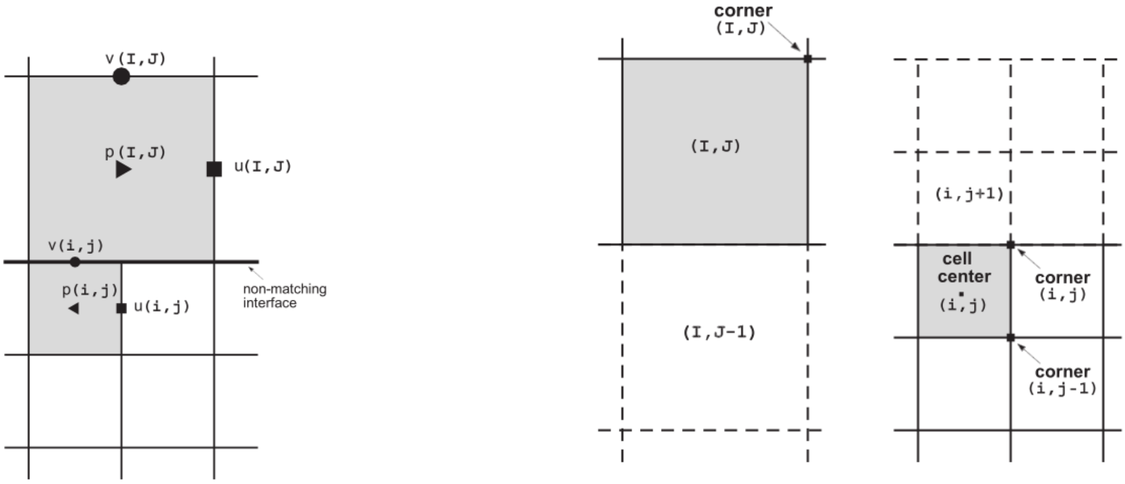

(a) Staggered arrangement (b) Indexing of fine and coarse ghost cells

Figure 4.1: The staggered variable arrangement and index location of coarse and fine ghost cells.

(Rodi et al., 2013). In Hydro3D, explicit second-order and fourth-order central differences for continuity, convective and viscous terms are available and for the sake of simplicity are presented here in two dimensions.

Second-order accurate approximations of the cell-centre partial derivatives in the continuity equation read:

$$\left(\frac{\partial u}{\partial x}\right)_{i,j} = \frac{u_{i,j} - u_{i-1,j}}{\Delta x} + O\left(h^2\right) \quad \text{and} \quad \left(\frac{\partial v}{\partial y}\right)_{i,j} = \frac{v_{i,j} - v_{i,j-1}}{\Delta y} + O\left(h^2\right) \tag{4.16}$$

Because of the staggered arrangement, the $x-$, $y-$ and $z-$momentum equations are solved at the cell faces. The second order accurate discretisations of convective and diffusive terms in the $x-$momentum equations are as follows:

$$\left(\frac{\partial u^2}{\partial x}\right)_{i,j} = \frac{\left(u_{i+1,j} + u_{i,j}\right)^2 - \left(u_{i,j} + u_{i-1,j}\right)^2}{4\Delta x} + O\left(h^2\right) \tag{4.17}$$

$$\left(\frac{\partial uv}{\partial y}\right)_{i,j}=\frac{\left(v_{i+1,j}+v_{i,j}\right)\left(u_{i,j+1}+u_{i,j}\right)-\left(v_{i+1,j-1}+v_{i,j-1}\right)\left(u_{i,j}+u_{i,j-1}\right)}{4\Delta y}+O\left(h^2\right) \tag{4.18}$$

$$\left(\frac{\partial^2 u}{\partial x^2}\right)_{i,j}=\frac{u_{i+1,j}-2u_{i,j}+u_{i-1,j}}{\left(\Delta x\right)^2}+O\left(h^2\right) \tag{4.19}$$

$$\left(\frac{\partial^2 u}{\partial y^2}\right)_{i,j}=\frac{u_{i,j+1}-2u_{i,j}+u_{i,j-1}}{\left(\Delta y\right)^2}+O\left(h^2\right) \tag{4.20}$$

And the $y-$momentum convective and diffusive terms are evaluated as:

$$\left(\frac{\partial v^2}{\partial y}\right)_{i,j}=\frac{\left(v_{i,j+1}+v_{i,j}\right)^2-\left(v_{i,j}+v_{i,j-1}\right)^2}{4\Delta y}+O\left(h^2\right) \tag{4.21}$$

$$\left(\frac{\partial uv}{\partial x}\right)_{i,j}=\frac{\left(u_{i,j+1}+u_{i,j}\right)\left(v_{i+1,j}+v_{i,j}\right)-\left(u_{i-1,j+1}+u_{i-1,j}\right)\left(v_{i,j}+v_{i-1,j}\right)}{4\Delta x}+O\left(h^2\right) \tag{4.22}$$

$$\left(\frac{\partial^2 v}{\partial x^2}\right)_{i,j}=\frac{v_{i+1,j}-2v_{i,j}+v_{i-1,j}}{\left(\Delta x\right)^2}+O\left(h^2\right) \tag{4.23}$$

$$\left(\frac{\partial^2 v}{\partial y^2}\right)_{i,j}=\frac{v_{i,j+1}-2v_{i,j}+v_{i,j-1}}{\left(\Delta y\right)^2}+O\left(h^2\right) \tag{4.24}$$

Analogous formulae are used to predict convective and diffusive terms for the $z-$momentum equation.

Fourth-order accurate approximations of the cell-centre partial derivatives in the continuity equation are:

$$\left(\frac{\partial u}{\partial x}\right)_{i,j}=\frac{-u_{i+1,j}+27u_{i,j}-27u_{i-1,j}+u_{i-2,j}}{24\Delta x}+O\left(h^4\right) \tag{4.25}$$

$$\left(\frac{\partial v}{\partial y}\right)_{i,j} = \frac{-v_{i,j+1} + 27v_{i,j} - 27v_{i,j-1} + v_{i,j-2}}{24\Delta y} + O\left(h^4\right) \tag{4.26}$$

Fourth-order accurate discretisations of convective and diffusive terms in the $x-$momentum equation are as follows:

$$\left(\frac{\partial u^2}{\partial x}\right)_{i,j} = \frac{-\widetilde{u_{i+2,j}}^2 + 27\widetilde{u_{i+1,j}}^2 - 27\widetilde{u_{i,j}}^2 + \widetilde{u_{i-1,j}}^2}{24\Delta x} + O\left(h^4\right) \tag{4.27}$$

$$\left(\frac{\partial uv}{\partial y}\right)_{i,j} = \frac{-\widetilde{u^c_{i,j+1}}\widetilde{v^c_{i,j+1}} + 27\widetilde{u^c_{i,j}}\widetilde{v^c_{i,j}} - 27\widetilde{u^c_{i,j-1}}\widetilde{v^c_{i,j-1}} + \widetilde{u^c_{i,j-2}}\widetilde{v^c_{i,j-2}}}{24\Delta y} + O\left(h^4\right) \tag{4.28}$$

$$\left(\frac{\partial^2 u}{\partial x^2}\right)_{i,j} = \frac{-u_{i+2,j} + 16u_{i+1,j} - 30u_{i,j} + 16u_{i-1,j} - u_{i-2,j}}{12\left(\Delta x\right)^2} + O\left(h^4\right) \tag{4.29}$$

$$\left(\frac{\partial^2 u}{\partial y^2}\right)_{i,j} = \frac{-u_{i,j+2} + 16u_{i,j+1} - 30u_{i,j} + 16u_{i,j-1} - u_{i,j-2}}{12\left(\Delta y\right)^2} + O\left(h^4\right) \tag{4.30}$$

The $y-$momentum convective and diffusive terms, at the north face of the cell indexed by $(i, j)$, are ultimately evaluated as:

$$\left(\frac{\partial v^2}{\partial y}\right)_{i,j} = \frac{-\widetilde{v_{i,j+2}}^2 + 27\widetilde{v_{i,j+1}}^2 - 27\widetilde{v_{i,j}}^2 + \widetilde{v_{i,j-1}}^2}{24\Delta y} + O\left(h^4\right) \tag{4.31}$$

$$\left(\frac{\partial uv}{\partial x}\right)_{i,j} = \frac{-\widetilde{u^c_{i+1,j}}\widetilde{v^c_{i+1,j}} + 27\widetilde{u^c_{i,j}}\widetilde{v^c_{i,j}} - 27\widetilde{u^c_{i-1,j}}\widetilde{v^c_{i-1,j}} + \widetilde{u^c_{i-2,j}}\widetilde{v^c_{i-2,j}}}{24\Delta x} + O\left(h^4\right) \tag{4.32}$$

$$\left(\frac{\partial^2 v}{\partial x^2}\right)_{i,j} = \frac{-v_{i+2,j} + 16v_{i+1,j} - 30v_{i,j} + 16v_{i-1,j} - v_{i-2,j}}{12\left(\Delta x\right)^2} + O\left(h^4\right) \tag{4.33}$$

$$\left(\frac{\partial^2 v}{\partial y^2}\right)_{i,j} = \frac{-v_{i,j+2} + 16v_{i,j+1} - 30v_{i,j} + 16v_{i,j-1} - v_{i,j-2}}{12\left(\Delta y\right)^2} + O\left(h^4\right) \tag{4.34}$$

where $\widetilde{u_{i,j}}$ and $\widetilde{v_{i,j}}$ are the interpolated velocities at the cell centre $(i,j)$:

$$\widetilde{u_{i,j}} = \frac{-u_{i+1,j} + 9u_{i,j} + 9u_{i-1,j} - u_{i-2,j}}{16} + O\left(h^4\right) \tag{4.35}$$

$$\widetilde{v_{i,j}} = \frac{-v_{i,j+1} + 9v_{i,j} + 9v_{i,j-1} - v_{i,j-2}}{16} + O\left(h^4\right) \tag{4.36}$$

and $\widetilde{u^c_{i,j}}$ and $\widetilde{v^c_{i,j}}$ are the interpolated velocities at the corner $(i,j)$:

$$\widetilde{u^c_{i,j}} = \frac{-u_{i,j+2} + 9u_{i,j+1} + 9u_{i,j} - u_{i,j-1}}{16} + O\left(h^4\right) \tag{4.37}$$

$$\widetilde{v^c_{i,j}} = \frac{-v_{i+2,j} + 9v_{i+1,j} + 9v_{i,j} - v_{i_1,j}}{16} + O\left(h^4\right) \tag{4.38}$$

The partial derivatives of the $z-$momentum equation are defined similarly.

It should be noted that Hydro3D is parallelized using domain decomposition, that is, the computational domain is divided into a number of smaller sub-domains to allow parallelization. Communication across internal boundaries between neighbouring sub-domains is achieved using layers of ghost cells that are located around the peripheries of the domains. The standard message passing interface (MPI) accomplishes communication between sub-domains.

In Eulerian-Lagrangian simulations, the effect of the bubbles are represented by the term $\xi_i$ in Equation (4.2), which is used to correct the predicted velocity $\tilde{u}$ obtaining the updated intermediate velocity $\tilde{u}^*(x,t)$, as indicated in Equation (4.39):

$$\tilde{u}^* = \tilde{u} + \xi_i \Delta T \tag{4.39}$$

Here, the corrected velocity satisfies the divergence-free condition once Equation (4.40) achieves a residual lower than a set tolerance $\varepsilon$ often set to a value $\leq 10^{-7}$.

$$\bigtriangledown \cdot \tilde{u}^* \leq \varepsilon \tag{4.40}$$

## 4.3 Local Mesh Refinement (LMR)

In the present study, a 2:1 reduction in grid element size between neighbouring subdomains is imposed on the staggered computational grid to achieve LMR in critical areas. In the following, the arrangement of ghost cell velocities and pressures is mostly depicted in two dimensions for simplicity.

The calculation of ghost cell pressures is achieved by adjusting the coarse pressure gradients at the coarse-fine interface to those computed for neighbouring fine cells, thereby coupling the pressure fields. Pressure values, the location of which are indicated by "**x**" symbols in Figure (4.2), are first quadratically interpolated using pressure values from the coarse grid computational cells (indicated by solid right triangles, (▶) in the same figure) as follows:

$$\begin{aligned} p^{\alpha}_{I,J} &= \frac{5p_{I-1,J} + 30p_{I,J} - 3p_{I+1,J}}{32} + O\left(h^2\right) \\ p^{b}_{I,J} &= \frac{5p_{I+1,J} + 30p_{I,J} - 3p_{I-1,J}}{32} + O\left(h^2\right) \end{aligned} \tag{4.41}$$

Another quadratic interpolation is then applied to calculate fine ghost pressures using the computational cells indicated by solid let triangles (◀) and the interpolated pressures:

$$\begin{aligned} p_{i,j+1} &= \frac{8p^{\alpha}_{I,J} + 10p_{i,j} - 3p_{i,j-1}}{15} + O\left(h^2\right) \\ p^{b}_{i+1,j+1} &= \frac{8p^{b}_{I,J} + 10p_{i+1,j} - 3p_{i+1,j-1}}{15} + O\left(h^2\right) \end{aligned} \tag{4.42}$$

In the restriction process, the edge-centred gradients of the fine grids, $F_{fine}\alpha$ and $F_{fine}b$ in Figure (4.2), are calculated as follows:

$$F^{\alpha}_{fine} = \frac{p_{i,j+1} - p_{i,j}}{\Delta y_{fine}} + O\left(h\right) \quad \text{and} \quad F^{b}_{fine} = \frac{p_{i+1,j+1} - p_{i+1,j}}{\Delta y_{fine}} + O\left(h\right) \tag{4.43}$$

The coarse grid pressure gradients are then taken as the arithmetic average of the fine-grid pressure gradients to enforce the continuity of the gradient across the interface. Ghost cell pressures from the coarse grid $(I, J-1)$ are calculated using the

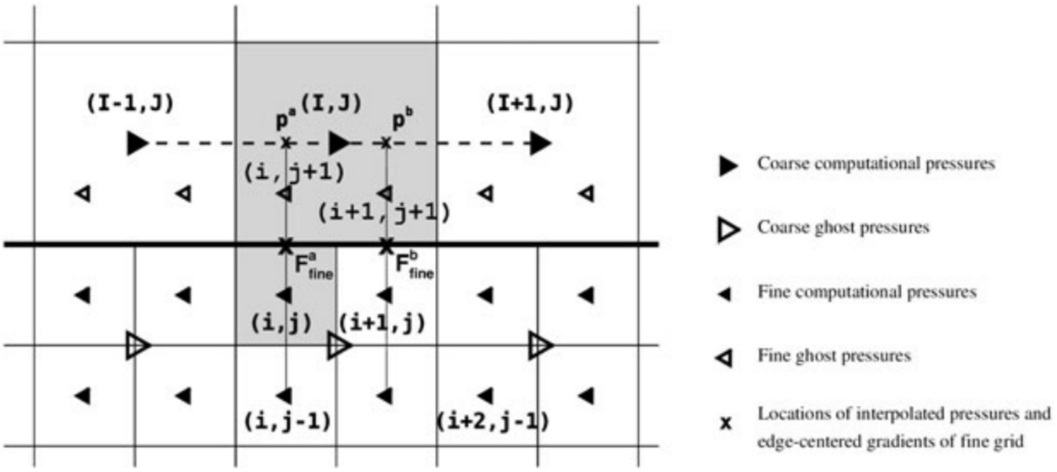

Figure 4.2: Pressure locations around the interface between a fine and a coarse grid.

following formula:

$$\frac{p_{I,J} - p_{I,J-1}}{\Delta y_{coarse}} = \left( \frac{F^{\alpha}_{fine} + F^{b}_{fine}}{2} \right) + O\left(h\right) \tag{4.44}$$

Although quadratic interpolations give first-order accurate approximations of the Laplacian operator along the interface, it is proposed in Cevheri and Stoesser (2018) that this is sufficient to ensure global second-order accuracy of the projected velocity field.

Figure (4.3) presents the indexing of neighbouring cells around a non-matching interface to illustrate the means by which pressure values are calculated in the three-dimensional domain. Considering refinement in the $y-$direction, a coarse cell, which is located on the north faces of four fine cells, is indexed as $(I, J, K)$, and the south neighbours associated with it are indexed as follows: $(i, j, k)$, $(i, j, k+1)$, $(i+1, j, k)$ and $(i+1, j, k+1)$. In the prolongation process, quadratic interpolations are performed to obtain the four ghost fine pressure values on the coarse side of the interface, which are denoted $p_a$, $p_b$, $p_c$ and $p_d$ in Figure (4.3):

$$\begin{aligned} p^{\alpha}_{I,J,K} = \frac{1}{1024}(25p_{I-1,J,K-1} + 150p_{I,J,K-1} - 15p_{I+1,J,K-1} + 150p_{I-1,J,K} \\ +900p_{I,J,K} - 90p_{I+1,J,K} - 15p_{I-1,J,K+1} - 90p_{I,J,K+1} + 9p_{I+1,J,K+1}) + O\left(h^2\right) \end{aligned} \tag{4.45}$$

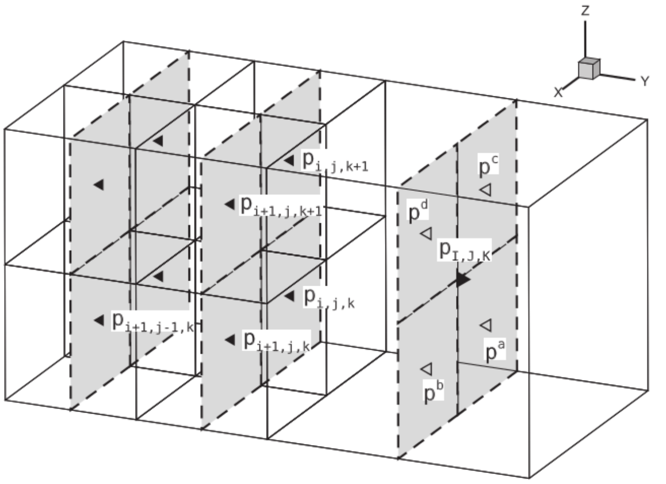

Figure 4.3: Pressure locations between fine and coarse grids for three-dimensional problems when the refinement is considered in the $y-$direction.

$$\begin{aligned} p^b_{I,J,K} = \frac{1}{1024}(&-15p_{I-1,J,K-1} + 150p_{I,J,K-1} + 25p_{I+1,J,K-1} - 90p_{I-1,J,K} \\ &+900p_{I,J,K} + 150p_{I+1,J,K} + 9p_{I-1,J,K+1} - 90p_{I,J,K+1} - 15p_{I+1,J,K+1}) + O\left(h^2\right) \end{aligned} \tag{4.46}$$

$$\begin{aligned} p^c_{I,J,K} = \frac{1}{1024}(&-15p_{I-1,J,K-1} - 90p_{I,J,K-1} + 9p_{I+1,J,K-1} + 150p_{I-1,J,K} \\ &+900p_{I,J,K} - 90p_{I+1,J,K} + 25p_{I-1,J,K+1} + 150p_{I,J,K+1} - 15p_{I+1,J,K+1}) + O\left(h^2\right) \end{aligned} \tag{4.47}$$

$$\begin{aligned} p^d_{I,J,K} = \frac{1}{1024}(&9p_{I-1,J,K-1} - 90p_{I,J,K-1} - 15p_{I+1,J,K-1} - 90p_{I-1,J,K} \\ &+900p_{I,J,K} + 150p_{I+1,J,K} - 15p_{I-1,J,K+1} + 150p_{I,J,K+1} + 25p_{I+1,J,K+1}) + O\left(h^2\right) \end{aligned} \tag{4.48}$$

Additional information pertaining to the derivation of Equations (4.45)-(4.48) can be found in Thorne (2003). Another quadratic interpolation is then applied to calculate fine ghost pressures using the computational cells indicated by solid left triangles (◀) and the interpolated pressures:

$$p_{i,j+1,k} = \frac{1}{15}\left(8p^{\alpha}_{I,J,K} + 10p_{i,j,k} - 3p_{i,j-1,k}\right) + O\left(h^2\right) \tag{4.49}$$

$$p_{i+1,j+1,k} = \frac{1}{15}\left(8p^{b}_{I,J,K} + 10p_{i+1,j,k} - 3p_{i+1,j-1,k}\right) + O\left(h^2\right) \tag{4.50}$$

$$p_{i,j+1,k+1} = \frac{1}{15}\left(8p^{c}_{I,J,K} + 10p_{i,j,k+1} - 3p_{i,j-1,k+1}\right) + O\left(h^2\right) \tag{4.51}$$

$$p_{i+1,j+1,k+1} = \frac{1}{15}\left(8p^{d}_{I,J,K} + 10p_{i+1,j,k+1} - 3p_{i+1,j-1,k+1}\right) + O\left(h^2\right) \tag{4.52}$$

In the restriction process, the coarse ghost pressure value, $p_{I,J-1,K}$, is calculated by adjusting the coarse pressure gradients at the coarse-fine interface to those computed for neighbouring fine cells in the following form:

$$\begin{aligned}\frac{p_{I,J,K} - p_{I,J-1,K}}{\Delta y_{coarse}} = \frac{1}{4}\left(\frac{p_{i,j+1,k} - p_{i,j,k}}{\Delta y_{fine}} + \frac{p_{i+1,j+1,k} - p_{i+1,j,k}}{\Delta y_{fine}} + \frac{p_{i,j+1,k+1} - p_{i,j,k+1}}{\Delta y_{fine}}\right) \\ + \frac{1}{4}\left(\frac{p_{i+1,j+1,k+1} - p_{i+1,j,k+1}}{\Delta y_{fine}}\right) + O\left(h\right)\end{aligned} \tag{4.53}$$

Prolongation and restriction of ghost velocities, which are tangential to the non-matching interface, are required in the discrete formulations of derivatives. The procedures are different for velocity components that are tangential and normal to the non-matching LMR interfaces; evaluation of tangential velocities is not as challenging as evaluation of normal velocities. Figure (4.4) is a schema illustrating the arrangement of ghost cell tangential velocities at a fine-coarse grid interface.

In the prolongation procedure, fine grid tangential ghost velocities are calculated using quadratic interpolations with mass conservation in the following forms for

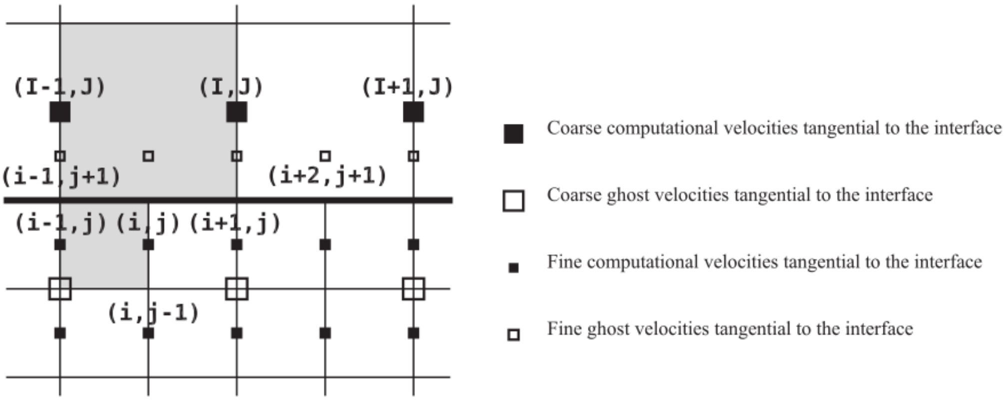

Figure 4.4: Location of velocities tangential to the LMR interface between fine and coarse grids.

two-dimensional and three-dimensional problems, respectively:

$$\begin{aligned} u_{i+1,j+1,k} = \frac{1}{128}(3u_{I,J-1,K-1} + 15u_{I,J,K-1} - 2u_{I,J+1,K-1} + 15u_{I,J-1,K} \\ +128u_{I,J,K} - 15u_{I,J+1,K} - 2u_{I,J-1,K+1} - 15u_{I,J,K+1} + u_{I,J+1,K+1}) + O\left(h^2\right) \end{aligned} \tag{4.54}$$

$$\begin{aligned} u_{i+1,j+1,k+1} = \frac{1}{128}(-2u_{I,J-1,K-1} - 15u_{I,J,K-1} + u_{I,J+1,K-1} + 15u_{I,J-1,K} \\ +128u_{I,J,K} - 15u_{I,J+1,K} + 3u_{I,J-1,K+1} + 15u_{I,J,K+1} - 2u_{I,J+1,K+1}) + O\left(h^2\right) \end{aligned} \tag{4.55}$$

The second-order average of these edge values is then taken to obtain the value at the location in between: $u_{i+2,j+1} = (u_{i+1,j+1} + u_{i+3,j+1})/2$ in 2D and $u_{i,j+1,k+1} = (u_{i-1,j+1,k+1} + u_{i+1,j+1,k+1})/2$ in 3D.

In the restriction procedure, the coarse tangential velocities are obtained by averaging the computed fine values, thus enforcing mass conservation at the interfaces. Mass conservation is also enforced for velocities normal to the interface. The coarse grid ghost velocity, indexed by $(I, J-1)$, is calculated as follows:

$$u_{I,J-1} = \frac{u_{i+1,j} + u_{i+1,j-1}}{2} + O\left(h^2\right) \tag{4.56}$$

and the three-dimensional procedure for the coarse grid ghost velocity indexed by $(I, J-1, K)$, which is prescribed for the three-dimensional pressure formulation, is achieved for both approaches as follows:

$$u_{I,J-1,K} = \frac{u_{i+1,j,k} + u_{i+1,j-1,k} + u_{i+1,j,k+1} + u_{i+1,j-1,k+1}}{4} + O\left(h^2\right) \tag{4.57}$$

Interpolation and restriction procedures for the velocity component normal to the interface differ slightly from those used for the tangential velocities. Figure (4.5) presents the arrangement of ghost cells.

In the prolongation process, the values marked with "**x**" symbols in Figure (4.5) are first calculated using coarse grid computational values as follows:

$$\begin{aligned} v_{i,j+2} &= \frac{v_{I-1,J} + 8v_{I,J} - v_{I+1,J}}{8} + O\left(h^2\right) \\ v_{i+1,j+2} &= \frac{v_{I+1,J} + 8v_{I,J} - v_{I-1,J}}{8} + O\left(h^2\right) \end{aligned} \tag{4.58}$$

One additional quadratic interpolation between computed coarse and fine grid values is then employed using $v_{i,j+2}$ and $v_{i+1,j+2}$, which are interpolated quadratically with mass conservation enforced. This interpolation is defined as follows:

$$\begin{aligned} v_{i,j+1} &= \frac{1}{3}\left(v_{i,j+2} + 3v_{i,j} - v_{i,j-1}\right) + O\left(h^2\right) \\ v_{i+1,j+1} &= \frac{1}{3}\left(v_{i+1,j+2} + 3v_{i+1,j} - v_{i+1,j-1}\right) + O\left(h^2\right) \end{aligned} \tag{4.59}$$

The formulation or three-dimensional problems is similar. First the normal velocities on the coarse edge are interpolated as follows:

$$\begin{aligned} v_{i,j+2,k} = \frac{1}{128}(&3v_{I-1,J,K-1} + 15v_{I,J,K-1} - 2v_{I+1,J,K-1} + 15v_{I-1,J,K} \\ &+128v_{I,J,K} - 15v_{I+1,J,K} - 2v_{I-1,J,K+1} - 15v_{I,J,K+1} + v_{I+1,J,K+1}) + O\left(h^2\right) \end{aligned} \tag{4.60}$$

$$\begin{aligned} v_{i+1,j+2,k} = \frac{1}{128}(&-2v_{I-1,J,K-1} + 15v_{I,J,K-1} + 3v_{I+1,J,K-1} - 15v_{I-1,J,K} \\ &+128v_{I,J,K} + 15v_{I+1,J,K} + v_{I-1,J,K+1} - 15v_{I,J,K+1} - 2v_{I+1,J,K+1}) + O\left(h^2\right) \end{aligned} \tag{4.61}$$

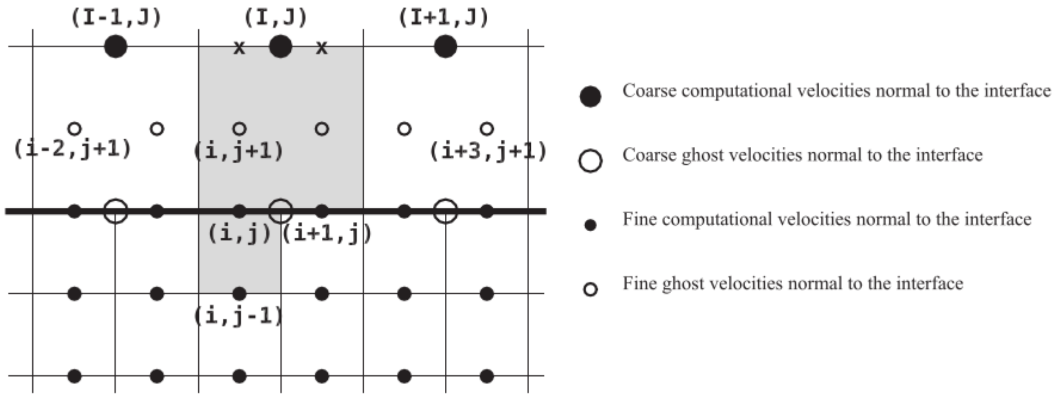

Figure 4.5: Location of velocities normal to the LMR interface between fine and coarse grids.

$$\begin{aligned} v_{i,j+2,k+1} = {} & \frac{1}{128}(-2v_{I-1,J,K-1} - 15v_{I,J,K-1} + v_{I+1,J,K-1} + 15v_{I-1,J,K} \\ & +128v_{I,J,K} - 15v_{I+1,J,K} + 3v_{I-1,J,K+1} + 15v_{I,J,K+1} - 2v_{I+1,J,K+1}) + O\left(h^2\right) \end{aligned} \tag{4.62}$$

$$\begin{aligned} v_{i+1,j+2,k+1} = {} & \frac{1}{128}(v_{I-1,J,K-1} - 15v_{I,J,K-1} - 2v_{I+1,J,K-1} - 15v_{I-1,J,K} \\ & +128v_{I,J,K} + 15v_{I+1,J,K} - 2v_{I-1,J,K+1} + 15v_{I,J,K+1} + 3v_{I+1,J,K+1}) + O\left(h^2\right) \end{aligned} \tag{4.63}$$

before the quadratic interpolation is performed according to Equation (4.59) to compute the values of $v_{i,j+1,k}, v_{i+1,j+1,k}, v_{i,j+1,k+1}$ and $v_{i+1,j+1,k+1}$.

In the restriction process, the fourth-order averages of computed fine grid values are used to calculate the coarse grid ghost velocities instead of second-order averages as was the case for the tangential velocities (Equations 4.56 & 4.57). The fourth-order formulation is as follows:

$$v_{I,J-1} = \frac{-v_{i-1,j} + 9v_{i,j} + 9v_{i+1,j} - v_{i+2,j}}{16} + O\left(h^4\right) \tag{4.64}$$

In 3D, the formulation of the fourth-order average is slightly more complicated than in 2D. Figure (4.6) presents a view of a 3D interface in the $x - z$ plane, with

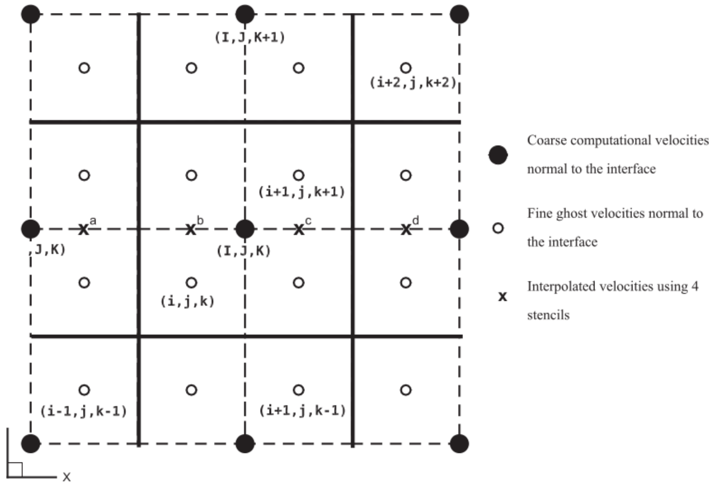

Figure 4.6: Location of velocities normal to the LMR interface between fine and coarse grids for 3D problems when the reinement is considered in the $y-$direction.

the locations of fine and coarse grid velocities denoted by hollow and solid circles, respectively. In the first step, the values marked with "**x**" symbols are calculated as follows, using the first "**x**" on the left side of Figure (4.6) as an example:

$$v^{\alpha} = \frac{-v_{i-1,j,k-1} + 9v_{i-1,j,k} + 9v_{i-1,j,k+1} - v_{i-1,j,k+2}}{16} + O\left(h^4\right) \tag{4.65}$$

The coarse grid ghost velocity is then evaluated using the calculated values at "**x**" locations as follows:

$$v_{I,J-1,K} = \frac{-v^{\alpha} + 9v^{b} + 9v^{c} - v^{d}}{16} + O\left(h^4\right) \tag{4.66}$$

Finally, it should be noted that although the generated grid consists of domains at different resolutions, refinement in time is not employed in the present study. Instead, all grids in all levels are advanced with a uniform time-step to simplify the implementation and to make for more straightforward parallelisation and CPU load distribution.

## 4.4 Simulation of the dispersed phase

Dispersed phase is simulated with a Lagrangian Particle Tracking (LPT) algorithm. Particles are represented by volumeless Lagrangian markers, considered as rigid and spheric with no direct interaction between them. Only linear interaction between interfacial forces is considered.

Newton's second law is applied to describe the motion of individual particles:

$$m_p \frac{\partial v_{p,i}}{\partial t} = F_{p,i} \tag{4.67}$$

where $m_p$ is the particle's mass, $v_{p,i}$ is the particle's velocity in spatial direction $i$ and $F_{p,i}$ is the sum of the interfacial liquid forces acting on the particle in direction $i$. The integral forces acting upon each particle are calculated by the semi-empirical expressions. The following five forces are considered (Delnoij et al., 1997): buoyancy, fluid stress, added mass, drag and lift.

The buoyancy force is computed as:

$$F_{G,i} = (m_p - m_l)g \tag{4.68}$$

where $m_p$ is the particle's mass, $m_l$ is the displaced liquid mass and $g$ the gravity acceleration. The buoyancy force applies only in the vertical direction $i$=3.

The fluid stress force, which accounts for part of the fluid's resistance to the particle's movement which is dependent to the slip velocity is computed as:

$$F_{S,i} = m_l \frac{Du_i}{Dt} \tag{4.69}$$

where $u_i$ the fluid velocity at the bubble's geometric center location.

The added mass force, which represents the fluid's resistance to the particle's movement which is dependent to the slip velocity is calculated as:

$$F_{A,i} = -C_A m_l \frac{\partial}{\partial t} \left(v_{p,i} - u_i\right) \tag{4.70}$$

where $C_A$ is an empirical coefficient assumed to be 0.5 for a sphere (Delnoij et al.,

1997) and the difference between particle and water velocity is often referred to as the slip velocity $u_{slip}$.

The drag force, which is exerted by the particle on the liquid (and vice versa) in the direction of motion, is computed as:

$$F_{D,i} = \frac{1}{2} C_D \varrho A_{fr} |\upsilon_{p,i} - u_i| (\upsilon_{p,i} - u_i) \tag{4.71}$$

where $A_{fr}$ is the frontal area of the particle and $\rho$ the fluid density. $C_D$ is the drag coefficient that depends on the local Reynolds number $Re_p$ and is calculated as:

$$C_D = \begin{cases} \frac{24}{Re_p}\left(1 + 0.15 Re_p^{0.687}\right) & Re_p \leq 800 \\ 0.44 & Re_p > 800 \end{cases} \tag{4.72}$$

The lift force, which is the force exerted on the particle perpendicular to the axis of motion and which is responsible for the particles spreading, is computed as:

$$F_{L,i} = -C_L m_p (\upsilon_{p,i} - u_i) \times \omega_i \tag{4.73}$$

where $\omega$ is the fluid vorticity and $C_L = 0.53$ (Delnoij et al., 1997) is the lift coefficient for a sphere.

$$F_{p,i} = F_{G,i} + F_{S,i} + F_{A,i} + F_{D,i} + F_{L,i} \tag{4.74}$$

## 4.5 Eulerian-Lagrangian mapping

The dispersed phase is accurately predicted with the aid of a Lagrangian Particle Tracking (LPT) algorithm using a two-way coupling approach. Firstly, the interfacial particle forces are calculated from Equations (4.68)-(4.74) and through Equation (4.67) the particles' velocities are obtained (forward coupling). Secondly, the contribution of the dispersed phase to the continuous phase is computed and added as a source term, $\xi_i$ (Equation 4.3), to the liquid's momentum equation (Eq. 4.2) (backward coupling). Forward and backward coupling are achieved by connecting randomly placed Lagrangian particles with fixed locations of the Eulerian framework through a mapping technique. Mapping consists of two basic elements: 1) the definition of the volume of fluid influenced by the particle and 2) interpolation techniques to transfer quantities between Eulerian and Lagrangian frameworks. The most straightforward approach to point 1) is the PSI-cell (Particle-Source-In Cell) mapping technique (Crowe et al., 1977). By employing the PSI-cell technique, only the fluid nodes of the cells in which the Lagrangian particle's center is located receive the momentum source. Hu and Celik (2008) developed the PSI-ball method, where the influence of individual particles on the fluid is within a prescribed volume (ball) around a Lagrangian point, including nodes outside the cell in which the particle is hosted. With regards to element 2) of the mapping, transfer of quantities, this has been a prime aspect for CFD modellers. For example Delnoij et al., 1997 proposed an area-weighted averaging; Lain et al., 1999 suggested linear interpolation plus a fluctuating component; Kitagawa et al., 2001 used a box or Gaussian template function; Deen et al., 2004 and Darmana et al., 2006 used a clipped fourth-order polynomial kernel; Sunkorn et al., 2011 and Hu and Celik, 2008 chose a truncated Gaussian for the forward coupling whilst applying a distance weighted function for the backward coupling.

In this work, the Eulerian-Lagrangian interpolation technique is based on second-order delta functions developed originally for immersed boundaries by Yang et al., 2009.

$$h = \begin{cases} \Delta x & \frac{D_p}{\Delta x} \leq 1 \\ D_p & \frac{D_p}{\Delta x} > 1 \end{cases} \tag{4.75}$$

where $h$ is the dynamic spacing based on the $D_p/\Delta x$ ratio to define the bubble's influence volume with minimum mesh dependency.

According to Equation (4.75), whenever a particle is smaller than the cell, the cell size $\Delta x$ will be the stencil for the delta function. Typically a second-order delta function is applied on a $5h$-sized cube. If $D_p \leq \Delta x$ then 5 nodes will be considered in each direction (the one that contains the particle and two more at the sides), making a total of 125 in the volume. The delta functions create a 3D Gaussian-like function centered in the Lagrangian point, so the nodes that are distant or near the corners of the resulting cube will have tiny influence or none. If the bubble is bigger than the cell, then an analogous volume based on its diameter $D_p$ would be defined.

Following the previous example, the resulting cube would have $5D_p$ edges. This procedure ensures the accuracy of the delta functions' interpolation with a large enough representation of points.

Regarding to interpolation, the delta functions have been successfully applied in recent years to immersed boundary problems, which have similarities with Lagrangian Particle Tracking. In both there are discrete forcing points which do not coincide with the Eulerian grid nodes and hence transferring forces between different frames of reference is a key element. The general expression of the three-dimensional delta function is as follows:

$$\delta(x_p - x_j) = \frac{1}{h^3}\phi\left(\frac{x_p - x_j}{h}\right)\phi\left(\frac{y_p - y_j}{h}\right)\phi\left(\frac{z_p - z_j}{h}\right) \tag{4.76}$$

where the subscript $j$ refers to the cell nodes, $p$ to the particles/bubbles $h$ is the size of the stencil, previously defined in Equation (4.75). The piecewise function $\phi$ chosen for the present case is second-order smooth polynomial.

## 4.6 Crossflow

Free-stream turbulence is an essential step in order to represent natural environmental flow conditions. Therefore, precursor simulations were initially run before the main simulation and then inlet planes fed into the latter (e.g. Rodi et al., 2013; Zhiyin, 2015; Shahriari et al., 2020). However, the precursor simulations demand a considerable amount of computational resources as LES require small time steps and fine grid resolutions. Moreover, it was found that the initial velocity profiles simulated by these precursor simulations were overestimated compared to the experimental initial profiles and result higher calculated ambient velocity profiles.

Therefore, the approach adopted for the generation of the crossflow conditions was the generation of artificial turbulent field using a Synthetic Eddy Method (SEM) Ouro, 2017. This method was initially developed by Jarrin et al., 2006 and has been widely applied specially for LES and in transition regions between RANS and LES.

The SEM is based on the generation of a finite number of eddies, $N_{ed}$ that are the source of velocity fluctuations on the generated inlet. The number of eddies is calculated based on the length-scale, $l_e$, and inlet plane dimensions. The resulting instantaneous velocity at the inlet results from the addition of the prescribed mean inlet velocity $U_0$, and the artificial velocity fluctuation $u_i^{'}(x)$, calculated as a function of the previously described parameters as following:

$$u_i^{'}(x) = \frac{1}{\sqrt{N_{ed}}} \sum_{k=1}^{N_{ed}} \alpha_{ij} \epsilon_j^k f_{\sigma_\epsilon}^k \left( \frac{x - x^k}{l_e^k} \right) \tag{4.77}$$

where $\alpha_{ij}$ is a tensor of the Lund coefficient presented in Equation (4.78) (Lund et al., 1998) related to the prescribed Reynold stresses ($R_{ij} = u_i^{'}u_j^{'}$) from Equation (4.78), $\epsilon_j^k$ is a random number between [-1,1], with zero average, $f_{\sigma_\epsilon}^k$ corresponds to a Gaussian shape function given to the vortex representation (Jarrin et al., 2006), and $x^k$ indicates the centre of coordinated of the $k^th$-eddy.

$$a_{ij} = \begin{pmatrix} \sqrt{R_{11}} & 0 & \\ R_{21}/\alpha_{11} & \sqrt{R_{22} - \alpha_{21}^2} & 0 \\ R_{31}/\alpha_{11} & (R_{32} - \alpha_{21}\alpha_{31})/\alpha_{22} & \sqrt{R_{33} - \alpha_{31}^2 - \alpha_{32}^2} \end{pmatrix} \tag{4.78}$$

In order to avoid any additional complexity to the generation of the artificial turbulent inflow, the turbulence at the inlet is considered isotropic, i.e. $u_i^{'}u_j^{'} = 0$, and homogeneous, i.e. $u_i^{'}u_i^{'} = u_j^{'}u_j^{'} = 2/3k$, (Otero, 2009). This yields to a Reynolds stresses tensor presented in Equation (4.79). Thus, this method allows to input the same turbulence intensity level measured during the experiments into the numerical simulations.

$$R_{HIT} = \begin{pmatrix} 2/3K & 0 & \\ 0 & 2/3k & 0 \\ 0 & 0 & 2/3k \end{pmatrix} = \begin{pmatrix} (I * U_0)^2 & 0 & 0 \\ 0 & (I * U_0)^2 & 0 \\ 0 & 0 & (I * U_0)^2 \end{pmatrix} \tag{4.79}$$

During the calculation of the inlet planes at each time step $n$, the eddies are convected based on the free-stream velocity as,

$$x^n(t + \Delta t) = x^n(t) + U_0 * \Delta t \tag{4.80}$$

where $\Delta t$ is the time step, which is usually assumed constant.

## 4.7 Stratification

Even though many types of flows can be treated with the equations of mass and momentum, determining the effects of temperature variations on the flow is necessary for stratified flows. The energy equation is adopted to determine effects of temperature variations on a number of cases of vertically stratified flow in a stagnant ambient.

The principal effect of temperature on a fluid results from the fact that changes in temperature cause variations in the fluid's density: when heated, a fluid's volume increases, thus making it lighter and causing it to rise. This results in the occurrence of buoyancy forces which depend on the temperature (thermal buoyancy forces). Incorporating yet further effects of temperature on the fluid and the flow leads to non-linear equations which are difficult to treat. The approach adopted in this thesis is the Boussinesq approximation:

- density is constant except in the buoyancy terms; i.e. the continuity equation retains its incompressible form and in the momentum equations, density varies only in the (gravitational) body force term;

- all other fluid properties are assumed constant;

- viscous dissipation is negligibly small.

The later two assumptions simplify the equations to the effect that the focus of interest is on the thermal buoyancy forces.

To describe the variations of density, the energy conservation equation is also included, for constant thermal diffusivity $\alpha$ and negligible viscous dissipation. The continuous phase temperature field is governed by the energy equation:

$$\frac{\partial T}{\partial t} + \frac{\partial T u_i}{\partial x_i} = \frac{1}{RePr}\frac{\partial^2 T}{\partial x_i \partial x_j} - \frac{\partial q_{ij}}{\partial x_j} \tag{4.81}$$

where $q_{ij}$ is the SGS thermal flux.

The momentum equation (4.2) thus take the form:

$$\frac{\partial u_i}{\partial t} + \frac{\partial (u_i u_j)}{\partial x_j} = -\frac{\partial p}{\partial x_j} + \frac{1}{Re}\frac{\partial^2 u_i}{\partial x_i \partial x_j} + (1 - \rho(T))g_i - \frac{\partial \tau_{ij}}{\partial x_j} + \xi_i \tag{4.82}$$

Following previous LES studies, a linear relation is assumed between the water density $\rho$ and the temperature T;

$$\rho = \rho_r[1 - \beta(T - t_r)] \tag{4.83}$$

with thermal expansion coefficient $\beta = 2 * 10^{-4} K^{-1}$ and $\rho_r$ and $T_r$ reference quantities.

## 4.8 Immersed Boundary Method

Immersed boundary method (IBM) was originally developed by (Peskin, 1972) with the aim of developing a methodology for the simulation of heart valves. Peskin (1972) developed a non-body conformal methodology that constituted a computationally cheap while accurate approach to biomechanical flows. In the 1990s, the popularity of IBM increased notably as the research community explored new improvements onto the method so as to enlarge its range of applications and accuracy. The main advantages of using IBM are: a) the capability to combine with structural meshes (usually rectangular Cartesian mesh) which allows the use of efficient flow solvers, such as fast Poisson equations (Sotiropoulos and Yang, 2014); and b) the relatively low computational cost compared to body-fitted models as highlighted by Fadlun et al. (2000).

There are mainly two IB method varieties: the continuum and discrete approaches. The continuum models use the geometrical description of a continuous surface to project the velocities over the normal vector to the body surface. It usually involved the categorisation of the Eulerian cells into solid, fluid or intermediate (Kang and Sotiropoulos, 2015). In the present study, the discrete approach is adopted. Discrete models are those where the body is built as a set of individual Lagrangian points that conform its shape. Figure (4.7) exhibits a two-dimensional representation of a staggered grid with uniform grid spacings ($\delta x$ & $\delta y$) and Lagrangian markers (red circles). Uhlmann (2005) developed the direct forcing (DF) method using delta functions to essentially form a two-way interpolation procedure between the Eulerian cells and Lagrangian cells where information between the fluid and solid frameworks are exchanged.

The direct forcing method follows a multi-step predictor-corrector procedure, which is adapted as follows: first the predicted Eulerian velocities ($u^*$) are calculated from Equations (4.10)-(4.11). A delta function ($\delta$) is used as an interpolation function to transfer $u^*$ onto the Lagrangian grid from its closest number of Eulerian neighbours, $n_e$ (filled black symbols in Figure 4.7) and the interpolated Lagrangian velocity, $U_L$ is obtained:

$$U_L = \sum_{ijk=1}^{n_e} u^*_{ijk} \delta(x_{ijk} - X_L) \Delta x_{ijk} \tag{4.84}$$

where $x_{ijk}$ is the vector of coordinates of the Eulerian mesh cells $ijk$. $X_L = (X_L, Y_L, Z_L)^T$ is the location of the Lagrangian marker, $L$ and $\Delta x_{ijk} = \Delta x \Delta y \Delta z$ is the Eulerian cell volume.

The interpolating delta functions are calculated from the multiplication of three one-dimensional kernels, $\phi$ as shown:

$$\delta(x_{ijk} - X_L) = \frac{1}{\Delta x_{ijk}} \phi\left(\frac{x_{ijk} - X_L}{\Delta x}\right) \phi\left(\frac{y_{ijk} - Y_L}{\Delta y}\right) \phi\left(\frac{z_{ijk} - Z_L}{\Delta z}\right) \tag{4.85}$$

The second step of the DF method is to compute the force $F_L$ that each Lagrangian marker needs to exert on the fluid to satisfy the no-slip condition at the marker's position. The force term is calculated as the difference between the desired velocity at the marker, $U^*_L$, and the velocity previously interpolated from the fluid mesh, $U_L$. In the case of a static body, the desired velocity at the neighbours used in marker $U^*_L$ is zero.

The third step constitutes the backwards procedure where the Lagrangian force is transferred back to the Eulerian mesh cells in order to obtain the Eulerian force, $f$. The same delta function as in Equation (4.85) is used to reverse interpolate $F_L$ from the closest Lagrangian cell and is performed as:

$$F_L = \frac{U^*_L - U_L}{\Delta t} \tag{4.86}$$

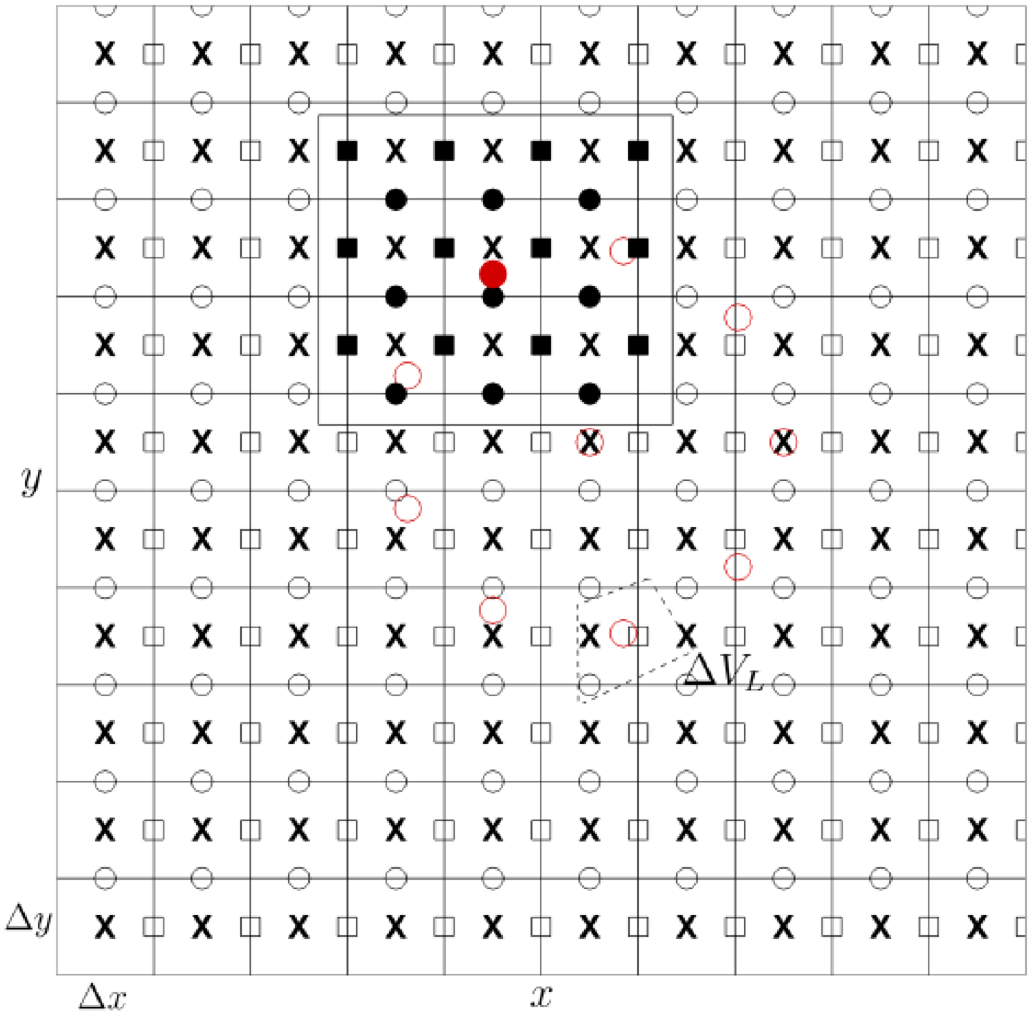

Figure 4.7: Two-dimensional representation of the Cartesian staggered grid. The neighbours used in the interpolation for a Lagrangian marker (filled red circle) are the black-filled symbols within the square boundary. $x$ represents pressure nodes, hollow squares are x-velocity nodes, hollow circles are y-velocity nodes, and red circles are the Lagrangian markers. $\Delta V_L$ denotes the Lagrangian marker volume.

$$f(x_{ijk}) = \sum_{L=1}^{n_L} F_L \cdot \delta\left(X_L - x_{ijk}\right) \cdot \Delta V_L \tag{4.87}$$

where $\Delta V_L$ is the Lagrangian volume, which should be approximately equal to $\Delta x_{ijk}$. In the final corrector step, the predicted Eulerian velocity, $u^*$ is updated with the Eulerian force from the IB method correction as follows:

$$u^* = \tilde{u}^* + f\Delta t \tag{4.88}$$

# Chapter 5

# Simulation of multi-phase plumes in crossflow

## 5.1 Introduction

Multi-phase plumes are buoyancy driven flows where the buoyancy is provided by a continuous release of an immiscible dispersed phase, such as gas bubbles, liquid droplets or solid particles (Socolofsky et al., 2002). Crossflow, i.e. ambient current, that is usually present in many of the aforementioned applications (Lima Neto et al., 2007), is very influential in determining the behavior of multi-phase plumes. Although the effect of crossflows on single-phase plumes and jets has been studied extensively (Muppidi and Mahesh (2005);Yuan et al. (1999)), little is known about their effect on multi-phase plumes (Salewski et al., 2007). In this chapter the effect of crossflow on multi-phase buoyant plume's dynamics has been investigated numerically with the aid of a thoroughly validated Large-Eddy Simulation Eulerian-Lagrangian algorithm (Fraga et al., 2016).

The main difference between single- and multi-phase plumes results from the discrete nature of the buoyant dispersed phase. In the case of a single-phase plume, the buoyancy arises by the changes in the density of the continuous phase -the advection of buoyancy is controlled by the motion of the entrained fluid. In contrast, in the case of a bubble plume the bubbles themselves comprise the buoyancy of the plume, entraining the surrounding fluid without mixing it, remaining discrete from the ambient fluid and following trajectories different from those of the entrained continuous phase. Crossflows affect a wide range of plume properties, changing the basic plume dynamics. Even in the case of single-phase plumes, crossflows can cause entrainment enhancement, deflection of the plume centerline, deformation of the plume shape into a counter-rotating vortex pair (Frict and Roshko, 1994), and fluid leakage in the downstream wake of the plume, i.e. ambient flow is detached from the main flow and is advected downstream away from the jet (Davidson and Pun, 1999).

The accurate prediction of bubble plumes has been a challenging task for both experimentalists and Computational Fluid Dynamics modellers due to the interaction between two strong sources of advection, the bulk velocity of the ambient flow and the buoyancy of the plume. Experimental studies that have investigated bubble plumes in crossflow are reported briefly. Socolofsky and Adams (2002) conducted bubble plume experiments in uniform and stratified crossflow, focusing on the trajectories of the dispersed phase and defining a characteristic critical height where the ambient fluid separates from the dominant dispersed phase. Rezvani (2016) measured the continuous phase dynamics inside and outside a bubble plume in turbulent crossflow. Zhang and Zhu (2013) focused on the bubble characteristics of bubble jets in crossflow by injecting air-water mixtures, showing that radial properties follow the Gaussian distribution and that the distribution of bubble diameter was affected primarily by the air and water rates and the distance from the nozzle.

Besides experimental studies, computational research on multi-phase plumes in crossflow is limited. Advanced 2D and 3D numerical simulations are performed mainly on multi-phase plumes in stagnant environment and/or vertically stratified ambient fluid and single-phase plumes in crossflow. Integral models have been employed in order to simulate oil and gas blowouts with emphasis on deep-water conditions; Yapa et al. (1999) simulated sub-sea blowouts with oil, gas and entrained sea water. The plume was considered as a mixture of non-miscible fluids (oil droplets and gas bubbles dispersed in seawater). Johansen (2000) developed a deepwater spill model capable of simulating gas hydrate formation/decomposition, gas dissolution and gas separation from the main plume. On the same note, Zheng et al. (2003)

and Chen and Yapa (2003) proposed a mathematical model to simulate the hydrodynamics and thermodynamics of the jet/plume; the thermodynamics and kinetics of hydrate formation and decomposition; and gas dissolution. The afforementionted models are applied to large-scale water bodies and even though they take into account the effect of cross currents and separation of continuous and dispersed phase, they focus more on the hydrates' dispersion rather on the change of dynamics of the surrounding fluid due to the dispersed phase.

Le Le Moullec et al. (2008) applied a three-dimensional EE two-phase numerical approach for the simulation of a crossflow gas-liquid wastewater treatment reactor using the CFD code FLUENT, testing two different turbulence models: $\kappa$-$\varepsilon$ and Reynolds Stress Model (RSM). Even though time-averaged horizontal velocity along the length of the reactor and vertical velocities at specific heights were presented, the study is focused on the mixing and flow within the reactor and not on the gas-liquid physics. Wang et al. (2012) presented instantaneous snapshots of the interface of deforming liquid bubbles and drops in a gas cross-flow, using a second-order hybrid level set-volume constraint method for numerically simulating a co-flowing liquid jet in gas deforming bubbles. Chen et al. (2003) applied a LES based model in order to simulate double-plume formation by oceanic $CO_2$, including seawater entrainment, gravity waves and peeling out of the plume. Momentum, mass and heat transfer phenomena are described using empirical formulae. Double-plume structure after the $CO_2$ injection and temperature field contours were simulated. Decrop et al. (2015) extensively studied negatively-buoyant, vertically downward injected turbidity plumes, i.e. mixtures of water and sediment particles, in crossflow using two-phase Large-Eddy Simulations. Fu et al. (2013) simulated solid particles discharged in gas crossflow using RANS, unsteady RANS (URANS) and detached eddy simulation (DES) techniques and presented the dynamics of the gas flow field and the dispersion of the solid particles.

In this chapter the results of Eulerian-Lagrangian LES simulations of a bubble plume in different crossflows are reported and discussed, with emphasis on fluid properties/dynamics. The EL-LES model is initially validated using a set of experiments conducted in Texas A&M University. The main objective of this study is to investigate the effect of crossflows on the dynamics of a bubble column and the resulting secondary flow.

The numerical simulations presented in the following chapters are conducted with the in-house code Hydro-3D which is a finite-difference-based large-eddy simulation code following the methodology described in Chapter 4.

## 5.2 Experimental Setup

In this section, details about the experiments conducted by Rezvani (2016) are given.

The experiments were carried out in a glass-walled flume 35m long by 0.9m wide and 1.2m deep in the Fluid Dynamics Laboratory of the Zachry Department of Civil Engineering at Texas A&M University. The tank was equipped with a recirculation pump system, which was used to simulate different ambient currents (generating a forced current). Independent sets of experiments were conducted for open channel crossflow.

To generate the bubble plume, Rezvani (2016) used a 2.5cm tall by 1.4cm in diameter porous aquarium airstone, which was located at the centerline of the wave flume at a depth of 0.68m. The bubble flow rates were chosen as $Q_o = 0.5, 1$ and 1.5L/min to match those of previous experiments with zero crossflow (Seol et al., 2009). The bubble flow rates at standard pressure and temperature were monitored by a calibrated gas flowmeter. As reported in Lai (2015), who used a similar setup, the generated air bubbles have a median diameter $d_{50}$ of 2.4mm (Figure 5.1) with a corresponding velocity of 24cm/s (Clift, 1978). The bubble size was visually validated from the raw images in the crossflow experiments.

Crossflows were generated using two centrifugal pumps equipped with a frequency controller. The pumps were capable of generating flows ranging between 1.32m$^3$/sec and 6.06m$^3$/sec. The flow rates were monitored by the inline propeller flow meter in the external recirculation piping as well as by ADV velocity measurements in the flume during the experiments. Recirculating flow entered the flume through a ramp inlet in the flume bottom creating a submerged wall jet. In order to destroy the jet structure of the inflow at the flume entrance, an array of bricks was placed immediately after the inflow (Ghisalberti and Nepf, 2002). A homogeneous grid of porous plates was then used to smooth the velocity profile as suggested by Stoker

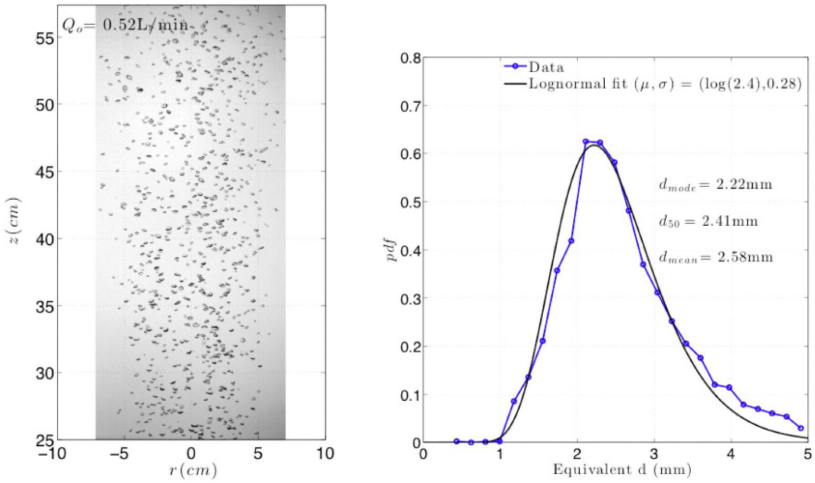

Figure 5.1: Bubbles size distribution from Lai (2015).

(1946). Flow straighteners made out of PVC pipes with a diameter of 2.54cm and length of 70cm were used to eliminate large scale turbulence and secondary currents. The bubble plume was located at 19 times the water depth downstream of the flow straightener, which was about 2/3 of the flume length. Measurements of the velocity field validated the uniform open channel flow condition in the measurement section.

In all the experiments, the center plane of the bubble plume was illuminated by a laser sheet. The vertical illumination plane along the centerline of the bubble diffuser was produced using continuous lasers along with a pair of cylindrical lenses that focused and expanded the beam, creating the light sheet. The light sheet was formed outside the tank and directed into the tank through the glass at the side of the tank and oriented upward by a mirror placed on the bottom of the tank.

Quantitative measurements for the forced current case were accomplished using Standard Particle Image Velocimeter (PIV), where the source of light sheet was a continuous Argon-ion laser (Spectra- Physics) capable of a peak power of 2.8W. The flume water was seeded with neutrally buoyant homopolymer polyamide particles (manufactured by Vestonic) with mean diameter of 56 microns and of specific gravity 1.03. Flow images were captured by a high speed Phantom camera (Phantom v5.1, Vision Research Inc.) mounted on a three-dimensional traverse and positioned perpendicularly to the light sheet. The camera frame rate was 200Hz and the expo-

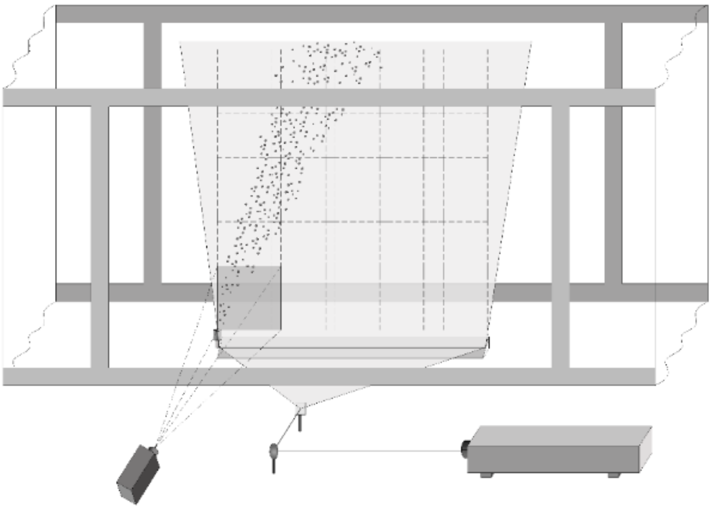

Figure 5.2: Schematic of the PIV setup from Rezvani (2016).

sure time was 300 microseconds collecting 2000 images for each measurement burst (e.g., 10sec burst duration, limited by camera physical memory). The resolution of the camera is 1024x1024 pixels at 10 bit gray scale resolution. In order to cover the whole field of interest, 25 fields of view (FOV) were used, starting from the center of the bubble diffuser. Each FOV is defined by two numbers; first number indicates the row number and the second number shows the number of column in our measurement matrix. Each FOV has the dimension of 15cmx15cm with 1.5cm overlap. Experiments were repeated three times at each FOV, which resulted in a total of 30 seconds of data, or 6015 images at each flow rate. The PIV processing of these images resulted in 30s of instantaneous velocity data (in 10sec bursts), providing the full-field velocity along the plume center plane. Meanwhile, PIV sequences were neither synoptic from FOV to FOV nor were the data contiguous over the whole 30 s at each measurement point; therefore, we rebuild the flow field from statistical averages of the results. Figure 5.2 shows a schematic of the experimental setup.

At the outset, three types of fluid velocities can be expected inside a bubble plume: (i) bulk entrained flow, (ii) bubble wakes and (iii) return flow due to rising bubbles. All must be registered by the chosen instrument for correct quantification of plume turbulence. The instrument must also have moderately high spatio-temporal resolutions, and preferably with all three components of the velocity vector available. This naturally rules out all intrusive single-point devices and suggests the use of particle image velocimetry (PIV). In multiphase flows, the technique is complicated by the need to discriminate between continuous liquid phase and dispersed gas phase. To this end, phase-discriminating PIV that uses fluorescent seedings and optical filters for phase selection has been developed. Two cameras are needed for the synoptic measurements of both phases. In (Simiano et al., 2006), the method is applied in the center plane of bubble plumes but only fluid velocities are captured. A simplified technique that uses only a single camera and standard algorithms of PIV and particle tracking velocimetry PTV for the calculation of phase velocity is proposed in (Seol et al., 2007). Inherent to this is the removal of bubble wake velocities that leads to an underestimation of the streamwise velocity and hence its stresses. In general, the major challenge in applying PIV to bubbly flows is the existence of shadowy regions behind bubbles which could render the measured velocities uncertain and inaccurate.

In addition to PIV experiments by Rezvani (2016), the author and Lai (2015) have measured the velocity of a bubble plume in crossflow using Acoustic Doppler Velocimeter (ADV). Hence, the PIV results can be compared against data measured by another instrument that has a different operating principle. The same experimental setup was applied for the ADV measurements. We have selected the Nortek Vectrino II for three-dimensional fluid velocity measurements. It is the latest generation of ADV and is capable of synoptic measurements along a 35mm strip at temporal frequencies up to 100Hz and at spatial resolutions from 4mm down to 1mm. Being calibration-free on the part of the experimenter, it is convenient. The coherent-pulse technology of ADVs is well understood and its performance in probing energetic turbulent flows has been well-documented. We are therefore led to explore its capabilities in probing the bubble plume, as an alternative to PIV. A concern arises on whether the returned measurements are correct in the presence of bubbles which are strong acoustic scatterers. It has long been considered that bubbles cause outliers to appear in the time series which have to replaced by some in-range values. Surprisingly, it turns out that no such replacement is necessary for the Vectrino II data obtained from our flow field (void fraction $< 2\%$).

## 5.3 Numerical Setup

The model has been previously validated for gas plume in a stagnant liquid tank by Fraga et al. (2016). The model performance is assessed by predicting the dynamics of a set of experiments conducted in Zachry Laboratory of the Department of Civil Engineering of Texas A&M University. The numerical setup (Fig. 5.3) follows the experimental setup (see Chapter 5.2).

| Case # | Crossflow velocity $u_{cf}$ (m/sec) | Water Depth (m) | Bubble flow rate $Q_b$ (l/min) |
|---|---|---|---|
| 1 | 0.04 | 0.82 | 0.5 |
| 2 | 0.10 | 0.82 | 0.5 |
| 3 | 0.15 | 0.82 | 0.5 |

Table 5.1: Flow characteristics of the three numerical cases.

Table 5.1 summarizes the main characteristics of the three cases reported in this chapter. More details for the experimental cases 1 and 2 can be found in Rezvani (2016). Case3 was only simulated numerically using LES.

| Case # | Mesh | $\Delta x$ (mm) | $\Delta y$ (mm) | $\Delta z$ (mm) | Total grid-points (Mio) | $\Delta_x^+$ | $\Delta_y^+$ | $\Delta_z^+$ | Exp. Data |
|---|---|---|---|---|---|---|---|---|---|
| 1 | Coarse | 7.5 | 4.5 | 4.1 | 22.4 | 25.5 | 15.3 | 13.9 | PIV & ADV |
| | Fine | 3.75 | 2.25 | 2.05 | 179.2 | 12.75 | 7.6 | 7.0 | |
| 2 | Coarse | 7.5 | 4.5 | 4.1 | 22.4 | 40.425 | 24.2 | 22.0 | PIV |
| | Fine | 3.75 | 2.25 | 2.05 | 179.2 | 20.175 | 12.1 | 11.0 | |
| 3 | Coarse | 7.5 | 4.5 | 4.1 | 22.4 | 57 | 34.2 | 31.2 | N/A |

Table 5.2: Grid details of the three Large-eddy simulations cases.

where $\Delta x$, $\Delta y$ and $\Delta z$ are the grid resolution in x, y and z direction respectively and $\Delta_x^+$, $\Delta_y^+$ and $\Delta_z^+$ is the grid resolution in wall units in x, y and z direction respectively.

The numerical simulations are carried out under analogous conditions to the experiments. A sketch of the numerical setup is given in Figure 5.3, where the distance $s$

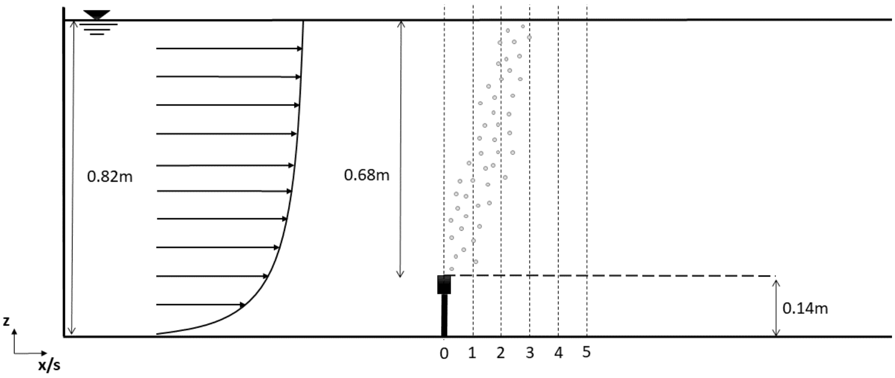

Figure 5.3: Schematic of side view of the experimental setup along with profile locations used in Figures 5.4-5.15.

is equal to 0.1m. Validation profiles of velocity and stress will be given every 0.1m, i.e., $s$, downstream the diffuser in the following. This is because the experimental measurements taken from Rezvani (2016) are within 0.6m downstream the diffuser.

For the numerical simulations, the channel is 4.2m long and the bubbles are released 1.4m downstream the inlet. This is to align with the experimental condition by Rezvani (2016): "The bubble plume was located at about 2/3 of the flume length". The generated air bubbles have a mean diameter $D_p$ of 2.5mm and a standard deviation of 0.28mm, following the log-normal distribution observed by Lai (2015) presented in Figure 5.1.

The average number of bubbles for a fully developed bubble plume is approximately 2500 for case1, and just over 2600 for case2 and case3. Boundary conditions for the fluid phase include the use of wall-functions boundary condition at all solid walls and a free slip condition at the water surface. Free slip condition at the water surface has been applied and validated in numerous LES gas-liquid studies, e.g. Delnoij et al., 1997; Torti et al., 2013; Fraga and Stoesser, 2016.

Two different mesh resolutions are used for cases 1 & 2, a coarse and a fine mesh (Table 5.3). Only the coarse mesh resolution is used for case3 as there are no experimental results for comparison. In the fine mesh simulation, LMR technique has been applied as described in Chapter 4, in an effort to keep computational cost low. The mesh resolutions in Table 5.3 were chosen based on the limit $D_p/\ Dx = 0.67$, as proposed by (Milelli et al., 2001) shown in Table 5.3. The selection of mesh is based on the grid size sensitivity study presented in Fraga et al. (2016) for plumes in stagnant liquid.

|  | Coarse mesh | Fine mesh | Milelli's limit |
|---|---|---|---|
| $D_p/\ \Delta_x$ | 0.33 | 0.66 | 0.67 |

Table 5.3: Bubble-to-mesh size ratio for the two mesh resolutions tested.

In their study, Fraga et al. (2016) used three different size of grid, i.e. coarse $\Delta x = 6.25$mm, medium $\Delta x = 3.125$mm and fine $\Delta x = 2.5$mm, and constant bubble diameter $D_p = 2$mm. The size of the medium mesh ($\Delta x = 3.125$mm) is very close to Milelli's proposed limit, the fine grid ($\Delta x = 2.5$mm) exceeds it and the coarse grid is considered reasonably fine to effectively resolve explicitly large-scale turbulence. The results showed that the profiles of the simulations on the coarse and medium meshes are almost identical, exhibiting very little sensitivity to the chosen resolution. However, mesh refinement over the Milelli's limit appears to give different results. This is because the smaller filter-width of the finer mesh does not help in capturing the eddies generated at (or below) the bubble scale. As a result, the same turbulence is distributed over a wider plume, resulting in under-prediction of the turbulent fluctuations.

In order to provide a realistic, fully turbulent inflow whilst avoiding extreme computational cost, the velocity inlet boundary conditions is generated using a Synthetic Eddy Method (SEM), as described in Chapter 4.6. The initial u-velocity time-averaged profile of the centerline is extracted from the same experimental setup as described previously but with crossflow only (Rezvani (2016)), and used as the mean velocity profile on which SEM fluctuations are applied. The outflow is treated with convective outflow boundary condition.

Two time steps are chosen, i.e. 0.001sec and 0.005sec, for Case1 and Case2 both for coarse and fine mesh. For Case3, only the 0.001sec time-step is used. The time-steps are chosen to be below the CFL-condition (Courant et al., 1928) and the DIF condition (Miller, 1971), as described in Chapter 2.6.1.

Total number of iterations is 1,500,000 for each case examined. This is because the simulations converged after 1,200,000 iterations. The averaging of the velocities and stresses started after 500,000 iterations.

## 5.4 Results

### 5.4.1 Validation profiles

A quantitative evaluation of the code's performance is detailed in this section by presenting the results of a series of simulations that have been performed on grids with different resolutions, as summarized in Tables 5.1&5.3, and different time-steps. Vertical profiles of simulated quantities at selected locations along the centerline of the computational domain are plotted against the PIV experimental data of Rezvani, 2016 and ADV experimental data. The six locations are shown in Figure (5.3). Data from the LES simulations; coarse mesh and 0.001sec time-step (solid line), fine mesh and 0.001sec time-step (dashed line), coarse mesh and 0.005sec time-step (dotted line) and fine mesh and 0.005sec time-step (dash-dot-dash line) are plotted, as well as experimental data; PIV (crosses) and ADV (rhombs). The horizontal dotted lines shown in Figures (5.5)-(5.20) indicate the area where the ambient fluid profiles are within the bubble plume.

Profiles of the initial time-averaged horizontal u-velocity normalized by the bulk velocity are presented in Figure (5.4). PIV measurements (cross symbols) were extracted from the experimental cases without bubbles and the curve that fit best to the data (solid line) is used as the mean velocity profile on which SEM fluctuations are applied.

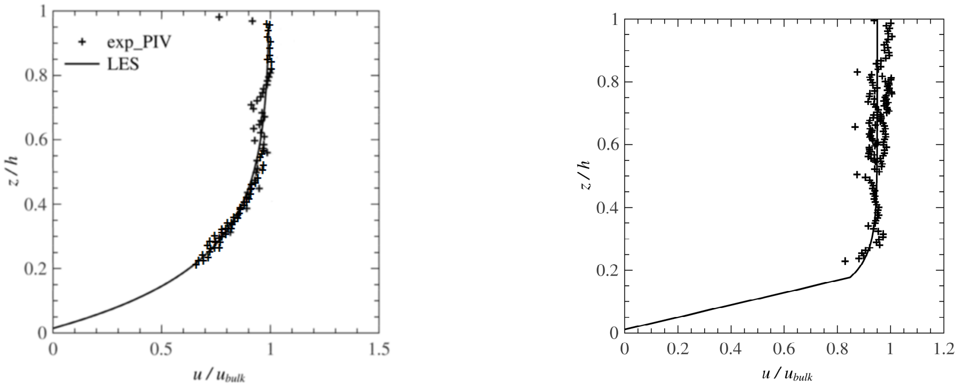

(a) Initial u-velocity profile for case1 (b) Initial u-velocity profile for case2

Figure 5.4: Initial time-averaged streamwise velocity profiles of LES and PIV experiments for cases 1&2.

In the following figures (5.5)-(5.20), the legend $exp\_PIV$ refers to experimental PIV results, $exp\_ADV$ to experimental ADV results, $LES\_coarse0.001$ to LES results with coarse mesh and 0.001sec time-step, $LES\_fine0.001$ to LES results with fine mesh and 0.001sec time-step, $LES\_coarse0.005$ to LES results with coarse mesh and 0.005sec time-step and $LES\_fine0.005$ to LES results with fine mesh and 0.005sec time-step

Figure (5.5) shows the vertical profiles of simulated time-averaged horizontal u-velocities at selected locations (every 0.1m downstream the diffuser) referenced in (Figure 5.3) along the centerline of the computational domain plotted against the experimental data. Note that velocities are normalized with the bulk u-velocity, $u_{bulk}$. The agreement between the LES and the experiments is generally good. There are some discrepancies in the profiles of time-averaged horizontal velocities at locations x/s=1, x/s=2 and x/s=3, i.e. within the bubble column and just downstream the bubble column. In these locations, the range of the experimental data is quite wide and it is difficult to identify a clear profile of the horizontal u-velocities. The match between simulations and experiments becomes better with increasing distance from the bubble plume. The agreement between the LES simulations is also good.

Figure (5.6) presents the vertical profiles of time-averaged vertical w-velocity at the same locations as in Figure (5.5). The match between simulations and experiments is good and becomes better with increasing distance from the bubble column, i.e. after x/s=3. The most significant discrepancies are observed at location x/s=2 and x/s=3, i.e. at the outer boundary of the bubble plume and just downstream of it, where the numerical results stand between the PIV and ADV data. There is however a good agreement between the numerical simulations for both velocity profiles. The comparison of profiles indicates that overall the coarse grid is capable of reproducing fairly well the flow and good agreement with the experimental data is observed.

Figures (5.7) and (5.8) present profiles of Reynolds stresses in the horizontal and vertical directions normalized by $u_{bulk}^2$. Numerical simulations are compared with PIV experiments. Similar patterns are observed in both figures. Significant peaks are observed at the bubble column boundaries and just downstream the bubble column, i.e. x/s=1 and x/s=2. The agreement between numerical and experimental results is good. However, the peaks of horizontal normal stress (Fig. 5.7) and the peaks of

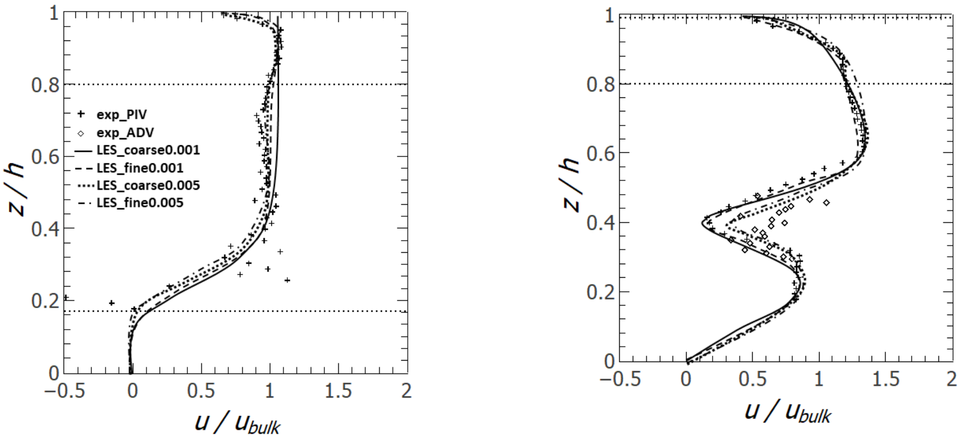

(a) x/s=0 (b) x/s=1

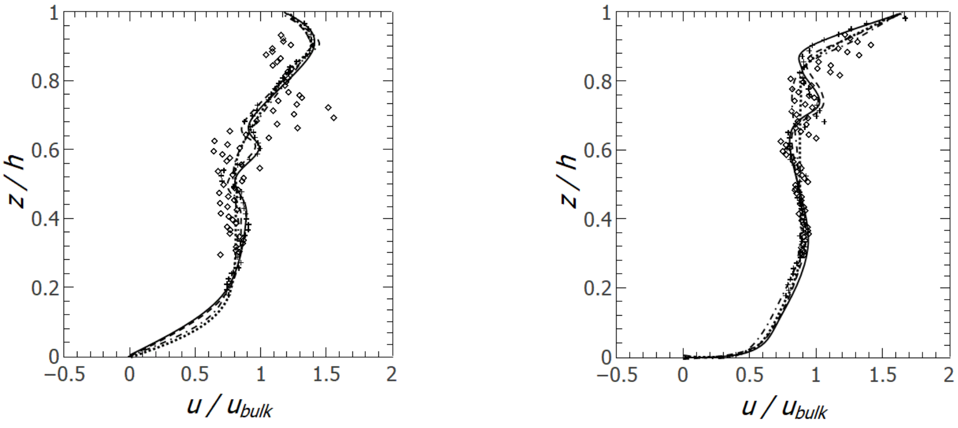

(c) x/s=2 (d) x/s=3

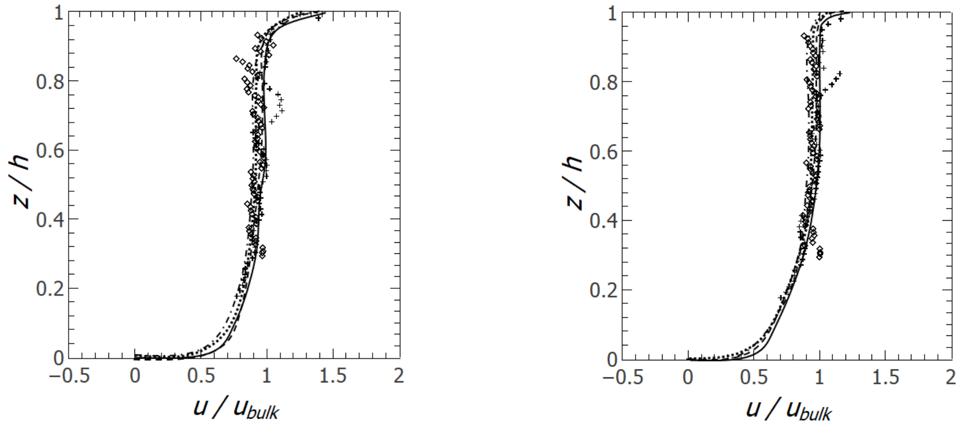

(e) x/s=4 (f) x/s=5

Figure 5.5: Case1: Vertical profiles of normalized u-velocities along the centerline of the domain.

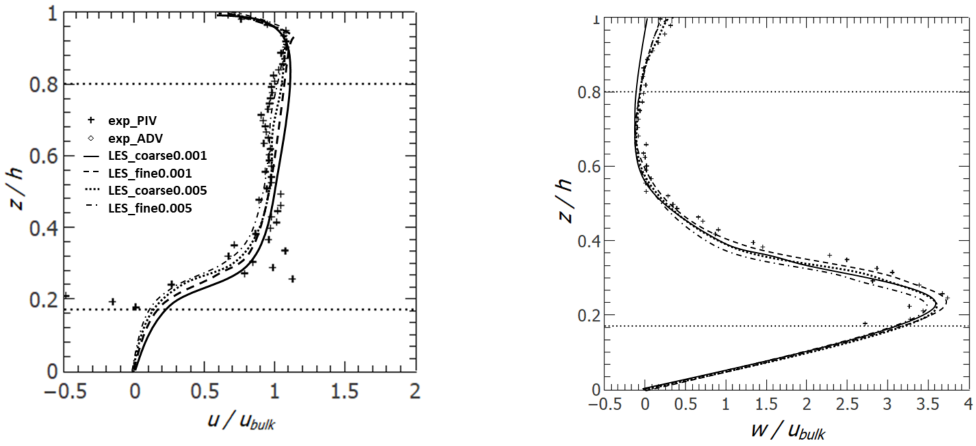

(a) x/s=0 (b) x/s=1

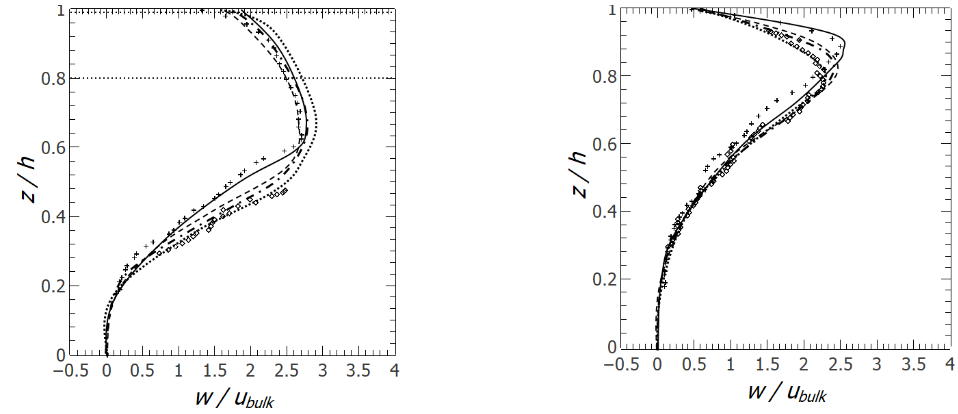

(c) x/s=2 (d) x/s=3

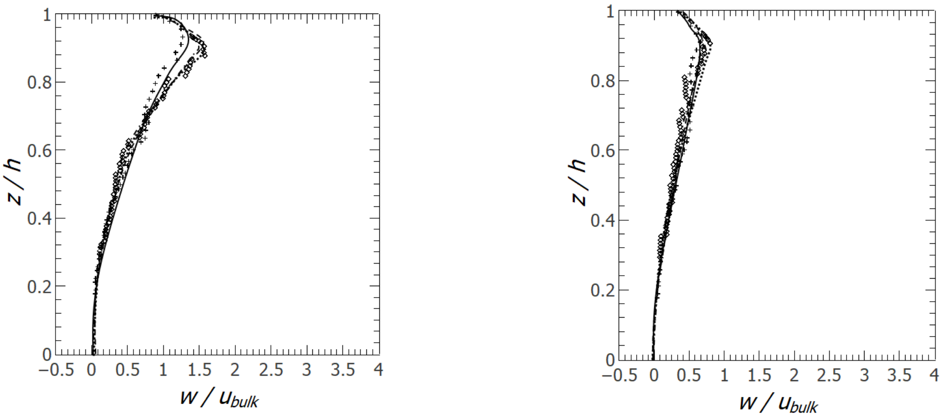

(e) x/s=4 (f) x/s=5

Figure 5.6: Case1: Vertical profiles of normalized w-velocities along the centerline of the domain.

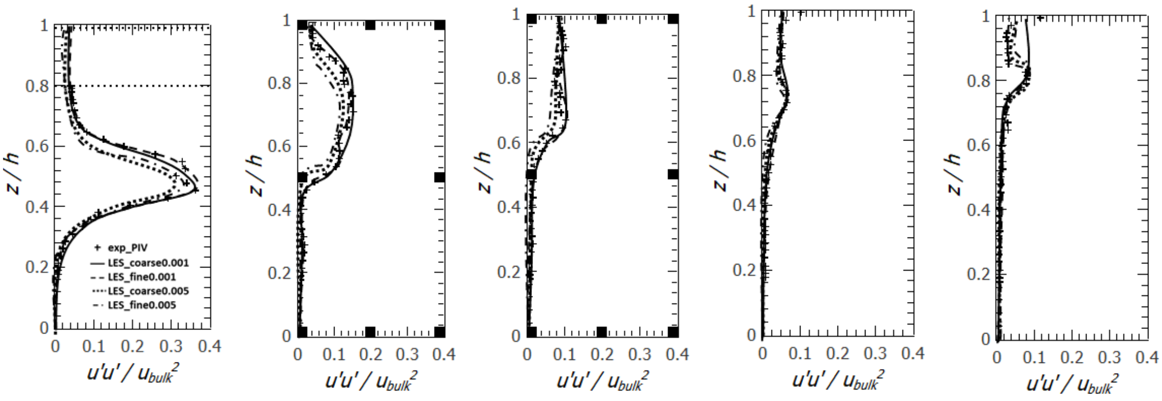

(a) x/s=1 (b) x/s=2 (c) x/s=3 (d) x/s=4 (e) x/s=5

Figure 5.7: Case1: Vertical profiles of normalized horizontal normal stress along the centreline of the domain.

vertical normal stress (Fig. 5.8) at x/s=1 and x/s=2 are slightly underestimated by the simulations with 0.005sec time-step. This is because the higher time-step does not help in capturing the eddies generated in the bubble scale. The match between simulations and experiment becomes better at the plume's wake.

Figure (5.9) shows horizontal profiles of time-averaged horizontal u-velocities every 0.1m above the diffuser. The velocities are normalised with the bulk u-velocity, $u_{bulk}$. The agreement between the numerical results is good. Comparing the numerical with the experimental PIV results, we notice that the peak velocity is underestimated from z/h=1 to z/h=3, in particular from the simulations with the higher 0.005sec time-step.

Figure (5.10) shows horizontal profiles of time-averaged vertical w-velocities every 0.1m above the diffuser. The numerical simulations with 0.005sec time-step underpredict the peak velocities along the entire height of the bubble column.

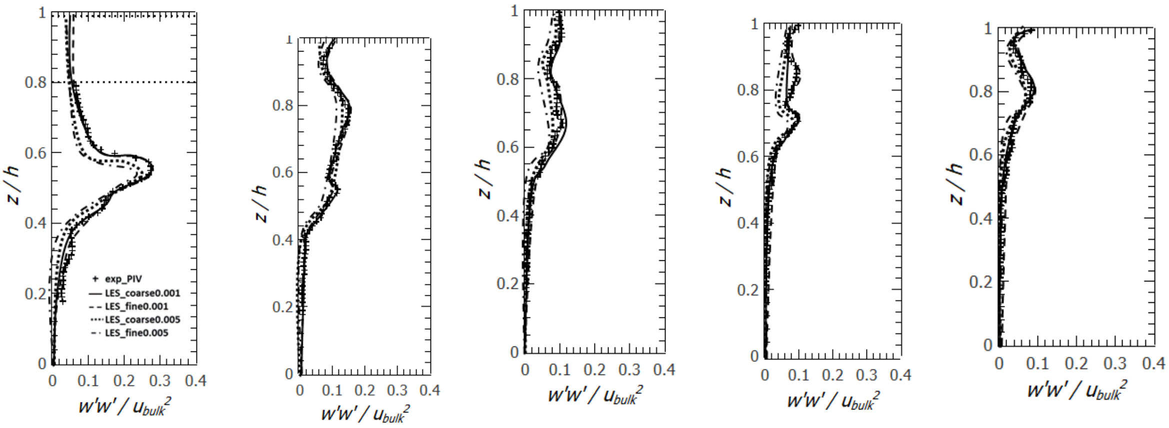

(a) x/s=1 (b) x/s=2 (c) x/s=3 (d) x/s=4 (e) x/s=5

Figure 5.8: Case1: Vertical profiles of normalized vertical normal stress along the centerline of the domain.

Figure (5.11) shows horizontal profiles of time-averaged Reynold stress $u'u'$ in the horizontal direction normalised by $u_{bulk}^2$, every 0.1m above the diffuser. The Reynold stress profiles have been captured by the numerical simulations. However, some under-prediction of the peak values is noticed, mainly from the fine mesh-high time-step LES simulation. Similar pattern is noticed at the horizontal profiles of time-averaged Reynold stress $w'w'$ in the vertical direction in Figure (5.12).

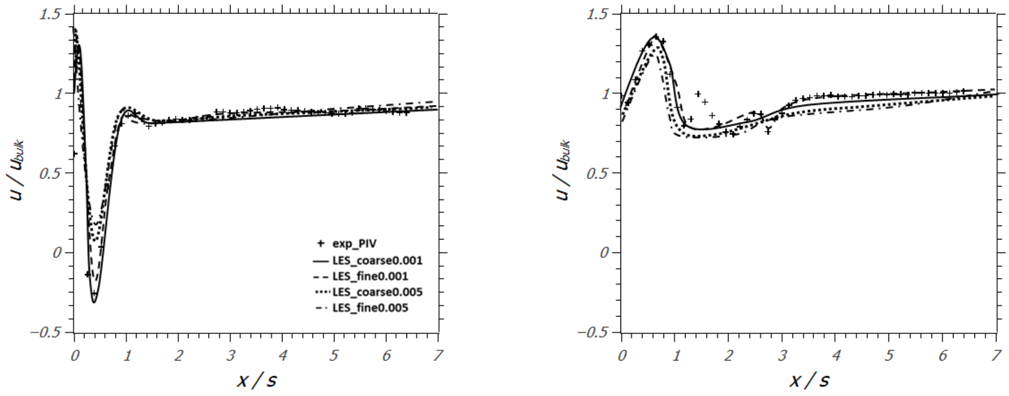

(a) z/h=1 (b) z/h=2

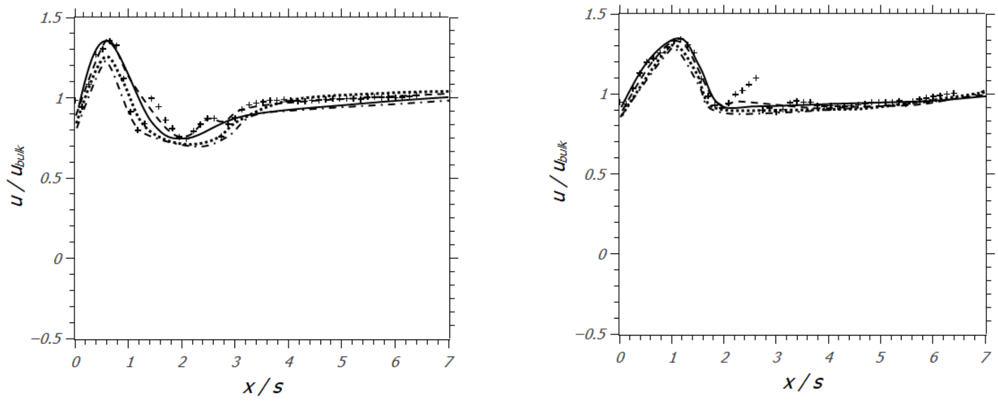

(c) z/h=3 (d) z/h=4

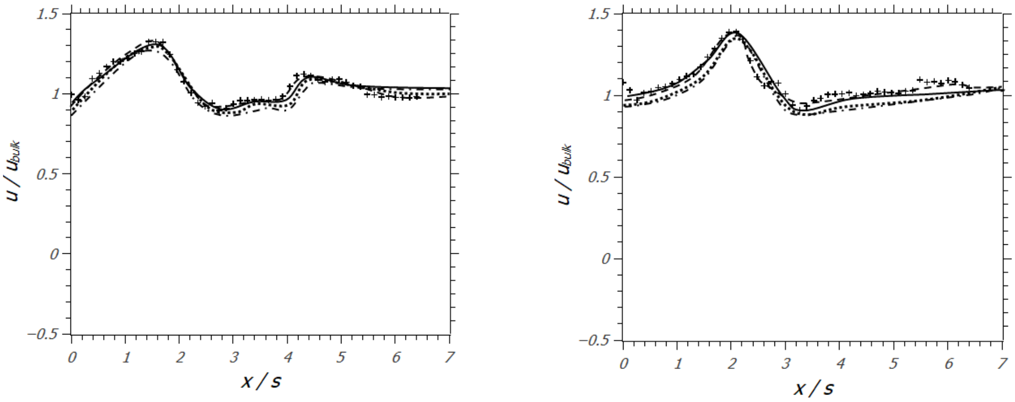

(e) z/h=5 (f) z/h=6

Figure 5.9: Case1: Horizontal profiles of normalized u-velocities along the centerline of the domain.

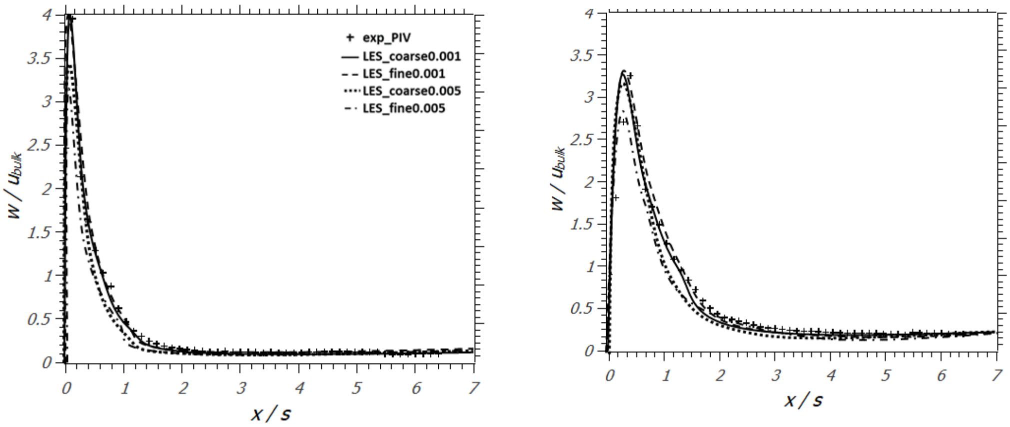

(a) z/h=1 (b) z/h=2

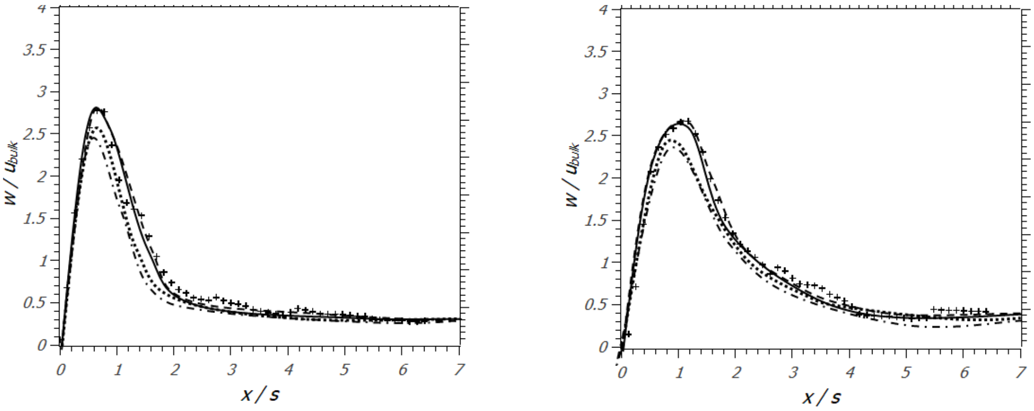

(c) z/h=3 (d) z/h=4

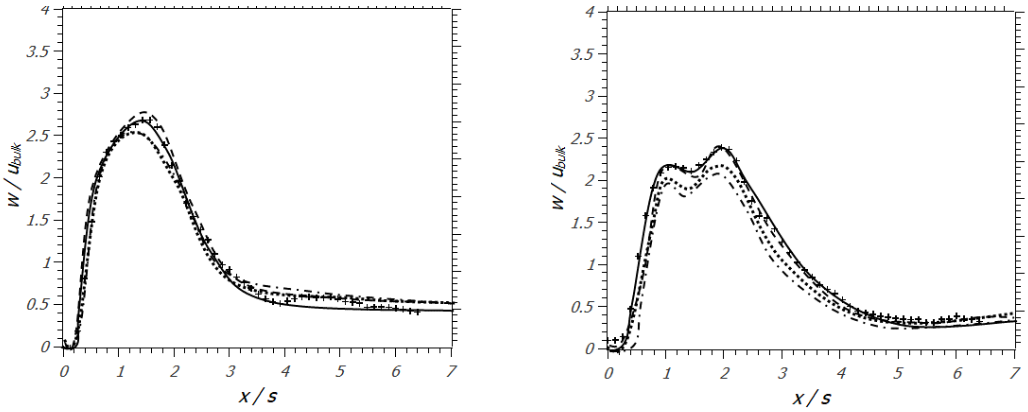

(e) z/h=5 (f) z/h=6

Figure 5.10: Case1: Horizontal profiles of normalized w-velocities along the centerline of the domain.

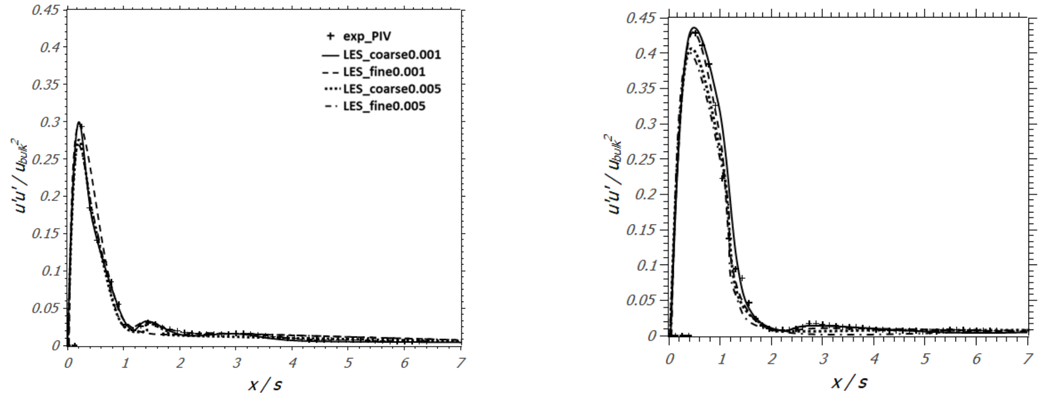

(a) z/h=1 (b) z/h=2

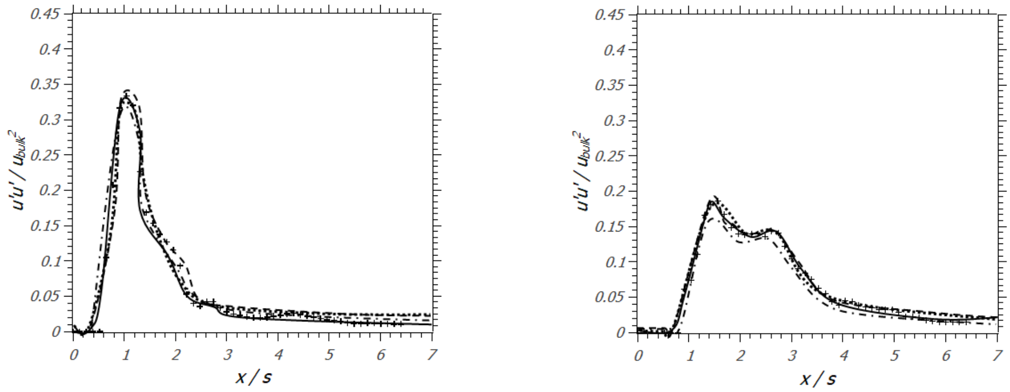

(c) z/h=3 (d) z/h=4

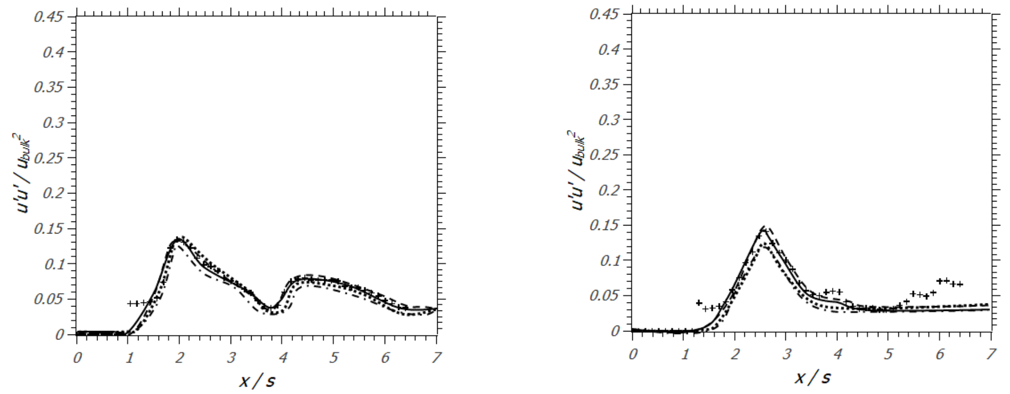

(e) z/h=5 (f) z/h=6

Figure 5.11: Case1: Horizontal profiles of normalized horizontal normal stress along the centerline of the domain.

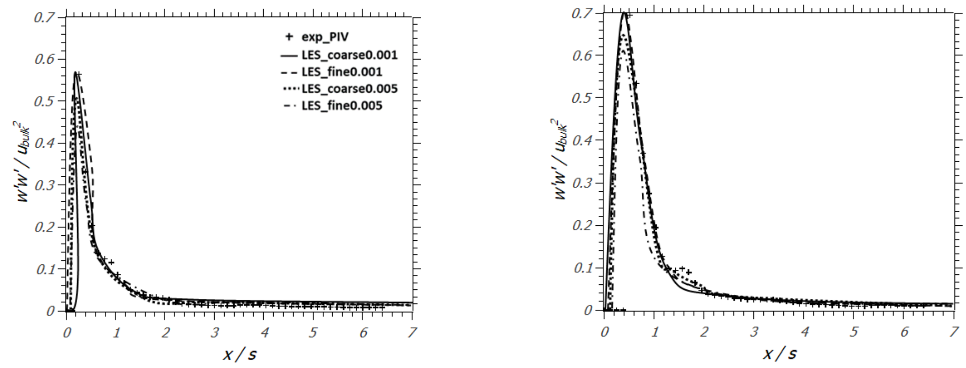

(a) z/h=1 (b) z/h=2

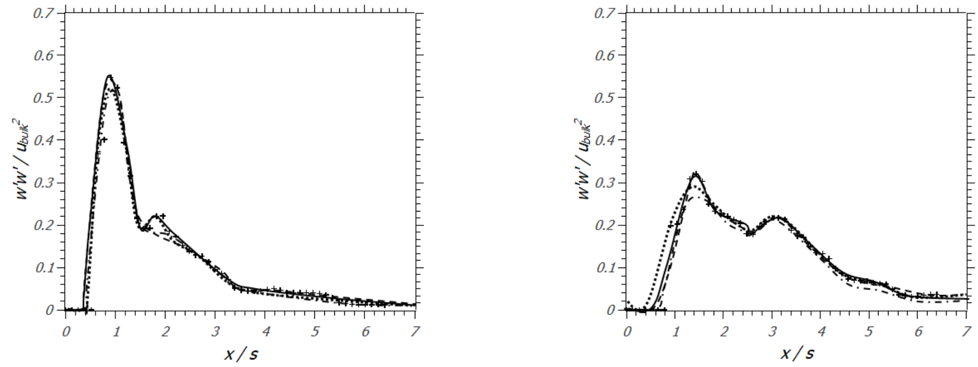

(c) z/h=3 (d) z/h=4

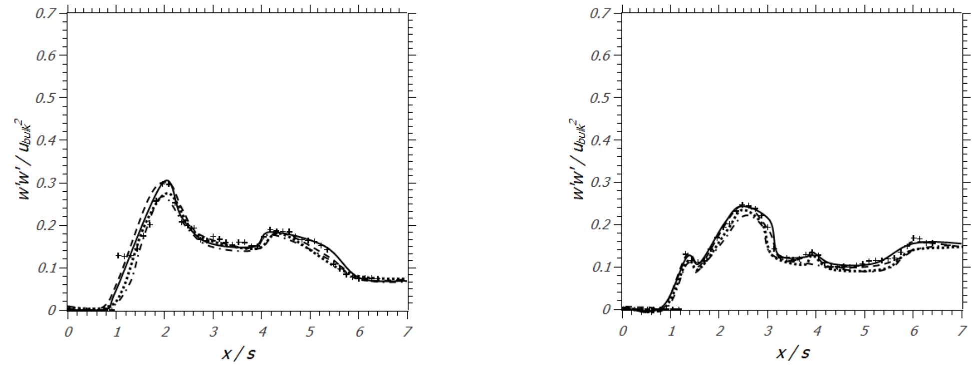

(e) z/h=5 (f) z/h=6

Figure 5.12: Case1: Horizontal profiles of normalized vertical normal stress along the centerline of the domain.

Results from Case2 are also used for the validation of the code in Figures (5.13)-(5.20). The agreement between the simulated velocities and the experimental measurements is good.

Figures (5.13) and (5.14) show the vertical profiles of the time-averaged horizontal velocity and the time-averaged vertical velocity respectively. Figures (5.15) and (5.16) show the vertical profiles of the time-averaged horizontal normal stress and the time-averaged vertical normal stress, respectively. There is a very good agreement between the experimental and the numerical results in all the vertical profiles of the aforementioned figures.

There is a very good agreement between numerical and experimental results for the horizontal profile plots (Figures 5.16 - 5.20 of the velocities and Reynolds stresses, with the exception of the peak of vertical velocity at z/h=1 (Figure 5.18(a)) and the peaks of horizontal normal stress between z/h=1 and z/h=3 (Figure 5.19).

It is evident in both cases that the areas, where most of the discrepancies between numerical and experimental velocities are observed, are these at the edge of the bubble plume and just downstream, i.e. 10cm and 20cm, of the bubble plume. This may be explained by the fact that the profiles closer to the plume are influenced by bubbles that have been pulled out of the plume due to the crossflow and this is where the PIV data are less reliable.

The EL-LES approach is able to accurately reproduce the horizontal turbulence generated within the bubble plume as well as the peak of turbulence in the direction of bubbles' motion. i.e. vertically. The fine mesh with 0.005sec simulation is the exception. This indicates that further investigation on the mesh size, time-step and bubble size correlation should be conducted.

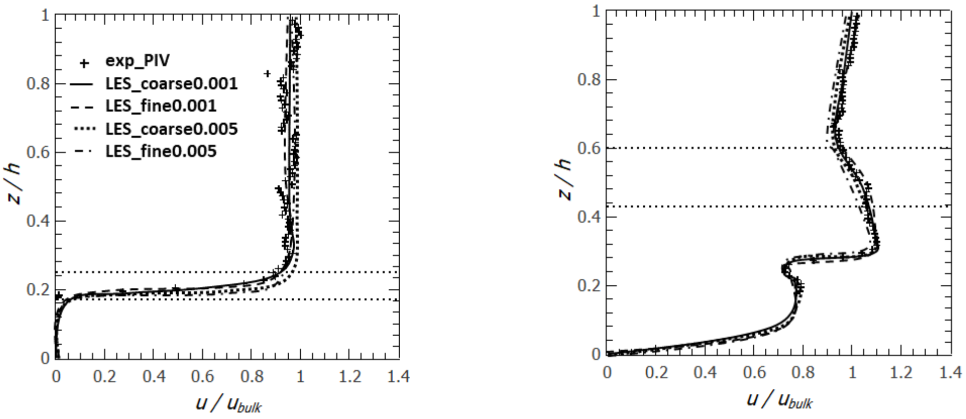

(a) x/s=0 (b) x/s=1

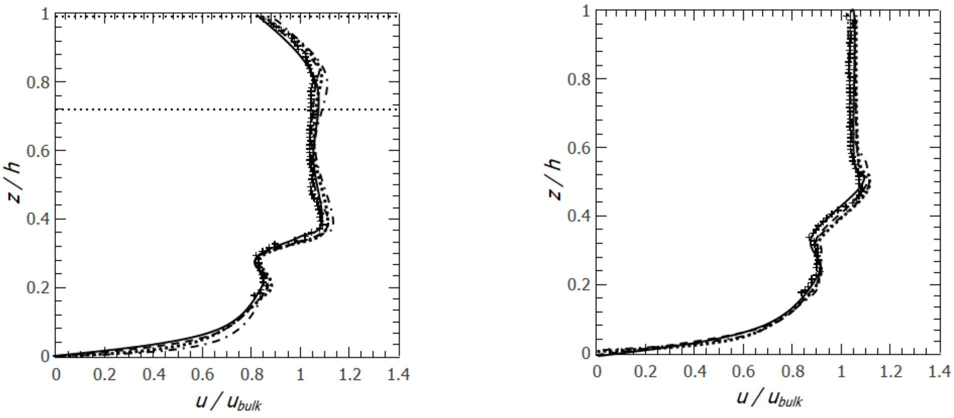

(c) x/s=2 (d) x/s=3

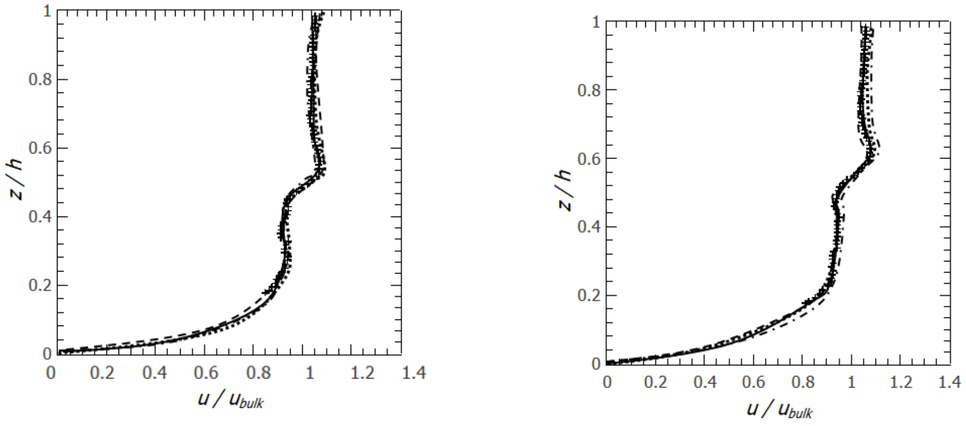

(e) x/s=4 (f) x/s=5

Figure 5.13: Case2: Vertical profiles of normalized horizontal velocities along the centerline of the domain.

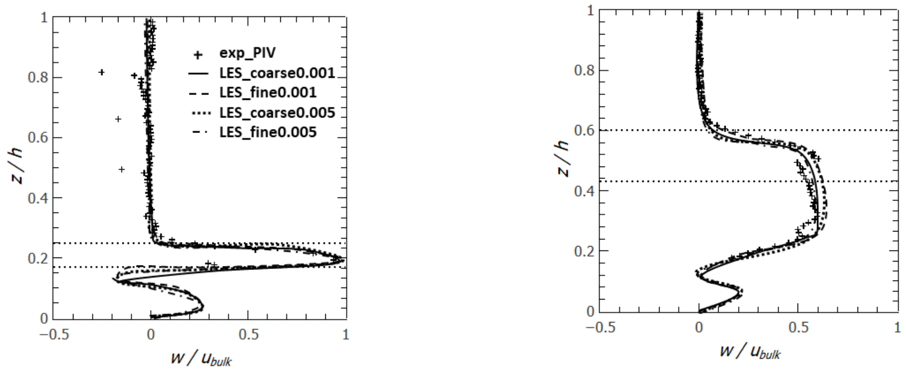

(a) x/s=0 (b) x/s=1

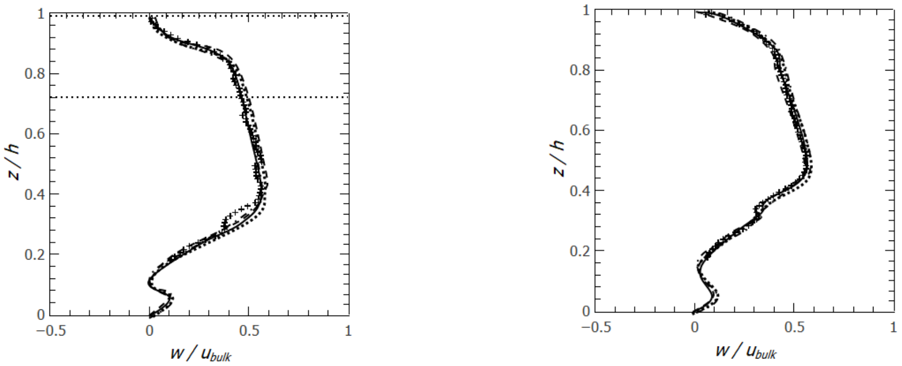

(c) x/s=2 (d) x/s=3

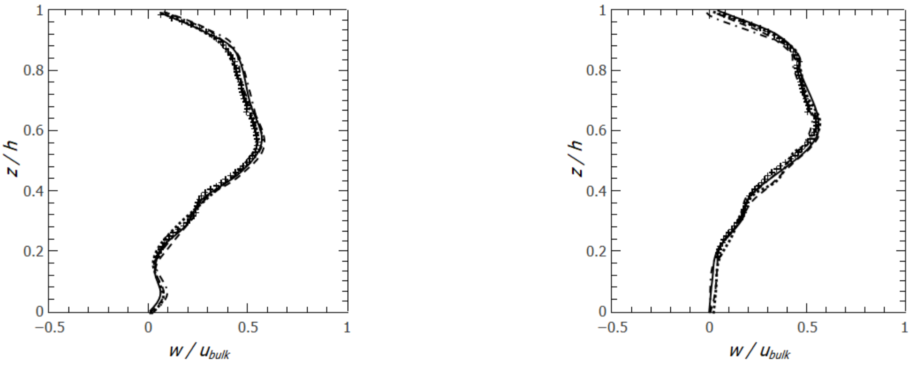

(e) x/s=4 (f) x/s=5

Figure 5.14: Case2: Vertical profiles of normalized vertical velocities along the centerline of the domain.

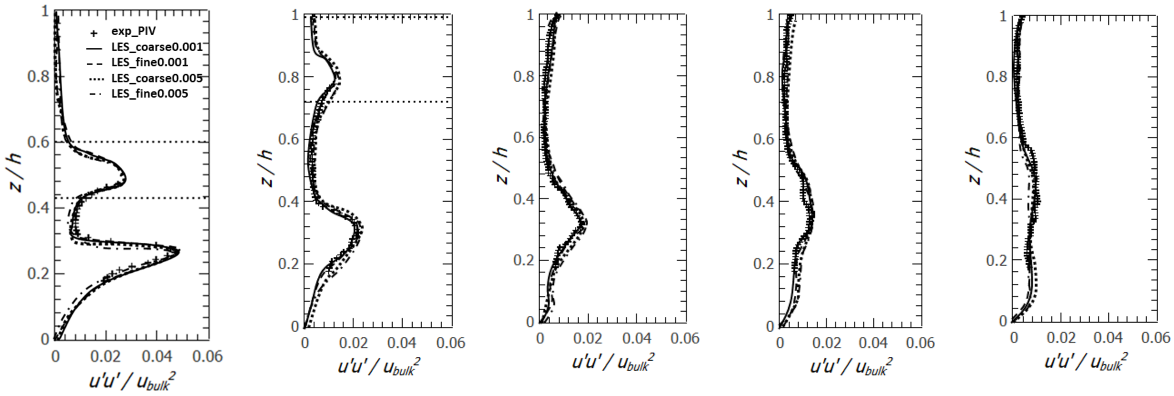

(a) x/s=1 (b) x/s=2 (c) x/s=3 (d) x/s=4 (e) x/s=5

Figure 5.15: Case2: Vertical profiles of normalized horizontal normal stress along the centerlinbe of the domain.

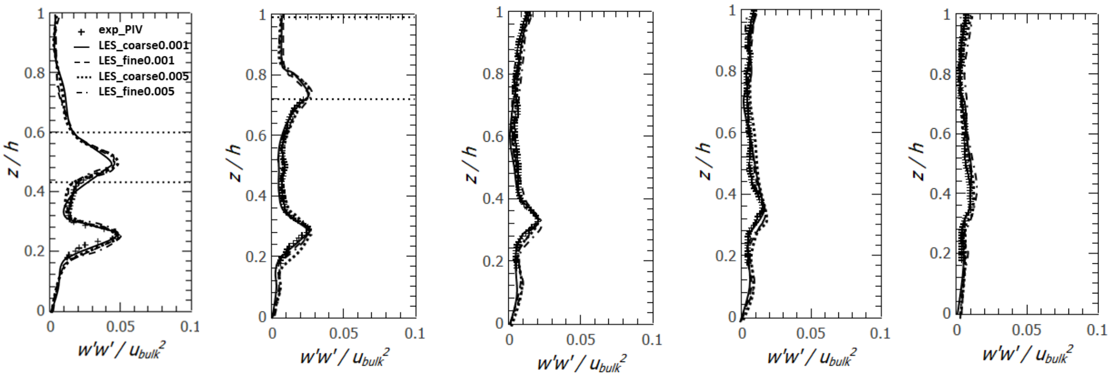

(a) x/s=1 (b) x/s=2 (c) x/s=3 (d) x/s=4 (e) x/s=5

Figure 5.16: Case2: Vertical profiles of normalized vertical normal stress along the centerline of the domain.

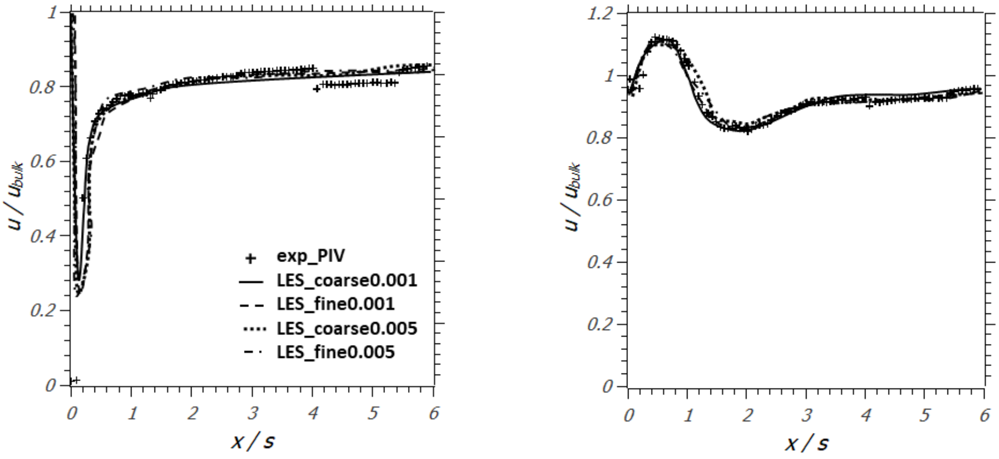

(a) z/h=1 (b) z/h=2

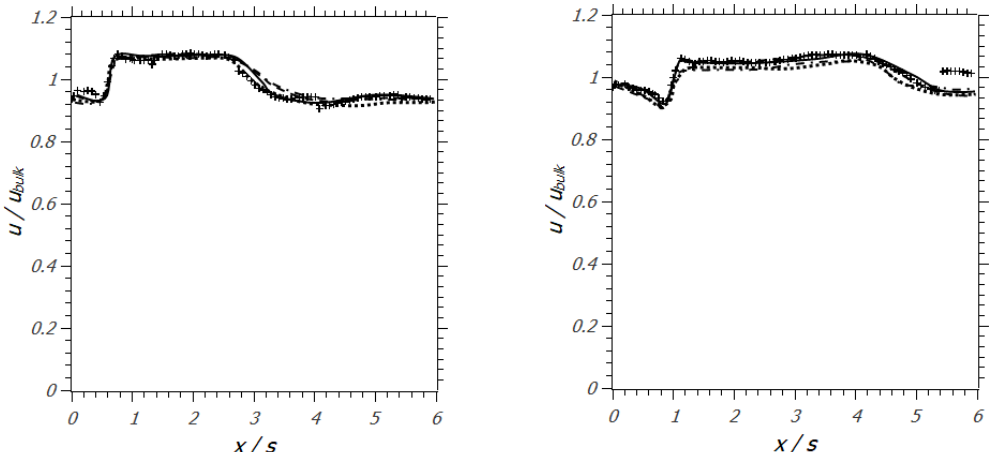

(c) z/h=3 (d) z/h=4

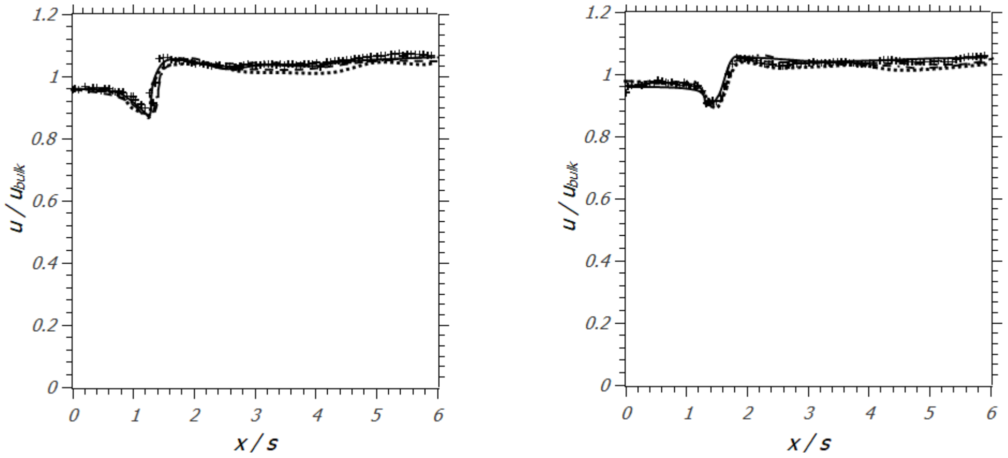

(e) z/h=5 (f) z/h=6

Figure 5.17: Case2: Horizontal profiles of normalized u-velocities along the centerline of the domain.

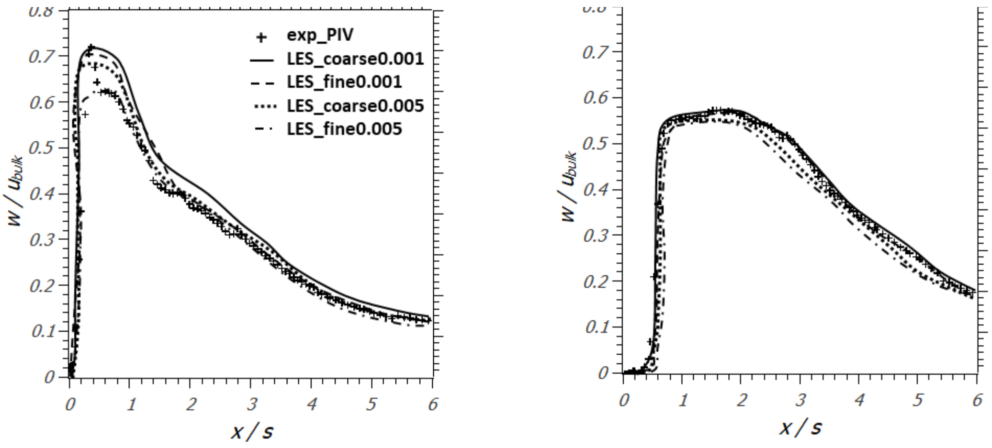

(a) z/h=1 (b) z/h=2

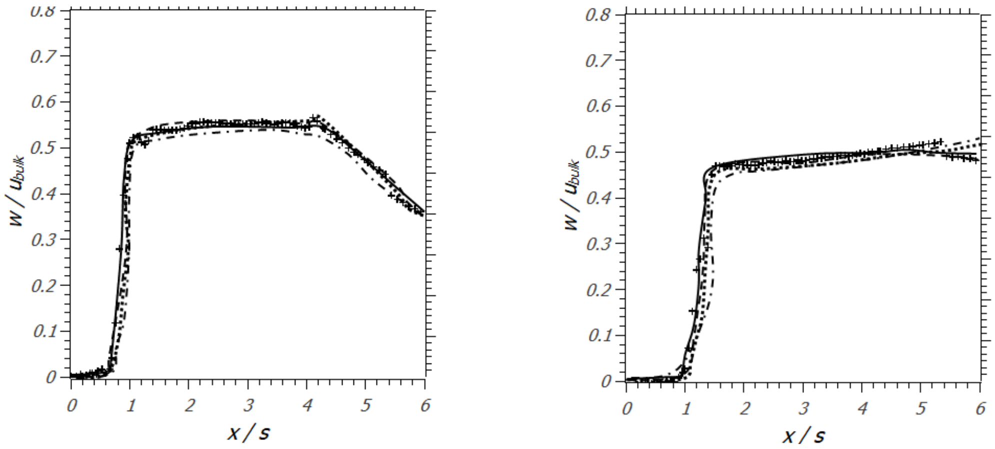

(c) z/h=3 (d) z/h=4

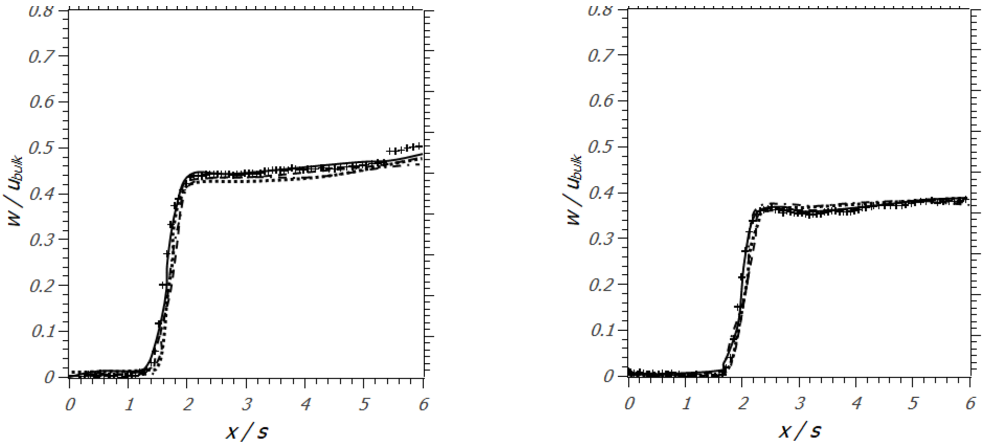

(e) z/h=5 (f) z/h=6

Figure 5.18: Case2: Horizontal profiles of normalized w-velocities along the centerline of the domain.

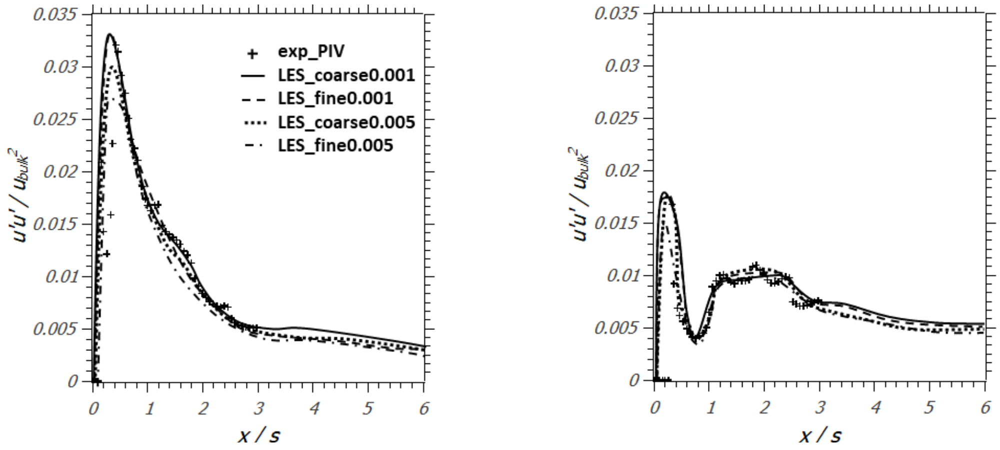

(a) z/h=1 (b) z/h=2

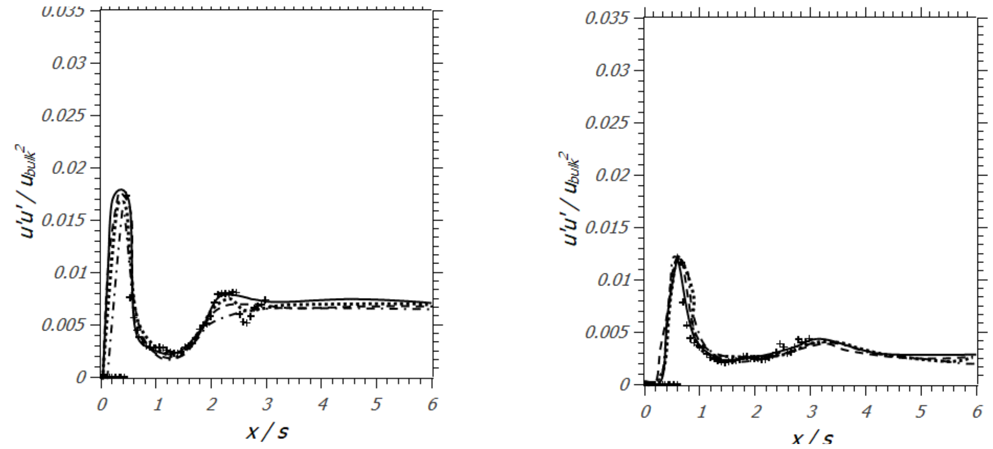

(c) z/h=3 (d) z/h=4

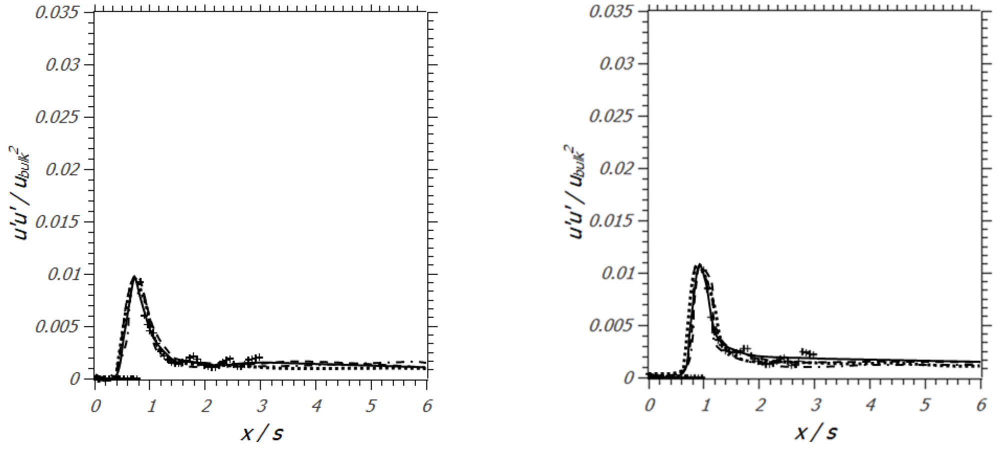

(e) z/h=5 (f) z/h=6

Figure 5.19: Case2: Horizontal profiles of normalized horizontal normal stress along the centerline of the domain.

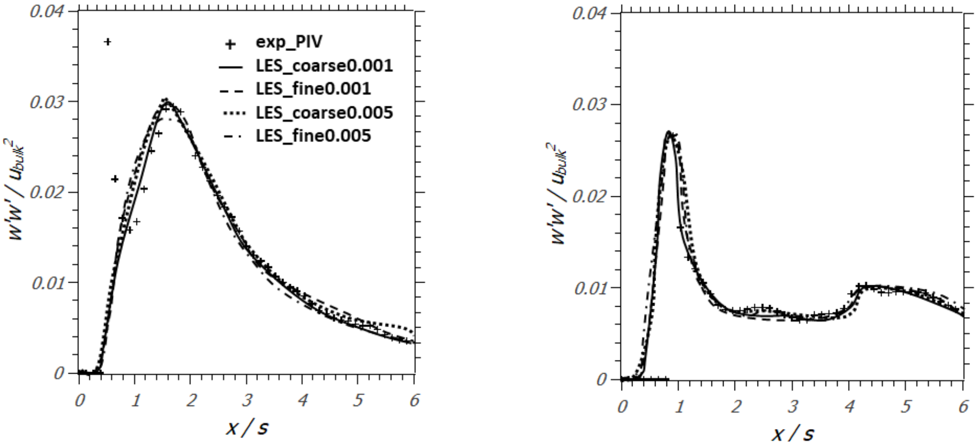

(a) z/h=1 (b) z/h=2

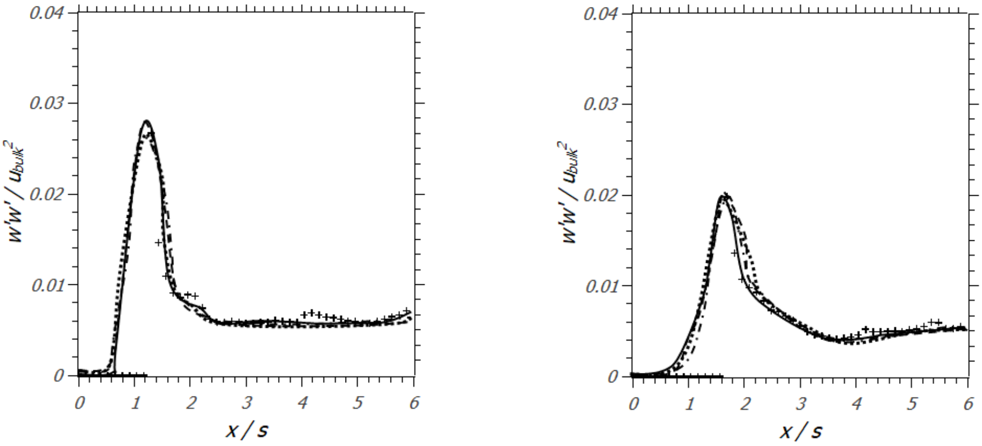

(c) z/h=3 (d) z/h=4

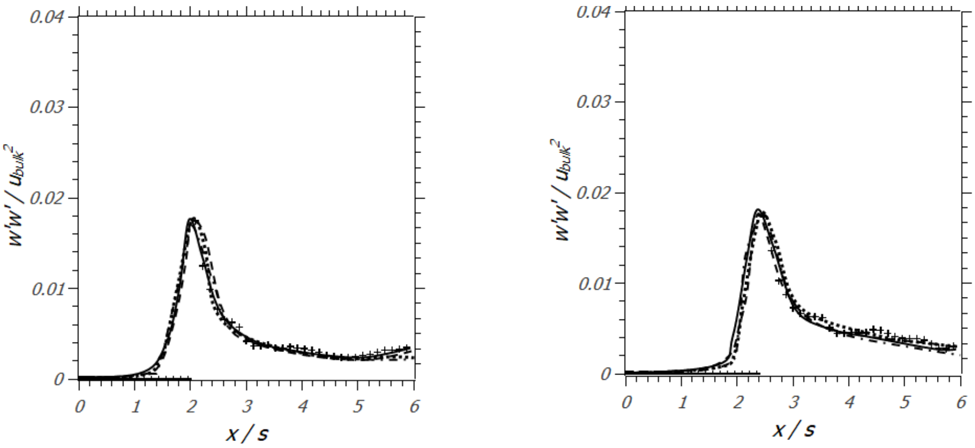

(e) z/h=5 (f) z/h=6

Figure 5.20: Case2: Horizontal profiles of normalized vertical normal stress along the centerline of the domain.

### 5.4.2 Time-averaged flow

Simulated time-averaged horizontal and vertical velocities of the surrounding fluid of the bubble column, normalized with the $u_{bulk}$, are shown in Figures 5.21 and 5.22 for the three different cases (Table 5.1) examined in Chapter 5.4.1. The bubbles are also pictured in Figure 5.21 as small spheres, whereas the area of the bubble plume is defined by two black lines. In Figures 5.22-5.24 only the black lines are used to define the bubble column.

The continuous phase (ambient flow) is continuously streamed towards the bubble column, where the bubbles transmit kinematic momentum flux to the flow. Once the ambient flow passes through the bubble column, it carries downstream the momentum gained from the bubble column. This process leads to a vertical motion downstream the bubble column. The induced motion is more apparent in cases with weaker crossflow (case1), hence showing longer contact time between the bubbles and the ambient fluid. As the crossflow gets stronger vertical momentum spreads over a larger area (cases 2 and 3). In weak crossflow, the bubble column in Case1 Fig. 5.24(a) and 5.25(a) acts as an obstacle generating greater velocity gradients. Some entrained fluid is captured within the bubble plume throughout the entire water depth, resulting separated plume; whereas in a stronger crossflow (cases 2 and 3), the entrained fluid separates from the bubbles and the separated fluid rises independently in the far field (Figures 5.21(b) and 5.21(c)).

As the plume rises towards the water surface it bends in the direction of flow, deflected by the crossflow and thus, horizontal and vertical velocity gradients are reduced. There is an area at the water surface where entrained fluid that contains vertical momentum is deflected into horizontal momentum, even leading to negative horizontal velocity (Fig. 5.21(a)), i.e. fluid that is being convected upstream and which creates recirculation near the surface upstream the plume.

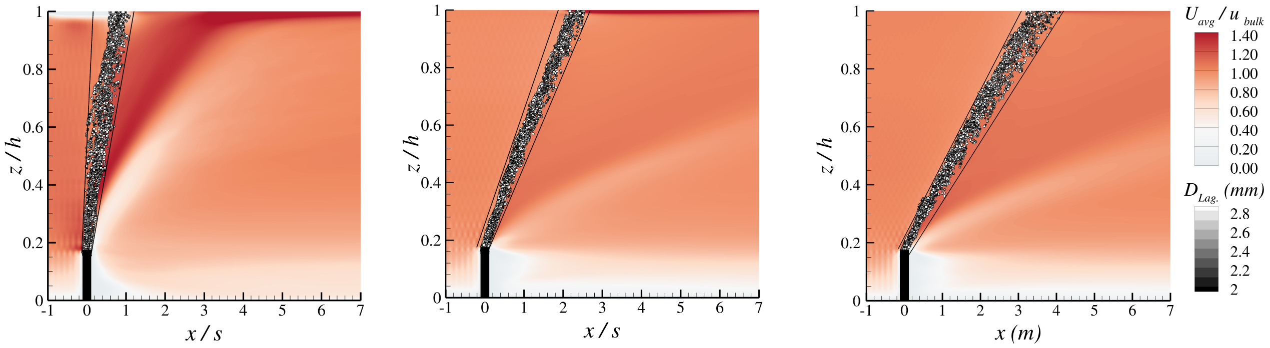

(a) Case1 (b) Case2 (c) Case3

Figure 5.21: Normalized time-averaged u-velocity contours for the three cases with crossflow velocities a) 0.04m/sec, b) 0.10m/sec and c) 0.15m/sec.

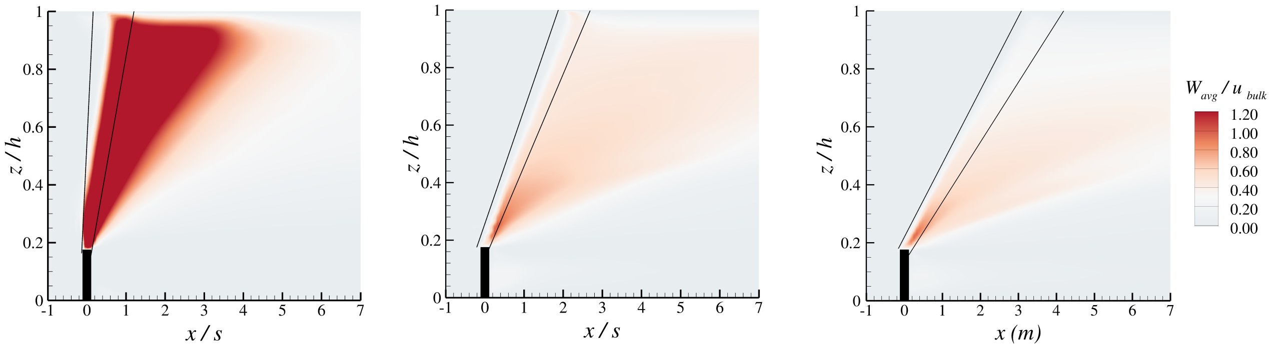

(a) Case1 (b) Case2 (c) Case3

Figure 5.22: Normalized time-averaged w-velocity contours for the three cases with crossflow velocities a) 0.04m/sec, b) 0.10m/sec and c) 0.15m/sec.

The normalized time-averaged w-velocity contour at the centerline of the channel and the vertical lines denoting the bubble column (Fig. 5.22) are in good agreement with the experimental time-averaged w-velocity contours in Fig. (5.23).

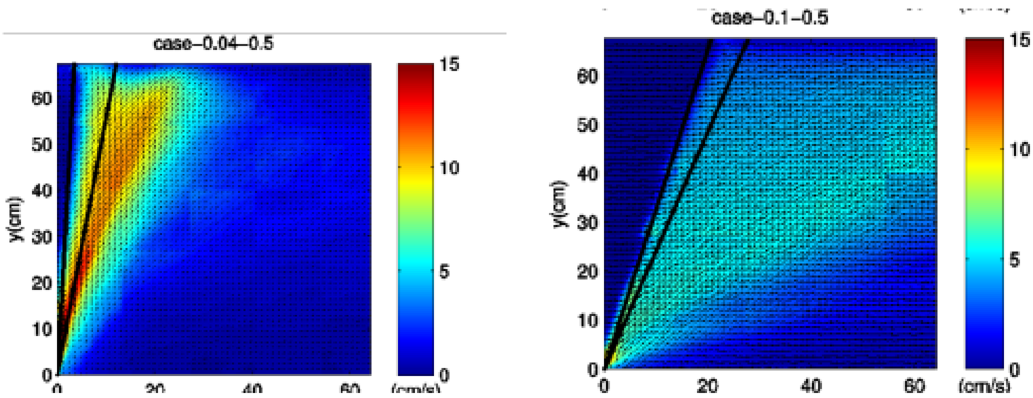

(a) Case1-experimental (b) Case2-experimental

Figure 5.23: Time-averaged w-velocity contours for the two experimental cases with crossflow velocities a) 0.04m/sec, b) 0.10m/sec.

Figure 5.24 shows the turbulence intensity contours of the three different cases examined in this section. Turbulence intensity is defined according to Panton (1984) as:

$$I = \frac{\sqrt{\frac{1}{3}(\overline{u'u'} + \overline{v'v'} + \overline{w'w'})}}{V_{ref}} \tag{5.1}$$

where $I$ is the overall turbulence intensity and $\overline{u'u'}$, $\overline{v'v'}$, $\overline{w'w'}$ are the $x-$, $y-$ and $z-$ components of the turbulent fluctuations and $V_{ref}$ is the reference mean velocity defined as, $V_{ref} = \sqrt{U_{mean}^2 + V_{mean}^2 + W_{mean}^2}$. where $U_{mean}$, $V_{mean}$ and $W_{mean}$ are the averaged velocities in x, y, and z axes respectively.

It is shown that turbulence intensity decreases with increasing the crossflow, which means that the bubbles are carried away by the crossflow. For the higher crossflow cases, i.e. Case2 and Case3, the regions of highest turbulence intensity correlate with the edges of upward rising separated fluid in the wake, indicating that the velocity shear between the bottom of the separated plume and the ambient exhibit the greatest turbulence intensities. High turbulence intensity is also noticed at the surface, where bubbles are gathered, at the bottom of the channel, due to the boundary effect, and around the diffuser, due to the separation caused by the diffuser. For Case 1, large turbulence is also found upstream of the plume, where the shear layer of the plume interacts with the oncoming flow.

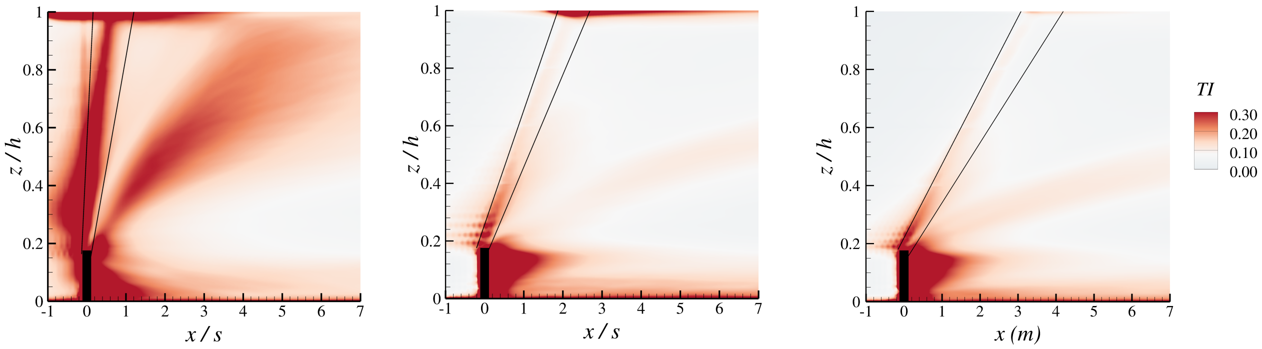

(a) Case1 (b) Case2 (c) Case3

Figure 5.24: Turbulence intensity contours for the three cases with crossflow velocities a) 0.04m/sec, b) 0.10m/sec and c) 0.15m/sec.

### 5.4.3 Flow structure

The previous section discussed the main features of time-averaged flow separation and recirculation. Of particular interest is the area around the bubble plume which is where the liquid and the gas phase interact.

Figures 5.25(a), 5.27(a) and 5.30(a) present isosurfaces of the Q-criterion, an appropriate tool of visualisation of coherent structures from large-eddy simulations (Rodi et al., 2013). The Q-criterion (Hunt et al., 1988) is defined as:

$$Q = \frac{1}{2}(|\Omega| - |S|) \tag{5.2}$$

where $\Omega$ is the rotation rate and $S$ is the strain rate, defined as follows:

$$|\Omega| = \sum_{i,j=1}^{3}[\frac{1}{2}(\frac{\partial u_i}{\partial x_j} - \frac{\partial u_j}{\partial x_i})]^2 \tag{5.3}$$

$$|S| = \sum_{i,j=1}^{3}[\frac{1}{2}(\frac{\partial u_i}{\partial x_j} + \frac{\partial u_j}{\partial x_i})]^2 \tag{5.4}$$

where $u_i$ and $u_j$ are instantaneous velocity components. Positive isosurfaces of $Q$ isolate areas where the strength of rotation overcomes the strain, thus visualising rotation in the form of vortex tubes. The Q-criterion isosurfaces are colour-coded with the streamwise vorticity $\omega_x$, which measures the rotation intensity around the streamwise $x$ axis. Positive streamwise vorticity (red) corresponds to clockwise rotation while blue represents anti-clockwise motion.

The water flow in the flume is illustrated in Figures 5.25 & 5.26 for Case1, Figures 5.27 & 5.29 for Case2 and Figures 5.30 & 5.31 for Case3. Figures 5.26, 5.29 & 5.31 display streamlines of the time-averaged flow at specific planes of the flume, coloured by the vertical mean velocity for the three cases examined in the paper. These planes are (a) the z-plane at the surface of the channel at $z/h = 1$, (b) the y-plane in the middle of the channel at $y/d = 0.5$ and the x-planes at (c) the diffuser $x = 0$, (d) 0.5m downstream the diffuser, (e) 1.5m downstream the diffuser and (f) 2.5m downstream the diffuser and where negative distances indicate the area upstream the diffuser.

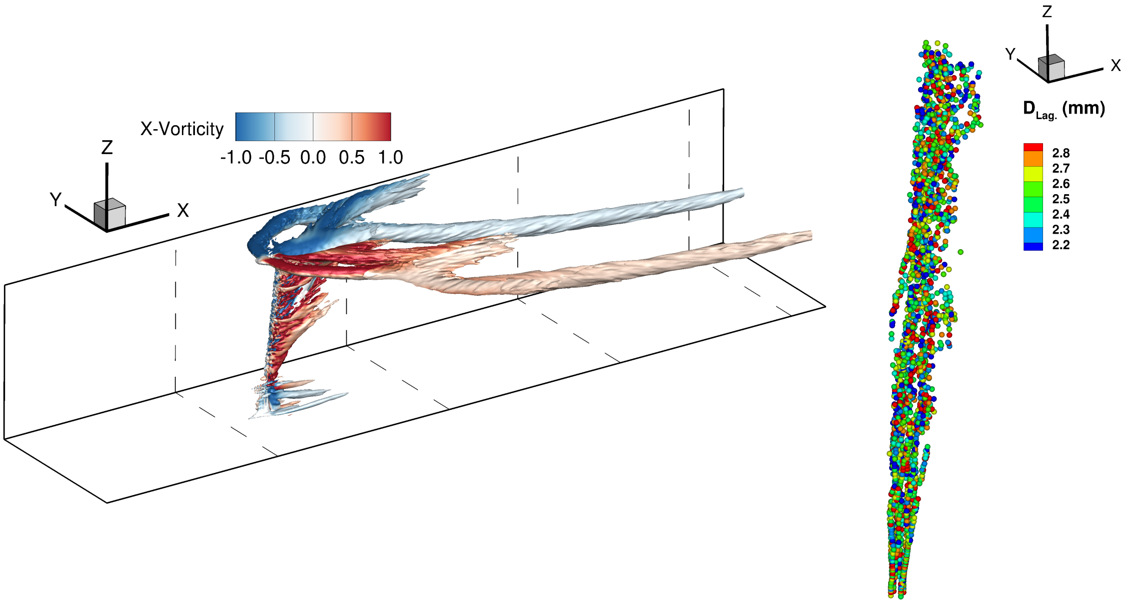

(a) Three-dimensional view of the generation of secondary currents.

(b) Fully developed bubble plume.

Figure 5.25: (a) Three-dimensional view of Q-criterion isosurfaces coloured by the vorticity in x-direction for Case1 and (b) Fully developed plume coloured by the size of the bubbles' diameter.

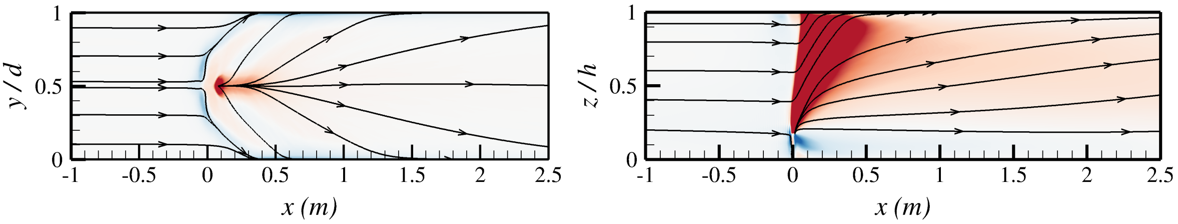

(a) z/h=1 (b) y/d=0.5

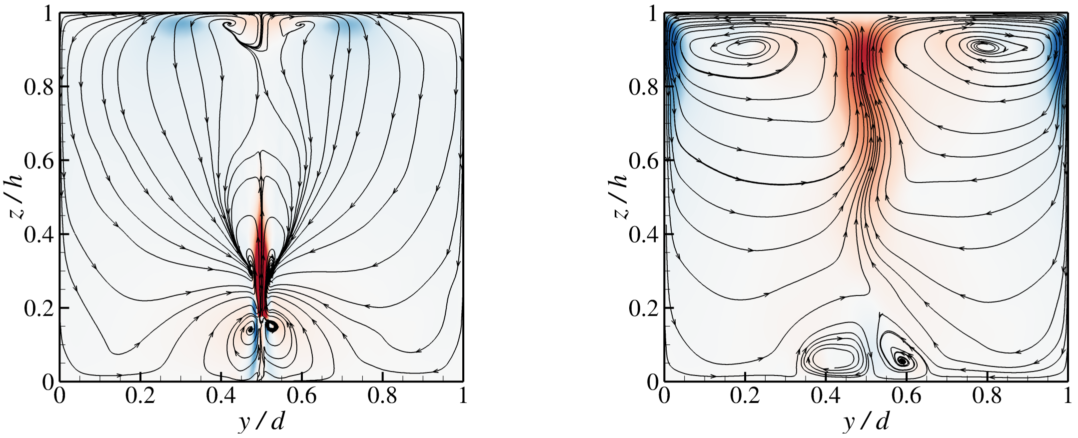

(c) x=0 (d) x=0.5

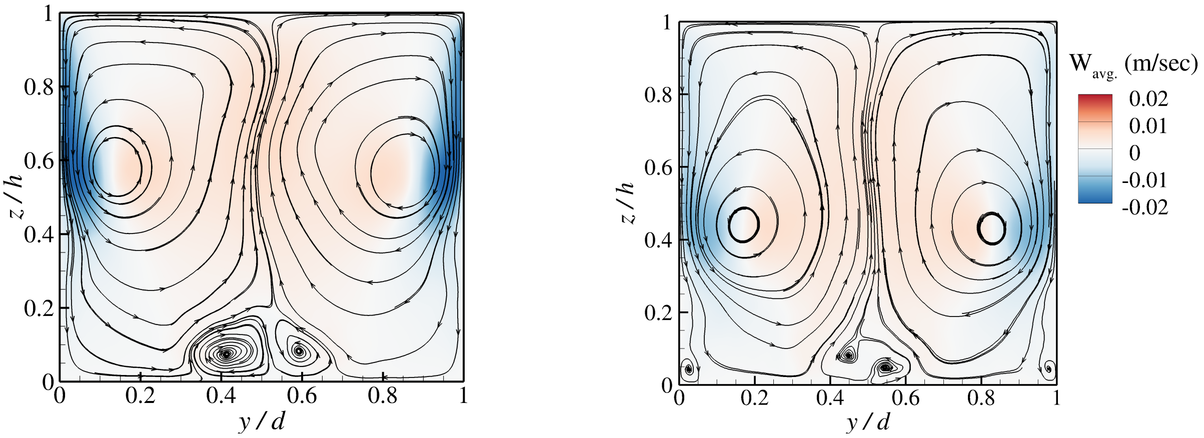

(e) x=1.5 (f) x=2.5

Figure 5.26: Time-averaged w-velocity contours and streamlines on (a) a horizontal plane close to the surface, (b) a vertical plane at the middle of the flume and (c)-(f) streamwise planes for Case1.

In all cases, the bubble plume triggers a secondary motion dominated by two counter-rotating vortices that develop downstream. In Figures 5.25(a), 5.27(a) & 5.30(a)

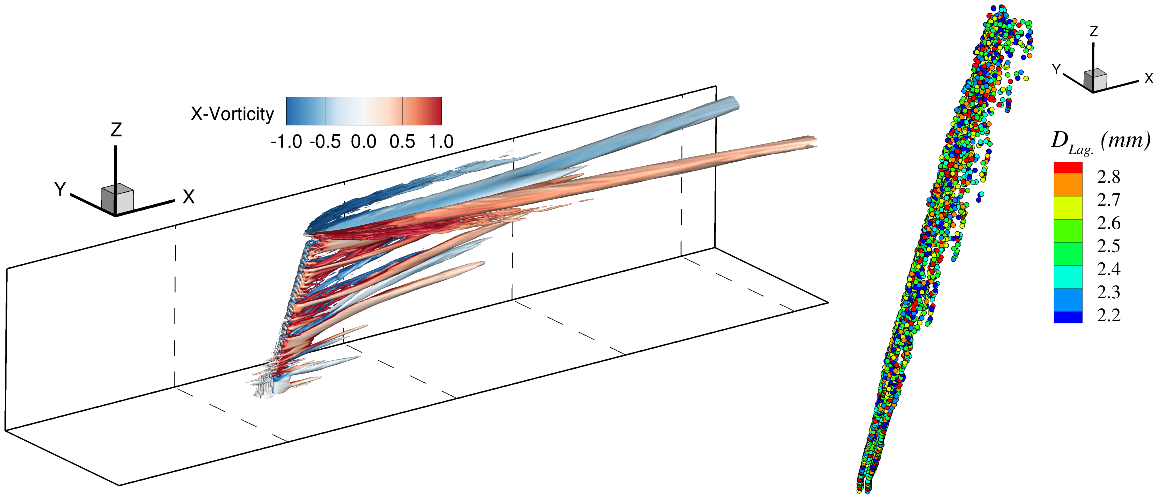

(a) Three-dimensional view of the generation of secondary currents.

(b) Fully developed bubble plume.

Figure 5.27: (a) Three-dimensional view of Q-criterion isosurfaces coloured by the vorticity in x-direction for Case2 and (b) Fully developed plume coloured by the size of the bubbles' diameter.

the isosurfaces reveal the presence of a roller that originates near the water surface upstream of the plume, a result of the negative flow seen in Figure 5.21(a). The roller is blocked by the bubble plume, pushed towards the sidewalls of the flume and it is converted into a pair of elongated counter-rotating streamwise vortices. These vortices are driven by the secondary flow and Figures 5.25(a), 5.27(a) & 5.30(a) illustrate their development throughout the entire length of the plume. Near the bottom of the plume a horseshoe vortex is formed but this vortex is rather weak compared to the vortex structure near the water surface.

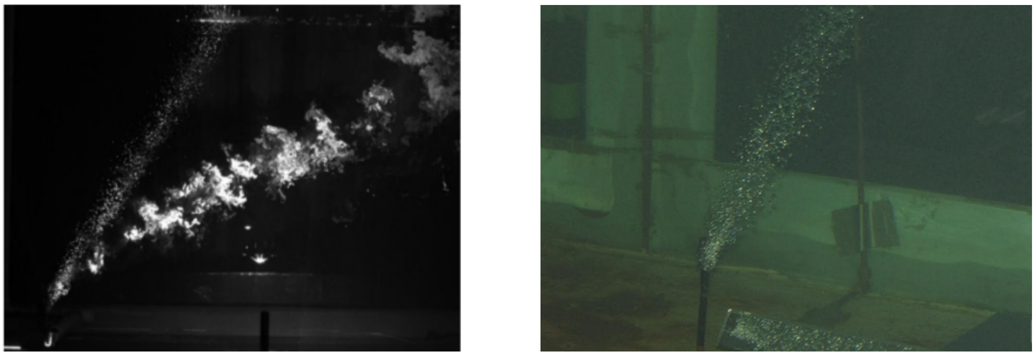
(a) (b)

Figure 5.28: Images of PIV experiments showing the bubble column for 0.10m/s crossflow and 0.5l/min bubble flow rate.

As bubbles move upwards, the crossflow is blocked by the bubble column and vice-versa the crossflow causes deflection to the bubble column downstream. The inclination of bubble plume is higher with stronger crossflows. In Case1 (Fig. 5.25(b)), where the crossflow is 0.04m/sec the bubble column is almost vertical to the flow forming an angle of $9^o$ with the vertical, while in Case2 (Fig. 5.27(b)), with 0.10m/sec crossflow, the bubble column is inclined $20^o$ vertically and in Case3 (Fig. 5.30(b)), with 0.15m/sec crossflow, the bubble column is inclined by $30^o$ from the vertical. While major separation within the bubble column does not occur, a detachment of bubbles with smaller diameter as they reach the flume surface is observed with stronger crossflow. Bubble plume forms a characteristic half moon shape in the streamwise direction, which becomes more obvious as the crossflow goes stronger (case3, Fig. 5.30(b)).

Similar geometry and dispersion to the numerical bubble column in Figure 5.27(b) was observed in the PIV experiments with the experimental bubble column depictured in Figure 5.28.

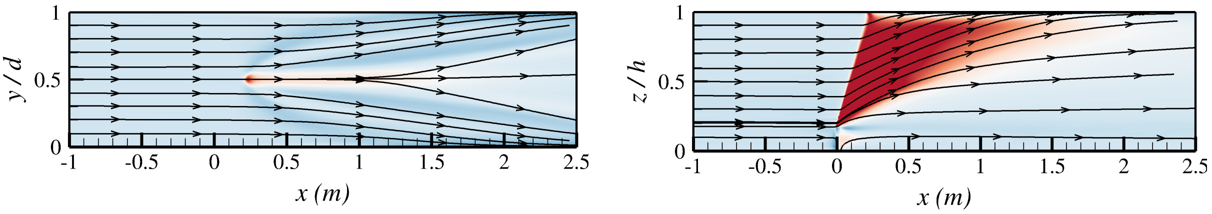

(a) z/h=1 (b) y/d=0.5

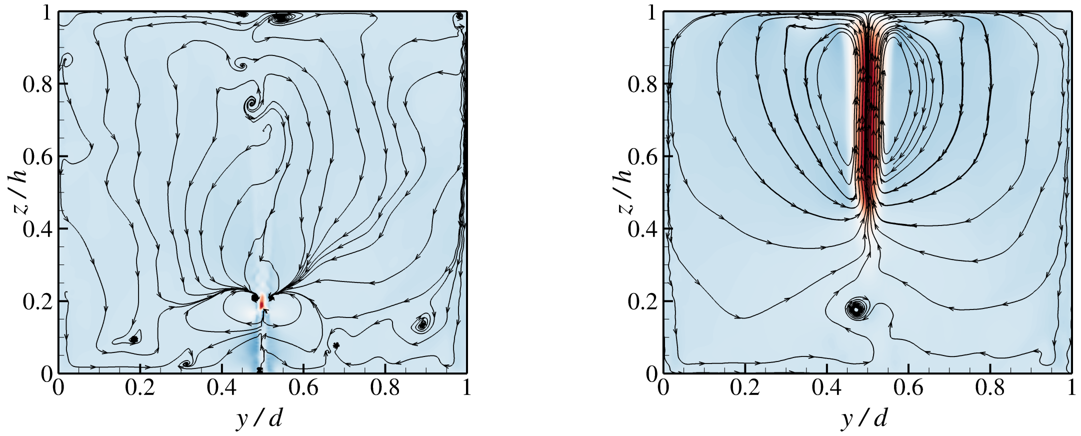

(c) x=0 (d) x=0.5

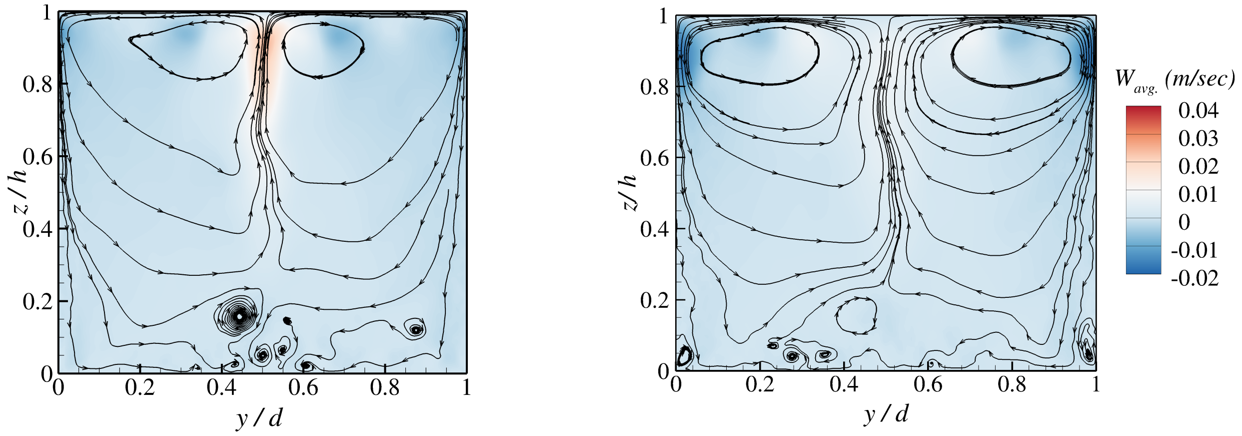

(e) x=1.5 (f) x=2.5

Figure 5.29: Time-averaged w-velocity contours and streamlines on (a) a horizontal plane close to the surface, (b) a vertical plane at the middle of the flume and (c)-(f) streamwise planes for Case2.

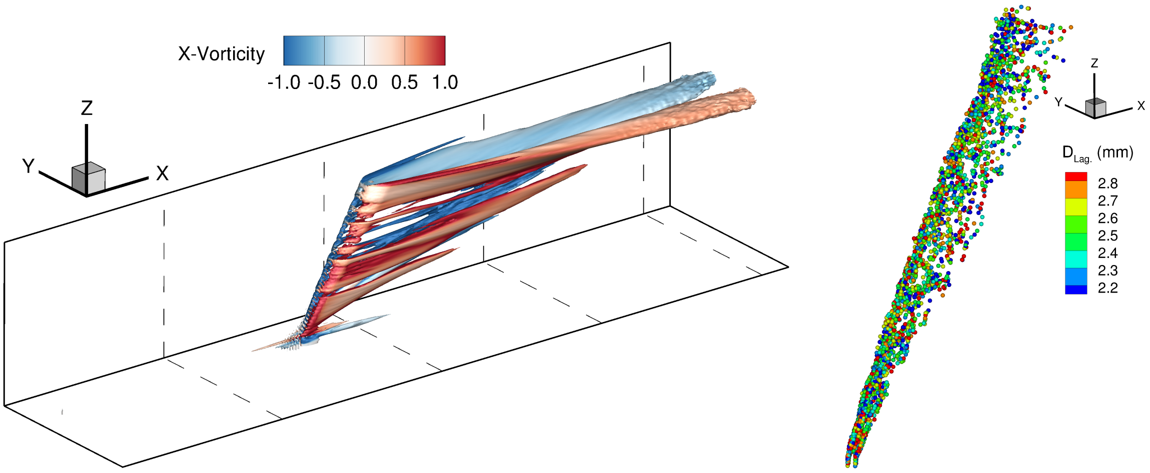

(a) Three-dimensional view of the generation of secondary currents.

(b) Fully developed bubble plume.

Figure 5.30: (a) Three-dimensional view of Q-criterion isosurfaces coloured by the vorticity in x-direction for Case3 and (b) Fully developed plume coloured by the size of the bubbles' diameter.

The cases studied in this chapter show that the background flow is essentially isotropic with some anisotropy created due to the existence of the diffuser structure at the bottom of the domain, which becomes larger by increasing the crossflow. With bubble injection, different degrees of separation between the weak and strong crossflow cause different behavior in the wake region, which is also observed in the experiments.

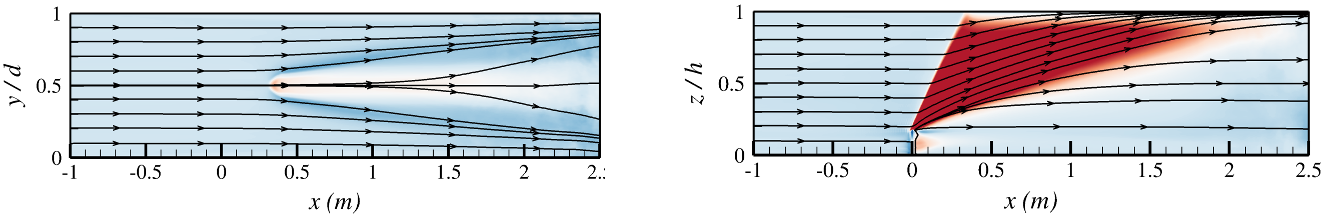

(a) z/h=1 (b) y/d=0.5

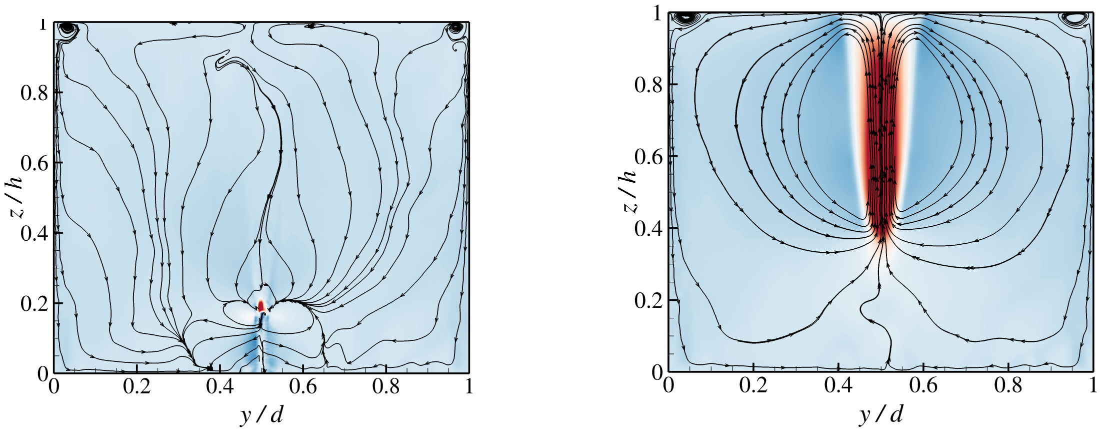

(c) x=0 (d) x=0.5

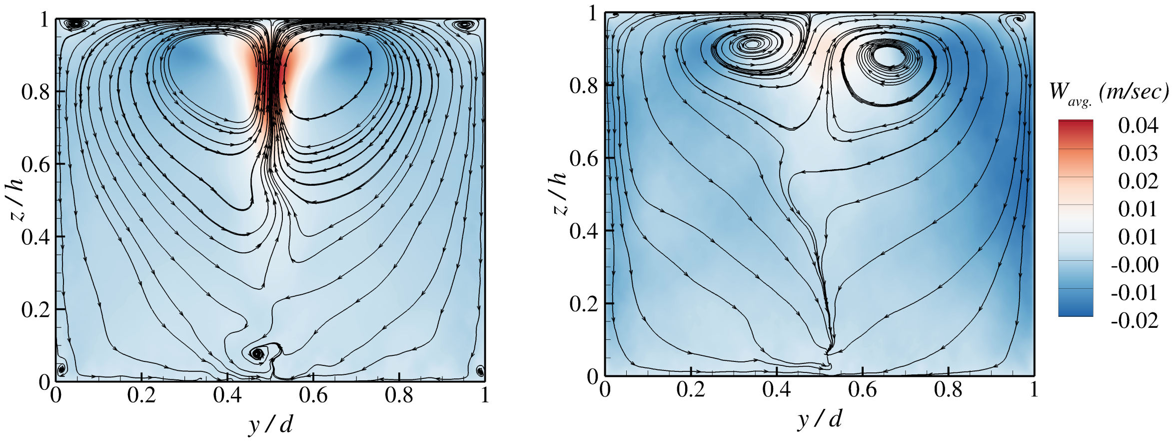

(e) x=1.5 (f) x=2.5

Figure 5.31: Time-averaged w-velocity contours and streamlines on (a) a horizontal plane close to the surface, (b) a vertical plane at the middle of the flume and (c)-(f) streamwise planes for Case3.

In weak crossflows, some entrained fluid stays within the bubble plume from the injection point until the surface (Case1 in Fig. 5.26(a)). In strong crossflows, there is significant separation between the dominant dispersed phase and the entrained fluid. The separated fluid continues to rise in the far field because of the acceleration gained within the bubble column (Socolofsky and Adams, 2002).

In Figures 5.27(a) and 5.30(a), it becomes evident that the cylindrical vortex that is formed close to the free surface becomes smaller with raising crossflow; then it streams towards the sidewalls and converts to a pair of elongated streamwise vortices, similar to case1 in Figure 5.25(a). In case2 and case3 however, the streamwise vortices remain closer to water surface throughout the length of the flume, whilst in case1 (Fig. 5.25) the streamwise vortices start close to the water surface and moving downwards with increasing distance from the bubble column. The isosurfaces reveal the presence of a wake formed by the separated fluid that originates from the height of the diffuser and continues upwards until the middle of the channel.

## 5.5 Conclusions

This study presented numerical simulations of multi-phase plumes and their dynamics in crossflow, using LES for resolving the turbulence for the continuous phase and a EL approach for the dispersed phase.

The code was validated by reproducing two sets of experiments conducted at Texas A&M University. The simulated horizontal and vertical velocities of the ambient flow are overall in a good agreement with the experimental results, with some discrepancies observed within the bubble column. The code underpredicts the horizontal and vertical normal stresses within the bubble plume and just downstream the bubble plume for the case with crossflow of 0.04m/sec and overpredicts the peak of the vertical normal stress for the case with crossflow of 0.10m/sec. This might suggest a limitation of the model to capture the entire spectra of turbulence generated at the bubble scale.

Regarding the different mesh resolutions that were tested, they are both in a very good agreement with the experimental measurements. Discrepancies on the simulated velocities of the two meshes are observed at the bottom of the channel, where there is also lack of experimental data. It is not clear though which one gives a more accurate prediction of the normal stresses.

The analysis of the secondary flow has shown that multi-phase plume behave as single-phase plumes up to a specific height, where the crossflow separates the entrained fluid from the dispersed phase. It has also revealed the formation of a roller upstream the bubble plume that cascades to two strong counter-rotating vortices at the upper half of the channel in the plume's wake and weaker horse-shoe vortices close to the bottom.

The effect of three different crossflows, i.e. 0.04m/sec, 0.10m/sec and 0.15m/sec, was examined on a bubble plume with contant bubble flow rate 0.5l/min. Bubble plume inclination is increasing proportionally with increasing the crossflow. Fully developed bubble plume forms a characteristic half moon shape. Stronger crossflow causes a smaller roller upstream the bubble plume, i.e. the entrained fluid flows through the bubble plume without being blocked.

# Chapter 6

# A Large-Eddy simulation-based Eulerian-Lagrangian approach of bubble plumes dynamics in stratified flow

## 6.1 Introduction

Stratified fluid environments are observed in numerous environmental problems, mainly large water bodies, such as lakes, reservoirs and the sea. Strong bubble-induced buoyancy fluxes can generate turbulent plumes that provide significant mixing for stratified fluid environments. For example, bubble plumes have been widely used for reservoir destratification and aeration systems (e.g. Wuest et al., 1992; Asaeda and Imberger, 1993; Lemckert and Imberger, 1993; Schladow, 1993). Bubble plumes have also been used to mix hot and toxic fluids in chemical engineering applications (Leitch and Daines, 1989). The interaction of bubble plume - continuous phase is significantly different from the interaction of bubble plume in crossflow or stagnant ambient without stratification. Stratification can cause fluid in the plume to peel off and form an annular plume that falls down along the outside of the inner plume, similar to a fountain. This peeling process and associated downward flow in the outer plume can lead to trapping of entrained fluid and weakly buoyant particles within the water layer. One such example with significant environmental impact is a multiphase hydrocarbon plume from underwater accidental oil well blow-outs (Camilli et al., 2010). The underwater trapping increases the opportunity for bio-degradation of the oil droplets, but also significantly increases the difficulty in estimating the total oil leak rate based on the surface plume signal as well as predicting the oil plume surfacing location.

Experimental studies on bubble plumes in stratified flows provide valuable data for understanding the complex interactions between buoyant plumes and the surrounding environment. Limited direct measurements of field data can be found in experimental studies, e.g. Johansen, 2003; Camilli et al., 2010; Socolofsky et al., 2011; Weber et al., 2012. On the same note, laboratory experiments in water tanks under controlled stratification conditions have played a vital role in understanding complex plume flow physics. Asaeda and Imberger (1993) observed various representative types of bubble plume structure and correlated plume behaviour with several key plume parameters using shadowgraph visualization of coloured dyes, and more recently Richards et al. (2014). Socolofsky (2001), Socolofsky and Adams (2003) and Socolofsky and Adams (2005) performed a series of laser-induced fluorescence (LIF) measurements for buoyant plumes driven by air bubbles or oil droplets, as well as for inverted plumes driven by settling sediments. Seol et al. (2009) performed LIF measurements to study both the instantaneous and the mean plume structures. Obtaining quantitative velocity information is very challenging in the laboratory due to the difficulty in controlling the bubble size in salt stratification and the complexity of matching the index of refraction throughout the ambient stratification.

Besides experimental studies, there is a number of numerical studies that have developed one-dimensional integral plume models as a tool for predicting mean plume dynamics in stratification (e.g. McDougall, 1978; Milgram, 1983; Wuest et al., 1992; Asaeda and Imberger, 1993; Crounse et al., 2007; Socolofsky et al., 2008). Integral plume models usually assume a self-similar cross-plume variation (e.g. top hat or Gaussian) for plume variables (Davidson, 1986). Even though the computational cost of calculating the mean plume characteristics with integral models is significantly reduced, there is a lack of accuracy. By performing cross-plume integration with the self-similarity assumption, the three-dimensional conservation laws are reduced to a set of coupled one-dimensional ordinary differential equations. Associated with the reduction of dimension, additional closures are required to model the turbulent entrainment fluxes between the inner and outer plumes as well as the peeling flux from the inner plume at the origin of the outer plume. These fluxes are usually parameterized based on the primary variables of the integral model, with model coefficients that usually require calibration based on data from experimental studies on single-phase plumes and/or multi-phase plumes in stratification (e.g. Morton et al., 1956; Papanicolaou and List, 1988; Asaeda and Imberger, 1993; Wang and Law, 2002; Carazzo et al., 2006).

In order to capture the three-dimensional structures of plumes, more advanced computational techniques are employed. Computational models based on Reynolds-averaged Navier–Stokes (RANS) equations have been developed and widely used in chemical engineering applications. RANS models rely on different closures to parameterize turbulent transport (e.g. Becker et al., 1994; Sokolichin and Eigenberger, 1994; Pfleger and Becker, 2001; Zhang et al., 2006; Tabib et al., 2008). LES has been used to simulate multiphase plumes in several recent studies (e.g. Deen et al., 2001; Niceno et al., 2008; Dhotre et al., 2013; Tabib et al., 2008; Fabregat et al., 2015). However, LES studies on multi-phase plumes in stratification are very limited to the author's knowledge. Yang et al. (2015) and Yang et al. (2014) developed a hybrid LES model for simulating hydrocarbon plume dispersion in ocean turbulence. Using their LES model, Yang et al. (2015) and Yang et al. (2014) studied the complex dispersion phenomena of oil plumes released into the ocean mixed layer, and investigated the effects of various environmental mixing mechanisms such as shear turbulence, waves and Langmuir circulations.

In this chapter, an EL-LES model (previously validated for bubble plumes in a tank by Fraga et al. (2016)) has been adopted and modified to simulate bubble-driven buoyant plumes in vertically stratified ambient fluid. To validate the model and investigate the essential plume characteristics in a controlled environment, the key simulation parameters are chosen to be similar to those of the laboratory measurements of Socolofsky (2001). In the simulation, a bubble plume is released from a localized source and rises through a stratified fluid column. The strength of the flow stratification is kept the same as in the experiment. Various bubble rise velocities relative to the fluid velocity are considered and their effects on the plume characteristics are studied.

## 6.2 Experimental & Numerical Setup

The model has been previously validated for gas plume in a stagnant homogeneous liquid matrix by Fraga et al. (2016). The model performance is assessed by predicting the dynamics of a set of experiments conducted by Socolofsky (2001) and Socolofsky and Adams (2005).

The experiments were carried out in a glass-walled stratified tank 1.2m square by 2.4m tall. The tank was stratified with salt (NaCl) using the two-tank method (Asaeda and Imberger, 1993). Figure (6.1) presents a schematic of this method, which derives its name from the second tank, used to prepare the salt solution before it is pumped into the experimental tank. Initially, the water in the stirred reactor has a density equal to the desired maximum density of the profile. As the experimental tank is filled, freshwater is added to the stirred reactor, making the density of water pumped into the experimental tank decrease monotonically during filling. A perforated splash plate dissipates the energy of the water as it enters the experimental tank so that a stratification profile develops. Using the two-tank method, any arbitrary stratification profile can be created.

Salinity profiles were recorded using a Head microscale conductivity and temperature (CT) probe and an Ocean Sensors OS300 CT probe, both mounted on a Parker linear actuator with 2.8m of travel, allowing a vertical resolution of less than 1cm. Initial profiles were taken a few minutes before each experiment. Profiles could not be taken during experiments because of internal waves; hence, post-experiment salinity profiles were made 1hr after an experiment when the waves had dispersed.

Rhodamine 6G fluorescent dye (excitation and emission frequencies 480 and 560 nm, respectively) was injected as a passive tracer at the base of the plume at a rate of 0.1mg/s using a collar diffuser. For visualization, laser induced fluorescence (LIF) images were created using a Coherent 6W argon-ion laser (two laser lines at 494 and 515 nm) connected by a fiber optic cable to a cylindrical lens, generating a 1.5cm

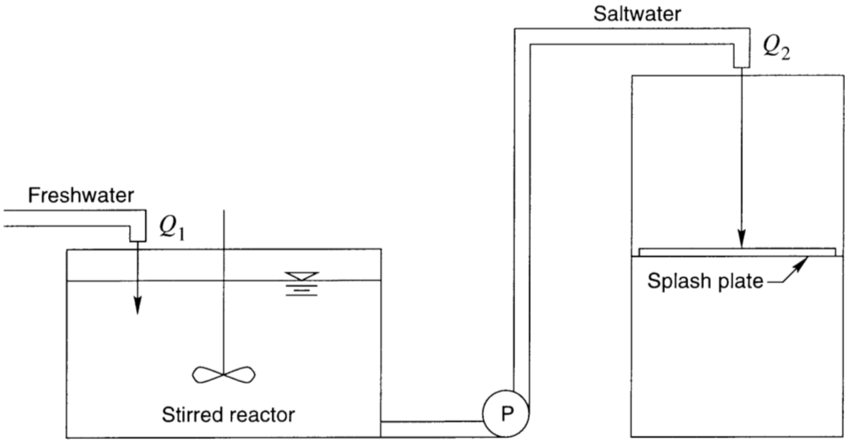

Figure 6.1: Schemantic of the two-tank stratification method

thick light sheet through the centerline of the plume. Using an optical filter that blocks light with a wavelength less than 530nm, laser light scattered by the bubbles could be removed, yielding images of the fluorescing dye only; removing the filter provided images of the bubbles.

Plumes were created from air bubbles (dispersed phase density $\rho_b = 0.0014\text{g/cm}^3$), oil droplets (vegetable oil with $\rho_b = 0.930\text{g/cm}^3$ and crude oil from the Gulf of Mexico with $\rho_b = 0.871\text{g/cm}^3$), and glass beads (creating an inverted plume with $\rho_b = 2.50\text{g/cm}^3$). For the air experiments two diffusers were used, a Coral Life limewood saltwater aquarium airstone (mean bubble diameter of 550$\mu$m) and slip velocity $u_s = 7.2\text{cm/s}$) and a standard composite aquarium airstone (mean bubble diameter of 2mm and $u_s = 23\text{cm/s}$). Both oils were injected through a 0.7mm diameter spray nozzle ($u_s = 10\text{cm/s}$ for the vegetable oil and $u_s$ ranged from $O(1)$mm/s to 10cm/s with the bulk of the oil rising at 8cm/s for the crude oil). Steady state was achieved in the experiments on the order of 2-3 times the travel time for the bubbles to reach the top of the tank (at most 1min for air and glass experiments). The steady state was maintained (trap and peel heights remained constant and the intrusion layers did not reach the tank walls) for between 20min and 30min on average. The experiments were run on average for 5min to achieve sufficient mixing, but to avoid boundary effects of the tank. More details for the experiments can be found in Socolofsky (2001) and Socolofsky and Adams (2005).

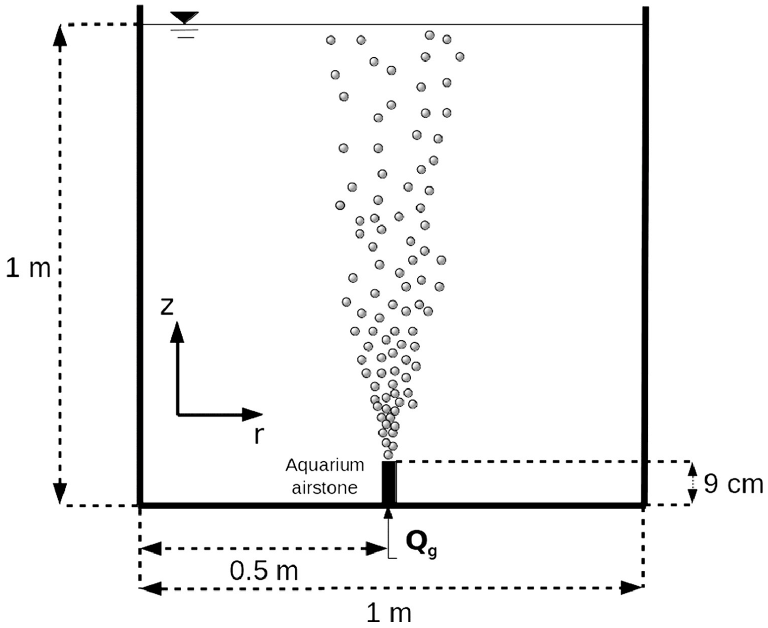

Figure 6.2: Schemantic of the numerical setup

Table 6.1 summarizes the main characteristics of the three cases reported in this study. In all cases the plumes are created from air bubbles with mean bubble diameter of 2mm, as per the experiments.

| Type | Experiment ID | $u_{slip}$ (m/sec) | $Q_b$ ($m^3/s$; $10^{-5}$) | $B$ ($m^4/s^3$; $10^{-5}$) | $N$ ($s^{-1}$) | $U_N$ |
|---|---|---|---|---|---|---|
| T1* | T04 | 0.072 | 0.67 | 6.63 | 0.36 | 1.03 |
| T2 | Shad1 | 0.233 | 6.72 | 65.86 | 0.25 | 2.06 |
| T3 | g50a | 0.233 | 6.83 | 6.7 | 0.25 | 3.64 |

Table 6.1: Flow characteristics of the three cases.

The numerical simulations are carried out under analogous conditions to the experiments. A sketch of the numerical setup is given in Figure 6.2. Boundary conditions for the fluid phase include the use of no-slip boundary condition at all solid walls and a free slip condition at the water surface. To limit the influence of the side boundaries and provide sufficient horizontal space for the intrusion layer to expand during the simulation, the numerical domain is chosen to be twice as wide as the experimental tank, i.e. 2.4m square by 4.8m tall.

Three different uniformly spaced grids are employed for the simulations. The three mesh resolutions are $\Delta x = 6.25$mm, $\Delta x = 4$mm and $\Delta x = 3.125$mm, yielding s total number of gridpoints of 14Mio, 54Mio and 113Mio, respectively. The time step for all simulations is 0.001sec and the simulation time is 600,000 iterations to allow for model on average. The averaging of the velocities and stresses started after 200,000 iterations.

## 6.3 Results

### 6.3.1 Model validation

A quantitative evaluation of the code's performance is detailed in this section by presenting the results of a series of simulations that have been performed on grids with different resolutions.

Socolofsky and Adams (2005) classified the plumes in three types based on their experimental study; i.e. Type 1*, Type 2 and Type 3 (Fig. 6.3(a)). Type 1* plumes have no subsurface intrusions; Type 2 plumes have distinct, steady subsurface intrusions and Type 3 plumes have irregular, unsteady subsurface intrusions. Moreover, characteristics of the plumes are defined, such as the intrusion level or trap height $h_T$ and the peel height $h_P$ (Fig. 6.3(b)).

Fig. 6.4(a) shows the correlation of the non-dimensional plume trap height $h_T/l_c$ (referred here as the trap height) with the non-dimensional slip velocity $U_N$ for the three cases studied in this chapter. Fig. 6.4(b) shows the non-dimensional plume peel height $h_P/l_c$ (referred here as the peel height) as a function of $U_N$. The non-dimensional slip velocity (Eq. 6.1) is proportional to the slip velocity $u_s$ normalized by the entrained plume fluid velocity at the characteristic length $l_c$ (Eq. 6.2):

$$U_N = \frac{u_s}{(BN)^{(1/4)}} \tag{6.1}$$

$$l_c = (\frac{B}{N^3})^{(1/4)} \tag{6.2}$$

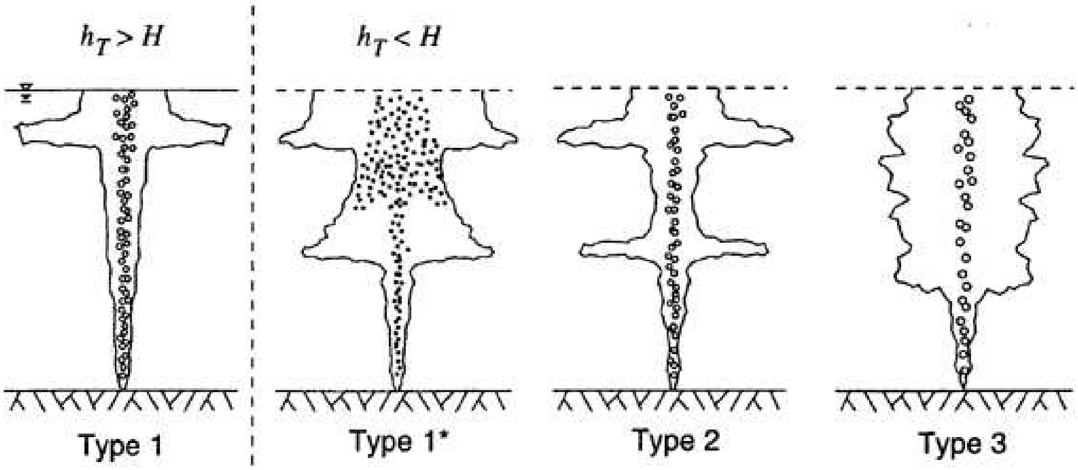

(a) Schemantic of multiphase plume type classification in stratification

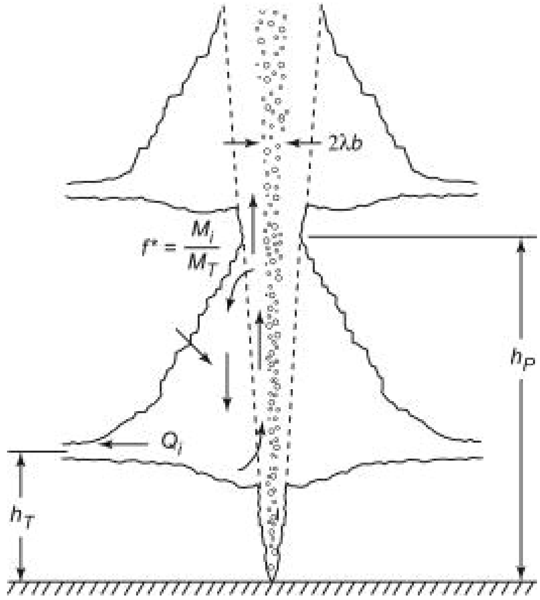

(b) Schemantic of trap height $h_T$ and peel height $h_P$

Figure 6.3: Schemantic of multiphase plume types and characteristics from Socolofsky and Adams, 2005.

where N is the buoyancy frequency:

$$N^2 = -\frac{g}{\rho}\frac{\partial \rho}{\partial z} \tag{6.3}$$

and B is the kinematic buoyancy flux of the dispersed phase, defined as:

$$B = \rho Q \frac{\rho - \rho_b}{\rho} \tag{6.4}$$

The trend for the peel height is similar to that for the trap height. Closed symbols are numerical results and open symbols are experimental results. The agreement between LES simulations and experiments is good. LES simulations with medium mesh (red symbols) and fine mesh (grey symbols) are in closer agreement to the experimental results for trap height and peel height (Figure 6.4).

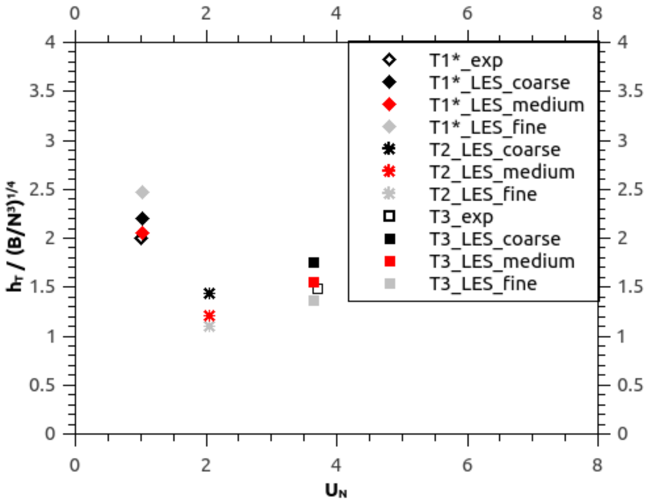

(a) Trap height $h_T$ comparison of experimental data and LES simulations

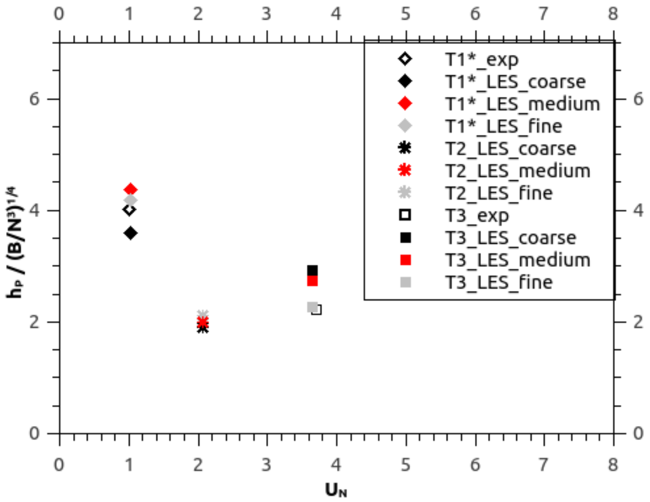

(b) Peel height $h_P$ comparison of experimental data and LES simulations

Figure 6.4: Correlation of plume trap height (a) and plume peel height (b) to $U_N$. Rhombes are Type1* plumes, stars are Type2 plumes and squares are Type3 plumes. Open symbols are experiments; closed symbols are LES simulations.

### 6.3.2 Time-averaged flow

Figures 6.5(b), 6.6(b) and 6.7(b) present contours of the time-averaged vertical velocity in a horizontal plane near the water surface and it shows how the high-momentum fluid from the plume is convected primarily to the corners of the tank. Figures 6.5(a), 6.6(a) and 6.7(a) show contours of the time-averaged vertical velocity in a radial plane and displays the plume and the upper cells of returning flow. The orientation of the axis of recirculation changes from radial for the upper loop of the "eight" to wall-parallel for the lower loop. Whilst the plume is radially symmetric about the centreline of the tank, the tank itself is not and hence the distance from the plume to the wall is maximal in the diagonal direction. This means that the fluid has to fill the low momentum in corners and hence it flows down faster in the corners of the tank thereby creating an imbalance of momentum in the horizontal plane.

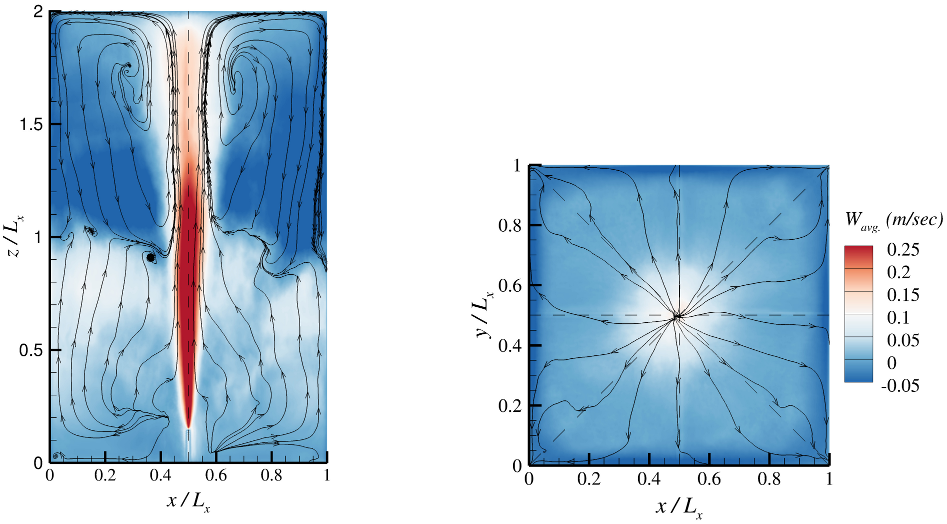

(a) $y/L_x$=0.5

(b) $z/L_x$=0.96

Figure 6.5: Time-averaged w-velocity contours and streamlines at heights (a) $y/L_x$=0.5, (b) $z/L_x$=0.96 for Type 1*.

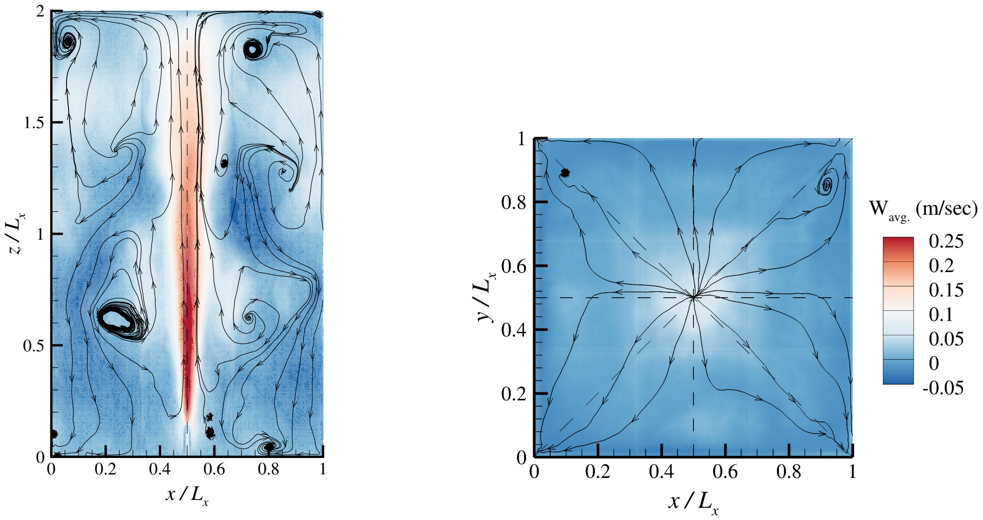

(a) $y/L_x$=0.5
(b) $z/L_x$=0.96

Figure 6.6: Time-averaged w-velocity contours and streamlines at heights (a) $y/L_x$=0.5, (b) $z/L_x$=0.96 for Type 2.

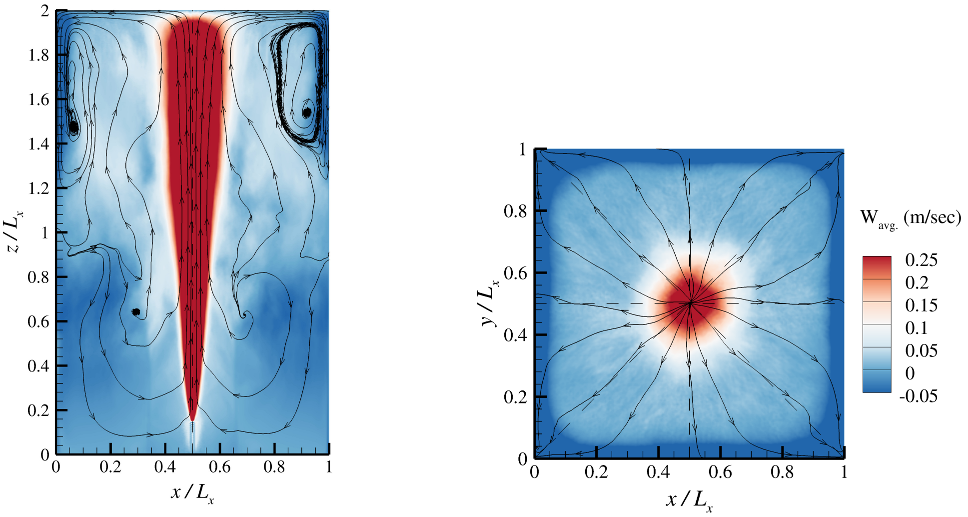

(a) $y/L_x$=0.5
(b) $z/L_x$=0.96

Figure 6.7: Time-averaged w-velocity contours and streamlines at heights (a) $y/L_x$=0.5, (b) $z/L_x$=0.96 for Type 2.

### 6.3.3 Flow structure

The water flow in the tank is illustrated in Figure 6.8 and Figure 6.9. In Fig. 6.8 the streamlines of the time-averaged flow coloured with the vertical velocity are presented in half of the tank (including half of the bubble plume). The hydrodynamic elements that are featured depend on the type of the plume and are as follows:

For Type 1* plumes:

As bubbles move upwards fluid is entrained creating a high-momentum vertical fluid flow towards the water surface. However, because the bubble motion is weak compared to the detraining eddy motion, the first peel disperses the bubble core horizontally, with some bubbles leaving the inner core. A distinct detrainment zone and intrusion layer with Type 2 characteristics is observed for the first peel. As bubbles rise, they also entrain some ambient fluid and carry it upward into the secondary plume. The secondary plume that form above the first peel has a more distributed inner bubble core. As the bubble plume continues to rise, it peels erratically, and the plume peel behaviour exhibits Type 3 characteristics, continuous and overlapping peels. The weak plume also swings back and forth as eddies detrain from side to side.

Once the fluid reaches the water surface it spreads laterally towards the walls before it moves back down, thereby creating a large recirculation in the radial plane that dominates the top half of the tank.

The momentum imbalance leads to a vortex/cell in a plane parallel to the walls in the lower half of the tank. The twisted double-vortex structure is similar to a number eight shape with the two loops. The upper vortex is larger and exhibits higher velocity magnitudes than the lower one.

A snapshot of the plume-fluid dynamics is provided in Fig. 6.9(a) which depicts isosurfaces of the Q-criterion, an appropriate tool to visualize coherent structures from large-eddy simulations (Rodi et al., 2013). The isosurfaces are color-coded with the averaged streamwise (vertical) velocity. Coherent structures in the form of horsehoe vortices are visible at the edge of the plume. The vortices are generated in the shear layer as a result of the large radial gradient of streamwise velocity in the radial direction indicated by the low velocities (blue color) at the edge of the plume. These structures start out as tubes around the plume.

The continuous upwards movement of the plume convects the tubes vertically upwards, but due to the radial velocity gradient they are gradually stretched and result in the form of coherent structures in the middle of the tank height.

Type 2 Plumes

As bubbles move upwards fluid is entrained creating a high-momentum vertical fluid flow towards the water surface. The first peel disperses the bubble core horizontally, with some bubbles leaving the inner core. A distinct detrainment zone and intrusion layer are observed for the first peel. As bubbles rise, they also entrain some ambient fluid and carry it upward into the secondary plume. The secondary plume that form above the first peel has a more distributed inner bubble core. As the bubble plume continues to rise, it peels erratically, and the plume peel behavior exhibits Type 3 characteristics, continuous and overlapping peels.

Once the fluid reaches the water surface it spreads laterally towards the walls before it moves back down, thereby creating a large recirculation in the radial plane that dominates the top half of the tank.

The momentum imbalance leads to a vortex/cell in a plane parallel to the walls in the lower half of the tank. The twisted double-vortex structure is similar to a number eight shape with the two distinct loops, where the lower vortex at the lower half of the tank is bigger and more dominant than in type 1* plumes.

A snapshot of the plume-fluid dynamics is provided in Fig. 6.9(b) which depicts isosurfaces of the Q-criterion. The isosurfaces are color-coded with the averaged streamwise (vertical) velocity. The continuous upwards movement of the plume convects the tubes vertically upwards, but due to the radial velocity gradient they are gradually stretched and result in the form of a horseshoe vortex. The different concentrations of bubbles and velocity fluctuations inside the plume generates two distinct detrainement zones. Intrusions do not overlap because most of the entrained fluid is ejected at each detrainment.

Type 3 Plumes

Comparing Type 3 plume with plumes Type 1* and Type2, the downdraft plume and intrusions appear less distinct and exhibit nearly constant width, indicating a

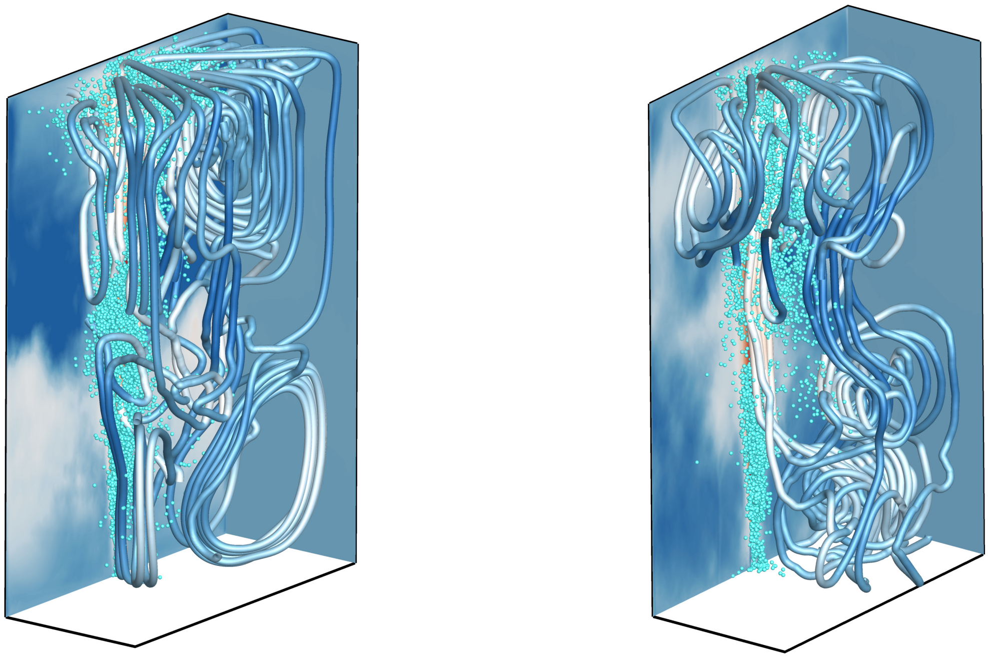

(a) Type1*

(b) Type2

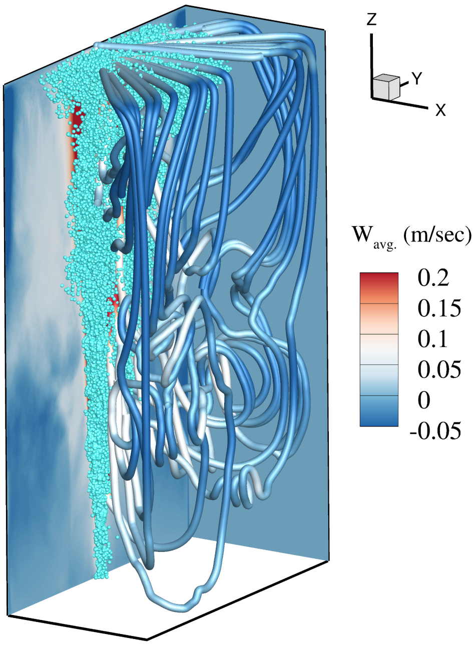

(c) Type3

Figure 6.8: Three-dimensional view of half of the tank including the bubble plume and the streamtracezs defining the secondary circulation for a) Type 1*, b) Type 2 and c) Type 3.

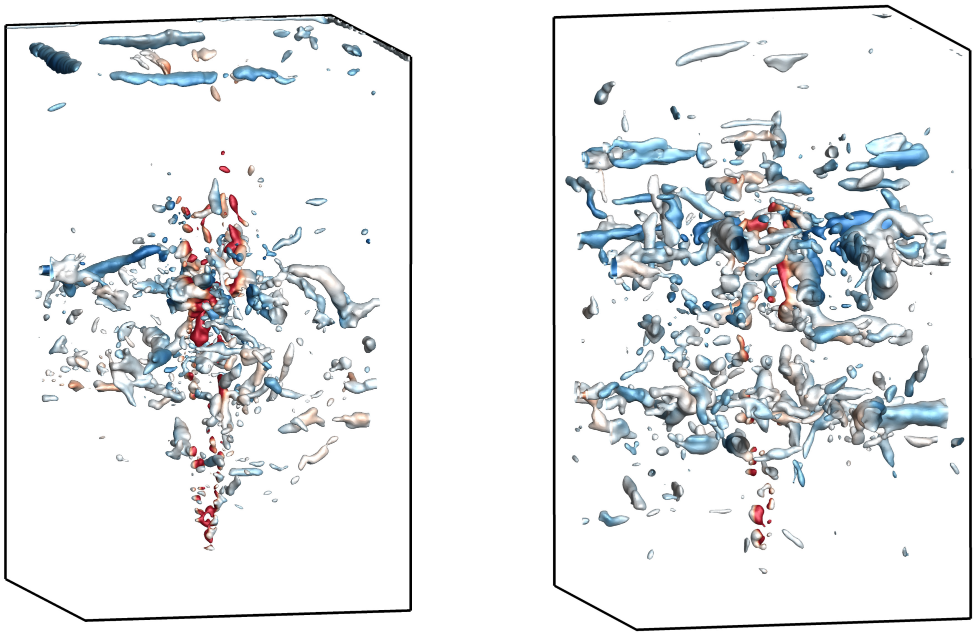

(a) Type1*

(b) Type2

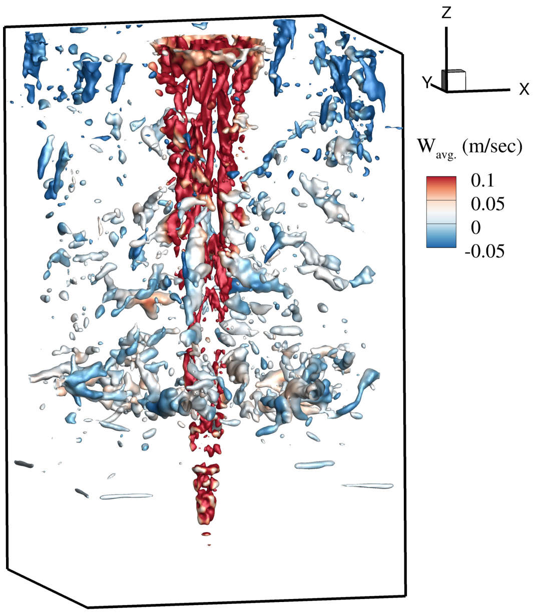

(c) Type3

Figure 6.9: Three-dimensional view of Q-criterion isosurfaces coloured by the averaged vertical velocity for a) Type 1*, b) Type 2 and c) Type 3.

uniform volume flux and exchange between the entrained and ambient fluid over the height of the plume. The bubbles velocity is higher than the detraining eddy motions. The bubbles create mixing by lifting packets of fluid short distances along the inner plume core. The detrained fluid completely shrouds the upward rising plume core. The bubbles remain in a tight core, unaffacted by the detrainment events.

The momentum imbalance leads to a vortex/cell in a plane parallel to the walls in the lower half of the tank. The characteristic double-vortex structure observed in plume Types 1* and 2, similar to a number eight shape with the two loops, is not observed in this type; there is a single vortex structure starting from the bottom of the tank and dominating the entire tank height.

A snapshot of the plume-fluid dynamics is provided in Fig. 6.9(c) which depicts isosurfaces of the Q-criterion. The isosurfaces are color-coded with the averaged streamwise (vertical) velocity.

## 6.4 Conclusions

This chapter presented numerical simulations of multi-phase plumes and their dynamics in vertically stratified flow, using LES for resolving the turbulence for the continuous phase and a EL approach for the dispersed phase.

The code was validated by reproducing three sets of experiments conducted by Socolofsky and Adams (2005) and Socolofsky (2001). There are no experimental data for the velocities of the ambient flow, as they cannot be measured due to the inner wake. Regarding the different mesh resolutions that were tested, they are both in a good agreement with the experimental measurements. The numerical analysis identified three types of plumes in accordance with the experimental findings.

The analysis of the secondary flow, using Q-criterion surfaces and 2D and 3D streamlines, has shown that the different plume types result from variations in peeling efficiency and from the relative magnitude of the initial velocity of the bubbles compared to the fluid velocities of the plume.

# Chapter 7

# Conclusions Outlook

## 7.1 Conclusions

This thesis focuses on the description of multi-phase plume dynamics using an advanced CFD model. A computational approach for turbulent multi-phase plume dynamics in crossflow and stratified ambient has been presented. A refined Large-Eddy Simulations (LES) code is used in conjunction with an Eulerian-Lagrangian (EL) approach which is adopted to represent the dispersed phase. The EL Lagrangian Particle Tracking (LPT) algorithm has been extensively validated, involving three flow cases for bubble plumes in crossflow and three cases for bubble plumes in vertically stratified tank. The predictions of the numerical code have been shown (in Chapter 5 and Chapter 6) to be in reasonably good agreement with the experiments in terms of mean horizontal and vertical velocities and turbulent Reynold stresses.

The effect of crossflow on bubble plume dynamics and vice versa has been carefully investigated and presented in Chapter 5. To the knowledge of author, such computational setup has rarely carried out in the past, less so with such a detailed prediction of the physics around bubble plumes. To achieve a faithful representation of the crossflow in a channel, a turbulent Synthetic Eddy Method has been adopted at the inlet boundary. Experimental data has been used to validate the simulations. A Local Mesh Refinement (LMR) technique was adopted for the fine mesh simulations to speed up the computational time. A good agreement of computed vertical and horizontal profiles of the continuous phase with the measured ones has been found. However, some discrepancies have been noticed within the bubble column and directly downstream the bubble column. This might suggest a limitation of the model to capture the entire spectra of turbulence generated at the bubble scale. Extensive analysis by means of streamwise velocity contours and turbulent intensity, 2D and 3D streamlines, and isosurfaces of Q-criterion has been carried out and several differences between the different cases have been identified. The analysis of the secondary flow has shown that multi-phase plume behaves as single-phase plumes up to a specific height, and it has also revealed the formation of a roller upstream the bubble plume that cascades to two strong counter-rotating vortices at the upper half of the channel in the plume's wake. The findings attempt to contribute to the design of more efficient environmental systems for aeration and/or destratification of reservoirs and more effective contamination control in accidental blow-outs.

The effect of vertically stratified ambient on bubble plume dynamics has been investigated and presented in Chapter 6. To the knowledge of the author, such computational setup has rarely carried out in the past, less so with an EL approach for the dispersed phase. The LES-computed results have been validated against experimental data and reasonable agreement has been found. Through contours of streamwise velocity, 2D and 3D streamlines and isosurfaces of Q-criterion, the dynamics of three different types of bubble plumes have been revealed. Trap heights and peel heights have been identified for each one of the cases. The analysis of the secondary flow has shown that the different plume types result from variations in peeling efficiency and from the relative magnitude of the initial velocity of the bubbles compared to the fluid velocities of the plume.

## 7.2 Contribution of Thesis

The contribution of the current thesis to the field of Computational Fluid Dynamics (CFD) and hydraulics engineering as follows:

- From numerical point of view, a two way coupling formulation is adopted between phases. PSI-cell technique utilises second-order smooth delta functions as the interpolation technique for the forward coupling and a volume average for the backward coupling between phases. The air diffuser has been represented by Lagrangian nodes using the immersed boundary method (IBM). A synthetic eddy method (SEM) has been adopted for the velocity inlet conditions, instead of precursor simulations; an approach that reduces the total computational time for each simulation. A local mesh refinement approach was adopted for fine mesh simulations to decrease the mesh size within the bubble plume and the area affected by the bubble plume; an approach that reduces the computational cost for LES simulations.

- From analysis point of view, a very detailed analysis of the interaction of dispersed and continuous phases and the resulting hydrodynamics has been carried out. The physics of each case examined have been reflected on the 3D streamlines, velocity profiles and contours, Q-criterion representation of coherent structures and Reynolds stresses.

## 7.3 Outlook

The present study has demonstrated the capability of the in-house built model Hydro3D to predict the flow in and around bubble plumes. In the author's view, there are promising research routes that can extend further the investigation accomplished in this thesis.

The motivation of the current thesis is environmental applications and contamination problems. Thus, it is an ultimate goal of a numerical model to be able to accurately model the multi-phase flows. Further research is necessary to address the limitations of LES-EL model in order to allow more accurate large-scale predictions of bubble dynamics. The inability of the model to fully capture smaller turbulent scales suggests that a more sophisticated large-eddy simulation closure model is needed, possibly to add bubble-induced turbulence production to the sgs-model.

# Appendix A

# Appendix

Following the numerical study conducted in Chapter 5 for multi-phase plumes of gas flow rate $Q_b = 0.5$l/min in three different crossflows with $u_{bulk}$ equal to 0.04m/sec, 0.10m/sec and 0.15m/sec respectively, a second set of simulations was conducted for higher gad flow rate, i.e. $Q_b = 1.5$l/min. Two different mesh resolutions were examined (fine and coarse) similar to the mesh resolution applied for the simulations in Chapter 3. Two different crossflow velocities $u_{bulk}$ are examined in this case, i.e. $u_b = 0.04$m/sec and $u_b = 0.15$m/sec. In the following figures, the Q-criterion isosurfaces are shown for the aforementioned two cases.

It is evident from Fig. 1 that even with higher gas flow rate (three times higher than the gas flow rate examined in Chapter 5), the hydrodynamics in the examined channel are very similar to those described in Chapter 5. In the case with the low crossflow, the bubbles act initially as an obstacle to the flow (Fig. 1(a)), making the fluid to move around the bubbles towards the side walls of the channel. In the case with the high crossflow, the bubble column is inclined due to the higher forces acting on it and it is easier for the flow to go through the bubbles.

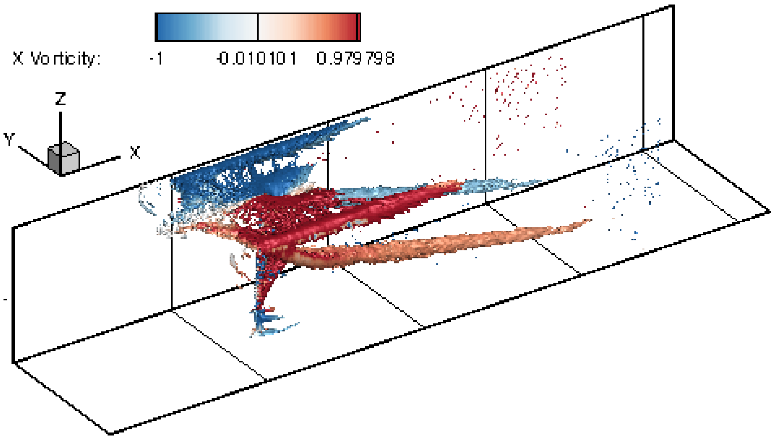

(a) Three-dimensional view of the generation of secondary currents for Case1.

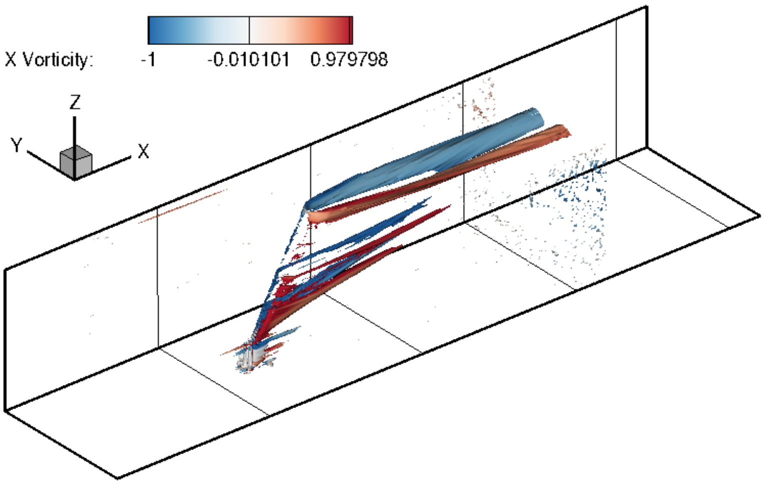

(b) Three-dimensional view of the generation of secondary currents for Case2.

Figure A.1: (a) Three-dimensional view of Q-criterion isosurfaces coloured by the vorticity in x-direction for (a) Case1 with $Q_b = 1.5$l/min and $u_{bulk} = 0.04$m/sec and (b) Case2 with $Q_b = 1.5$l/min and $u_{bulk} = 0.15$m/sec

# References

Akselvoll K. and Moin P. (1993). "Large eddy simulation of a backward-facing step flow". In: *Enineering Turbulence Modeling and Experiments*. Ed. by W. Rodi and F. Martelli. Vol. 2. Elsevier, pp. 303–313.

Anagbo P. E. and Brimacombe J. K. (1990). "Plume characteristics and liquid circulation in gas injection through a porous plug". In: *Metallurgical Transactions B* 21 (4), pp. 637–648. ISSN: 1543-1916. DOI: `10.1007/BF02654242`. URL: `https://doi.org/10.1007/BF02654242`.

Andren A., Brown A. R., Graf J., Mason P. J., Moeng C. H., Nieuwstadt F. T. M., and Schumann U. (1994). "Large-eddy simulation of the neutrally stratified boundary layer: A comparison of four computer codes". In: *Quarterly Journal of the Royal Meteorological Society* 120, pp. 1457–1484.

Armenio V., Piomelli U., and Fiorotto V. (1999). "Effect of the subgrid scales on particle motion". In: *Physics of Fluids* 11, pp. 3030–3042.

*arup.com* (2018). `https://www.arup.com/projects/cardiff-bay-aeration-system`. Accessed: 2018-09-30.

Asaeda T. and Imberger J. (1993). "Structure of bubble plumes in linearly stratified environments". In: *Journal of Fluid Mechanics* 249, pp. 35–79.

Ashton G. D. (1982). "Theory of thermal control and prevention of ice in rivers and lakes". In: *Advances in Hydroscience* 13, pp. 131–185.

Auton T. R. (1987). "The lift force on a spherical body in a rotational flow". In: *Journal of Fluid Mechanics* 183, pp. 199–218.

Badreddine H., Sato Y., Niceno B., and Prasser H.M. (2015). "Finite size Lagrangian particle tracking approach to simulate dispersed bubbly flows". In: *Chemical Engineering Science* 122, pp. 321–335.

Baggett J. S., Jimenez J., and Kravchenko A. G. (1997). “Resolution requirements in large-eddy simulation of shear flows”. In: *CTR Annual Research Briefs*, pp. 51–66.

Bai W., Deen N. G., and Kuipers J. A. M. (2012). “Numerical investigation of gas holdup and phase mixing in bubble column reactors”. In: *Industrial and Engineering Chemistry Research* 51.4, pp. 1949–1961. ISSN: 0888-5885. DOI: `10.1021/ie102557h`.

Balaras E., Benocci C., and Piomelli U. (1995). “Finite-difference computations of high reynolds number flows using the dynamic subgrid-scale model”. In: *Theoretical and Computational Fluid Dynamics* 7 (3), pp. 207–216. ISSN: 1432-2250. DOI: `10.1007/BF00312363`. URL: `https://doi.org/10.1007/BF00312363`.

Bardina J., Ferziger J. H., and Reynolds W. C. (1980). “Improved subgrid scale models for large eddy simulation”. In: *13th Fluid and Plasma Dynamics Conference*, pp. 80–1357. DOI: `10.2514/6.1980-1357`. URL: `https://arc.aiaa.org/doi/abs/10.2514/6.1980-1357`.

Batchelor G. K. (1967). *An Introduction to Fluid Dynamics.* Cambridge: Cambridge University Press.

Becker S., Sokolichin A., and Eigenberger G. (1994). “Gas-liquid flow in bubble columns and loop reactors. Part II: Comparison of detailed experiments and flow simulations”. In: *Chemical Engineering Science* 49.24, Part 2, pp. 5747–5762. ISSN: 0009-2509. DOI: `https://doi.org/10.1016/0009-2509(94)00290-8`. URL: `http://www.sciencedirect.com/science/article/pii/0009250994002908`.

Bestion D. (2012). “Applicability of two-phase CFD to nuclear reactor thermalhydraulics and elaboration of Best Practice Guidelines”. In: *Nuclear Engineering and Design* 253, pp. 311–321. ISSN: 0029-5493. DOI: `https://doi.org/10.1016/j.nucengdes.2011.08.068`. URL: `http://www.sciencedirect.com/science/article/pii/S0029549311006935`.

Beutel M. W. and Horne A. J. (1999). “A review of the effects of hypolimnetic oxygenation on lake and reservoir water quality”. In: *Lake and Reser. Manage.* 4.15, pp. 285–297.

Bhaganagar K., Kim J., and Coleman G. (2004). “Effect of Roughness on Wall-Bounded Turbulence”. In: *Flow, Turbulence and Combustion* 72 (2), pp. 463–492.

ISSN: 1573-1987. DOI: `10.1023/B:APPL.0000044407.34121.64`. URL: `https://doi.org/10.1023/B:APPL.0000044407.34121.64`.

Bhole M. R. and Joshi J. B. (2005). “Stability analysis of bubble columns: Predictions for regime transition”. In: *Chemical Engineering Science* 60.16, pp. 4493–4507. ISSN: 0009-2509. DOI: `https://doi.org/10.1016/j.ces.2005.01.004`. URL: `http://www.sciencedirect.com/science/article/pii/S0009250905000540`.

Bhole M. R., Roy S., and Joshi J. B. (2006). “Laser Doppler Anemometer Measurements in Bubble Column: Effect of Sparger”. In: *Industrial & Engineering Chemistry Research* 45 (26), pp. 9201–9207. ISSN: 0888-5885. DOI: `10.1021/ie060745z`. URL: `https://doi.org/10.1021/ie060745z`.

Birkhoff G. (1960). *Hydrodynamics: a Study in Logic, Fact and Similitude.* Princeton, NJ: Princeton University Press.

Bois G., Jamet D., and Lebaigue O. (2010). “Towards Large Eddy Simulation of two-phase flow with phase-change: Direct Numerical Simulation of a pseudo-turbulent two-phase condensing flow”. In: *Proceedings of the 7th International Conference on Multiphase Flow (ICMF ’10).* Tampa, FL, USA.

Bomminayuni S. K. and Stoesser T. (2011). “Turbulence statistics in an open-channel flow over a rough bed”. In: *Journal of Hydraulic Engineering* 11.137, pp. 1347–1358.

Bove S., Solberg T., and Hjertager B. H. (2004). “Numerical Aspects of Bubble Column Simulations”. In: *International Journal of Chemical Reactor Engineering* 2.1, pp. 1–22. URL: `https://www.degruyter.com/view/journals/ijcre/2/1/article-ijcre.2004.2.1.1125.xml.xml`.

Brennen C. E. (1982). *A review of added mass and fluid inertial forces.* Tech. rep. Port Hueneme, California: Naval Civil Engineering Laboratory.

Breuer M. (1998). “Large eddy simulation of the subcritical flow past a circular cylinder: Numerical and modeling aspects”. In: *International Journal of Numerical Methods in Fluids* 28, pp. 1281–1302.

– (2000). “A challenging test case for large eddy simulation: High Reynolds number circular cylinder flow”. In: *International Journal of Heat and Fluid Flow* 21, pp. 648–654.

– (2002). *Direkte Numerische Simulation und Large-Eddy Simulation turbulenter Strömungen auf Hochleistungsrechnern.* Shaker.

Breuer M. and Rodi W. (1994). "Large-eddy simulation of turbulent flow through a straight square duct and a 180 bend". In: *Fluid Mechanics and its Applications* 26, pp. 273–285.

Breugem W. P. (2012). "A second-order accurate immersed boundary method for fully resolved simulations of particle-laden flows". In: *Journal of Computational Physics* 231, pp. 4469–4498.

Bröder D. and Sommerfeld M. (2002). "An advanced LIF-PLV system for analysing the hydrodynamics in a laboratory bubble column at higher void fractions". In: *Experiments in Fluids* 33 (6), pp. 826–837. ISSN: 1432-1114. DOI: `10.1007/s00348-002-0502-z`. URL: `https://doi.org/10.1007/s00348-002-0502-z`.

Bunner B. and Tryggvason G. (2002). "Dynamics of homogeneous bubbly flows. Part 1: Rise velocity and microstructure of the bubbles". In: *Journal of Fluid Mechanics* 466, pp. 17–52.

Cai X. and Wallis G. B. (1993). "The added mass coefficient for rows and arrays of spheres oscillating along the axes of tubes". In: *Physics of Fluids A: Fluid Dynamics* 5.7, pp. 1614–1629. DOI: `10.1063/1.858838`. URL: `https://doi.org/10.1063/1.858838`.

Calhoun R. J. and Street R. L. (2001). "Turbulent flow over a wavy surface: Neutral case". In: *Journal of Geophysical Research: Oceans* 106.C5, pp. 9277–9293. DOI: `10.1029/2000JC900133`. URL: `https://agupubs.onlinelibrary.wiley.com/doi/abs/10.1029/2000JC900133`.

Calhoun R. J., Street R. L., and Koseff J. R. (2001). "Turbulent flow over a wavy surface: Stratified case". In: *Journal of Geophysical Research: Oceans* 106.C5, pp. 9295–9310. DOI: `10.1029/2001JC900002`. URL: `https://agupubs.onlinelibrary.wiley.com/doi/abs/10.1029/2001JC900002`.

Camilli R., Reddy C. M., Yoerger D. R., Van Mooy B. A. S., Jakuba M. V., Kinsey J. C., McLntyre C. P., Sylva S. P., and Maloney J. V. (2010). "Tracking hydrocarbon plume transport and biodegradation at Deepwater Horizon". In: *Science* 330, pp. 201–204.

Carazzo G., Kaminski E., and Tait S. (2006). "The route to self-similarity in turbulent jets and plumes". In: *Journal of Fluid Mechanics* 547, pp. 137–148.

Cebeci T. and Bradshaw P. (1977). *Momentum transfer in boundary layers.* New York, NY: McGraw-Hill.

Cevheri M., McSherry R., and Stoesser T. (2016). “A local mesh refinement approach for large eddy simulations of turbulent flows”. In: *International Journal of Numerical Methods in Fluids* 5.82, pp. 261–285.

Cevheri M. and Stoesser T. (2018). “Large-eddy simulation of a jet in cross-flow using local mesh refinement”. In: *Progress in Computational Fluid Dynamics* 18.3.

Chahed J., Roig V., and Masbernat L. (2003). “Eulerian–Eulerian two-fluid model for turbulent gas–liquid bubbly flows”. In: *International Journal of Multiphase Flow* 29.1, pp. 23–49. ISSN: 0301-9322. DOI: `https://doi.org/10.1016/S0301-9322(02)00123-4`. URL: `http://www.sciencedirect.com/science/article/pii/S0301932202001234`.

Chang K., Constantinescu G., and Park S. O. (2006). “Analysis of the flow and mass transfer process for the incompressible flow past an open cavity with a laminar and a fully turbulent incoming boundary layer”. In: *Journal of Fluid Mechanics* 561, pp. 113–145.

Chapman D. R. (1979). “Computational Aerodynamics Development and Outlook”. In: *AIAA Journal* 17.12, pp. 1293–1313. DOI: `10.2514/3.61311`. URL: `https://doi.org/10.2514/3.61311`.

Chen B., Song Y., Nishio M., and Akai M. (2003). “Large-eddy simulation of bubble plume formation induced by $CO_2$ dissolution in the ocean”. In: *Tellus* 55B, pp. 723–730.

Chen F. and Yapa P. D. (2003). “A model for simulating deepwater oil and gas blowouts - Part II: Comparison of numerical simulations with ”Deepspill” field experiments”. In: *Journal of Hydraulic Research* 41.4, pp. 353–365.

Chorin J. (1968). “Numerical solution of the Navier-Stokes equations”. In: *Math. Comput.* 104.22, pp. 745–762.

Chow F. K., Street R. L., Xue M., and Ferziger J. H. (2005). “Explicit filtering and reconstruction turbulence modeling for large-eddy simulation of neutral boundary layer flow”. In: *Journal of the Atmospheric Sciences* 62, pp. 2058–2077.

Clift R. (1978). *Bubbles, Drops and Particles.* New York: Dover Publications.

Constantinescu S. G., Sukhodolov A., and McCoy A. (2009). “Mass exchange in a shallow channel flow with a series of groynes: LES study and comparison with laboratory and field experiments”. In: *Environmental Fluid Mechanics* 9 (6), pp. 587–615.

Courant R., Friedrichs K., and Lewy H. (1928). “On the Partial Difference Equations of Mathematical Physics”. In: *Mathematische Annalen* 100 (1). Translated by W. L. Gates and M. H. Oberlunder, University of California, Los Angeles, pp. 32–74.

Crounse B. C., Wannamaker E. J., and Adams E. E. (2007). “Integral model of a multiphase plume in quiescent stratification”. In: *Journal of Hydraulic Engineering* 133, pp. 70–76.

Crowe C. T., Sharma M. P., and Stock D. E. (1977). “The particle-source-in cell (PSI-CELL) model for gas-droplet flows”. In: *Journal of Fluids Engineering* 99.2, pp. 325–332.

Cui J., Patel V. C., and Lin C.-L. (2003). “Prediction of Turbulent Flow Over Rough Surfaces Using a Force Field in Large Eddy Simulation”. In: *Journal of Fluids Engineering* 125 (1), pp. 2–9. ISSN: 0098-2202. DOI: `10.1115/1.1524587`. URL: `https://doi.org/10.1115/1.1524587`.

Darmana D., Deen N. G., and Kuipers J. A. M. (2005). “Detailed modeling of hydrodynamics, mass transfer and chemical reactions in a bubble column using a discrete bubble model”. In: *Chemical Engineering Science* 60.12, pp. 3383–3404. ISSN: 0009-2509. DOI: `https://doi.org/10.1016/j.ces.2005.01.025`. URL: `http://www.sciencedirect.com/science/article/pii/S0009250905000850`.

– (2006). “Parallelization of an Euler-Lagrange model using mixed domain decomposition and mirror domain technique: Application to dispersed gas-liquid two-phase flow”. In: *Journal of Computational Physics* 220.1, pp. 216–248.

Darmana D., Deen N. G., Kuipers J. A. M., Harteveld W. K., and Mudde R. F. (2009). “Numerical study of homogeneous bubbly flow: Influence of the inlet conditions to the hydrodynamic behavior”. In: *International Journal of Multiphase Flow* 35.12, pp. 1077–1099. ISSN: 0301-9322. DOI: `https://doi.org/10.1016/j.ijmultiphaseflow.2009.08.003`. URL: `http://www.sciencedirect.com/science/article/pii/S0301932209001323`.

Davidson G. A. (1986). “Gaussian versus top-hat profile assumptions in integral plume models”. In: *Atmos. Environ.* 20, pp. 471–478.

Davidson L. (1998). “Large eddy simulation: A dynamic one equation subgrid model for three dimensional recirculating flow”. In: *8-11 September 1997*. Ed. by Proceedings of the 11th Turbulent Shear Flows, pp. 26.1–26.6.

Davidson M. J. and Pun K. L. (1999). “Weakly advected jets in cross-flow”. In: *Journal of Hydraulic Engineering* 125 (1), pp. 47–58.

de Bertodano M. L. (1992). “Turbulent bubbly two-phase flow in a triangular duct”. PhD thesis. Troy, NY, USA: Rensselaer Polytechnic Institute.

Deardorff J. W. (1974). “Three dimensional numerical study of turbulence in an entraining mixed layer”. In: *Boundary-Layer Methodology* 7, pp. 199–226.

Decrop B., De Mulder T., Toorman E., and Sas M. (2015). “Large-eddy simulations of turbidity plumes in crossflow”. In: *European Journal of Mechanics B/Fluids* 53, pp. 68–84.

Deen N. G., Annaland M. V. S., and Kuipers J. A. M. (2004). “Multi-scale modeling of dispersed gas-liquid two-phase flow”. In: *Chemichal Engineering Science* 59, pp. 1853–1861.

Deen N. G., Solberg T., and Hjertager B. H. (2001). “Large eddy simulation of the gas-liquid flow in a square cross-sectioned bubble column”. In: *Chemichal Engineering Science* 56.21-22, pp. 6341–6349.

Delnoij E., Kuipers J. A. M., and van Swaaij W. P. M. (1999). “A three-dimensional CFD model for gas-liquid bubble columns”. In: *Chemical Engineering Science* 54.13-14, pp. 2217–2226.

Delnoij E., Lammers F. A., Kuipers J. A. M., and van Swaaij W. P. M. (1997). “Dynamic simulation of dispersed gas-liquid two-phase flow using a discrete bubble model”. In: *Chemical Engineering Science* 52 (9), pp. 1429–1458.

Dhotre M. T., Deen N. G., Niceno B., Khan Z., and Joshi J.B. (2013). “Large eddy simulation for dispersed bubbly flows: A review”. In: *International Journal of Chemical Engineering*, pp. 1–22.

Dhotre M. T., Niceno B., and Smith B. L. (2008). “Large eddy simulation of a bubble column using dynamic sub-grid scale model”. In: *Chemical Engineering Journal* 136.2-3, pp. 337–348.

Dhotre M. T., Niceno B., Smith B. L., and Simiano M. (2009). “Large eddy simulation (LES) of the large scale bubble plume”. In: *Chemical Engineering Science* 64.11, pp. 2692–2704.

Dissanayake A. L., Gros J., and Socolofsky S. A. (2018). “Integral models for bubble, droplet, and multiphase plume dynamics in stratification and crossflow”. In:

*Environmental Fluid Mechanics* 18 (5), pp. 1167–1202. DOI: `10.1007/s10652-018-9591-y`. URL: `https://doi.org/10.1007/s10652-018-9591-y`.

Drew D. A. (1971). "Averaged field equations for two-phase media". In: *Studies in Applied Mathematics* 50.2, pp. 133–165.

Einstein H. A. (1942). "Formulas for the Transportation of Bed Load". In: *ASCE Transactions* 107 (1), pp. 561–577.

Elgobashi S. (1991). "Particle-laden turbulent flows: direct simulation and closure models". In: *Applied Scientific Research* 48.3-4, pp. 301–314.

Esmaeeli A. and Tryggvason G. (1996). "An inverse energy cascade in two-dimensional low Reynolds number bubbly flows". In: *Journal of Fluid Mechanics* 314, pp. 315–330.

– (1998). "Direct numerical simulations of bubly flows. Part 1: Low Reynolds number arrays". In: *Journal of Fluid Mechanics* 377, pp. 313–345.

Fabregat A., Dewar W. K., Özgökmen T. M., Poje A. C., and Wienders N. (2015). "Numerical simulations of turbulent thermal bubble and hubrid plumes". In: *Ocean Modelling* 90, pp. 16–28.

Fadlun E. A., Verzicco R., Orlandi P., and Mohd-Yusof J. (2000). "Combined immersed-boundary finite-difference methods for three-dimensional complex flow simulations". In: *Journal of Computational Physics* 161 (1), pp. 35–60.

Ferziger J. H. and Peric M. (2002). *Computational Methods for Fluid Dynamics*. Berlin: Springer. DOI: `10.1007/978-3-642-56026-2`.

Fogelson A. L. and Peskin C. S. (1988). "A fast numerical method for solving the three-dimensional stokes' equations in the presence of suspended particles". In: *Journal of Computational Physics* 79 (1), pp. 50–69.

Fraga B. and Stoesser T. (2016). "Influence of bubble size, diffuser width, and flow rate on the integral behavior of bubble plumes". In: *Journal of Geophysic Research Oceans* 121, pp. 3887–3904.

Fraga B., Stoesser T., Lai C. C. K., and Socolofsky S.A. (2016). "A LES-based Eulerian-Lagrangian approach to predict the dynamics of bubble plumes". In: *Ocean Modelling* 97, pp. 27–36.

Frict T. F. and Roshko A. (1994). "Vortical structure in the wake of a transverse jet". In: *Journal of Fluid Mechanics* 279, pp. 1–47.

Fröhlich J. (2006). *Lage-Eddy Simulation Turbulenter Strömungen.* Wiesbaden: Teubner Verlag.

Fu Y., Wang T., and Gu C. (2013). “Experimental and numerical analyses of gas-solid-multiphase jet in crossflow”. In: *Journal of Aerospace Engineering* 227 (1), pp. 61–79.

Fulgosi M., Lakehal D., Banerjee S., and Angelis V. De (2003). “Direct numerical simulation of turbulence in a sheared air–water flow with a deformable interface”. In: *Journal of Fluid Mechanics* 482, pp. 319–345. DOI: `10.1017/S0022112003004154`.

Fureby C. (1999). “Large eddy simulation of rearward-facing step flow”. In: *AIAA Journal* 37, pp. 1401–1410.

Garcia-Villalba M., Li N., Rodi W., and Leschziner M. A. (2009). “Large-eddy simulation of separated flow over a three-dimensional axisymmetric hill”. In: *Journal of Fluid Mechanics* 627, pp. 55–96.

Germano M., Piomelli U., Moin P., and Cabot W. H. (1991). “A dynamic subgrid-scale eddy viscosity model”. In: *Physics of Fluids A* 3 (7), pp. 1760–1765.

Ghisalberti M. and Nepf H. M. (2002). “Mixing layers and coherent structures in vegetated aquatic flows”. In: *Journal of Geophysical Research: Oceans* 107.C2, pages. DOI: `10.1029/2001JC000871`. URL: `https://agupubs.onlinelibrary.wiley.com/doi/abs/10.1029/2001JC000871`.

Ghosal S., Lund T. S., Moin P., and Akselvoll K. (1995). “A dynamic localization model for large-eddy simulation of turbulent flows”. In: *Journal of Fluid Mechanics* 286, pp. 229–255.

Gullbrand J. and Chow F. K. (2003). “The effect of numerical errors and turbulence models in large-eddy simulations of channel flow, with and without explicit filtering”. In: *Journal of Fluid Mechanics* 495, pp. 323–341.

Harlow F. H. and Welch J. E. (1965). “Numerical Calculation of TimeDependent Viscous Incompressible Flow of Fluid with Free Surface”. In: *Physics of Fluids* 8.12, pp. 2182–2189. DOI: `10.1063/1.1761178`. URL: `https://aip.scitation.org/doi/abs/10.1063/1.1761178`.

Harteveld W. K., Julia J. E., Mudde R. F., and Akker H. E. A. van den (2004). “Large scale vortical structures in bubble columns for gas fractions in the range of 5–25%”. In: *Prague, Czech Republic.* Ed. by Proceedings of the 16th International Congress of Chemical and Process Engineering (CHISA ’04).

Hengel E. I. V. van den, Deen N. G., and Kuipers J. A. M. (2005). “Application of Coalescence and Breakup Models in a Discrete Bubble Model for Bubble Columns”. In: *Industrial Engineering Chemistry Research* 44 (14), pp. 5233–5245. ISSN: 0888-5885. DOI: `10.1021/ie0492449`. URL: `https://doi.org/10.1021/ie0492449`.

Hey R. D. (1978). “Determinate Hydraulic Geometry of River Channels”. In: *ASCE, Journal of the Hydraulics Division* 104 (6), pp. 869–885.

Hibiki T. and Ishii M. (1999). “Experimental study on interfacial area transport in bubbly two-phase flows”. In: *International Journal of Heat and Mass Transfer* 42.16, pp. 3019–3035. ISSN: 0017-9310. DOI: `https://doi.org/10.1016/S0017-9310(99)00014-9`. URL: `http://www.sciencedirect.com/science/article/pii/S0017931099000149`.

Hibiki T., Ishii M., and Xiao Z. (2001). “Axial interfacial area transport of vertical bubbly flows”. In: *International Journal of Heat and Mass Transfer* 44.10, pp. 1869–1888. ISSN: 0017-9310. DOI: `https://doi.org/10.1016/S0017-9310(00)00232-5`. URL: `http://www.sciencedirect.com/science/article/pii/S0017931000002325`.

Hibiki T., Situ R., Mi Y., and Ishii M. (2003). “Local flow measurements of vertical upward bubbly flow in an annulus”. In: *International Journal of Heat and Mass Transfer* 46.8, pp. 1479–1496. ISSN: 0017-9310. DOI: `https://doi.org/10.1016/S0017-9310(02)00421-0`. URL: `http://www.sciencedirect.com/science/article/pii/S0017931002004210`.

Hinterberger C., Frohlich J., and Rodi W. (2008). “2D and 3D turbulent fluctuations in open channel flow with $Re_\tau = 590$ studied by large eddy simulation”. In: *Flow Turbulence and Combustion* 80 (2), pp. 225–253. ISSN: 1573-1987. DOI: `10.1007/s10494-007-9122-2`. URL: `https://doi.org/10.1007/s10494-007-9122-2`.

Hinze J. O. (1975). *Turbulence*. New York: McGraw-Hill.

Hirsch C. (2007). *Numerical Computation of Internal and External Flows*. West Sussex: John Wiley & Sons Ltd.

Hirt C. W (1968). “Heuristic stability theory for finite-difference equations”. In: *Journal of Computational Physics* 2 (4), pp. 339–355. ISSN: 0021-9991. DOI: `https://doi.org/10.1016/0021-9991(68)90041-7`. URL: `http://www.sciencedirect.com/science/article/pii/0021999168900417`.

Hirt C. W and Nichols B. D (1981). “Volume of fluid (VOF) method for the dynamics of free boundaries”. In: *Journal of Computational Physics* 39 (1), pp. 201–225. ISSN: 0021-9991. DOI: `https://doi.org/10.1016/0021-9991(81)90145-5`. URL: `http://www.sciencedirect.com/science/article/pii/0021999181901455`.

Hodges B. R. and Street R. L. (1999). “On Simulation of Turbulent Nonlinear Free-Surface Flows”. In: *Journal of Computational Physics* 151.2, pp. 425–457. ISSN: 0021-9991. DOI: `https://doi.org/10.1006/jcph.1998.6166`. URL: `http://www.sciencedirect.com/science/article/pii/S0021999198961666`.

Hofler K. and Schwartzer S. (2000). “Navier-Stokes simulation with constraint forces: Finite-difference method for particle-laden flows and complex geometries”. In: *Physical Review* E 61.7146.

Hoyas S. and Jimenez J. (2006). “Scaling of the velocity fluctuations in turbulent channels up to $\mathrm{Re}_{tau} = 2003$”. In: *Physics of Fluids* 18.1, p. 011702. DOI: `10.1063/1.2162185`. URL: `https://doi.org/10.1063/1.2162185`.

Hu G. (2005). “Towards large eddy simulation of dispersed gas-liquid two-phase turbulent flows”. PhD thesis. Morgantown, WV, USA: Mechanical and Aerospace Engineering Department, West Virginia University.

Hu G. and Celik I. (2008). “Eulerian–Lagrangian based large-eddy simulation of a partially aerated flat bubble column”. In: *Chemical Engineering Science* 63.1, pp. 253–271. ISSN: 0009-2509. DOI: `https://doi.org/10.1016/j.ces.2007.09.015`. URL: `http://www.sciencedirect.com/science/article/pii/S000925090700735X`.

Hunt J. C. R., Wray A. A., and Moin P. (1988). “Eddies, Streams, and Converegence zones in turbulent flows”. In: *Center of Turbulece Research, Proceedings of the Summer Program*, pp. 193–208.

Iaccarino G. and Verzicco R. (2003). “Immersed boundary technique for turbulent flow simulations”. In: *Applied Mechanics Review* 56, pp. 331–347.

Ikeda T. and Durbin P. A. (2007). “Direct simulations of a rough-wall channel flow”. In: *Journal of Fluid Mechanics* 571, pp. 235–263. DOI: `10.1017/S002211200600334X`.

Imberger J. and Patterson J. C. (1989). “Physical Limnology”. In: *Advances in Applied Mechanics* 27, pp. 303–475.

Ishii M. and Chawla T. C. (1979). *Local drag laws in dispersed two-phase flow.* Report. Argonne National Laboratory.

Jakobsen H. A. (2005). “Modeling of bubble column reactors: progress and limitations”. In: *Industrial and Engineering Chemistry Research* 44, pp. 5107–5151.

Jarrin N., Benhamadouche S., Laurence D., and Prosser R. (2006). “A synthetic-eddy-method for generating inflow conditions for large-eddy simulations”. In: *Int. J. Heat Fluid Flow* 4.27, pp. 585–593.

Jimenez J. (2004). “Turbulent Flows Over Rough Walls”. In: *Annual Review of Fluid Mechanics* 36.1, pp. 173–196. DOI: `10.1146/annurev.fluid.36.050802.122103`. URL: `https://doi.org/10.1146/annurev.fluid.36.050802.122103`.

Johansen Ø. (2000). “DeepBlow - a Lagrangian plume model for deep water blowouts”. In: *Spill Science & Technology Bulletin* 6.2, pp. 103–111.

– (2003). “Simulation of buoyancy driven bubbly flow: established simplifications and open questions”. In: *Spill Science & Technology Bulletin* 50, pp. 433–443.

Joshi J. B. (2001). “Computational flow modelling and design of bubble column reactors”. In: *Chemical Engineering Science* 56.21–22, pp. 5893–5933.

Kanda M. and Hino M. (1994). “Organized structures in developing turbulent flow within and above a plant canopy, using a Large Eddy Simulation”. In: *Boundary-Layer Meteorology* 68 (3), pp. 237–257. ISSN: 1573-1472. DOI: `10.1007/BF00705599`. URL: `https://doi.org/10.1007/BF00705599`.

Kang S., Lightbody A., Hill C., and Sotiropoulos F. (2011). “High resolution numerical simulation of turbulence in natural waterways”. In: *Advances in Water Resources* 1.34, pp. 98–113.

Kang S. and Sotiropoulos F. (2015). “Large-Eddy Simulation of three-dimensional turbulent free surface flow past a complex stream restoration structure”. In: *Journal of Hydraulic Engineering* 141.10.

Kariyasaki A. (1987). “Behaviour of a gas bubble in a liquid flow with a linear velocity profile”. In: *Proceedings of the 1987 ASME/JSME.* Thermal Engineering Conference, pp. 261–267.

Kempe T. and Frolich J. (2012). “An improved immersed boundary method with direct forcing for the simulation of particle laden flows”. In: *Journal of Computational Physics* 231, pp. 3663–3684.

Kendoush A., Sulaymon A., and Mohammed S. (2007). “Experimental evaluation of the virtual mass of two solid spheres accelerating in fluids”. In: *Experimental*

*Thermal and Fluid Science* 31, pp. 813–823. DOI: `10.1016/j.expthermflusci.2006.08.007`.

Kim J. and Moin P. (1985). "Application of a Fractional-Step Method to Incompressible Navier-Stokes Equations". In: *Journal of Computational Physics* 59 ((2)), pp. 308–323.

Kim W. W. and Menon S. (1995). "A new dynamic one equation subgrid scale model for large eddy simulations". In: *AIAA Paper*, pp. 95–0356.

Kitagawa A., Murai Y., and Yamamoto F. (2001). "Two-way coupling of Eulerian-Lagrangian model for dispersed multiphase flows using filtering functions". In: *International Journal of Multiphase Flow* 12 (27), pp. 2129–2153.

Klein A., Sadiki A., and Janicka J. (2003). "A digital filter based generation of inflow data for spatially developing direct numerical or large eddy simulations". In: *Journal of Computational Physics* 186, pp. 652–665.

Komori S., Nagaosa R., Murakami Y., Chiba S., Ishii K., and Kuwahara K. (1993). "Direct numerical simulation of threedimensional openchannel flow with zeroshear gas–liquid interface". In: *Physics of Fluids A: Fluid Dynamics* 5.1, pp. 115–125. DOI: `10.1063/1.858797`. URL: `https://doi.org/10.1063/1.858797`.

Kondo K., Tsuchiya M., Mochida A., and Murakami S. (2002). "Generation of inflow turbulent bounary layer for LES computation". In: *Wind and Structures* 5, pp. 209–226.

Krajnovic S. and Davidson L. (2002). "Large-eddy simulation of the flow around a bluff boy". In: *AIAA Journal* 40, pp. 927–936.

Lai C. C. K. (2015). "An analysis of bubble plumes in unstratified stagnant water". p. 22. PhD thesis. Texas, USA: Texas A&M University.

Lai M.-C. and Peskin C. S. (2000). "An immersed boundary method with formal second-order accuracy and reduced numerical viscosity". In: *Journal of Computational Physics* 160.2, pp. 705–719.

Lain S. (2009). "Dynamic three-dimensional simulation of gas liquid flow in cylindrical bubble column". In: *Latin American Applied Research* 39, pp. 317–329.

Lain S., Broöder D., and Sommerfeld M. (1999). "Experimental and numerical studies of the hydrodynamics in a bubble column". In: *Chemical Engineering Science* 54, pp. 4913–4920.

Lakehal D., Fulgosi M., Banerjee S., and Yadigaroglu G. (2008). “Turbulence and heat exchange in condensing vapor-liquid flow”. In: *Physics of Fluids* 20.6, p. 065101. DOI: `10.1063/1.2919803`. URL: `https://doi.org/10.1063/1.2919803`.

Lam K. and Banerjee S. (1992). “On the condition of streak formation in a bounded turbulent flow”. In: *Physics of Fluids A: Fluid Dynamics* 4.2, pp. 306–320. DOI: `10.1063/1.858306`. URL: `https://doi.org/10.1063/1.858306`.

Lamb H. (1932). *Hydrodynamics.* New York: Cambridge University Press.

Le Moullec Y., Potier O., Gentric C., and Leclerc J. P. (2008). “Flow field and residence time distribution simulation of a cross-flow gas-liquid wastewater treatment reactor using CFD”. In: *Chemical Engineering Science* 63, pp. 2436–2449.

Le H., Moin P., and Kim J. (1997). “Direct numerical simulation of turbulent flow over a backward-facing step”. In: *Journal of Fluid Mechanics* 330, pp. 349–374.

Lee S., Lele S. K., and Moin P. (1992). “Simulation of spatially evolving turbulence and the applicability of Taylor hypothesis in compressible flow”. In: *Physics of Fluids A - Fluid Dynamics* 4, pp. 1521–1530.

Legendre D. and Magnaudet J. (1998). “The lift force on a spherical bubble in a viscous linear shear flow”. In: *Journal of Fluid Mechanics* 368, pp. 81–126. DOI: `10.1017/S0022112098001621`.

Legendre D., Magnaudet J., and Mougin G. (2003). “Hydrodynamic interactions between two spherical bubbles rising side by side in a viscous liquid”. In: *Journal of Fluid Mechanics* 497, pp. 133–166. DOI: `10.1017/S0022112003006463`.

Leitch A. M. and Daines W. D. (1989). “Liquid volume flux in a weak bubble plume”. In: *Journal of Fluid Mechanics* 205, pp. 77–98.

Lemckert C. J. and Imberger J. (1993). “Energetic bubble plumes in arbitrary stratification”. In: *Journal of Hydraulic Engineering* 119.(6), pp. 680–703.

Leonard A. (1975). “Energy cascade in large-eddy simulations of turbulent fluid flows”. In: *Turbulent Diffusion in Environmental Pollution Proceedings of a Symposium held at Charlottesville* 18, pp. 237–248.

Leonardi S., Orlandi P., Smalley R. J., Djenidi L., and Antonia R. A. (2003). “Direct numerical simulations of turbulent channel flow with transverse square bars on one wall”. In: *Journal of Fluid Mechanics* 491, pp. 229–238.

Leon-Becerril E., Cockx A., and Line A. (2002). “Effect of bubble deformation on stability and mixing in bubble columns”. In: *Chemical Engineering Science* 57.16, pp. 3283–3297. ISSN: 0009-2509. DOI: `https://doi.org/10.1016/S0009-2509(02)00199-9`. URL: `http://www.sciencedirect.com/science/article/pii/S0009250902001999`.

Leon-Becerril E. and Line A. (2001). “Stability analysis of a bubble column”. In: *Chemical Engineering Science* 56.21, pp. 6135–6141. ISSN: 0009-2509. DOI: `https://doi.org/10.1016/S0009-2509(01)00254-8`. URL: `http://www.sciencedirect.com/science/article/pii/S0009250901002548`.

Lesieur M., Metais O., and Comte P. (2005). *Large-Eddy Simulations of Turbulence.* Cambridge: Cambridge University Press.

Lilly D. K. (1992). “A proposed moification of the Germano subgrid-scale closure method”. In: *Physics of Fluids* 4.A, p. 633.

Lima Neto I., Zhu D., Rajaratnam N., Yu T., Spafford M., and McEachern P. (2007). “Dissolved oxygen downstream of an effluent outfall in an ice-covered river: natural and artificial Aeration”. In: *Journal of Environmental Engineering* 133.11, pp. 1051–1060.

Liu T. J. (1993). “Bubble size and entrance length effects on void development in a vertical channel”. In: *International Journal of Multiphase Flow* 19.1, pp. 99–113. ISSN: 0301-9322. DOI: `https://doi.org/10.1016/0301-9322(93)90026-Q`. URL: `http://www.sciencedirect.com/science/article/pii/030193229390026Q`.

Liu Y., Stoesser T., Fang H., Papanicolaou A., and Tsakiris A. G. (2016). “Turbulent flow over an array of boulders placed on a rough, permeable bed”. In: *Computers and Fluids* 158, pp. 120–132.

Lu J., Fernandez A., and Tryggvason G. (2005). “The effect of bubbles on the wall drag in a turbulent channel flow”. In: *Physics of Fluids* 9.17, pp. 95–102.

Lund T. S., Wu X., and Squires K. D. (1998). “Generation of turbulent inflow data for spatially-developing boundary layer simulations”. In: *Journal of Computational Physics* 140, pp. 223–258.

Magdeleine S., Mathieu B., Lebaigue O., and Morel C. (2010). “DNS up-scaling applied to volumetric interfacial area transport equation”. In: *Proceedings of the 7th International Conference on Multiphase Flow (ICMF ’10).* Tampa, FL, USA.

Magnaudet J., Takagi S., and Legendre D. (2003). “Drag, deformation and lateral migration of a buoyant drop moving near a wall”. In: *Journal of Fluid Mechanics* 476, pp. 115–157.

Mathey F. and Cokljat D. (2005). "Zonal multi-domain RANS/LES simulation of airflow over the Ahmed body". In: *Engineering Turbulence Modelling and Experiments, Vol. 6*. Ed. by W. Rodi and M. Mulas. Amsterdam: Elsevier Science B.V., pp. 647–656. ISBN: 978-0-08-044544-1. DOI: `https://doi.org/10.1016/B978-008044544-1/50062-5`. URL: `http://www.sciencedirect.com/science/article/pii/B9780080445441500625`.

Mathey F., Cokljat D., Bertoglio J.-P., and Sergent E. (2006). "Specification of LES inlet boundary condition using vortex method". In: *Progress in Computational Fluid Dynamics* 6, pp. 58–67. DOI: `10.1504/PCFD.2006.009483`.

McDougall T. G. (1978). "Bubble plumes in stratified environments". In: *Journal of Fluid Mechanics* 85, pp. 655–672.

McGinnis D. F., Lorke A., Wüest A., Stöckli A., and Little J. C. (2004). "Interaction between a bubble plume and the near field in a stratified lake". In: *Water Resources Research* 40.10.

McLaughlin J. B. (1991). "Inertial migration of a small sphere in linear shear flows". In: *Journal of Fluid Mechanics* 224, pp. 261–274. DOI: `10.1017/S0022112091001751`.

McSherry R., Chua K. V., Stoesser T., and Mulahasan S. (2018). "Free surface flow over square bars at intermediate relative submergence". In: *Journal of Hydraulic Research*, pp. 1–19.

Melaaen M. C. (1992). "Calculation of fluid flows with staggered and non-staggered curvilinear non-orthogonal grids - the theory". In: *Numerical Heat Transfer B* 21, pp. 1–19.

Meneveau C., Lund T. S., and Cabot W. (1996). "A Lagrangian dynamic subgrid-scale model of turbulence". In: *Journal of Fluid Mechanics* 319, pp. 353–385.

Menon S., Yeung P. K., and Kim W. W. (1996). "Effect of subgrid models on the computed interscale energy transfer in isotropic turbulence". In: *Computers and Fluids* 2.25, pp. 165–180.

Michaelides E. E. (2006). *Particles, Bubbles and Drops: Their Motion, Heat and Mass Transfer*. Singapore: World Scientific. DOI: `10.1142/6018`. URL: `https://www.worldscientific.com/doi/abs/10.1142/6018`.

Milelli M. (2002). "A numerical analysis of confined turbulent bubble plume". PhD thesis. Zurich, Switzerland: Swiss Federal Institute of Technology.

Milelli M., Smith B., and Lakehal D. (2001). “Large-Eddy Simulation of turbulent shear flows laden with bubbles”. In: *Direct and Large-Eddy Simulation IV*. Ed. by B. Geurts, R. Friedrich, and O. Metais. Vol. 8 of ERCOFTAC Series. Netherlands: Springer, pp. 461–470.

Milgram J. H. (1983). “Mean flow in round bubble plumes”. In: *Journal of Fluid Mechanics* 133, pp. 345–376.

Miller J. J. H. (1971). “On the location of zeros of certain classes of polynomials with application to numerical analysis”. In: *Journal of the Institute of Mathematics and its Applications* 8, pp. 397–406.

Miller T. F. and Schmidt F. W. (1988). “Use of pressure-weighted interpolation method for the solution of the incompressible Navier-Stokes equations on a non-staggered grid system”. In: *Numerical Heat Transfer* 14, pp. 213–233.

Milne-Thomson L. M. (1968). *Theoretical Hydrodynamics*. New York: Dover Publications.

Mittal R. and Jaccarino G. (2005). “Immersed boundary method”. In: *Annual Review of Fluid Mechanics* 37, pp. 239–261.

Moeng C. H. (1984). “A large-eddy-simulation model for the study of planetary bounary-layer turbulence”. In: *Journal of the Atmospheric Sciences* 41, pp. 2052–2062.

Moin P., Squires K., Cabot W., and Lee S. (1991). “A dynamic subgrid-scale model for compressible turbulence and scalar transport”. In: *Physics of Fluids* 3, pp. 2746–2757.

Monahan S. M., Vitankar V. S., and Fox R. O. (2005). “CFD predictions for flow-regime transitions in bubble columns”. In: *A.I.Ch.E. Journal* 51.7, pp. 1897–1923. DOI: `10.1002/aic.10425`. URL: `https://aiche.onlinelibrary.wiley.com/doi/abs/10.1002/aic.10425`.

Morton B. R., Taylor G. I., and Turner J. S. (1956). “Turbulent gravitational convection from maintained and instantaneous sources”. In: *Proc. R. Soc. Lond. A* 234, pp. 1–23.

Moser R. D., Kim J., and Mansour N. N. (1999). “Direct numerical simulation of turbulent channel flow up to $Re_\tau = 590$”. In: *Physics of Fluids* 11, pp. 943–946.

Mudde R. F. and Simonin O. (1999). “Two- and three-dimensional simulations of a bubble plume using a two-fluid model”. In: *Chemical Engineering Science* 54.21, pp. 5061–5069. ISSN: 0009-2509. DOI: `https://doi.org/10.1016/S0009-2509(99)00234-1`. URL: `http://www.sciencedirect.com/science/article/pii/S0009250999002341`.

Muppidi S. and Mahesh K. (2005). “Study of trajectories of jets in crossflow using direct numerical simulations”. In: *Journal of Fluid Mechanics* 530, pp. 81–105.

Nakayama A. and Sakio D. (2002). “Simulation of flows over wavy rough boundaries”. In: *Center for Turbulence Research, Annual Research Briefs, Stanford University/NASA Ames Research Center* 313.

Newman J. N. (1977). *Marine Hydrodynamics*. London: The MIT Press.

Nezu I. and Nakagawa H. (1993). *Turbulence in open-channel flows*. IAHR Monograph, Rotterdam: A. A. Balkema.

Niceno B., Boucker M., and Smith B. L. (2009). “Euler-Euler Large Eddy Simulation of a Square Cross-Sectional Bubble Column Using the Neptune$_CFDCode$”. In: *Science and Technology of Nuclear Installations*. DOI: `10.1155/2009/410272`. URL: `https://doi.org/10.1155/2009/410272`.

Niceno B., Dhotre M. T., and Deen N. G. (2008). “One-equation sub-grid scale (SGS) modelling for Euler-Euler large eddy simulation (EELES) of dispersed bubble flow”. In: *Chemical Engineering Science* 63.15, pp. 3923–3931.

Nicoud F. and Ducros F. (1999). “Subgrid-scale stress modelling based on the square of the velocity gradient tensor”. In: *Flow, turbulence and combustion* 3.62, pp. 183–200.

Nikora V., McEwan I., McLean S., Coleman S., Pokrajac D., and Walters R. (2007). “Double-Averaging Concept for Rough-Bed Open-Channel and Overland Flows: Theoretical Background”. In: *Journal of Hydraulic Engineering* 133.8, pp. 873–883. DOI: `10.1061/(ASCE)0733-9429(2007)133:8(873)`. URL: `https://ascelibrary.org/doi/abs/10.1061/(ASCE)0733-9429(2007)133:8(873)`.

Noh W. F. and Woodward P. (1976). “SLIC (Simple Line Interface Calculation)”. In: *Proceedings of the Fifth International Conference on Numerical Methods in Fluid Dynamics June 28–July 2, 1976 Twente University, Enschede*. Ed. by A. I. van de Vooren and P. J. Zandbergen. Berlin, Heidelberg: Springer, pp. 330–340. ISBN: 978-3-540-37548-7.

Odar F. and Hamilton W. S. (1964). “Forces on a sphere accelerating in a viscous fluid”. In: *Journal of Fluid Mechanics* 18.2, pp. 302–314. DOI: `10.1017/S0022112064000210`.

Oey R. S., Mudde R. F., and van den Akker H. E. A. (2003). “Sensitivity study on interfacial closure laws in two-fluid bubbly flow simulations”. In: *AIChE Journal* 49.7, pp. 1621–1636. DOI: `10.1002/aic.690490703`. URL: `https://aiche.onlinelibrary.wiley.com/doi/abs/10.1002/aic.690490703`.

Omidyeganeh M. and Piomelli U. (2011). “Large-eddy simulation of two-dimensional dunes in a steady, unidirectional flow”. In: *Journal of Turbulence* N42.12, pp. 1–31.

Osher S. and Sethian J. A. (1988). “Fronts propagating with curvature-dependent speed: Algorithms based on Hamilton-Jacobi formulations”. In: *Journal of Computational Physics* 79.1, pp. 12–49. ISSN: 0021-9991. DOI: `https://doi.org/10.1016/0021-9991(88)90002-2`. URL: `http://www.sciencedirect.com/science/article/pii/0021999188900022`.

Otero E. (2009). “Synthetic inflow condition for large eddy simulation (Synthetic Eddy Method)”. MA thesis. KTH.

Ouro P. (2017). “Large Eddy simulation of tidal turbines”. PhD thesis. Cardiff: Cardiff University.

Ouro P., Wilson C. A., Evans P., and Angeloudis A. (2017). “Large-eddy simulation of shallow turbulent wakes behind a conical island”. In: *Physics of Fluids* 12.29.

Pan Y. and Banerjee S. (1995). “A numerical study of freesurface turbulence in channel flow”. In: *Physics of Fluids* 7.7, pp. 1649–1664. DOI: `10.1063/1.868483`. URL: `https://doi.org/10.1063/1.868483`.

Panton R. L. (1984). *Incompressible flow*. John Wiley & sons.

Papanicolaou P. N. and List E. J. (1988). “Investigations of round vertical turbulent buoyant jets”. In: *J. Fluid Mech.* 195, pp. 341–391.

Patel V. C. (1998). “Perspective: Flow at High Reynolds Number and Over Rough Surfaces—Achilles Heel of CFD”. In: *Journal of Fluids Engineering* 120.3, pp. 434–444. ISSN: 0098-2202. DOI: `10.1115/1.2820682`. URL: `https://doi.org/10.1115/1.2820682`.

Peskin C. S. (1972). “Flow patterns around heart valves: A numerical method”. In: *Journal of Computational Physics* 10.2, pp. 252–271.

Pfleger D. and Becker S. (2001). "Modelling and simulation of the dyanmic flow behavior in a bubble column". In: *Chem. Engng Sci.* 56, pp. 1737–1747.

Pfleger D., Gomes S., Gilbert N., and Wagner H. G. (1999). "Hydrodynamic simulations of laboratory scale bubble columns fundamental studies of the Eulerian–Eulerian modelling approach". In: *Chemical Engineering Science* 54.21, pp. 5091–5099. ISSN: 0009-2509. DOI: `https://doi.org/10.1016/S0009-2509(99)00261-4`. URL: `http://www.sciencedirect.com/science/article/pii/S0009250999002614`.

Piomelli U. (2008). "Wall-layer models for large-eddy simulations". In: *Progress in Aerospace Sciences* 44.6. Large Eddy Simulation - Current Capabilities and Areas of Needed Research, pp. 437–446. ISSN: 0376-0421. DOI: `https://doi.org/10.1016/j.paerosci.2008.06.001`. URL: `http://www.sciencedirect.com/science/article/pii/S037604210800047X`.

Piomelli U., Ferziger J., Moin P., and Kim J. (1989). "New approximate boundary-conditions for large eddy simulations of wall-bounded flows". In: *Physics of Fluids A-Fluid Dynamics* 1, pp. 1061–1068.

Piomelli U. and Liu J. (1995). "Large-eddy simulation of rotating channel flows using a localized dynamic model". In: *Physics of Fluids* 7, pp. 839–849.

Pope S. (2000). *Tubulent Flows.* Cambridge: Cambridge University Press.

Porte-Agel F., Meneveau C., and Parlange M. B. (2000). "A scale-dependent dynamic model for large-eddy simulations: Application to a neutral atmospheric boundary layer". In: *Journal of FLuid Mechanics* 415, pp. 261–284.

Prosperetti A. and Tryggvason A. (2007). *Computational Methods for Multiphase Flow.* New York: Cambridge University Press.

Rampure M. R., Mahajani S. M., and Ranade V. V. (2009). "CFD Simulation of Bubble Columns: Modeling of Nonuniform Gas Distribution at Sparger". In: *Ind. Eng. Chem Res.* 48, pp. 8186–8192.

Ranade V. V. (2002). *Computational Flow Modeling for Chemical Reactor Engineering.* New York: Academy Press.

Reynolds W. C. (1990). "The potential and limitations of direct and large-eddy simulations". In: *Whither Turbulence? Turbulence at the Crossroads, Lecture Notes in Physics.* Ed. by J. L. Lumley. Berlin: Springer.

Rezvani M. (2016). “Bubble plumes in crossflow: laboratory and field measurements of their fluid dynamic properties with application to lake aeration and management”. PhD thesis. Texas, USA: Texas A&M University.

Rhie C. M. and Chow W. L. (1983). “A numerical study of the turbulent flow pas an isolated airflow with trailing edge separation”. In: *AIAA Journal* 21, pp. 1525–1532.

Richards T. S., Aubourg Q., and Sutherland B. R. (2014). “Radial intrusions from turbulent plumes in uniform stratification”. In: *Physics of Fluids* 26.

Rijn L. C. van (2007). “Unified View of Sediment Transport by Currents and Waves. I: Initiation of Motion, Bed Roughness, and Bed-Load Transport”. In: *Journal of Hydraulic Engineering* 133.6, pp. 649–667. DOI: `10.1061/(ASCE)0733-9429(2007)133:6(649)`. URL: `https://ascelibrary.org/doi/abs/10.1061/(ASCE)0733-9429(2007)133:6(649)`.

Robertson J. M. and Sibulkin M. (1965). “Hydrodynamics in Theory and Application”. In: *Journal of Applied Mechanics* 32.4, pp. 958–958. ISSN: 0021-8936. DOI: `10.1115/1.3627366`. URL: `https://doi.org/10.1115/1.3627366`.

Rodi W. (1993). *Tubulence models an their Applications in Hydraulics*. Rotterdam: IAHR Monograph.

Rodi W., Constantinescu G., and Stoesser T. (2013). *Large-Eddy Simulation in Hydraulics*. CRC Press.

Rodi W., Ferziger J. H., Breuer M., and Pourquie M. (1997). “Status of large eddy simulation: Results of a workshop”. In: *Journal of Fluids Engineering-Transactions of the ASME* 119, pp. 248–262.

Roghair I., Mercado J. M., Annaland M. V. Sint, kuipers H., Sun C., and Lohse D. (2011). “Energy spectra and bubble velocity distributions in pseudoturbulence: Numeical simulations vs. experiments”. In: *International Journal of Multiphase Flow* 9.37, pp. 1093–1098.

Rollet-Miet P., Laurence D., and Ferziger J. (1999). “LES and RANS of turbulent flow in tube bundles”. In: *International Journal of Heat Fluid Flow* 20, pp. 241–254.

Saffman P. G. (1965). “The lit on a small sphere in a slow shear flow”. In: *Journal of Fluid Mechanics* 22, pp. 385–400.

Sagaut P. (2006). *Large-Eddy Simulation for Incompressible Flows - An Introduction.* Berlin: Springer.

Saito N., Pullin D. I., and Inoue M. (2012). "Large eddy simulation of smooth-wall, transitional and fully rough-wall channel flow". In: *Physics of Fluids* 24.7, p. 075103. DOI: `10.1063/1.4731301`. URL: `https://doi.org/10.1063/1.4731301`.

Salewski M., Stankovic D., and Fuchs L. (2007). "A comparison of single and multiphase jets in a crossflow using large eddy simulations". In: *Journal of Engineering Gas Turbines Power* 129.1, pp. 61–68.

Salvetti M. V. and Banerjee S. (1995). "A priori tests of a new dynamic subgrid-scale model for finite-difference large-eddy simulations". In: *Physics of Fluids* 7, pp. 2831–2847.

Salvetti M. V., Zang Y., Street R. L., and Banerjee S. (1997). "Large-eddy simulation of free-surface decaying turbulence with dynamic subgrid-scale models". In: *Physics of Fluids* 9, pp. 2405–2420.

Sarghini F., Piomelli U., and Balaras E. (1999). "Scale-similar models for large-eddy simulations". In: *Physics of Fluids* 11, pp. 1596–1607.

Sato Y., Sadatomi M., and Sekoguchi K. (1981). "Momentum and heat transfer in two-phase bubble flow—I. Theory". In: *International Journal of Multiphase Flow* 7.2, pp. 167–177. ISSN: 0301-9322. DOI: `https://doi.org/10.1016/0301-9322(81)90003-3`. URL: `http://www.sciencedirect.com/science/article/pii/0301932281900033`.

Sato Y. and Sekoguchi K. (1975). "Liquid velocity distribution in two-phase bubble flow". In: *International Journal of Multiphase Flow* 2.1, pp. 79–95. ISSN: 0301-9322. DOI: `https://doi.org/10.1016/0301-9322(75)90030-0`. URL: `http://www.sciencedirect.com/science/article/pii/0301932275900300`.

Schladow S. G. (1992). "Bubble plume dynamics in a stratifies medium and the implications for water quality amelioration in lakes". In: *Water Resources Research* 28.2, pp. 313–321.

– (1993). "Lake destratification by bubbleplume systems: design methodology". In: *J. Hydraul. Engng* 119, pp. 350–368.

Schumann U. (1975). "Subgrid scale model for finite difference simulations of turbulent flows in plane channels and annuli". In: *Journal of Computational Physics*

18.4, pp. 376–404. ISSN: 0021-9991. DOI: `https://doi.org/10.1016/0021-9991(75)90093-5`. URL: `http://www.sciencedirect.com/science/article/pii/0021999175900935`.

Schwartz S., Kempe T., and Frolich J. (2015). “A temporal discretization scheme to compute the motion of light particles in viscous flows by an immersed boundary method”. In: *Journal of Computational Physics* 281, pp. 591–613.

Seol D. G., Bhaumik T., Bergmann C., and Socolofsky S. A. (2007). “Particle image velocimetry measurements of the mean flow characteristics in a bubble plume”. In: *Journal of Hydraulic Engineering* 133.6, pp. 665–676.

Seol D. G., Bryant D. B., and Sokolofsky S. A. (2009). “Measurement of behavioral properties of entrained ambient water in a stratified bubble plume”. In: *Journal of Hydraulic Engineering* 135.(11), pp. 983–988.

Serizawa A. and Kataoka I. (1994). “Disperse Flow - I”. In: *Multiphase Science and Technology* 8.1-4, pp. 125–194. ISSN: 0276-1459.

Shahriari S., Schneider J., and Zenz G. (2020). “Selected applications of an open-source three-dimensional computational fluid dynamic code in hydraulic engineering”. In: *Osterreichische Wasser-und Abfallwirtschaft* 72 (7), pp. 291–307. ISSN: 1613-7566. DOI: `10.1007/s00506-020-00676-7`. URL: `https://doi.org/10.1007/s00506-020-00676-7`.

Shaw R. H. and Schumann U. (1992). “Large-eddy simulation of turbulent flow above and within a forest”. In: *Boundary-Layer Meteorology* 61 (1), pp. 47–64. ISSN: 1573–1472. DOI: `10.1007/BF02033994`. URL: `https://doi.org/10.1007/BF02033994`.

Shi J., Thomas T. G., and Williams J. J. R. (2000). “Free-Surface Effects in Open Channel Flow at Moderate Froude and Reynold’s Numbers”. In: *Journal of Hydraulic Research* 38.6, pp. 465–474. DOI: `10.1080/00221680009498300`. URL: `https://doi.org/10.1080/00221680009498300`.

Simcik M., Ruzicka M. C., and Drahos J. (2008). “Computing the added mass of dispersed particles”. In: *Chemical Engineering Science* 63.18, pp. 4580–4595. ISSN: 0009-2509. DOI: `https://doi.org/10.1016/j.ces.2008.06.011`. URL: `http://www.sciencedirect.com/science/article/pii/S000925090800331X`.

Simiano M. (2005). “Experimental investigation of large-scale three dimensional bubble plume dynamics”. PhD thesis. Zurich, Switzerland: Swiss Federal Institute of Technology.

Simiano M., Zboray R., Cachard F. de, Lakehal D., and Yadigaroglu L. (2006). “Comprehensive experimental investigation of the hydrodyanmics of large-scale, three-dimensional bubble plumes”. In: *International Journal of Multiphase Flow* 32.10, pp. 1160–1181.

Singh K. M., Sandham N. D., and Williams J. J. R. (2007). “Numerical simulation of flow over a rough bed”. In: *Journal of Hydraulic Engineering* 133.4, pp. 386–398. URL: `https://eprints.soton.ac.uk/48560/`.

Smagorinsky J. (1963). “General circulation experiments with the primitive equations”. In: *Mon. Eather Rev.* 3.91, pp. 99–164.

Socolofsky S. A. (2001). “Laboratory experiments of multi-phase plumes in stratification and crossflow”. PhD thesis. Cambridge, MA: Massachusetts Institute of Technology.

Socolofsky S. A. and Adams E. E. (2002). “Multi-phase plumes in uniform and stratified crossflow”. In: *Journal of Hydraulic Research* 40.6, pp. 661–672.

– (2003). “Liquid volume fluxes in stratified multiphase plumes”. In: *Journal of Hydraulic Engineering* 129, pp. 905–914.

– (2005). “Role of slip velocity in the behavior of stratified multiphase plumes”. In: *Journal of Hydraulic Engineering* 131.4, pp. 273–282.

Socolofsky S. A., Adams E. E., Boufadel M. C., Aman Z. M., Johansen Ø., Konkel W. J., Lindo D., Madsen M. N., North E. W., Paris C. B., Rasmussen D., Reed M., Rønningen P., Sim L. H., Uhrenholdt T., Anderson K. G., Cooper C., and Nedwed T. J. (2015). “Intercomparison of oil spill prediction models for accidental blowout scenarios with and without subsea chemical dispersant injection”. In: *Marine Pollution Bulletin* 96, pp. 110–126.

Socolofsky S. A., Adams E. E., and Sherwood C. R. (2011). “Formation dynamics of subsurface hydrocarbon intrusions following the Deepwater Horizon blowout”. In: *Geophys. Res. Lett.* 131.4, pp. 273–282.

Socolofsky S. A., Bhaumik T., and Seol D. G. (2008). “Double plume integral models for near-field mixing in multiphase plumes”. In: *Journal of Hydraulic Engineering* 134.6, pp. 772–783.

Socolofsky S. A., Crounse B. C., and Adams E. E. (2002). “Multi-phase plumes in uniform, stratified, and flowing environments”. In: *Environmental fluid mechanics: theories and applications*. Ed. by H. H. Shen, A. H. D. Cheng, K. H. Wang, M. H. Teng, and C. C. K. Liu. ASCE Publications, pp. 85–126.

Sokolichin A. and Eigenberger G. (1994). “Gas-liquid flow in bubble columns and loop reactors. Part I. Detailed modeling and numerical simulation”. In: *Chemical Engineering Science* 49, pp. 5735–5746.

– (1999). “Applicability of the standard k– turbulence model to the dynamic simulation of bubble columns: Part I. Detailed numerical simulations”. In: *Chemical Engineering Science* 54.13, pp. 2273–2284. ISSN: 0009-2509. DOI: `https://doi.org/10.1016/S0009-2509(98)00420-5`. URL: `http://www.sciencedirect.com/science/article/pii/S0009250998004205`.

Sokolichin A., Eigenberger G., Lapin A., and Lubbert A. (1997). “Dynamic numerical simulation of gas-liquid two-phase flows: Euler/Euler versus Euler/Lagrange”. In: *Chemical Engineering Science* 52.4, pp. 611–626. ISSN: 0009-2509. DOI: `https://doi.org/10.1016/S0009-2509(96)00425-3`. URL: `http://www.sciencedirect.com/science/article/pii/S0009250996004253`.

Sommerfeld M. (2001). “Validation of a stochastic Lagrangian modelling approach for inter-particle collisions in homogeneous isotropic turbulence”. In: *International Journal of Multiphase Flow* 27.10, pp. 1829–1858. ISSN: 0301-9322. DOI: `https://doi.org/10.1016/S0301-9322(01)00035-0`. URL: `http://www.sciencedirect.com/science/article/pii/S0301932201000350`.

Sommerfeld M., Kohnen G., and Rueger M. (1993). “Some open questions and inconsistencies of Lagrangian particle dispersion models”. In: *Proceedings of the 9th Symposium on Turbulent Shear Flows*. Kyoto, Japan.

Sotiropoulos F. and Yang X. (2014). “Immersed boundary methods for simulating fluid-structure interaction”. In:

Spalart P. R., Jou W.-H., Strelets M., and Allmaras S. R. (1997). “Comments on the Feasibility of LES for Wings, and on a Hybrid RANS/LES Approach”. In: *Advances in DNS/LES: Direct numerical simulation and large eddy simulation*. Ed. by C. Liu, Z. Liu, and L. Sakell. Columbus, OH, USA: Greyden Press, pp. 137–148. ISBN: 1570743657.

Sridhar G. and Katz J. (1995). “Drag and lift forces on microscopic bubbles entrained by a vortex”. In: *Physics of Fluids* 7.2, pp. 389–399. DOI: `10.1063/1.868637`. URL: `https://doi.org/10.1063/1.868637`.

Stoesser T. (2014). “Large-eddy simulation in hydraulics: Quo Vadis?” In: *Journal of Hydraulic Research* 52, pp. 441–452. DOI: `10.1080/00221686.2014.944227`.

Stoesser T., Braun C., García-Villalba M., and Rodi W. (2008). “Turbulence Structures in Flow over Two-Dimensional Dunes”. In: *Journal of Hydraulic Engineering* 134.1, pp. 42–55. DOI: `10.1061/(ASCE)0733-9429(2008)134:1(42)`. URL: `https://ascelibrary.org/doi/abs/10.1061/(ASCE)0733-9429(2008)134:1(42)`.

Stoesser T., McSherry R., and Fraga B. (2015). “Secondary currents and turbulence over a non-uniformly roughened open-channel bed”. In: *Water* 9.7.

Stoesser T. and Nikora V. I. (2008). “Flow structure over square bars at intermediate submergence: Large Eddy Simulation study of bar spacing effect”. In: *Acta Geophysica* 56.3, pp. 876–893. ISSN: 0001-5725. DOI: `10.2478/s11600-008-0030-1`.

Stoesser T., Palau-Salvador G., and Rodi W. (2009). “Large eddy simulation of turbulent flow through submerged vegetation”. In: *Transport in Porous Media* 78, pp. 347–365.

Stoker R. L. (1946). “Methods of Producing Uniform Velocity Distribution”. In: *Industrial & Engineering Chem* 38, pp. 622–624.

Stolz S. and Adams N.A. (1999). “An approximate deconvolution procedure for large-eddy simulation”. In: *Physics of Fluids* 11, pp. 1699–1703.

Stolz S., Adams N.A., and Kleiser L. (2001). “An approximate deconvolution model for large-eddy simulation with application to incompressible wall-bounded flows”. In: *Physics of Fluids* 13, pp. 997–1015.

Stolz S., Schlatter P., and Kleiser L. (2005). “High-pass filtered eddy viscosity models for LES for compressible wall bounded flows”. In: *Journal of Fluids Engineering* 127, pp. 666–673.

– (2007). “LES of sub-harmonic transition in a supersonic boundary layer”. In: *AIAA Journal* 5.45, pp. 1019–1027.

Sunkorn R., Derksen J. J., and Khinast J. G. (2011). “Modeling of turbulent gas-liquid bubbly flows using stochastic Lagrangian model and lattice-Boltzman scheme”. In: *Chemical Engineering Science* 66, pp. 2745–2757.

Tabib M. V., Roy S. A., and Joshi J. B. (2008). “CFD simulation of bubble column - an analysis of interphase forces and turbulence models”. In: *Chemical Engineering Science* 139.3, pp. 589–614.

Tabib M. V. and Schwarz P. (2011). “Quantifying sub-grid scale (SGS) turbulent dispersion force and its effect using one-equation SGS large eddy simulation (LES) model in a gas–liquid and a liquid–liquid system”. In: *Chemical Engineering Science* 66.14, pp. 3071–3086. ISSN: 0009-2509. DOI: `https://doi.org/10.1016/j.ces.2011.03.058`. URL: `http://www.sciencedirect.com/science/article/pii/S0009250911002399`.

Takagi S. and Matsumoto Y. (1995). “Three dimensional calculation of a rising bubble”. In: *Proceedings of the Second International Conference of Multiphase Flow*. Kyoto, Japan.

Takahashi K., Endoh K., Oyama H., and Mori S. (1992). “A Virtual Mass and a Drag Coefficients for an Oscillating Particle”. In: *Journal of Chemical Engineering of Japan* 25.6, pp. 683–685. DOI: `10.1252/jcej.25.683`.

Takemura F. and Magnaudet J. (2003). “The transverse force on clean and contaminated bubbles rising near a vertical wall at moderate Reynolds number”. In: *Journal of Fluid Mechanics* 495, pp. 235–253. DOI: `10.1017/S0022112003006232`.

Thomas T. G., Leslie D. C., and Williams J. J. R. (1995). “Free Surface Simulations Using a Conservative 3D Code”. In: *Journal of Computational Physics* 116.1, pp. 52–68. ISSN: 0021-9991. DOI: `https://doi.org/10.1006/jcph.1995.1005`. URL: `http://www.sciencedirect.com/science/article/pii/S0021999185710054`.

Thomas T. G. and Williams J. J. R. (1995). “Large eddy simulation of turbulent flow in an asymmetric compound open channel”. In: *Journal of Hydraulic Research* 33.1, pp. 27–41. DOI: `10.1080/00221689509498682`. URL: `https://doi.org/10.1080/00221689509498682`.

Thompson J. F., Warsi U. A., and Mastin C. W. (1985). “Numerical grid generation: Foundations and applications”. In:

Thorne D. T. (2003). “Multigrid with Cache Optimizations on Adaptive Mesh Refinement Hierarchies”. PhD thesis. Lexington, Kentucky: Kentucky University.

Tomiyama A. (2004). “Drag, lift and virtual mass forces acting on a single bubble”. In: *Third International Symposium on Two-Phase Flow Modeling and Experimentation*. Pisa, Italy, pp. 22–24.

Tomiyama A., Sou A., Zun I., Kanami N., and Sakaguchi T. (1995). “Effects of E””number and dimensionless liquid volumetric flux on lateral motion of a bubble in a laminar duct flow”. In: *Advances in Multiphase Flow*, pp. 3–15.

Tomiyama A., Tamai H., Zun I., and Hosokawa S. (2002). “Transverse migration of single bubbles in simple shear flows”. In: *Chemical Engineering Science* 57, pp. 1849–1858.

Tomiyama A., Zun I., Sou A., and Sakaguchi T. (1993). “Numerical analysis of bubble motion with the VOF method”. In: *Nuclear Engineering Design* 141, pp. 69–82.

Torti E., Sibilla S., and Raboni M. (2013). “An Eulerian-Lagrangian method for the simulation of the oxygen concentration dissolved by a two-phase turbulent jet system”. In: *Computers and Structures* 129, pp. 207–217.

Touber E. and Sandham N. D. (2009). “Large-eddy simulation of low-frequency unsteadiness in a turbulent shock-induced separation bubble”. In: *Theoretical and Computational Fluid Dynamics* 23, pp. 79–107.

Toutant A., Chandesris M., Jamet D., and Lebaigue O. (2009a). “Jump conditions for filtered quantities at an under-resolved discontinuous interface. Part 1: Theoretical development”. In: *International Journal of Multiphase Flow* 35.12, pp. 1100–1118. ISSN: 0301-9322. DOI: `https://doi.org/10.1016/j.ijmultiphaseflow.2009.07.009`. URL: `http://www.sciencedirect.com/science/article/pii/S030193220900130X`.

– (2009b). “Jump conditions for filtered quantities at an under-resolved discontinuous interface. Part 2: A priori tests”. In: *International Journal of Multiphase Flow* 35.12, pp. 1119–1129. ISSN: 0301-9322. DOI: `https://doi.org/10.1016/j.ijmultiphaseflow.2009.07.010`. URL: `http://www.sciencedirect.com/science/article/pii/S0301932209001293`.

Tryggvason G., Bunner B., Esmaeeli A., Juric D., Al-Rawahi N., Tauber W., Han J., Nas S., and Jan Y. J. (2001). “A front-tracking method for the computations of multi-phase flow”. In: *Journal of Computational Physics* 169.2, pp. 708–759.

Uhlmann M. (2005). “An immersed boundary method with direct forcing for the simulation of particulate flows”. In: *J. Comp. Physics* 209, pp. 448–476.

Van Driest E. R. (1956). “On the turbulent flow near wall”. In: *Journal of Aeronautical Science* 23, pp. 1007–1011.

van Rijn L. C. (1984). “Sediment Transport, Part III: Bed forms and Alluvial Roughness”. In: *Journal of Hydraulic Engineering* 110.12, pp. 1733–1754. DOI: `10.1061/(ASCE)0733-9429(1984)110:12(1733)`. URL: `https://ascelibrary.org/doi/abs/10.1061/(ASCE)0733-9429(1984)110:12(1733)`.

Veloudis I., Yang Z., Mcguirk J. J., Page G. J., and Spencer A. (2007). “Novel implementation and assessment of a digital filter based approach for the generation of LES inlet conditions”. In: *Flow Turbulence and Combustion* 79, pp. 1–24.

Versteeg H. K. and Malalasekera W. (2007). *An introduction to computational fluid dynamics: The finite volume method.* Harlow: Pearson Education Limited.

Vreman A. W. (2004). “An eddy-viscosity subgrid-scale model for turbulent shear flow: Algebraic theory and applications”. In: *Physics of Fluids* 16.10, pp. 3670–3681. DOI: `10.1063/1.1785131`. URL: `https://doi.org/10.1063/1.1785131`.

Wallis G. B. (1990). “Inertial coupling in two-phase flow: macroscopic properties of suspensions in an inviscid fluid”. In: *Advances in Multiphase Science and Technology* 5.1-4, pp. 239–361. ISSN: 0276-1459.

Wang H. and Law A. W.-K. (2002). “Second-order integral model for a round turbulent buoyant jet”. In: *J. Fluid Mech.* 459, pp. 397–428.

Wang Y., Simakhina S., and Sussman M. (2012). “A hybrid level set-volume constraint method for incompressible two-phase flow”. In: *Journal of Computational Physics* 231, pp. 6438–6471.

Watts A. (2018). *wattsupwiththat.com.* `wattsupwiththat.com/2018/06/26/scientists-use-sophisticated-microphones-to-listen-to-the-ocean-pass-gas`. Accessed: 2018-08-10.

Weber T. C., Robertis A. D., Greenaway S. F., Smith S., Mayer L., and Rice G. (2012). “Estimating oil concentration and flow rate with calibrated vessel-mounted acoustic echo sounders”. In: *Proc. Natl Acad. Sci.* 109, pp. 240–245.

Werner H. and Wengle H. (1993). “Large-Eddy Simulation of Turbulent Flow Over and Around a Cube in a Plate Channel”. In: *Turbulent Shear Flows 8.* Ed. by

F. Durst, R. Friedrich, B. E. Launder, F. W. Schmidt, U. Schumann, and J. H. Whitelaw. Berlin, Heidelberg: Springer, pp. 155–168. ISBN: 978-3-642-77674-8.

Wuest A., Brooks N. H., and Imboden D. M. (1992). “Bubble plume model for lake restoration”. In: *Water Resources Research* 28, pp. 3235–3250.

Xie Z. T. and Castro I. P. (2008). “Efficient generation of inflow conditions for large eddy simulation of street-scale flows”. In: *Flow Turbulence and Combustion* 81, pp. 449–470.

*xylemanaltics.co.uk* (2000). `https://https://www.xylemanalytics.co.uk/applications`. Accessed: 2020-09-30.

Yang D., Chamecki M., and Meneveau C. (2014). “Inhibition of oil plume dilution in Langmuir ocean circulation”. In: *Geophs. Res. Lett.* 41, pp. 1632–1638.

Yang D., Chen B., Chamecki M., and Meneveau C. (2015). “Oil plumes and dispersion in Langmuir, upper-ocean turbulence: large-eddy simulations and K-profile parametrization”. In: *J. Geophys. Res. Oceans* 120, pp. 4729–4759.

Yang X., Zhang X., Li Z., and He G. W. (2009). “A smoothing technique for discrete delta functions with application to immersed boundary method in moving boundary simulations”. In: *Journal of Computational Physics* 228.20, pp. 7821–7836.

Yapa P. D., Zheng L., and Nakata K. (1999). “Modeling underwater oil/gas jets and plumes”. In: *Journal of Hydraulic Engineering* 125.5, pp. 481–491.

Yih C. S. (1988). *Fluid Mechanics.* CT, USA: West River Press.

Yoshizawa A. (1982). “A statistically-derived subgrid model for the large-eddy simulation of turbulence”. In: *Physics of Fluids* 25, pp. 1532–1539.

Yoshizawa A. and Horiuti K. (1985). “A statistically-derived subgrid-scale kinetic energy model for the large-eddy simulation of turbulent flows”. In: *Journal of the Physical Society of Japan* 54, pp. 2834–2839.

Youngs D. L. (1982). “Time-Dependent Multi-Material Flow with Large Fluid Distortion”. In: *Numerical Methods for Fluid Dynamics.* Ed. by K. W. Morton and M. J. Baines. New York, NY, USA: Academic Press, pp. 273–285. URL: `https://ci.nii.ac.jp/naid/10027152303/en/`.

Yuan L. L., Street R. L., and Ferziger J. H. (1999). “Large-eddy simulations of a round jet in crossflow”. In: *Journal Fluid Mechanics* 379, pp. 71–104.

Yue W., Lin C.-L., and Patel V. C. (2005a). “Coherent Structures In Open-Channel Flows Over a Fixed Dune”. In: *Journal of Fluids Engineering* 127.5, pp. 858–864. ISSN: 0098-2202. DOI: `10.1115/1.1988345`. URL: `https://doi.org/10.1115/1.1988345`.

– (2005b). “Large eddy simulation of turbulent open-channel flow with free surface simulated by level set method”. In: *Physics of Fluids* 17.2, p. 025108. DOI: `10.1063/1.1849182`. URL: `https://doi.org/10.1063/1.1849182`.

– (2006). “Large-Eddy Simulation of Turbulent Flow over a Fixed Two-Dimensional Dune”. In: *Journal of Hydraulic Engineering-ASCE* 132, pp. 643–651. DOI: `10.1061/(ASCE)0733-9429(2006)132:7(643)`.

Yujie Z., Mingyan L., Yonggui X., and Can T. (2012). “Three-dimensional volume of fluid simulations on bubble formation and dynamics in bubble columns”. In: *Chemical Engineering Science* 73, pp. 55–78.

Zang Y., Street R. L., and Koseff J. R. (1993). “A dynamic mixed subgrid-scale model and its application to turbulent recirculating flows”. In: *Physics of Fluids* 5, pp. 3186–3196.

Zedler E. A. (2001). “Large-eddy simulation of sediment transport: Currents over ripples”. In: *ASCE, Journal of Hydraulic Engineering* 127, pp. 444–452.

Zhang D., Deen N. G., and Kuipers J. A. M. (2006). “Numerical simulation of the dynamic flow behavior in a bubble column: a study of closures fir turbulence and interface forces”. In: *Chemical Engineering Science* 61.23, pp. 7593–7608.

– (2009). “Euler-euler modeling of flow, mass transfer, and chemical reaction in a bubble column”. In: *Industrial and Engineering Chemistry Research* 48.1, pp. 47–57.

Zhang W. and Zhu D. Z. (2013). “Bubble characteristics of air-water bubble jets in crossflow”. In: *International Journal of Multiphase Flow* 55, pp. 156–171.

Zheng L., Yapa P. D., and Chen F. (2003). “A model for simulating deepwater oil and gas blowouts-Part I: Theory and model formulation”. In: *Journal of Hydraulic Research* 41.4, pp. 339–351.

Zhiyin Y. (2015). “Large-eddy simulation: Past, present and the future”. In: *Chinese Journal of Aeronautics* 28.1, pp. 11–24. ISSN: 1000-9361. DOI: `https://doi.org/10.1016/j.cja.2014.12.007`. URL: `http://www.sciencedirect.com/science/article/pii/S1000936114002064`.